University of California
Santa Barbara

Spin-polarized electrons in topological materials and III-V photocathodes

A dissertation submitted in partial satisfaction
of the requirements for the degree

Doctor of Philosophy
in
Materials

by

Aaron Nathan Engel

Committee in charge:

Professor Christopher J. Palmstrøm, Chair
Professor John W. Harter
Professor Stephen D. Wilson
Marcy L. Stutzman, PhD., Jefferson Lab

June 2024

The Dissertation of Aaron Nathan Engel is approved.

Professor John W. Harter

Professor Stephen D. Wilson

Marcy L. Stutzman, PhD., Jefferson Lab

Professor Christopher J. Palmstrøm, Committee Chair

June 2024

Spin-polarized electrons in topological materials and III-V photocathodes

by

Aaron Nathan Engel

Acknowledgements

Doing a PhD. is a marathon, not a sprint. This work would not have been possible without all of the support I received over the last five years both within UCSB and outside of it. First I would like to thank my advisor, Chris Palmstrøm, for teaching me how to be the best scientist I could be. His enthusiasm for my own ideas allowed me to succeed (and fail) on my own merits, while also being provided with a constant supply of experiments to try. His hands-on, can-do attitude, insistence on good science, and dislike of "black boxes" was inspiring. I am proud to have been trained in his group. The rest of my committee—Marcy Stutzman, John Harter, and Stephen Wilson—helped me focus on the forest rather than the leaves. Marcy in particular was invaluable in teaching me the constraints and history of spin-polarized photocathodes (and performed the actual measurement of the spin polarization).

I would like to thank past and current students in the Palmstrøm group for their guidance and support. A long day of maintenance in lab or a particularly difficult problem being discussed in the hallways and office are not things I will soon forget. Specifically, I would like to thank Mihir and Tony for being the wise postdocs that answered my unending questions and triple-checks on whether a valve was open or closed in my first year. I want to thank Hadass for teaching me about growth, ARPES, how to be stressed about beamtime, and the right way to do things both in and out of the lab. Connor and Jason, thank you for riding through our synced courses and PhDs together. Our discussions were always rewarding, informative, and most importantly, fun. The physics postdocs Wilson and Paul, thank you for teaching me to think in Hamiltonians and for reminding me just how cool it is to do what we do. I also want to thank the new(ish) students in the group Yu, Teun, and Shirshendu for letting me teach them and keeping the lab running into the future. Thank you to Wilson, Paul, Hadass, Shinichi, and Alex

for enjoying (suffering?) beamtime and exploring the varied food options in the Bay Area.

The ARPES in this work would not have been possible without the extraordinary effort that it takes to keep the endstations running. Alexei Fedorov (ALS 10.0.1.2) and Makoto Hashimoto and Donghui Lu (SSRL 5-2), the hard work to keep these state-of-the-art systems available is much appreciated. A special thanks is due to Alexei for all of his help with our own ARPES set up and his support for our experiments. I would also like to thank Doug Rehn and the rest of the Physics Machine shop staff. The dreaded 6 AM trip for a rush job always resulted in the solution to our problem. His contributions to the Palmstrøm ARPES manipulator and the vacuum suitcases were essential.

A large portion of the work in this thesis benefited heavily from collaboration with other research groups. Prof. Paul Crowell's group at University of Minnesota fabricated and performed anomalous Hall and Nernst measurements on my Heusler thin films. The discussions I had with George de Coster, Patrick Taylor, Owen Vail, and Patrick Folkes at ARL; Arnold Kiefer and Alex Khaetskii at AFRL; Stefan Zollner at NMSU; Yilmaz Gul and Stuart Holmes at University College London; Malcolm Jardine and newly Zefeng Cai in the group of Noa Marom at CMU; resulted in a much better understanding of the electronic structure of α-SnGe and how best to grow it. Some of these discussions with ARL are even turning into a paper, discussed in Chapter 6.

I appreciate the constant small- and large-scale discussions with the folks in the MBE Lab concerning both their research and equipment troubles and successes; commiseration is the best way to deal with things going wrong. Kurt Olsson and John English, who have kept the MBE lab running, have always been quick to help out by donating their time, equipment, and knowledge when I end up in a pickle. The environment of the MBE Lab, including our weekly MBE Meeting, provided me a path to learn so much more beyond my direct field of research and strongly influenced my career choices.

My friends inside and outside of Santa Barbara helped make the times outside of work so enjoyable: Caelin, Jenny, Rick, Nat, Michael, Tyler, Diana, *et al.* you provided great balance to my time at UCSB. The love and support of my family was invaluable: Mom, Dad, Kurt, Val, Erica, Suzy, Mimi and everyone else made hard days easy even though I could never really figure out how to tell you what I was working on.

Even after this outpouring of gratitude, there are still so many unnamed who have helped and guided me throughout this process however small or large their part was. You are not forgotten, but the acknowledgements section *probably* should not be as long as the actual dissertation. Finally, last and the absolute opposite of least I would like to thank Mary, my phenomenal fiancée, for her love, support, and sacrifices throughout most of my PhD. process while also going through her very own PhD. experience. Thank you for adding so much joy to the last few years and putting up with the travel, deadlines, and too-often late nights. Our splitting will continue and continue.

Curriculum Vitæ

Aaron Nathan Engel

Education

2024	Ph.D. in Materials, University of California, Santa Barbara. Advisor: Christopher J. Palmstrøm
2019	B.S. Chemical Engineering & B.A. Economics, University of Rochester

Academic Experience

2019–2024	Graduate Student Researcher, Palmstrøm Group. University of California, Santa Barbara. Santa Barbara, CA.
Summer 2019	Plasma Physics and Materials Science Intern, Sandia National Laboratory. Livermore, CA.
Spring 2019	Undergraduate Researcher, Nanoelectronic and Quantum Device Laboratory. University of Rochester. Rochester, NY.
Summer 2018	Plasma Physics and Materials Science Intern, Sandia National Laboratory. Livermore, CA.
Spring 2018	Undergraduate Researcher, Shestopalov Lab, University of Rochester. Rochester, NY.

Teaching Experience

Winter 2021–2024	Teaching Assistant, MATR 215B: Semiconductor Device Processing
Fall 2020	Teaching Assistant, MATR 200A: Thermodynamic Foundation of Materials

Publications

"Determining the bulk and surface electronic structure of α-Sn/InSb(001) with spin- and angle-resolved photoemission spectroscopy" **Aaron N. Engel**, Paul J. Corbae, Hadass S. Inbar, Connor P. Dempsey, Shinichi Nishihaya, Wilson Yánez-Parreño, Yu Hao Chang, Jason T. Dong, Alexei V. Fedorov, Makoto Hashimoto, Donghui Lu, Christopher J. Palmstrøm arXiv:2403.01051 (2024).

"Cryogenic growth of tantalum thin films for low-loss superconducting circuits" Teun A. J. van Schijndel, Anthony P. McFadden, **Aaron N. Engel**, Jason T. Dong, Wilson J. Yánez-Parreño, Manisha Parthasarathy, Raymond W. Simmonds, Christopher J. Palmstrøm arXiv:2405.12417 (2024).

"Growth and characterization of α-Sn thin films on In- and Sb-rich reconstructions of InSb(001)" **Aaron N. Engel**, Connor P. Dempsey, Hadass S. Inbar, Jason T. Dong,

Shinichi Nishihaya, Yu Hao Chang, Alexei V. Fedorov, Makoto Hashimoto, Donghui Lu, Christopher J. Palmstrøm *Phys. Rev. Materials* **8**, 044202 (2024). *Editor's Suggestion*

"Strain Solitons in an Epitaxially Strained van der Waals-like Material" Jason T. Dong, Hadass S. Inbar, Connor P. Dempsey, **Aaron N. Engel**, and Christopher J. Palmstrøm *Nano Letters* **24** 4493–4497 (2024).

"Inversion Symmetry Breaking in Epitaxial Ultrathin Bi (111) Films" Hadass S. Inbar, Muhammad Zubair, Jason T. Dong, **Aaron N. Engel**, Connor P. Dempsey, Yu Hao Chang, Shinichi Nishihaya, Shoaib Khalid, Alexei V. Fedorov, Anderson Janotti, Chris J. Palmstrøm arXiv:2302.00803 (2023).

"Tuning the band topology of GdSb by epitaxial strain." Hadass S. Inbar, Dai Q. Ho, Shouvik Chatterjee, **Aaron N. Engel**, Shoaib Khalid, Connor P. Dempsey, Mihir Pendharkar, Yu Hao Chang, Shinichi Nishihaya, Alexei V. Fedorov, Donghui Lu, Makoto Hashimoto, Dan Read, Anderson Janotti, Christopher J. Palmstrøm *APL Mater.* **11** 111106 (2023).

"First-Principles Assessment of CdTe as a Tunnel Barrier at the α-Sn/InSb Interface" Malcolm J. A. Jardine, Derek Dardzinski, Maituo Yu, Amrita Purkayastha, An-Hsi Chen, Yu-Hao Chang, **Aaron Engel**, Vladimir N. Strocov, Moïra Hocevar, Chris Palmstrøm, Sergey M. Frolov, and Noa Marom *ACS Appl. Mater. Interfaces* **15**,16288–16298 (2023).

"Epitaxial growth, magnetoresistance, and electronic band structure of GdSb magnetic semimetal films" Hadass S. Inbar, Dai Q. Ho, Shouvik Chatterjee, Mihir Pendharkar, **Aaron N. Engel**, Jason T. Dong, Shoaib Khalid, Yu Hao Chang, Taozhi Guo, Alexei V. Fedorov, Donghui Lu, Makoto Hashimoto, Dan Read, Anderson Janotti, and Christopher J. Palmstrøm *Phys. Rev. Materials* **6**, L121201 (2022).

"Deciphering the influence of high-flux helium plasma exposure on tungsten nanostructure growth using real-time, in situ spectroscopic ellipsometry" Robert D. Kolasinski, Chun-Shang Wong, **Aaron Engel**, Josh A. Whaley, Frances I. Allen, Dean A. Buchenauer *J. Appl. Phys.* **131**, 063303 (2022).

Presentations

Aaron N. Engel, Paul J. Corbae, Hadass S. Inbar, Connor P. Dempsey, Shinichi Nishihaya, Alexei V. Fedorov, Makoto Hashimoto, Donghui Lu, Christopher J. Palmstrøm **Electronic structure of strain- and thickness-tuned epitaxial α-$Sn_{1-x}Ge_x$ thin films as studied by ARPES and spin-ARPES** *American Physical Society (APS) March Meeting 2024, Minneapolis, MN, USA, March 2024*

Aaron N. Engel, Hadass S. Inbar, Paul J. Corbae, Connor P. Dempsey, Shinichi Nishihaya, Yuhao Chang, Alexei V. Fedorov, Makoto Hashimoto, Donghui Lu, Christopher J. Palmstrøm **Growth and angle-resolved photoemission of strain- and thickness-tuned epitaxial α-Sn thin films** *Physics and Chemistry of Solids and Interfaces (PCSI-49), Santa Fe, NM, USA, January 2024*

Aaron N. Engel, Marcy L. Stutzman, Jason T. Dong, Christopher J. Palmstrøm **Strained superlattice InAlGaAs/AlGaAs spin-polarized photocathodes implemented with random and digital alloying** *Photocathode Physics for Photoinjectors (P^3), Stony Brook, NY, USA, October 2023* **Invited Speaker**

Aaron N. Engel, Marcy L. Stutzman, Jason T. Dong, Christopher J. Palmstrøm **Strained superlattice InAlGaAs/AlGaAs spin-polarized photocathodes implemented with random and digital alloying** *North American Molecular Beam Epitaxy Conference (NAMBE), Madison, WI, USA, September 2023*

Aaron N. Engel, Marcy L. Stutzman, Jason T. Dong, Christopher J. Palmstrøm **Molecular beam epitaxy of strained superlattice InAlGaAs/AlGaAs spin-polarized photocathodes** *Electronic Materials Conference (EMC-67), June 2023* **Best Oral Presentation Finalist**

Aaron N. Engel, Connor P. Dempsey, Shinichi Nishihaya, Yuhao Chang, Makoto Hashimoto, Donghui Lu, Christopher J. Palmstrøm **Substrate preparation and MBE growth of high quality α-Sn topological insulator thin films on InSb(001) surfaces** *North American Molecular Beam Epitaxy Conference (NAMBE), Rehoboth Beach, DE, USA, October 2022*

Aaron N. Engel, Dai Quoc Ho, Han Yu, Shinichi Nishihaya, Kaifeng (Felix) Yang, Hadass S. Inbar1 , Paul A. Crowell, Anderson Janotti, and Christopher J. Palmstrøm **Molecular beam epitaxy growth of Co_2FeSn: a Heusler nodal line semimetal candidate with theorized giant room remperature anomalous transport** *Materials Research Society (MRS) Spring 2022, Honolulu, HI, USA, May 2022*

Abstract

Spin-polarized electrons in topological materials and III-V photocathodes

by

Aaron Nathan Engel

As Moore's law approaches its end, the search for other computing architectures becomes more important. One of these alternatives is spintronics, which relies on the generation of spin-polarized electrons in thin film heterostructures. In recent years, topological materials have been found as a promising method of producing solid state spin-polarized electrons. In addition, III-V photocathodes can be used to produce spin-polarized electrons in vacuum. This dissertation presents growth optimization of different materials intended for spin-polarized electron production. After this, we sought a better understanding of the properties and electronic structure of these materials through a variety of *in situ* and *ex situ* characterization techniques.

Co_2FeSn is a Heusler alloy proposed to have giant anomalous Hall and Nernst conductivities at room temperature. A variety of methods before, during, and after growth were explored to improve the crystalline ordering of Co_2FeSn thin films; it was found that higher disorder actually led to higher anomalous transport coefficients at room temperature. Further development of this material system could lead to high performance room temperature spin-transfer and spin-orbit torque devices.

α-Sn thin films grown by molecular beam epitaxy on InSb substrates have been found to be relatively easily tuned through multiple topologically non-trivial phases, each with different applications. This material has already demonstrated exceptional potential for low power current-induced spin-orbit torque based devices at room temperature—likely owing to the presence of spin-polarized surface states. Using spin- and angle-resolved pho-

toemission spectroscopy, we clarified the number and the nature of spin-polarized surface states in this system. The confinement-induced three-dimensional topological insulator phase was clearly benchmarked on the topological phase diagram of α-Sn. Hybridization with the substrate changes the film thickness-induced boundaries in the topological phase diagram. In addition, the substrate appears to contribute to a bulk inversion symmetry breaking in α-Sn films which further modifies the α-Sn topological phase diagram.

Alloying isostructural, isovalent Ge into α-Sn allows for the application of tensile strain to these films, opening up an as-yet unexplored section of this topological phase diagram. High concentrations of Ge ($> 5\%$) were alloyed into ultrathin α-Sn films, leading to the discovery of unexpected spin-polarized surface states and an unexpected topological phase transition. These studies provide an avenue for deterministic control of the topological phase of the α-$Sn_{1-x}Ge_x$ system. Control of the bulk band gap and the dispersion of spin-polarized surface states is essential for optimizing the performance of devices which use this material.

Finally, we developed strained superlattice InAlGaAs/AlGaAs spin-polarized photocathodes grown by molecular beam epitaxy. This materials system presents a less expensive alternative to the usual GaAs/GaAsP superlattice system; InAlGaAs/AlGaAs superlattices are both easier to grow and more compatible with epitaxial wafer foundries. We successfully demonstrated acceptable spin polarization and quantum efficiency from InAlGaAs/AlGaAs photocathodes and further improved performance by incorporating a digital alloy scheme. These photocathodes may be used in a range of materials characterization techniques which make use of incident electrons and as spin-polarized electron sources in high energy physics and nuclear physics experiments.

Contents

Chapter 1

Introduction

Spintronics—a portmanteau of spin and electronics—is associated with seeking to use the spin degree of freedom (a vector quantity) to replace the charge degree of freedom (a scalar quantity) for information storage or transfer. As Moore's law comes to a close, spintronics has been positioned as an alternative to conventional electronics [1]. This is evident in the unabated growth of the (over 30-year-old) field over recent years, seen in Fig. 1.1. In the growing use and scope of "the cloud", the waste heat produced and resources consumed by computation and data storage is becoming a significant driver of climate change and other environmental effects [2]. Devices based on the transfer of the electron spin, rather than the electron charge, produce much lower Joule heating and can operate with lower waste heat and power consumption [3]. Spintronics-based devices such as the magnetic tunnel junction have already been adopted in the read heads of non-volatile hard disk drive memories and more recently into new MRAM (magnetoresistive random access memory) devices [3]. Other devices such as spin-based nano-oscillators can be used for efficient microwave components on integrated circuits [4]. New applications and devices architectures are continuously proposed while making use of novel materials and fabrication techniques (Fig. 1.2). The newest tool to increase the performance of

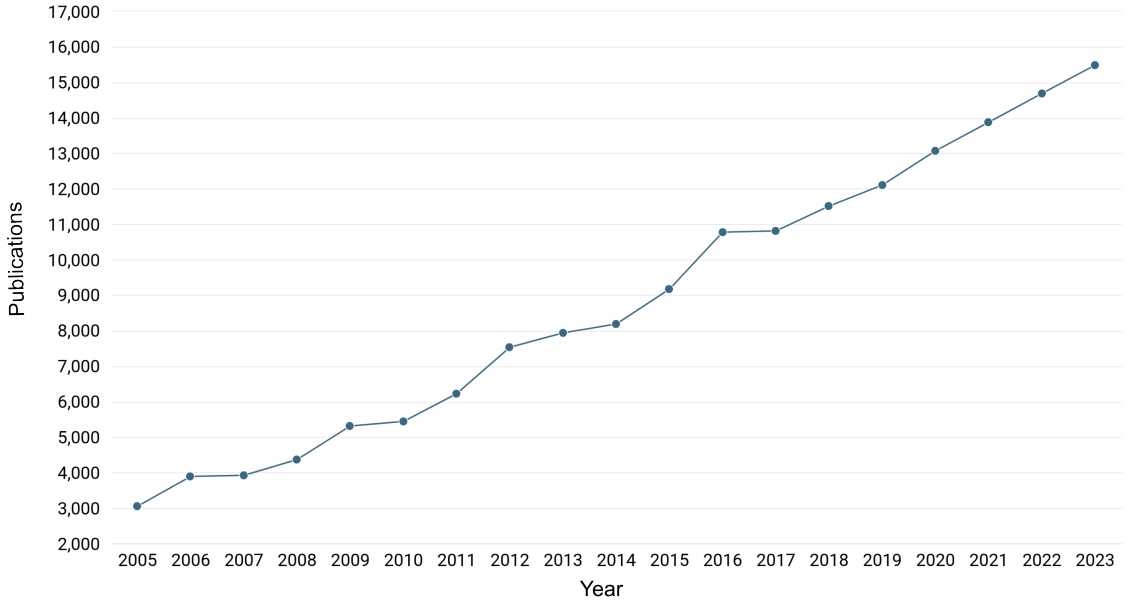

Figure 1.1: Publications per year related to spintronics. Data accessed via [6].

various spintronic devices is the incorporation of topologically non-trivial materials; these materials come in many phases with different properties but are typically characterized by the efficient generation of a spin current which can serve as a key component in the above technologies [5].

Over a similar time period that spintronics has grown as a field while taking advantage of low energy spin-polarized electrons (on the order of meV$\rightarrow$ eV), the field of particle physics has been studying the fundamental mysteries of the universe using high energy (GeV) spin-polarized electrons [7]. Spin-polarized photocathodes, typically based on III-V semiconductors, are used to generate these spin-polarized electron beams [8, 9]. With more efficient spin-polarized photocathodes, new high energy or nuclear physics experiments may be designed and "old" experiments may be run more quickly, allowing for more physics to be explored faster [7]. These electron sources can also be incorporated into various materials science techniques which, coincidentally, can allow a deeper study

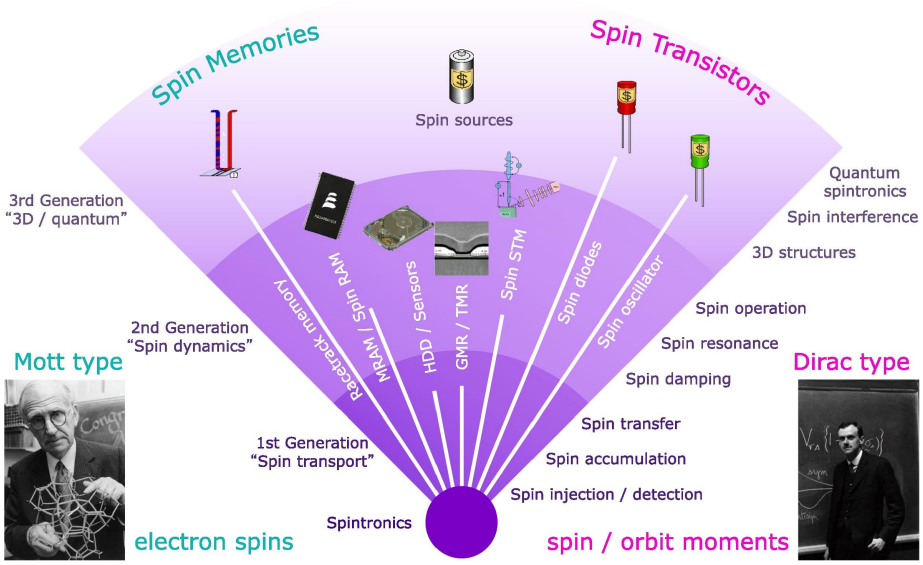

Figure 1.2: Survey of various spintronic devices. Reprinted from [3] via the Creative Commons CC BY license.

of topologically non-trivial phases.

There has even recently been more direct cross-talk between these fields. Attempts have been made to use a spin-polarized photocathode in a vacuum-based spin light emitting diode [10] or to use topological insulators as photocathodes [11].

In order to understand these materials, we first discuss the basic physics governing spin at the atomic limit and in the solid state. From here we explore the physics and applications of topologically non-trivial materials and spin-polarized photocathodes and the benefits that the materials discussed in this thesis—Co_2FeSn, α-Sn, and InAlGaAs/AlGaAs strained superlattices—can provide.

1.1 Electron spin physics at the hydrogenic limit

During the development of the quantum theory in the late 1800s and early 1900s, it was well known that the emission spectra of certain elements showed sharp lines at discrete energies [12]. Balmer and Rydberg were able to show that the formula describing

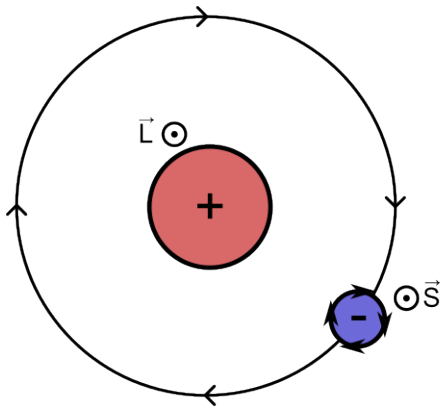

Figure 1.3: A simplified picture of the hydrogenic atom. Electrons have an an orbital angular moment L and an intrinsic angular momentum S, but do not truly spin around their centers.

the spacing between these lines was controlled by two integer values. In addition, by the Rydberg-Ritz combination rule it was known that the energy of any two emission lines was equal to the sum or difference of two other emission lines [12]. Niels Bohr first explained these observations in the famous Bohr model by treating electrons such that they have a stationary (classically forbidden) orbit (Fig. 1.3). The radii of these stationary orbits were then set at discrete intervals given by a quantized angular momentum. The integer-based transitions experimentally found were then measuring the transitions of electrons between different energies set by the angular momentum. While the Bohr theory is now known to be only an approximation to the "electron cloud" description given by Heisenberg and Schrödinger, it allows us to understand much of the basic physics of an electron [12]. The success of this theory is evident in a simple example: the Rydberg constant derived using the Bohr model is 99.9985% of the modern accepted value [12].

Before the discovery of electron spin, the first three (typically used) quantum numbers—n

the principal quantum number, l the azimuthal quantum number, and m_l, the magnetic quantum number—were known. The angular momentum of an electron is defined as

$$\mathbf{L} = \hbar\sqrt{l(l+1)} \tag{1.1}$$

The angular momentum along a reference direction (usually z in Cartesian coordinates) is then defined as

$$L_z = m_l\hbar \tag{1.2}$$

The Bohr theory still did not explain many experimental results [12]. Among these were the existence of doublets with very small energy spacing in the aforementioned atomic emission spectra. The Zeeman effect in atomic emission spectra was also not well explained. Finally, although the periodic table had mostly been worked out in agreement with the "closed shell" model of the first three quantum numbers, it still did not have a full theoretical explanation. In 1925 Wolfgang Pauli was able to explain these phenomena with a fourth, binary-valued, quantum number. The Pauli exclusion principle then stated that no two electrons in an atom may have the same four quantum numbers. At the time, this approach was *ad hoc*. While explaining experiment well, it did not appear to have a physical basis and could not be derived [13].

In 1922, in an attempt to confirm the quantization of l, Stern and Gerlach had directed a beam of Ag atoms through an inhomogenous magnetic field along a direction and expected to split the beam into $2l + 1$ components [12]. Instead the beam split into only two components corresponding to $l = \frac{1}{2}$, which was inconsistent with the integer quantization expected from this quantum number. Finally, in 1925 Uhlenbeck and Goudsmit showed that this binary quantum number represented an intrinsic angular momentum of an electron, as if the electron was "spinning", although it does not truly

have this motion in real space [12]. The spin is quantized in the same manner as angular momentum

$$|\mathbf{S}| = \hbar\sqrt{s(s+1)} \tag{1.3}$$

$$S_z = m_s\hbar \tag{1.4}$$

and may have a value of $\pm\frac{\hbar}{2}$. Other types of particles may have other allowed momenta. The spin angular momentum and orbital angular momentum can then each be associated with a magnetic moment, since an electron is a charged particle

$$\mu_l = -\frac{|e|}{2m_e}\mathbf{L} \tag{1.5}$$

$$\mu_s = -g\frac{|e|}{2m_e}\mathbf{S} \tag{1.6}$$

where $g = 2$ corresponds to the gyromagnetic ratio, m_e is the free electron mass, and e is the electron charge. This value of the gyromagnetic ratio of an electron was originally an anomalous factor, but was clarified in later theories. These magnetic moment vectors (provided they are not orthogonal which they are not required to be) couple, leading to *spin-orbit coupling*, an effect at the root of this thesis. While spin-orbit coupling effects are weak in hydrogen, the magnitude increases with higher atomic number Z—as do other relativistic effects.

In the original formulation of the theory, spin physics was appended to current quantum physics [12]. Dirac later derived his namesake equation, which describes relativistic quantum mechanics. From here, electron spin arises naturally (as does the value of the electron gyromagnetic ratio). The Dirac equation for a stationary state is given by

$$(i\hbar c\boldsymbol{\alpha}\cdot\boldsymbol{\nabla} + \boldsymbol{\beta}mc^2 + V)\boldsymbol{\psi} = E\boldsymbol{\psi} \tag{1.7}$$

where V is a scalar potential, $\alpha_i = \begin{bmatrix} \sigma_i & 0 \\ 0 & \sigma_i \end{bmatrix}$ and σ_i are the Pauli spin matrices, a 2×2 matrix representation of the electron spin, and $\beta = \begin{bmatrix} I & 0 \\ 0 & I \end{bmatrix}$ [14]. The Dirac equation can also be used to describe some quasiparticles that exist in crystalline solids investigated later in this thesis.

The approximation of relativistic corrections into the Schrödinger equation for a hydrogenic atom gives

$$H = \left(\frac{\boldsymbol{p}^2}{2m} + V\right)_1 + \left(-\frac{\boldsymbol{p}^4}{8m^3c^2}\right)_2 + \left(-\frac{\hbar^2}{8m^2c^2}\frac{dV}{dr}\frac{\partial}{\partial r}\right)_3 + \left(\frac{1}{2m^2c^2}\frac{1}{r}\frac{dV}{dr}\boldsymbol{L}\cdot\boldsymbol{S}\right)_4 \quad (1.8)$$

where V is the Coulomb potential $-\frac{Ze^2}{4\pi\epsilon_0 r}$ [14]. The first term is the nonrelativistic hydrogenic Hamiltonian. The second term is the mass correction (or Einstein) term where the energy shift is

$$E_{Einstein} = -\frac{1}{2}mc^2Z^4\alpha^4\left(-\frac{3}{4n^4} + \frac{1}{n^3\left(l+\frac{1}{2}\right)}\right) \quad (1.9)$$

where α is the fine structure constant and Ry is the hydrogen ground state energy (the aforementioned Rydberg constant) [15].

The third term is called the Darwin correction. The energy shift corresponds to

$$E_{Darwin} = \frac{mc^2\alpha^4Z^4}{2n^3} \quad (1.10)$$

but only when $l = 0$ [15]. This accounts for an interaction with a virtual positron. In other words, in the timescale of interest (given by the energy of the particle via the Heisenberg uncertainty principle), there is a reasonable likelihood of an electron-positron pair existing. Nonrelativistically, this can be thought of as a smearing of the electric

potential as $r \to 0$.

The last term is the spin-orbit coupling term discussed earlier. Spin-orbit coupling, while it can be understood nonrelativistically, is a relativistic effect. The spin-orbit coupling is represented as

$$E_{SOC} = \frac{mc^2 Z^4 \alpha^4}{4n^3 l\left(l+\frac{1}{2}\right)(l+1)} \begin{cases} l & j = l + \frac{1}{2} \\ -(l+1) & j = l - \frac{1}{2} \end{cases} \tag{1.11}$$

where j corresponds to the values of total angular momentum [15]. Since L and S are now coupled, solutions are usually written in terms of the total angular moment $J = L + S$ and $|l - s| \leq j \leq l + s$.

The total energy shift from incorporating relativity may be written as

$$E_{Rel.Corr.} = \frac{mc^2}{2}\left(\frac{\alpha Z}{n}\right)^4 \left(\frac{3}{4} - \frac{n}{j+\frac{1}{2}}\right) \tag{1.12}$$

the sum of E_{SOC}, E_{Darwin} and $E_{Einstein}$ [15].

Relativistic effects clearly are enhanced in high Z materials, which is why spin-orbit effects are so entwined with high Z topological materials. However for α-Sn, the subject of much work in this thesis, the Darwin and mass correction terms are important as they shift the $5s$ orbital down in energy below the $5p$ orbital. Now that we understand how a single electron behaves in a hydrogenic atom, we investigate how to describe similar physics in a crystalline solid.

1.2 Describing electrons in solids

In solids, there is a crystalline array of atoms with translational symmetry (i.e. infinite periodic extension) in all directions. This requires us to rewrite the above terms into a

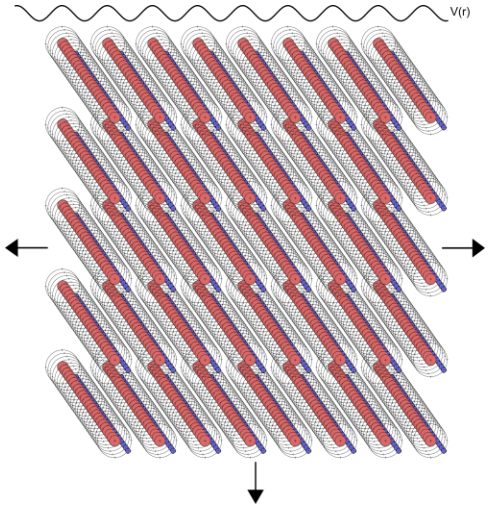

Figure 1.4: A lattice of hydrogenic atoms with translational symmetry in all directions. The periodic potential is shown.

more complex model than the hydrogenic case.

The total Hamiltonian for a crystal with no external potential is given by

$$H = \left(\sum_i \frac{\boldsymbol{P}_i^2}{2M_i}\right)_{KE_{ion}} + \left(\sum_j \frac{\boldsymbol{p}_j^2}{2m}\right)_{KE_{el}} + \left(\frac{(Ze)^2}{2}\sum_{i,i'} \frac{1}{|\boldsymbol{R}_i - \boldsymbol{R}_{i'}|}\right)_{V_{ion-ion}} + \left(\frac{e^2}{2}\sum_{j,j'} \frac{1}{|\boldsymbol{r}_j - \boldsymbol{r}_{j'}|}\right)_{V_{el-el}} + \left(\frac{-Ze^2}{2}\sum_{i,j} \frac{1}{|\boldsymbol{r}_j - \boldsymbol{R}_i|}\right)_{V_{el-ion}} \tag{1.13}$$

where $\boldsymbol{p}$ corresponds to the momentum, m to the mass, and $\boldsymbol{r}$ to the position and uppercase (lowercase) terms correspond to the ion (electron) being indexed by i (j). This may first be simplified by only considering the valence/conduction electrons. The core electrons are localized to the nucleus, whereas the valence electrons are delocalized [16]. The full equation can then be written as

$$(KE_{ion} + KE_{val.el} + V_{ion-ion} + V_{el-el} + V_{el-ion} + E_{core})\psi = E\psi \tag{1.14}$$

Since the mass of electrons is very small compared to the nuclear mass, the Born-Oppenheimer approximation treats ionic effects, including the core electrons, as a perturbation to the Coulomb potential [16]. The electronic portion of the Hamiltonian is then separated out as

$$(KE_{val.el} + V_{el-el} + V_{el-ion})\psi_{el} = E_{el}\psi_{el} \tag{1.15}$$

For a first order approximation, electron-electron effects are shut off leaving the Schrödinger equation for a single electron in a crystal

$$\left(\frac{p^2}{2m} + V(r)\right)\psi(r) = E\psi(r) \tag{1.16}$$

Many body interactions, ignored here, can be measured in angle-resolved photoemission discussed in more detail in Chapter 2. Since a crystal is periodic according to its lattice structure, the potential which is derived from this lattice is also periodic [17]. Rather than discrete energy levels in the atomic case, the energies here become bands described by an $E - k$ dispersion, where k is the reciprocal lattice point in the Brillouin zone. An intuitive description of the conversion from atomic-like energy levels to a band structure or "spaghetti" diagram is given by Roald Hoffman in Ref. [18]. Due to this periodicity, by Bloch's theorem the wavefunction of an electron gains the form

$$\psi_{nk}(r) = e^{ik\cdot r}u_{nk}(r) \tag{1.17}$$

where $u_{nk}(r)$ is periodic in the same manner as $V(r)$ [17].

The spin orbit interaction in the one electron approximation simply appends the spin-orbit term $\frac{1}{2m^2c^2}(\nabla\mathbf{V} \times \mathbf{p}) \cdot \mathbf{S}$ to the one electron bare Hamiltonian (Eq. 1.16) [19]. The incorporation of spin-orbit coupling means that spin symmetries must be considered in

the symmetries of the solid. The point group that typically describes only the spatial symmetries should be replaced by the double group representation [19]. The irreducible representations of the double groups are used to label the bands of the materials of interest in this dissertation, following the solid state notation. In chemistry, the Mulliken notation is typically used instead.

The spin-orbit coupling introduced here typically breaks degeneracies between bands as it breaks the degeneracy in between certain energy levels in the atomic case. Because the spatial and spin symmetries are codependent, the spatial symmetry varies with k and thus the spin-orbit splitting varies with k [19]. The Darwin and mass correction effects discussed in the hydrogenic case apply in the solid state as well.

The presence of spin-orbit coupling necessitates relating certain crystalline symmetries to spin degeneracy-breaking in the band structure. If a crystal has inversion symmetry, then $E_n(k) = E_n(-k)$. If there is time reversal symmetry (non-magnetic crystal), then $E_{\uparrow n}(k) = E_{\downarrow n}(-k)$ (and its conjugate). Combining these symmetries results in $E_{\uparrow n}(k)$ and $E_{\downarrow n}(k)$ being degenerate at all k. This two-fold degeneracy is called the Kramer's degeneracy [19]. When inversion symmetry is broken, the Kramer's degeneracy is lifted at all k except certain high symmetry points at the Brillouin zone. In zincblende semiconductors with bulk inversion asymmetry, the spin-splitting of these bulk bands is referred to as Dresselhaus spin-orbit coupling [20]. This spin splitting scales as k^3,

$$H_D \propto p_x(p_y^2 - p_z^2)\sigma_x + p_y(p_z^2 - p_x^2)\sigma_y + p_z(p_x^2 - p_y^2)\sigma_z \tag{1.18}$$

where the splitting is maximized/minimized along certain high symmetry lines [21]. Rashba spin-orbit coupling arises from the abrupt loss of inversion symmetry (structural inversion asymmetry) typically found at the surface or interface of a crystal [21].

In addition to the bulk bands discussed so far, the dangling bonds and the recon-

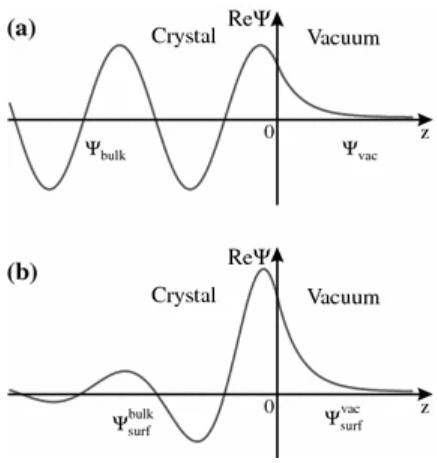

Figure 1.5: Real part of the wave function, for (a) a bulk band Bloch wave matched to an exponentially decaying tail in the vacuum and (b) a surface state wave function. The surface state lives mostly on the surface, but has some penetration into the bulk. Copyright Springer [22].

struction of atoms at the surface which fill these dangling bonds result in dispersive bands localized to the surface (or interface) of the crystal [23]. The differences between surface-localized bands and bulk bands are shown in Fig. 1.5. When these bands are in a projected bulk band gap, they are termed surface *states*. When these bands are degenerate with the projected bulk spectrum, they are termed surface *resonances*. Because these states arise from the 2D surface, they only have a 2D dispersion. Surface states and resonances do not disperse in the momentum direction perpendicular to the surface. These states are summarized in Fig. 1.6.

The effective potential arising from structural inversion symmetry primarily acts on states localized near the surface and interfaces, such as quantum well states or surface states. The Rashba spin-orbit coupling can be Taylor expanded in the lowest order to consider $J = 1/2$ electrons. For more complicated particles (i.e. heavy holes which are $J = 3/2$) higher order effects must be considered [21]. This simple case leads to the Rashba Hamiltonian

$$H_R = \alpha_R(k_x\sigma_y - k_y\sigma_x) \tag{1.19}$$

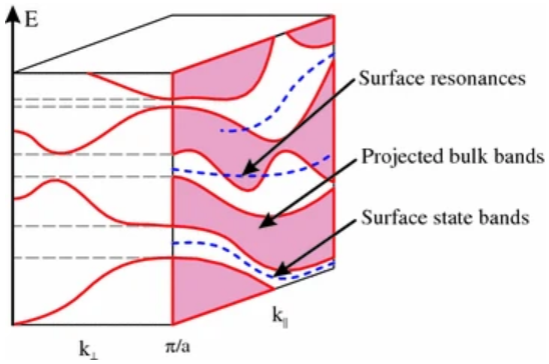

Figure 1.6: The bulk band structure dispersing in all k directions while surface states and resonances do not disperse in k_z. A resonance is where the surface bands are degenerate with the surface projection of the bulk band structure, while a state is where the surface bands exist in a gap of the surface projection. Copyright Springer [22].

where α_R is the Rashba coefficient $\frac{e\hbar^2}{4m^2c^2}E_z$ where E_z is the surface potential—either built-in or applied externally [24]. This definition of the Rashba coefficient is only an approximation, however, and is more accurately computed using third-order perturbation theory taking into account the band structure of the material of interest [21]. For electrons in III-V/IV semiconductors, it depends sensitively on the spin-orbit gap and fundamental gap [21]. The dispersion for a Rashba-split two-dimensional electron gas is shown in Fig. 1.7 and results in spin-split paraboloids described by a Fermi surface of two concentric spin-polarized surface states with equal and opposite spin polarization. The spin polarization is orthogonal to the k vector and in the plane of the surface, referred to as spin-momentum locking. The Kramer's degeneracy of the Rashba-split state is at Γ.

Now that the general physics describing spin and spin-orbit coupling in solids is understood, we may introduce the topics at the heart of this thesis.

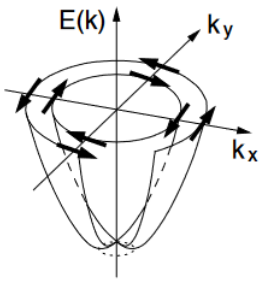

Figure 1.7: Dispersion of parabolic surface states exposed to the Rashba effect. Copyright Springer [21].

1.3 Topological materials

Topology is the branch of mathematics that concerns categorization of objects (however real or abstract that object may be) under certain deformations. The most famous example of topology is the number of holes in an object in real space (Fig. 1.8). A cup made of soft clay may be deformed into any shape including a ball, bowl, football, etc. and still have no holes. Tearing a hole in the clay, the cup can now be deformed into a mug. The number of holes is now different, so the topology of a mug vs. a cup is different. Similarly, the mug may be continuously deformed into a hula-hoop, a ring, a necklace, etc. all of which have a fundamentally different topology than an object with zero holes. This idea may be extrapolated to an object with any number of holes, where the parameter describing these different "phases"—the topological invariant—is the number of holes. This idea can then also be extrapolated to describe the electronic structure of materials rather than holes in clay. The 2016 Nobel prize in physics was awarded to Thouless, Haldane, and Kosterlitz for their description of the electronic properties of matter through topology, including an understanding of the integer quantum Hall effect [25].

There are now a number of topological phases of matter, each of which is described with a different topological invariant. Various topological phases have already been proposed to slot into a number of applications in modern devices, notwithstanding

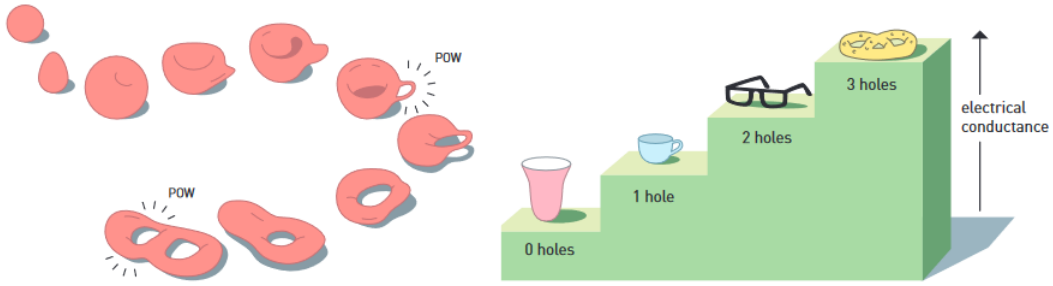

Figure 1.8: Topology in real space can be thought of, in a simple case, as the step-wise changes to the number of holes in a ball of clay. This idea can be extrapolated to explain the step-wise integer steps in the integer quantum Hall effect. Copyright The Nobel Foundation [25].

Herb Kroemer's famous *Lemma of New Technology*: "The principal applications of any sufficiently new and innovative technology always have been—and will continue to be—applications *created* by that technology" [26]. While topological non-triviality in some form or fashion turns out to describe most materials ($> 80\%$ at some point in their band structure [27]), there are few stable materials that have the feature of interest near the Fermi level (a necessary condition for most current applications). Below we will summarize some of the topological phases of matter relevant to this dissertation and their applications before introducing the extraordinary promise of both α-Sn and magnetic topological Heusler alloys.

1.3.1 A zoo of topological phases

Topological insulators

While describing the integer quantum Hall effect (or the quantum Hall insulator phase) with topology [28], Haldane attempted to recreate this phase *without* the application of an external magnetic field [29]. This Chern insulator phase or quantum Anomalous Hall insulator (Fig. 1.9, has recently been experimentally demonstrated in a few different materials systems, but is not the focus of this work [30, 31].

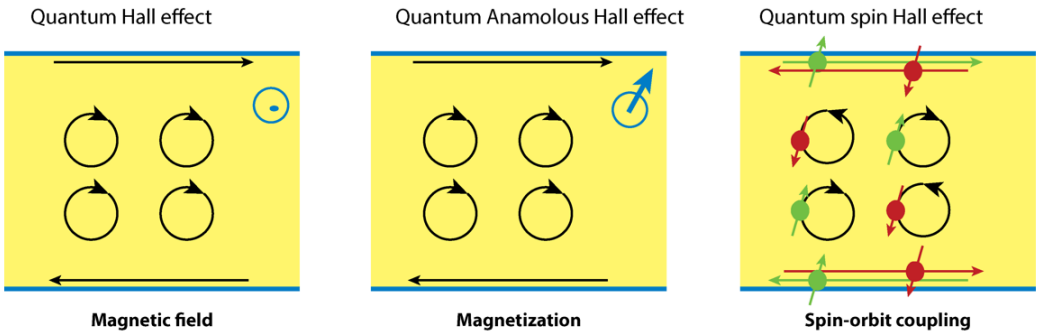

Figure 1.9: Schematic for the integer quantum Hall effect, the quantum anomalous Hall effect, and the quantum spin Hall effect. Used with permission from [31]; permission conveyed through Copyright Clearance Center, Inc.

In the mid-2000s, a time reversal symmetric analogue of the Chern insulator was proposed [32,33]. This quantum spin Hall insulator, commonly known as a 2D topological insulator, was quickly experimentally demonstrated [34].

A 2D topological insulator phase is described by the $\mathbb{Z}_2$ topological invariant. This invariant describes either trivial matter ($\mathbb{Z}_2 = 0$) or non-trivial matter ($\mathbb{Z}_2 = 1$) [35, 36]. The path to calculate $\mathbb{Z}_2$ can be rather complicated, but if inversion symmetry is preserved then it may be calculated by the following process. First the δ term is computed,

$$\delta_a = \prod_m \xi_m(\Lambda_a) \tag{1.20}$$

describing the product for occupied bands of $\xi_m(\Lambda_a)$, the parity (± 1) of the pair of bands at a time reversal invariant momentum (TRIM) point (defined by momenta at which $k = -k \bmod \mathbf{G}$, or the corners, center, and edges of the Brillouin zone) [35]. This is then evaluated for each TRIM and mutiplied together by

$$(-1)^\nu = \prod_a \delta_a \tag{1.21}$$

where ν is the value of the invariant. From these definitions, it is clear why the invariant

is $\mathbb{Z}_2$: there are only two independent possible values for ν. These rules were extended to three dimensions by assuming a cubic system with six planes. The planes are defined by the 8 TRIMs in this system which result in only four independent $\mathbb{Z}_2$ invariants ν_0, ν_1, ν_2, and ν_3 which are defined as

$$(-1)^{\nu_0} = \prod_a \delta_a \tag{1.22}$$

for all 8 TRIMs and

$$(-1)^{\nu_i} = \prod_a \delta_a \tag{1.23}$$

for $i = 1, 2, 3$ for the 4 TRIMs corresponding to each surface in the 3D system (analogous to three 2D system invariants) [35]. This then defines a strong 3D topological insulator (henceforth 3D topological insulator) as the case where all $\nu = 1$. A weak topological insulator arises when $\nu_0 = 0$ and any number of $\nu_{1,2,3} = 1$. The weak topological insulator phase is not relevant to the materials discussed in this thesis. The parity evaluations which determine the topological phase represent the inversion of band character at an odd number of TRIMs in the Brillouin zone [37].

In order to understand band inversion in topological insulators, we must first understand "normal" insulators also known as band insulators. In a band insulator, such as GaAs, the conduction band derives from the $4s$ gallium orbitals while the valence band derives from the $4p$ arsenic orbitals. This is the expected energy ordering in the atomic case. However in a topological insulator, the character of these bands *invert* such that the conduction band would be $4p$-like and the valence band now has $4s$ character. The band inversion is driven by previously discussed relativistic effects such as the Darwin and mass corrections (Eq. 1.9 and Eq. 1.10) and spin-orbit splitting (Eq. 1.11) which all scale with Z^4, but also the relativistic inert pair effect. Thus topological insulators

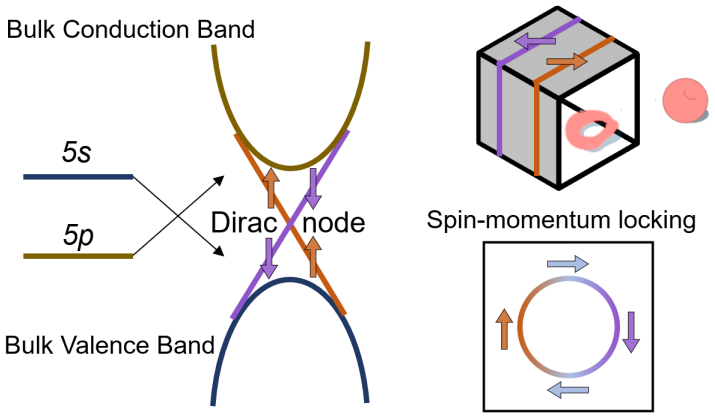

Figure 1.10: The insulating bulk with conducting 2D Dirac surface states. The surface states are fully spin-polarized and counter-propagate with opposite spin. The helical spin texture is spin-momentum locked. The Dirac node is the point where the spin-polarized surface states are degenerate

are generally seen in materials which incorporate some number of high Z elements.

In the 2D case, the untwisting of this band inversion when interfaced with vacuum (or a topologically-trivial insulator layer) gives rise to the 1D spin-polarized edge states shown in Fig. 1.9 at this boundary. For the 3D case, the topological insulator is represented by a 3D bulk insulator state with 2D spin-polarized surface states (Fig. 1.10). These surface/edge states correspond to a linear 2D/1D Dirac cone. The crossing point of these linear states is named the Dirac node and these states are so-called because they follow the results of a massless Dirac fermion (Eq. 1.7).

These spin-polarized boundary states in the ideal case obey spin-momentum locking, as Rashba surface states do, giving a helical spin polarization [35,36]. The key difference between trivial and non-trivial boundary states is given in Fig. 1.11 where there is now only a single spin-polarized Fermi surface. Time reversal symmetry is still obeyed in these systems, such that the total spin polarization integrates to zero and the surface is non-magnetic. Due to their topology, these massless boundary states are robust to non-magnetic disorder and are protected against backscattering [35,36], leading to many exciting applications discussed in Sec. 1.3.2.

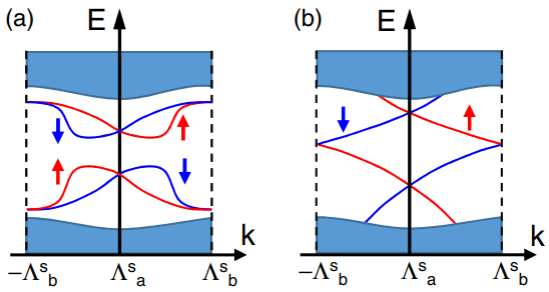

Figure 1.11: (a) Trivial spin-polarized nonmagnetic surface states (b) non-trivial spin-polarized surface states. Copyright 2013 The Physical Society of Japan [35].

Topological semimetals

Topological semimetals are fundamentally different from topological insulators in that they do not have a band gap. They still rely on band inversion, albeit in a slightly different manner. In the case of a topological semimetal, the band character inverts on either side of a crossing [38]. Just because two bands disperse such that they should cross does not mean they will when all symmetries are considered. The presence of a degeneracy (i.e. crossing) may be disallowed by point group symmetries (in the absence of spin-orbit coupling) or double group symmetries (in the presence of spin-orbit coupling). If there is no crossing in this case, then the phase is not that of a topological semimetal; it can be either a trivial or non-trivial insulator depending on the details of the band inversion via the discussion in the preceding section.

In the case of time reversal symmetry and inversion symmetry, each bulk band is two-fold degenerate. When these bands cross there is a four-fold degenerate crossing point corresponding to a 3D Dirac node (akin to the Dirac nodes in the topological insulator case) [38, 40]. These Dirac nodes arrive in pairs (Fig. 1.12(a)) displaced from the zone center by $\pm k_D$, which is generally a small value (a few percent of the reciprocal lattice vector length). The degeneracy at $\pm k_D$ is also protected by some symmetry operator [38]. In the most well-studied Dirac semimetals Na_3Bi and Cd_3As_2 this is a C_4 rotation around

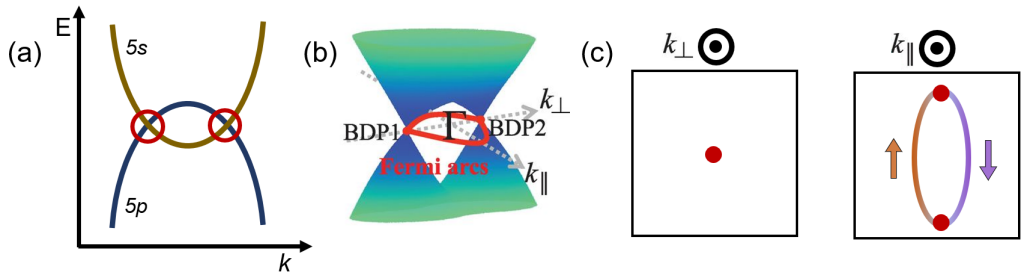

Figure 1.12: (a) Schematic of band inversion in a topological Dirac semimetal. (b) 3D band structure of Na_3Bi with projected Fermi arcs. (c) Orientation-dependent topological surface states on the Fermi surface. In the surface plane normal to the vector connecting the pairs of bulk Dirac points $k_\perp$, there is no Fermi arc. In the orthogonal plane (plane normal to $k_{||}$), the spin-polarized Fermi arcs appear. Adapted from [39]. Reprinted with permission from AAAS.

the axis along which the Dirac nodes lie [40]. Dirac semimetals may also be created which are entirely symmetry enforced and do not rely on band inversion; these exist in a narrow grouping of nonsymmorphic space groups of which few can form stable compounds at stoichiometries such that the node is near the Fermi level [40].

The topological surface states in Dirac semimetals are termed Fermi arcs. They connect the pair of projected Dirac nodes and are not topologically protected [40]. They only exist on surfaces where the Dirac nodes do not project onto each other (self-annihilation). However on surfaces where they exist, they are spin-polarized and generate a loop reminiscent of the contour of Dirac-like surface state (Fig. 1.12(b,c)).

In a Weyl semimetal, the crossing points between inverted bands are two-fold degenerate rather than four-fold degenerate. In order to generate this two-fold crossing, some symmetry must be broken. The two flavors of symmetry breaking are inversion symmetry breaking (as discussed in Chapter 7) or time reversal symmetry breaking (Fig. 1.13) [38, 40]. These two-fold crossings are Weyl nodes and electrons near the Weyl node behave as massless, chiral Weyl fermions in the Dirac equation (Eq. 1.7). There should be no net chirality in Weyl semimetals formed in this manner, as the crystals are not chiral [41]. Each Weyl node formed has a partner (Fig. 1.13) of opposite chirality at its

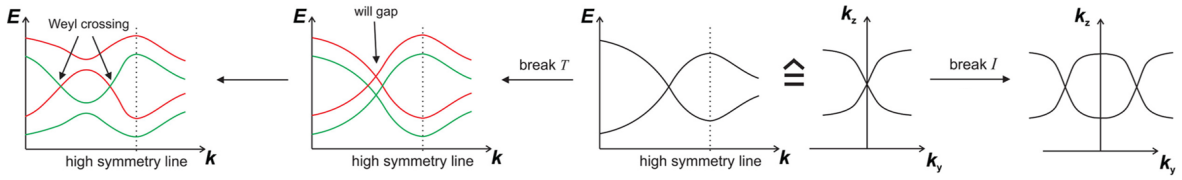

Figure 1.13: Formation of Weyl semimetal phase from Dirac semimetal phase exposed to time reversal symmetry or inversion symmetry breaking. Reprinted with permission from [38]. Copyright 2018 American Chemical Society.

inverted k location [40].

When Weyl semimetals are formed from inversion symmetry breaking, the Dresselhaus effect results in spin splitting at certain k not equivalent to a high symmetry TRIM [20]. Because of this, there are usually many Weyl nodes in inversion-asymmetric Weyl semimetals as the Weyl nodes are copied via the symmetries of the system (e.g. 24 in the TaAs family) [42, 43].

The trivial mechanism of breaking time reversal symmetry would be applying an external magnetic field to a Dirac semimetal. The Zeeman splitting here is small, but an important parameter to explain some magnetotransport results in this system [44]. Intrinsically magnetic samples, which can be either ferromagnets [38, 40], non-collinear antiferromagnets [45], or ferrimagnets [46], generate time reversal symmetry breaking. An intrinsic magnet formed from a Dirac semimetal would produce the simplest case of one pair of Weyl nodes, although this case has not yet been realized.

Like Dirac semimetals, Weyl semimetals also present Fermi arc surface states. In Weyl semimetals the Fermi arcs connect opposite chirality pairs of Weyl nodes (Fig. 1.14). At energies away from the bulk Weyl nodes, the Fermi arcs merge into the bulk Fermi surface but do not disappear [40]. These Fermi arcs were first demonstrated in the inversion-asymmetric Weyl semimetals [47–49], but were later confirmed in magnetic Weyl semimetals [50, 51]. In the inversion-asymmetric case, the Fermi arcs have a large in-plane spin polarization [52].

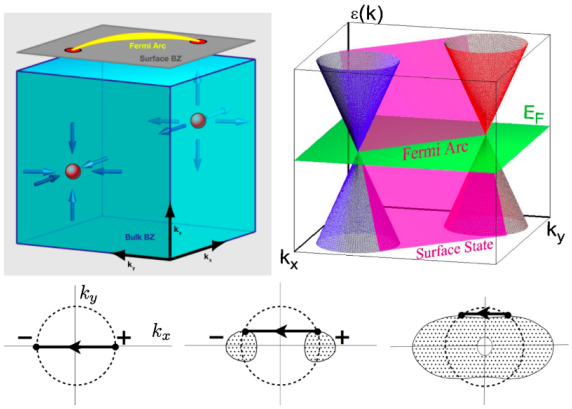

Figure 1.14: The nature of Fermi arcs in a Weyl semimetal. Reprinted with permission from [40]. Copyright 2018 by the American Physical Society.

The final group of topological semimetals relevant to this dissertation is nodal line semimetals; they can generally be thought of as the above band crossings (bulk Dirac/Weyl nodes) but instead of the four-fold or two-fold crossing existing at a single (symmetry matched) k-point, the crossing disperses as a nodal line into a loop (Fig. 1.15). Since the node is replaced with a nodal line, the Fermi arc is replaced with a drumhead surface state. These have been demonstrated in Co_2MnGa (unmagnetized) via angle-resolved photoemission spectroscopy [53]. In addition, only Type I semimetals have been discussed so far where the Weyl or Dirac cone is oriented such that a point-like constant energy countour exists. In Type II semimetals, the cone is tilted and this leads to different and more exotic phenomena [40].

Phenomena other than surface states associated with these semimetals are the chiral anomaly and axion electrodynamics, among others [40], but will not be discussed in detail. The property of topological semimetals most relevant to the rest of this thesis is that these nodes and nodal lines act as a source and/or sink of Berry curvature [40]. The Berry curvature $\mathbf{\Omega}_n(k)$ acts as an analogue to magnetic field in k-space [55]. It can be calculated from the details of the band structure for each band and is related to how close bands disperse [55]. Thus when there are nodes, narrowly avoided crossings, or

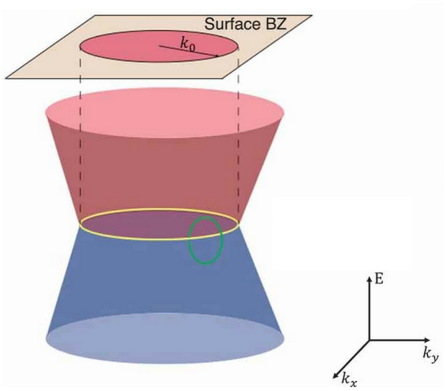

Figure 1.15: Bulk and surface band structure of a toy nodal line semimetal. Reprinted from [54] via the Creative Commons CC BY license.

nodal lines near the Fermi level at a given k, the Berry curvature at that k will be high.

The Berry curvature gives an anomalous velocity $\frac{dr}{dt} = \frac{\partial E}{\hbar \partial k} + \frac{e}{\hbar} E \times \mathbf{\Omega}_n(k)$ [55]. This anomalous velocity would then be the reciprocal space analogue to the Lorentz force. If inversion symmetry is preserved, $\mathbf{\Omega}_n(-k) = -\mathbf{\Omega}_n(k)$. If time reversal symmetry is preserved $\mathbf{\Omega}_n(-k) = -\mathbf{\Omega}_n(k)$. If both of these symmetries are preserved, as in a Dirac semimetal, then the Berry curvature must be zero at all k. Breaking either of these symmetries lifts this requirement, allowing non-zero Berry curvature. In the inversion-asymmetric Weyl semimetals, this results in a large intrinsic spin Hall effect [56]. In the magnetic Weyl semimetals, this results in a large intrinsic anomalous Hall and anomalous Nernst effect [40].

1.3.2 Applications of topological materials

In addition to the pursuit of a deeper understanding of the world around us, the study of these topological materials has resulted in numerous proposals for different applications for various topologically non-trivial phases. This is notwithstanding the earlier discussed Kroemer's Lemma of New Technology [25]. Among some of the most famous applications of topological materials are metrics and standards [57], competing forms of

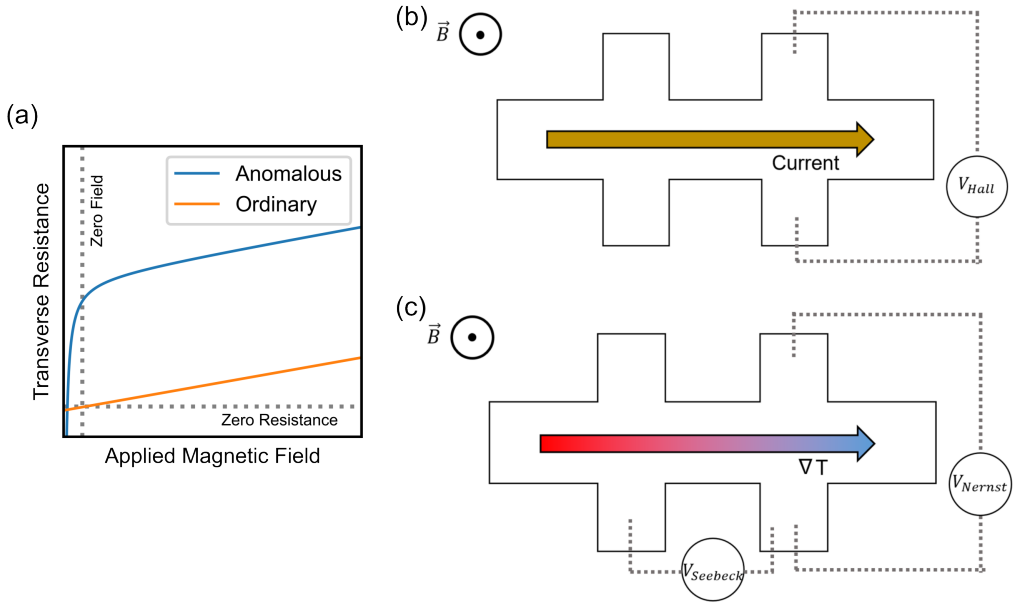

Figure 1.16: (a) Schematic of the measured anomalous Hall and Nernst effects for a soft ferromagnet. There is a small zero-field offset from the intrinsic magnetic field (Berry curvature). Hall bar device for measurement of (b) the Hall effect and (c) the Nernst effect, which are driven by applied current and applied temperature gradient, respectively, in the presence of a perpendicular magnetic field.

quantum computing [58,59], interconnects [60,61], efficient catalysts [62,63], novel axion electrodynamics [64], THz photodetectors [65–68], and more [69]. The application we focus on here, as it is well-suited for the materials in question, is spintronics [5,69].

In magnetic topological semimetals, the integrated Berry curvature over the Fermi sea is no longer required to be zero. This then results in an intrinsic contribution to the anomalous Hall conductivity and anomalous Nernst conductivity (where the latter is proportional to the derivative of the former) [55]. The ordinary Hall and Nernst effects are a voltage that is generated in a material applied to a magnetic field and a current (Hall effect) or temperature gradient (Nernst effect). This voltage is orthogonal to both vectors. In the anomalous case, the magnetism of the system (i.e. the Berry curvature) acts as an internal magnetic field, offsetting this voltage generation following the magnetic hysteresis of the sample (Fig. 1.16(a)).

Materials with a large AHE have seen interest as magnetic sensors. Although it is unlikely they can match the effectiveness of semiconductor-based sensors in most cases, AHE-based sensors seem to offer the best low noise field detectability in low frequency magnetic fields [70]. Furthermore, semiconductor-based sensors fail at high temperatures (dopant diffusion and semiconductor degradation) whereas many large AHE materials are relatively stable at high temperatures [71].

The quantum anomalous Hall effect (QAHE) has many of the same properties that has motivated interest in the quantum Hall effect, specifically dissipation-less current, and can potentially be generated by forming quantum wells from topologically non-trivial large AHE materials [31].

Materials with large AHE could replace those currently used in, for example, magnetic tunnel junctions. Since the AHE stores magnetization information electrically, the spin information can be interrogated electrically rather than magnetically: a simpler, lower power approach (Fig. 1.16(b)) [72]. Finally, the AHE generates a spin-polarized current which is of interest in spintronics for spin-transfer torque-based devices [73]. The AHE effect has also been demonstrated to show large spin-orbit torques [74] Clearly there are many avenues in the broad field of spintronics where a material with large AHE can have impact.

The anomalous Nernst effect opens up new device architectures in spin caloritronics. Current on-chip thermal energy harvesting (i.e. from the power generated by another device on-chip) is inefficient and difficult to integrate with real devices [75]. Thermoelectric conversion based on patterned metal films showing the ordinary Nernst effect requires an applied magnetic field. In the case of the Seebeck effect (which does not require magnetic field to occur), the power is generated along the direction of the temperature gradient (i.e. an in-plane temperature gradient, Fig. 1.16(c)). These devices cannot be scaled efficiently. In devices based on the anomalous Nernst effect, the temperature gradient

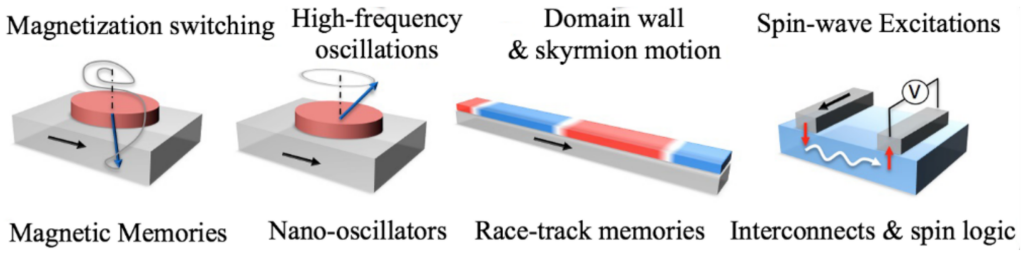

Figure 1.17: Applications of current-induced spin-orbit torques. Reprinted with permission from [4]. Copyright 2019 by the American Physical Society.

can be along the growth direction of the patterned film, minimizing the footprint of the device [76]. These devices also do not require an external magnetic field to operate.

For topological insulators, the main spintronics application is the generation of current-induced spin-orbit torques [5]. Current-induced spin-orbit torques were first studied in heavy metal/ferromagnet bilayers [4]. Applying a current parallel to the interface of these layers, through the heavy metal layer, can drive magnetization effects in the magnetic layer. This includes switching the magnetization vector of the magnetic layer or driving a spin-wave excitation. Both of these effects may be used to write, read, or transport information in a spintronic device (Fig. 1.17).

The spin-charge conversion efficiency, defined simply as the spin Hall angle $\Theta_{SH} = \frac{J_{spin}}{J_{charge}}$, is an essential parameter for low power consumption devices. These heavy metal bilayers have low efficiency, so there has been a constant search to find alternate architectures to improve performance [4]. The first alternative found was applying a spin-orbit torque via the spin accumulation in Rashba-split states [77].

The mechanism for this spin accumulation is shown in Fig. 1.18. Applying a bias (or current) through the thin film shifts the center of the Fermi sea away from zone center such that the integrated spin polarization no longer goes to zero. Because the Rashba effect leads to two concentric Fermi surfaces with opposite spin, the net spin polarization partially cancels itself out. Topological insulators, on the other hand, have only one spin-

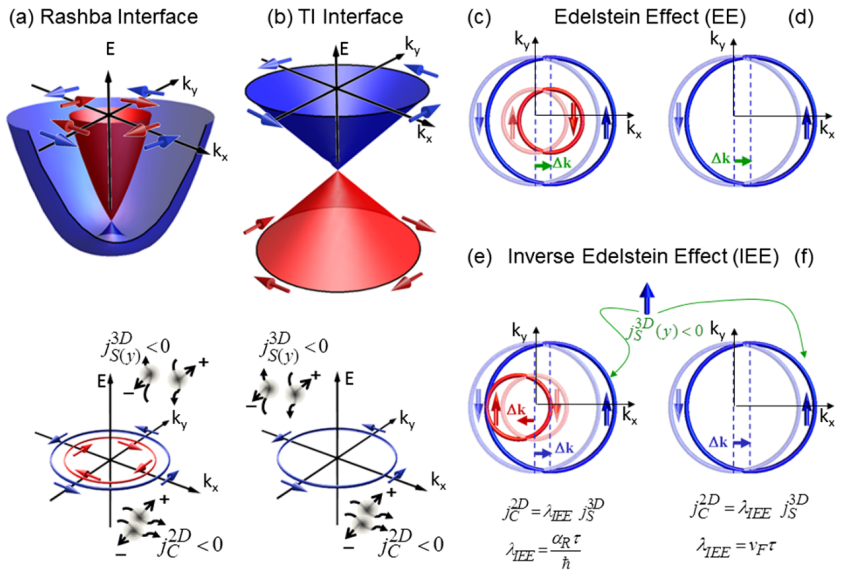

Figure 1.18: Spin polarization and dispersion of (a) Rashba surface states and (b) the Dirac surface states of a 3D TI. Charge current drives spin current in the Edelstein effect (c) Rashba surface states and (d) Dirac surface states. Spin current drives charge current in the inverse Edelstein effect in (e) Rashba surface states and (f) Dirac surface states. Reprinted with permission from [78]. Copyright 2016 by the American Physical Society.

polarized Fermi surface. Running a current through the surface states of a topological insulator will generate a large spin polarization and thus spin-orbit torque (Fig. 1.18).

The chemical potential in the topological insulator may also be tuned such that the bulk is fully insulating and all charge current is passed through the spin-polarized surface states. Spin-polarized current should then be achieved with low power consumption since there is no parasitic bulk channel. Warping of the spin-momentum locking (as seen in $(Sb,Bi)_2(Se,Te)_3$, derived inherently from Fermi surface warping due to the crystalline symmetries of the system [79]), can negate the net spin polarization and turn the spin polarization vector away from the desired direction. So far topological insulators have shown record-breaking efficiencies up to room temperature (Fig. 1.19). The performance is already much greater than that of heavy metal bilayers and further optimization is still ongoing. This technology is exceptionally promising.

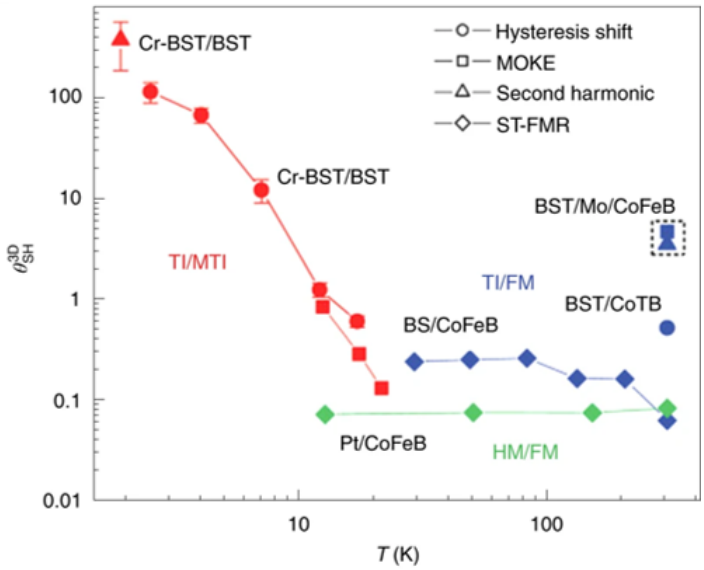

Figure 1.19: Temperature-dependent comparison of the spin-charge conversion efficiency of different topological systems with the heavy metal bilayer baseline. Reproduced from [5] with permission from Springer Nature.

Similar effects should be possible in the spin-polarized Fermi arcs in Dirac and Weyl semimetals, however, there are now bulk transport effects since there is no bulk band gap. These bulk effects have their own contribution to spin-charge conversion. It remains to be seen whether the enhanced power consumption from bulk transport diminishes the viability of the device.

1.3.3 Heusler alloys

Heusler alloys were first discovered by mining engineer Friedrich Heusler in 1903, who found that an alloy of three nonmagnetic elements Cu_2MnAl formed a ferromagnetic compound [80, 81]. The base Heusler alloy forms with composition X_2YZ in the $L2_1$ crystal structure shown in Fig. 1.20(a). It may be thought of as an XX rock salt lattice where the two independent tetrahedral interstitial sites are each filled with an X atom and a Y atom. There are other flavors of Heusler alloys such as inverse Heuslers, half-Heuslers and quaternary Heuslers [81]. A broad array of elements can fill the X, Y, and

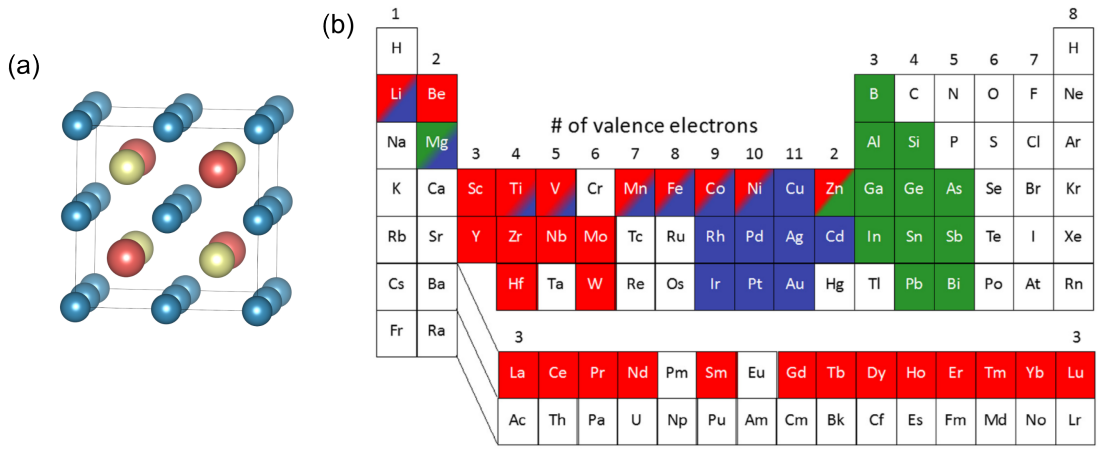

Figure 1.20: (a) Crystal structure of a full Heusler compound with stoichiometry X_2YZ. Blue corresponds to X, red to Y and yellow to Z. (b) Periodic table of Full Heusler alloys. Atoms which can sit on the X site (blue), Y site (red), and Z site (green). Reprinted from [82], with permission from Elsevier.

Z sites, summarized in Fig. 1.20(b).

Due to this wide range of stability, full Heuslers are famously tunable through a variety of X/Y/Z choices allowing designer control of material properties by the valence electron count of the Heusler [80–83]. They can be normal metals, ferromagnets, antiferromagnets, half metals, shape memory alloys, superconductors, and more (Fig. 1.21) [82]. The variety and promise of Heusler alloys is evidenced by their extensive coverage in books and review articles. Recently many of the $(Co,Fe,Ni)_2$-based full Heuslers have been predicted to be topological semimetals, which when demagnetized are nodal line semimetals and when magnetized are magnetic Weyl semimetals [84–86].

Many of these Heusler alloys are lattice-matched or close to lattice-matched to conventional semiconducting or insulating substrates [82]. Heusler alloys are generally able to be grown with acceptable quality with industry-compatibile thin film techniques such as sputtering. Any realistic spintronic or spin caloritronic application of topological semimetals requires thin films. One major problem with using topological semimetals for large anomalous Hall and Nernst effects is that since they depend the details of the bands

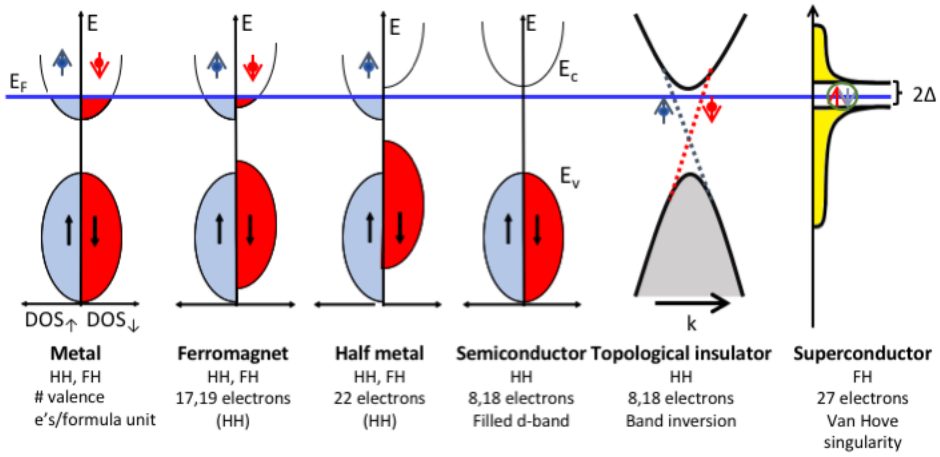

Figure 1.21: Some examples of different electronic phases that exist in Heusler alloys as a function of the valence electron count. Reprinted from [82], with permission from Elsevier.

in the neighborhood of the Fermi sea, the magnitude of these effects is directly related to the chemical potential in the grown-crystal. The chemical potential of the grown crystal is not required to be near the energy corresponding to the largest AHE or ANE in the band structure (and in fact usually is not [38, 58]). In Heusler alloys, tuning the valence electron count is frequently and successfully performed with chemical substitution. The chemical potential may then be (relatively) rigidly shifted to generate as large an AHE or ANE as possible in that system. Many Heusler alloys also retain their magnetic ordering at room temperature; many large AHE and large ANE materials only demonstrate these effects below liquid nitrogen temperatures. Heusler alloys are positioned as an important material for the production of realistic devices based on topological semimetals.

1.3.4 α-Sn

Grey (α) Sn, the diamond structure allotrope of Sn (Fig. 1.22(a)), has been investigated for centuries [87]. This phase is stable at low temperatures, transitioning from the tetragonal superconducting white (β) Sn phase at -13 °C. Perhaps most famously,

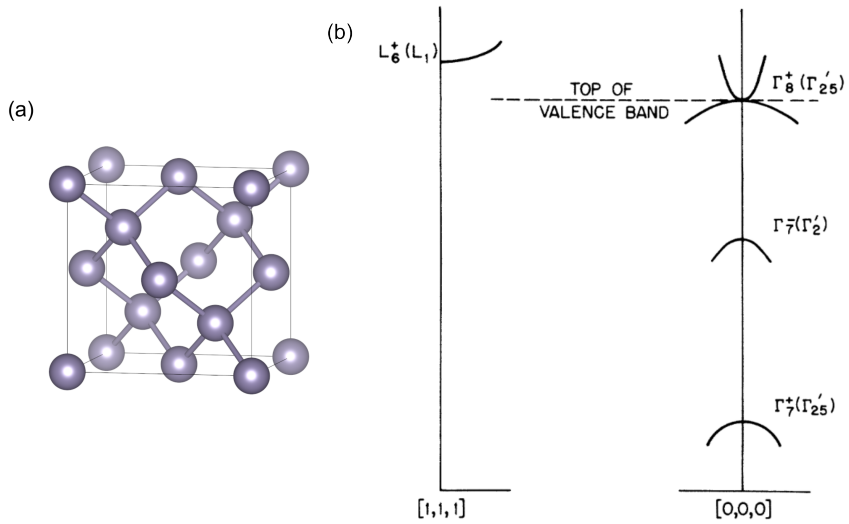

Figure 1.22: (a) The diamond cubic crystal structure of α-Sn. (b) Groves-Paul band structure of α-Sn, which has since been extensively experimentally confirmed. Reprinted with permission from [88]. Copyright 1963 by the American Physical Society.

tin "pest" has the urban legend of single-handedly causing Napoleon's defeat in the Russian invasion by dissolving the buttons on the jackets of his soldiers in the cold (that is, Russian) winter. Tin pest is also well-known for leading to the poor low temperature performance of Pb-free solders [87].

α-Sn single crystals were first synthesized and studied deeply in the 1950s, 1960s, and 1970s, spearheaded by the group of A. W. Ewald at Northwestern University [89–98, and references therein]. There was confusion over the band structure of α-Sn until the Groves-Paul model of a zero-gap semiconductor was proposed and verified in 1963 [88]. This model shows a gapless semiconductor with inverted bands at Γ, where the indirect gap at the L valley is small (Fig. 1.22(b)). The zero band gap made α-Sn of interest to demonstrate an excitonic insulator state, as suspected by Walter Kohn in 1968 [99]. However to our knowledge this phase has neither been proven nor expicitly disproven. The first experimental evidence of an excitonic insulator was given in 1991 in a completely different materials system [100].

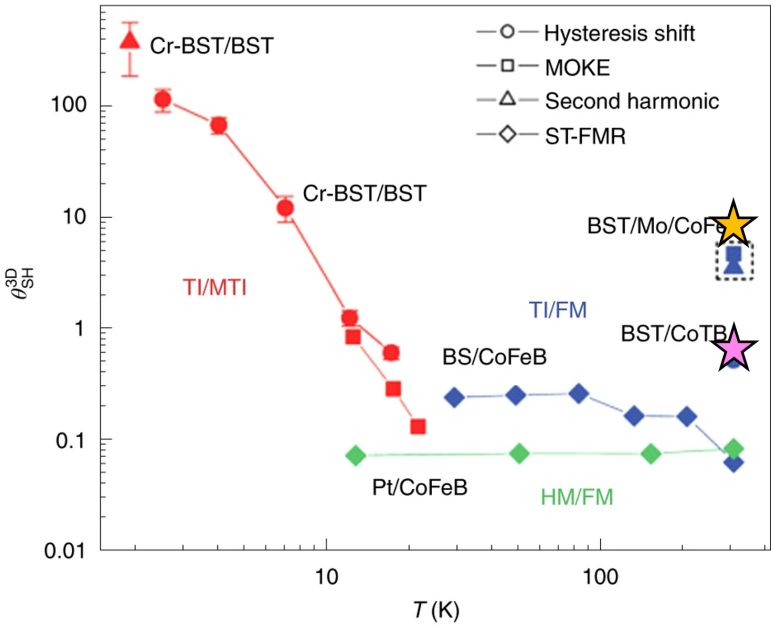

Figure 1.23: Demonstration of α-Sn's remarkable spin Hall efficiency. Adapted from [5] with permission from Springer Nature. The yellow star corresponds to the results of Ref. [103]. The pink star corresponds to the results of Ref. [78].

α-Sn crystals were difficult to synthesize and fabricate due to the low temperature stability (and the use of Hg flux in the synthesis). Research on α-Sn slowed before Farrow *et al.* demonstrated that α-Sn thin films could be stabilized by interaction with the substrate when grown by molecular beam epitaxy [101]. In addition, alloying these films with Ge increased the stability further [101]. This led to a resurgence in α-Sn research to (1) better understand the semiconductor physics describing the system and (2) provide a non-toxic alternative to HgTe for infrared detectors [102]. Much of this work was spearheaded by the group of Hartmut Höchst at the Synchrotron Radiation Center in Wisconsin. As HgCdTe asserted dominance over the field of infrared detectors, this resurgence slowed until the demonstration of the 2D TI phase in HgTe quantum wells [34], leading to the third wave of α-Sn research.

α-Sn, the inversion-symmetric analogue of HgTe, can be tuned through many different topological phases as a function of strain: 3D and 2D TIs, 3D and 2D DSMs, and 3D

WSMs [104–109]. α-Sn can be thought of as the parent topological phase of many other systems, as it can be adiabatically connected to HgTe, half-Heusler compounds, ternary chalcopyrites, ternary famatinites, quaternary chalcogenides, honeycomb LiAuSe compounds, and β-Ag_2Te compounds—all of which each form their own field of study [110]. Clarification to the behavior of α-Sn then allows extrapolation to these many other phases.

α-Sn has shown much promise in various spintronic architectures [78, 103, 111–113], most excitingly showing current-induced spin-orbit torque magnetization switching with spin-charge conversion efficiency at room temperature greater than those yet seen in the $(Sb,Bi)_2(Se,Te)_3$ system (Fig. 1.23). These are also representative of limited optimization by only a few research groups, compared to the large ongoing effort to develop the $(Sb,Bi)_2(Se,Te)_3$ system in this platform.

α-Sn films can also be converted to β-Sn lithographically to generate a large and controllable superconducting diode effect [114] or to generate proximitized topological superconductivity [58]. One issue with these device architectures is that once β-Sn is nucleated, it will continue to grow and will eventually consume the whole α-Sn film. The time constant for this change is slow in our experience, likely arising from the large volume change in the $\alpha \rightarrow \beta$ conversion.

1.4 Spin-polarized photocathodes

Spin-polarized photocathodes are used to produce spin-polarized electron beams, which are an essential tool for nuclear and particle physics experiments. These GeV scale experiments fall into three categories "(1) experiments performed that use the phenomenon of parity violation to measure the contribution of the strange quark to nucleon structure, (2) experiments to study the distribution of neutrons in nuclear matter, and (3)

experiments that look for physics beyond the standard model" [7]. There has also been recent interest in using spin-polarized electron beams for producing spin-polarized positron beams, which can then be used in a new suite of particle physics experiments [115]. This technique has a low efficiency ($< 0.01\%$) and thus requires very large electron currents (on the order of 10 mA or more) [115]. In addition, new accelerators being built such as the Electron Ion Collider at Brookhaven National Laboratory also require large beam currents with $> 80\%$ spin polarization [116]. Lower energy (eV to keV) spin-polarized electron beams are used in various electron-in materials science techniques such as transmission electron microscopy [117], low energy electron microscopy [118], inverse photoemission spectroscopy [119], and more which can provide deeper probes of magnetic and strongly spin-orbit coupled materials.

Various materials have been used for spin-polarized photocathodes over the years, but the direct band gap III-V semiconductor family is most consistently used due to the simplicity of spin polarization production, high quantum efficiencies, and low mean transverse energy (the in-plane momentum of the emitted photoelectrons) [8, 9].

1.4.1 Mechanisms

In order to understand how to improve the performance of spin-polarized photocathodes we must understand their operation principles. We begin with the mechanism of spin-integrated semiconductor photocathodes. A photocathode is a material that, upon excitation with light (photo-), produces electrons (-cathode).

The photoemission process in a photocathode may be separated into three steps (Fig. 1.24), following Spicer's model [120, 121]. First, light approximately resonant with the direct band gap is directed onto the semiconductor. An electron is excited into the conduction band. Second, this electron travels to the surface. Third, the electron is

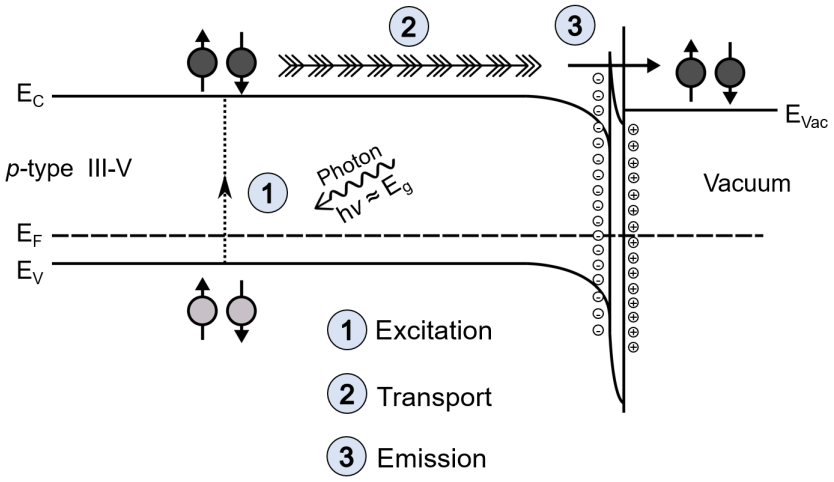

Figure 1.24: Spicer's three step model of photoemission. The semiconductor is p-type doped to achieve the negative electron affinity condition without an external bias. The negative electron affinity condition (NEA) is achieved by the formation of a surface dipole by the exposure of a clean surface, in vacuum, to an alkali (usually Cs) and an oxidizer (O_2 or NF_3).

emitted out of the surface. To actually make use of these photoelectrons, the working environment of photocathodes is usually vacuum so that the electron mean free path is long.

The photocathode quantum efficiency (QE) can be calculated directly from

$$QE(\lambda) = \frac{B(1-R)}{1+1/(\alpha(\lambda)L)} \tag{1.24}$$

where B is the surface escape probability, R is the reflectivity of incident light at the cathode-vacuum interface, $\alpha(\lambda)$ is the absorption coefficient in the photocathode, and L is the electron diffusion length in the photocathode [122]. L and $\alpha(\lambda)$ are material parameters related to the design, quality, and choice of semiconductor. R is set by the surface condition, but generally ignored in terms of material optimization. This leaves B, the surface escape probability as the primary mechanism to improve quantum efficiency in photocathodes.

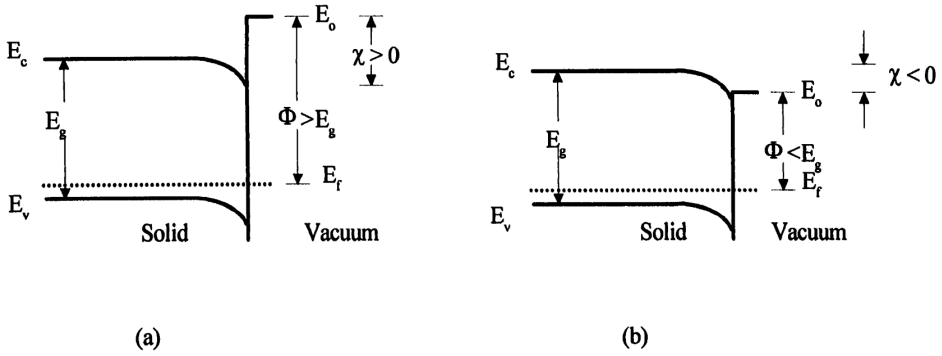

Figure 1.25: A direct band gap semiconductor with (a) a positive electron affinity condition and (b) a negative electron affinity condition. Copyright Old Dominion University 1999 [123].

Typically III-V semiconductors have a positive electron affinity, shown in Fig. 1.25(a). By forming a Cs-O/F layer on the III-V surface, a dipole is formed which creates the negative electron affinity (NEA) condition (Fig. 1.25(b)). The NEA condition greatly enhances the surface escape probability since the electrons will need much lower kinetic energy in order to escape the crystal. The NEA condition is best achieved (and results in highest quantum efficiencies) when a p-type semiconductor is used, which results in downward band bending at the surface (Fig. 1.24). III-V photocathodes are then usually p-type doped. The dopant density results in a trade off between L and B: higher hole densities reduce the electron diffusion length, but increase the escape probability. The experimental quantum efficiency is measured by

$$QE(\lambda) = \frac{I}{W}\frac{hc}{e\lambda} \tag{1.25}$$

where I is the emitted electron current and W is the power of incident light. In order for the NEA to be formed with optimal quality, the Cs-O/F layer must be grown on a pristine and flat III-V surface. The optimal cleaning of III-V surfaces for activation has been thoroughly studied. GaAs is the most common bulk III-V photocathode due to its

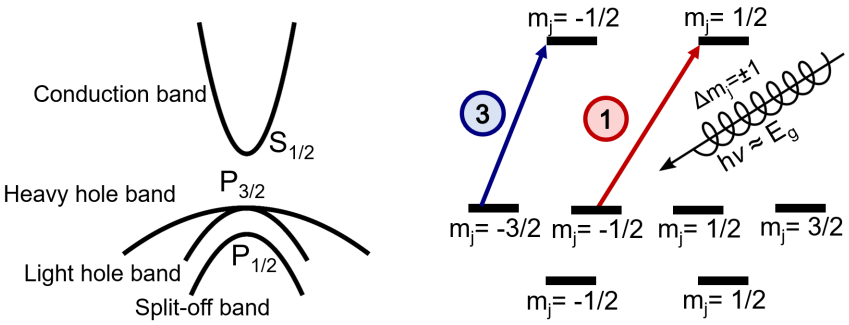

Figure 1.26: Mechanism of photoelectron spin generation in a III-V photocathode. Circular polarized light adds the $\Delta m_j = \pm 1$ selection rule, where the sign is changed by the helicity (right vs. left) of the polarization. The selection rule requires the heavy hole and light hole bands ($m_j = \pm\frac{3}{2}$ and $m_j = \pm\frac{1}{2}$, respectively) to excite to opposite spin directions in the conduction band.

high quality, easy heat cleaning procedure, and well-formed NEA.

An electric field (i.e. field-assisted photocathode) can be used in vacuum [124] or in air [125] to simulate an NEA photocathode or improve the performance of an NEA photocathode, but this technique is typically impractical at the conditions where spin-polarized photocathodes are operated. The high voltages involved require very smooth surfaces in vacuum and vacuum levels in the XHV range. Field-assistance is of most use in infrared photocathodes where the band gap energy (approximately the electron energy after excitation) is less than the surface barrier height.

We are still missing, at this point, the ingredient that generates spin polarization in III-V photocathodes. The spin polarization of photoelectrons is generated by the use of circular polarized light. The circular polarized light couples to the angular momentum of the electrons and adds $\Delta m_j = \pm 1$ as a selection rule (Fig. 1.26) where the heavy hole and light hole bands excite to opposite spin polarization directions in the conduction band. The relative transition rate between the heavy hole band and light hole band to

the conduction band is given by

$$\frac{\langle 1/2, -1/2|Y_1^1|3/2, -3/2\rangle}{\langle 1/2, 1/2|Y_1^1|3/2, -1/2\rangle} = 3 \tag{1.26}$$

where Y_1^1 is the spherical harmonic corresponding to the dipole operator of circular polarized light [1]. Transitions from the heavy hole band to the conduction band are clearly more intense. In addition, the heavy hole band and the light hole band excite to opposite spin channels. The *direction* of the majority spin channel may be switched by switching the helicity of incident light. The spin-polarized photoelectrons are transverse polarized parallel/anti-parallel to the incident light propagation direction. Off-normal light will reduce the spin polarization.

The theoretical maximum spin polarization is given by

$$P = \frac{N_\uparrow - N_\downarrow}{N_\uparrow + N_\downarrow} \tag{1.27}$$

and is thus limited to 50% for a bulk III-V. The spin polarization is usually measured by Mott polarimetry [8, 9]. The figure of merit for photocathodes is given by P^2QE and is related to the statistics in a spin-dependent measurement. This 50% value is the *theoretical maximum*, in experiment the maximum achieved is usually near 30–40% due to spin scattering during the transport and emission steps of the photoemission process [126]. In order to improve the theoretical maximum of spin polarization, the degeneracy between the heavy and light hole bands is broken through confinement and strain [127]. Confinement lifts the heavy hole band above the light hole band. Epitaxial biaxial compressive strain has the same effect as confinement, while biaxial tensile strain raises the light hole band. Because the heavy hole transition is much more intense, compressive strain is preferred. Then, as long as only the heavy hole band is excited

(photon energy is less than the light hole-conduction band gap) the theoretical maximum for the electron spin polarization is 100%.

For some modern experiments the goal is to maximize spin polarization, and then quantum efficiency at that polarization as a secondary effort, rather than to maximize the figure of merit. This is because these experiments require large bunch charges at which point the quantum efficiency is not a limiting factor. Instead, the lifetime of the photocathode becomes a limiting factor where the lifetime is the 1/e reduction in QE in terms of total charge (in Coulomb) extracted from the photocathode [128]. We have not yet directly investigated the lifetime of the photocathodes investigated in this thesis, but any improvement in lifetime is highly desired.

Another effect which occurs at large bunch charges is the surface charge limit. This is a surface photovoltage effect due to electron pile up in the downward band bending region at the III-V surface faster than they can be emitted into vacuum [129]. This pile up can be reduced by two methods. First is increasing the surface escape probability, as already discussed. The second is by narrowing the barrier (the width of the surface band bending region) such that the electrons recombine with bulk holes. The narrower the barrier, the easier it is for holes to tunnel into the band bending region and recombine. This is typically achieved with a highly p-doped layer at the surface [130, 131]. These effects are shown schematically in Fig. 1.27.

Originally GaAs wafers, also intended as substrates for epitaxial semiconductor device growth, were used as spin-polarized photocathodes. Compressive strained GaAs thin films on GaAsP metamorphic buffers replaced bulk GaAs as spin polarization requirements increased, but the quantum efficiency was lower than desired [132]. Growing the GaAs layer thicker to increase the quantum efficiency 1) nucleates dislocations reducing the quantum efficiency and spin polarization and 2) becomes thicker than the length over which spin polarization during transport to the surface is preserved. The modern

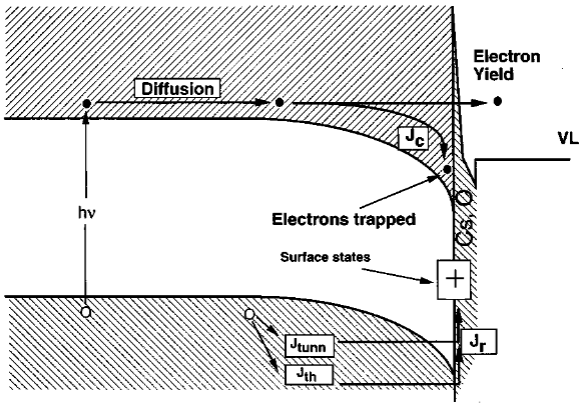

Figure 1.27: Photoelectrons diffuse to the surface. Some of them escape through the surface barrier; the rest are trapped by surface states (J_c). The restoring currents, thermionic (J_{th}), and tunneling (J_{tunn}) neutralize the charge trapped at the surface states. Reprinted from [129], with the permission of AIP Publishing.

approach of incorporating a superlattice quantum well preserves the strain and confinement (spin polarization) while increasing the thickness (quantum efficiency) [131]. This modern device is schematized in Fig. 1.28. A key factor not yet discussed is the addition of an epitaxial dielectric mirror, the distributed Bragg reflector, to increase the amount of light absorbed by the photocathode.

1.4.2 Distributed Bragg reflectors

Distributed Bragg reflectors (DBRs) are mirrors that use repeating pairs of dielectrics with a large refractive index mismatch. There is a Fresnel reflection at each interface which all add up to create a mirror with >99.99% reflectivity across a certain wavelength range [134]. DBRs based on III-V semiconductor layers are commonly used for high precision applications [135] or for integration in a vertical cavity surface emitting laser. In this scenario, a high gain region is sandwiched between two DBRs such that a standing wave of light is formed. This resonant enhancement of the absorption of the generated light allows the lasing process to proceed. In spin-polarized photocathodes,

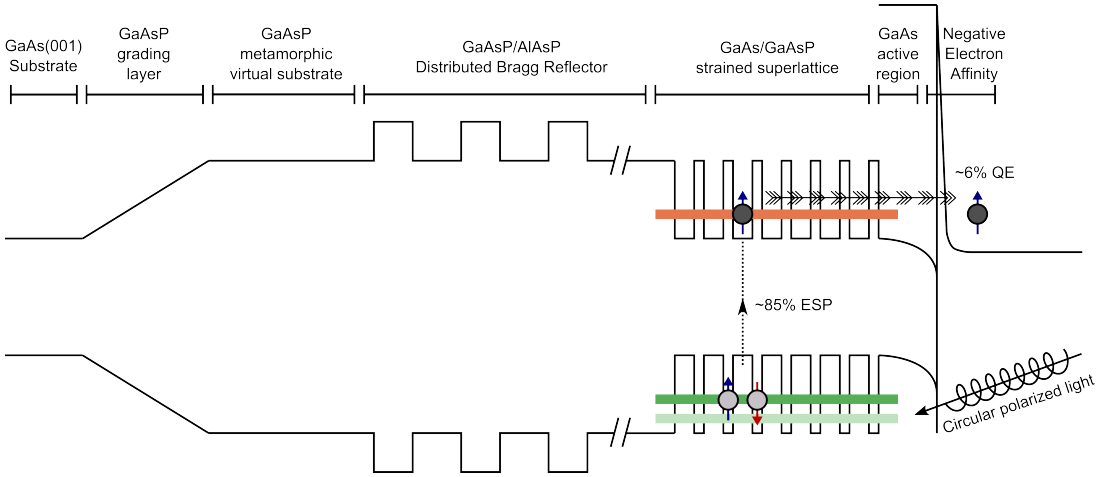

Figure 1.28: State of the art GaAs strained superlattice photocathodes described in Ref. [133]. Further details of the structure are discussed in Chapter 9.

half of this structure is grown such that the standing wave is made between the NEA functionalization layer and the DBR. Since there is only one high quality mirror in this scenario, the confinement of the light is worse than in a vertical cavity laser.

The reflectivity of the DBR at the designed wavelength is related to the refractive indices of the component layers as

$$R = \left(\frac{n_0 n_2^{2N} - n_s n_1^{2N}}{n_0 n_2^{2N} + n_s n_1^{2N}} \right)^2 \tag{1.28}$$

where n_0 is the refractive index of vacuum, n_1 and n_2 are the refractive indices of the two component layers in the DBR stack, n_s is the refractive index of the substrate and N is the number of period repeats in the superlattice mirror [134]. With a few repeats (usually greater than 8 pairs), the peak reflectivity approaches 100%.

The wavelength corresponding to the peak reflectivity is determined by the optical thicknesses of the layers in the heterostructure. It is designed into the device via the quarter-wave condition where $n_i t_i$, the optical length for a given layer, is set to $\lambda_{desired}/4$. For the creation of the desired standing wave resonant condition, reflectivity losses on the

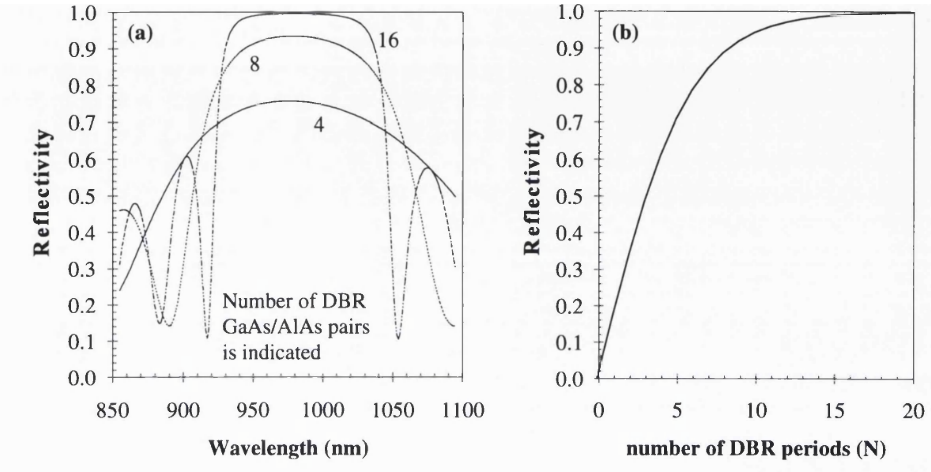

Figure 1.29: Caculations for a GaAs/AlAs DBR optimized for $\lambda = 980$ nm. (a) Reflectivity spectrum vs. number of periods. (b) Peak reflectivity vs. number of periods. For a vertical cavity laser using this mirror structure, > 20 periods would typically be used. Copyright 1995 University College London [134].

order of 0.01% can be significant. The wavelength window where this high reflectivity is sustained is also related to the same optical constants via

$$\Delta\lambda = \frac{4\lambda_{pump}}{\pi}\sin^{-1}\left(\frac{n_2 - n_1}{n_2 + n_1}\right) \tag{1.29}$$

where λ_{pump} is the wavelength designed to be at the peak mirror reflectivity [134]. The behavior of a typical GaAs/AlGaAs DBR is shown in Fig. 1.29. These equations show that the key material parameter for maximized DBR performance (high reflectivity and high bandwidth of reflectivity) is a high refractive index mismatch between the two components of the DBR superlattice at the pump wavelength.

1.5 Overview

This dissertation seeks to further our understanding of materials which can be used to generate electron spin in the solid state. By furthering this understanding, new device

architectures are possible and improvements to performance may be made. The techniques used to synthesize and characterize these materials are overviewed in Chapter 2. In Chapter 3 we attempt to demonstrate a Heusler alloy with large anomalous Hall and Nernst effects at room temperature. In Chapters 4, 5, 6, and 7 we optimize the growth of α-Sn thin films and clarify many of the inconsistencies in the literature with regard to the topological phases in this system as a function of epitaxial strain and quantum confinement. In Chapter 8, we build on these results to demonstrate an unexpected topological phase transition in Ge alloyed α-Sn, related to the mechanism behind the formation of topological surface states in this system. In Chapter 9, InAlGaAs/AlGaAs is benchmarked as an alternate materials system for III-V superlattice spin-polarized photocathodes. Finally in Chapter 10 we summarize our results and point toward the bright futures possible in each of these systems.

Chapter 2

Methods

A variety of growth and characterization techniques were necessary in order to grow and study the high quality thin films in this dissertation. Many of these techniques are surface sensitive and require little to no surface contamination. Here we leverage the capabilities of the interconnected ultra high vacuum (UHV) system in the Palmstrøm Lab at the University of California, Santa Barbara (Fig. 2.1). This system consists of 7 interconnected epitaxy chambers and two chambers for metal and dielectric deposition. Two systems are equipped for low substrate temperature depositions, one near liquid helium temperatures and one near liquid nitrogen temperatures.

These growth chambers are integrated with *in situ* angle-resolved photoemission spectroscopy, scanning tunneling microscopy/spectroscopy, and X-ray photoemission spectroscopy. A suite of vacuum suitcases has been developed that allows samples to be shipped to collaborators or driven to beamline 10.0.1.2 at the Advanced Light Source or beamline 5.2 at the Stanford Synchrotron Radiation Lightsource for spin- and angle-resolved photoemission experiments.

These capabilities allow measurement of surfaces and interfaces without the compounding variables of oxidation and atmospheric contamination. This system also allows

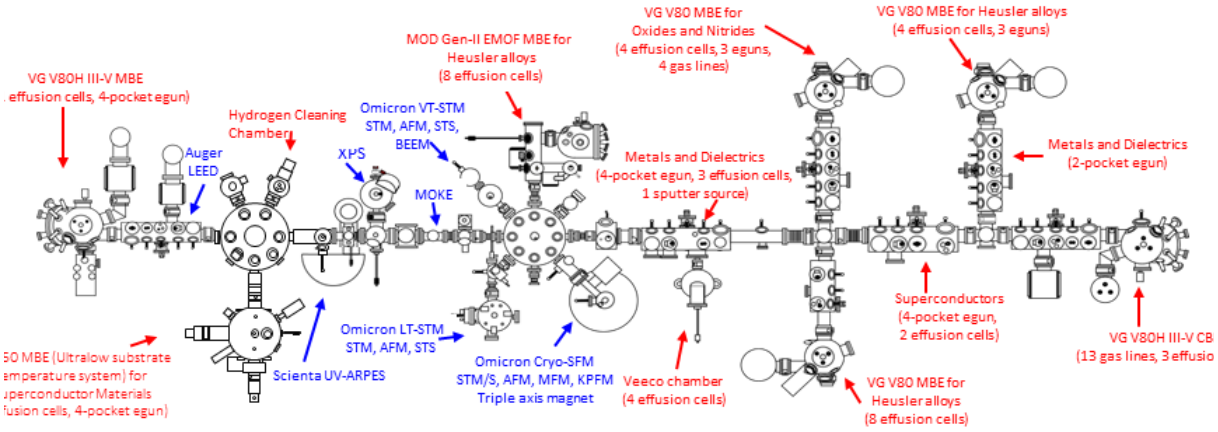

Figure 2.1: Schematic of the Palmstrøm Lab

deposition of elements and compounds that are not compatible in the same epitaxy system (e.g. Group IV elements in a dedicated III-V system).

2.1 Ultrahigh vacuum

Ultrahigh vacuum is a necessary requirement for (a) keeping surfaces and interfaces clean (b) keeping unintentional dopants low and (c) acquiring the molecular beam condition that allows the epitaxy techniques discussed below to function. Ultrahigh vacuum is defined for the pressure range $10^{-9} - 10^{-12}$ Torr, where the residual species in this range are usually hydrogen and nitrogen. Sometimes hydrocarbons are not fully evacuated and contribute a non-negligible residual partial pressure.

The application of the kinetic theory of gases to an ideal gas scenario gives the mean free path (λ) between gas-particle collisions as

$$\lambda = \frac{\sqrt{2}k_B T}{2\pi P d^2} \tag{2.1}$$

where T is the temperature, P is the gas pressure, and d is the diameter of the molecule/atom

in the gas [136]. The flux incident on a surface exposed to a gas at this pressure/temperature condition is given by

$$J = P\sqrt{\frac{N_a}{2\pi k_B MT}} \tag{2.2}$$

where M is the atomic/molecular weight of the gas [136]. For most materials with atomic densities on the order of 10^{22}–10^{23} atoms/cm^3, the surface density is on the order of 10^{15} atoms/cm^3. The flux of a residual gas at room temperature would expose a surface to one monolayer worth of material in one second at a pressure of 10^{-6} Torr. This leads to the definition of a Langmuir (i.e. equivalent monolayers) as 10^{-6} Torr·sec. These results also assume that any particle that hits a surface adsorbs to that surface. This is equivalent to setting a unity sticking coefficient, the probability of a given adatom on a given surface sticking to that surface. Sticking coefficients are frequently not unity, especially for high vapor pressure elements like the pnictogens.

The flux of a material (either given off by a chamber wall or intentionally evaporated) is proportional to the vapor pressure which is defined by

$$P = Ae^{\frac{-E_a}{k_B T}} \tag{2.3}$$

where E_a is the heat of sublimation or evaporation where A groups together geometric terms and other material constants. This equation is also only an approximation—in real systems the heat of sublimation and heat of evaporation do have a temperature and pressure dependence. The dependence on pressure can usually be ignored as all materials are always in ultrahigh vacuum conditions. The temperature dependence sometimes must be corrected for in calibrations.

In ultra-high vacuum (UHV) the mean free path of atoms approaches kilometers and the time for one monolayer of contamination approaches hours or days. In order to achieve

these low pressures, the equipment involved in construction of these systems must have low residual outgassing rates at room temperature. This requires well-polished surfaces so the total area-in-vacuum which outgasses is reduced. The construction is usually all metal or all glass. Certain ceramics and polymers with low outgassing rates can be incorporated in select applications as well. In addition, any exposure to hydrocarbons or water (e.g. by venting a system to air), requires a bake of the system above 115 °C, typically 150 °C to 200 °C. The pumping speed of the vacuum pumps on a UHV system must also match the outgassing of all parts, convoluted with the conductances of the valves, tubes, etc. Conductances and outgassing rates in series add in inverse, while in parallel they add directly. Design of an ultrahigh vacuum system is then very similar to the design of other gas or liquid handling systems.

2.2 Growth techniques

2.2.1 Molecular beam epitaxy

In molecular beam epitaxy (MBE), deposition sources in an ultrahigh vacuum chamber are directed toward a substrate surface where growth proceeds. The substrate typically acts as a crystal nucleation source, allowing for true epitaxy to proceed rather than deposition of amorphous or polycrystalline structures. Molecular beam epitaxy is so named because it refers to the molecular beam regime of gas flow. Via Eq. 2.1, the mean free path of atoms is longer than the dimensions of the chamber (critically the source-sample distance). There are thus no gas-phase interactions and no boundary layer effects; the growth of the crystal is entirely dictated by the kinetics and thermodynamics on the crystal surface. Atomic fluxes can be turned on and off abruptly via mechanical shutters with transients on the order of milliseconds. Abrupt heterojunctions limited

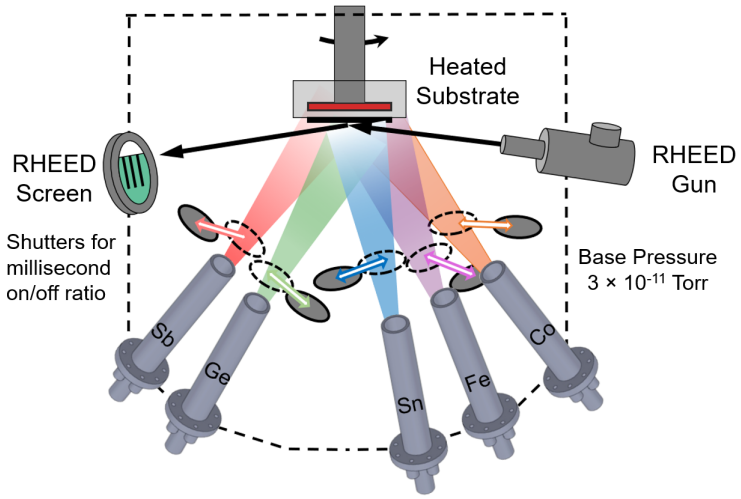

Figure 2.2: Schematic of a molecular beam epitaxy chamber equipped with reflection high energy electron diffraction and effusion cells.

only by the materials being interfaced can be synthesized.

Because this is a vacuum-based technique, the partial pressure of anything *not* the atomic fluxes from the deposition sources is incredibly low (ideally <ppm) resulting in low unintentional doping. This vacuum-based technique may be controlled by the impingement rate of atomic sources and the surface temperature the impinged atoms experience. Molecular beam epitaxy is an out-of-equilibrium technique that can allow stabilization of metastable or unstable alloys and compounds. This class includes most of the materials discussed in this dissertation. Another benefit of MBE as a vacuum-based technique is its compatibility with vacuum-based *in situ* characterization techniques, described in Sec. 2.3.

2.2.2 Deposition sources

Molecular beam epitaxy is the name of both the group of deposition techniques and the name of the family among this group taking advantage of solid source deposition material. Gas source molecular beam epitaxy (GSMBE) uses gas-based (usually hydride)

group V sources. Metal-organic molecular beam epitaxy (MOMBE) uses metal-organic group III precursors. Chemical beam epitaxy (CBE) uses both metal-organic group III precursors and hydride group V sources. All growth discussed in this dissertation uses conventional solid source molecular beam epitaxy.

Elements with vapor pressures between 10^{-5} and 10^{-2} Torr at temperatures <1400 °C may be evaporated from conventional effusion cells (Fig. 2.3(a)). The basic effusion cell works on the principle of resistive heating of a refractory wire wound around an inert ceramic crucible. The wire radiatively heats the ceramic which conductively heats the source material. The typical crucible material is pBN, but other materials like BeO are sometimes necessary to reduce reaction between the ceramic and the source material. Certain crucible materials, such as graphite, increase the maximum temperature available in the effusion cell. For materials with very low vapor pressures such as Ti and V, all metal designs are used which increase the maximum cell temperature to near 2000 °C. Any ceramic spacers or supports are removed from the hot zone, and refractory metal crucibles are used. For all systems the effusion cell is directed toward the substrate surface. The effusion cell/crucible geometry is such that the flux uniformity and flux magnitude are stable during a growth campaign. Certain materials require more complex crucible shapes than that shown in Fig. 2.3(a).

Many materials evaporate as atoms, but some evaporate as clusters. Pnictogens in particular evaporate as tetramers (Sb_4, As_4, etc.) at the temperatures necessary to produce reasonable beam flux values [137]. These tetramers have a lower sticking coefficient on the substrate and result in a narrower growth window [138]. To expand the growth window and (depending on system/device) to improve optical quality, the dimer or monomer species is preferred [139–141]. The temperatures required to produce these species in a single zone effusion cell (>800 °C) would produce unreasonably large beam fluxes. Instead, a cracking zone above the base is operated at these temperatures. This is

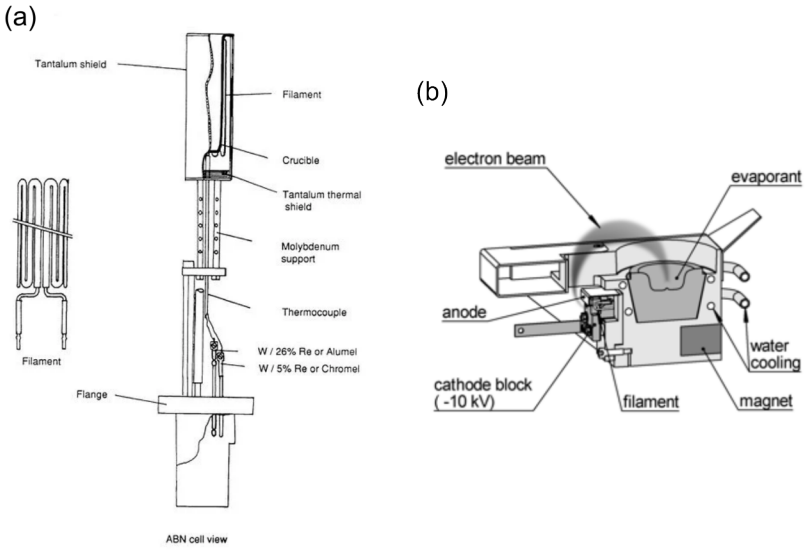

Figure 2.3: (a) Schematic of an effusion cell. Copyright Riber. (b) Schematic of an e-beam source. Copyright MBE Komponenten.

coupled with a valved stopper to continuously tune the Group V flux without modifying the temperatures of the cell. Since these cells hold material on the order of kilograms, any change in temperature has a large transient and should be avoided. Thermally evaporated Sn and Ge does not only consist of monomer species, but the population of non-monomer species is less than ppm compared to the monomer case [137].

While the term is solid-source MBE, sometimes the material held in the effusion cell is molten at the temperatures which produce reasonable fluxes. These elements, such as gallium and indium, benefit from having a dual zone cell where the region near the lip is kept 50–150 °C hotter than the base. This hot lip configuration eliminates recondensation at the lip. Recondensation leads to flux instability and the generation of oval defects in grown thin films, so should be avoided. Certain elements like molten aluminum wet the crucible and creep up the walls. To reduce this effect, a cold lip design is used. The dual zone design may be achieved by variable filament winding density across the length of the crucible or by using two separate filaments controlled on different PID controllers.

The latter is more typical as it gives greater control and stability, but is more expensive to manufacture.

For materials with very low vapor pressures like refractory elements or some compound oxides (MgO, AlO_x), a reasonable flux cannot be achieved by radiative/conductive heating. Instead, an electron-beam is generated via thermionic emission from a tungsten filament, accelerated via an electric field, and directed via a magnetic field into a source charge (Fig. 2.3(b)). This allows heating well in excess of 2000 °C. However, for materials that sublimate (like many oxides) the flux depends very sensitively on the position of the beam on the source charge and depletion of the source charge. Molten materials give slightly more consistent fluxes, but have issues with spitting and damage to equipment from rapid heating/cooling. Complex electron beam raster designs can give much more consistent fluxes in these materials. Any e-beam source ideally has its flux monitored continuously during the growth process, but this is sometimes not experimentally possible. In these cases, the flux must be calibrated before and after the growth. For long growths, the growth may sometimes need to be interrupted to verify the flux.

2.2.3 Temperature control

Other than controlling the incident flux of constituent atoms during growth, the other main tuning knob in MBE is the substrate temperature. Substrate heating is achieved by radiative heat transfer from a resistive refractory wire encapsulated in pBN. The substrate of interest is held onto a refractory block by an indium or gallium solder or by refractory clips. In the latter case a hole is drilled into the refractory block so that there is line-of-sight between the heater and the substrate. If the substrate is IR transparent, a thick metal layer is deposited on the backside to act as an absorber layer. A thermocouple is placed in between the substrate heater and the back of the refractory block. Due to this

design, the thermocouple temperature is very different from the true surface temperature. This difference varies system to system and varies by heating power, but usually ranges between 50 °C and 150 °C. The thermocouple temperature can be calibrated via a variety of mechanisms, but the relationship between thermocouple temperature and substrate temperature is highly nonlinear. These calibrations should only be trusted in a narrow temperature range near where the calibration is performed.

A more direct measurement of the surface temperature is used for III-V growths in this work. Pyrometry measures the intensity of radiated light at a certain wavelength (usually in the infrared) and, if the emissivity of the material is known, can be calibrated to the true surface temperature. The wavelength of light must be lower than the wavelength of the band gap of the semiconductor substrate. Other sources of light at this wavelength from hot effusion cells and crackers can give false temperature readings. The emissivity is usually calibrated on a sample-to-sample basis.

Temperature calibration for both pyrometers and thermocouples are performed with transitions from oxide removal, between temperature-dependent surface reconstruction changes, via removal of an arsenic or antimony volatile cap, and by the melting and freezing points of indium and gallium. These transitions are all monitored *in situ* with reflection high energy electron diffraction. Other techniques such as band-edge thermometry, blackbody radiation spectroscopy, spectroscopic ellipsometry, and emissivity-corrected pyrometry can also be used to precisely control substrate temperature. The key in molecular beam epitaxy is not to be accurate, but to be consistent and reproducible.

2.2.4 Flux calibrations

In growth, it is necessary to know the relationship between the nominal structure (composition, thickness, etc.) and the true structure. Ideally, the nominal and true

structure are as close as possible. This equivalence is found by calibrating the flux of atoms (or atomic clusters) evaporating out of an effusion cell and incident on the sample. Rather than only calibrating for a single effusion cell temperature, flux calibrations are generally performed across a reasonable temperature range such that relative compositions may be tuned easily. Generally absolute flux control better than 1% is achievable with a good calibration procedure. Control better than 0.1% can be achieved in limited cases depending on effusion cell design, source material, and other variable experimental parameters.

In this work, Group IV atomic fluxes were calibrated with oscillations in the intensity of reflection high energy electron diffraction (RHEED) and Rutherford backscattering spectrometry (RBS) and cross-checked with X-ray diffraction of final samples. Group III and Group V fluxes were calibrated with superlattice X-ray diffraction and RHEED oscillations and cross-checked with X-ray diffraction of final samples. All else was calibrated only by RBS. These techniques are discussed in more detail in the following sections. Flux transients for all cells were measured with a beam flux gauge to ensure a uniform composition profile during growth. For the MBE system used for many of the growths in this dissertation, irreproducibility of the beam flux gauge measurements dominated over true variation in day-to-day fluxes.

Growth rate calibrations are fit to the semilog Arrhenius equation (Eq. 2.3). Ideally the temperatures used during growth are interpolated rather than extrapolated. Calibrations are plotted against historical calibrations (Fig. 2.4) such that the emptying of a cell may be monitored. In addition, the activation energy for a given material should be close to constant, as it is primarily dictated by the heat of evaporation or sublimation. Significant changes to this value indicate potential contamination or damage to the cell.

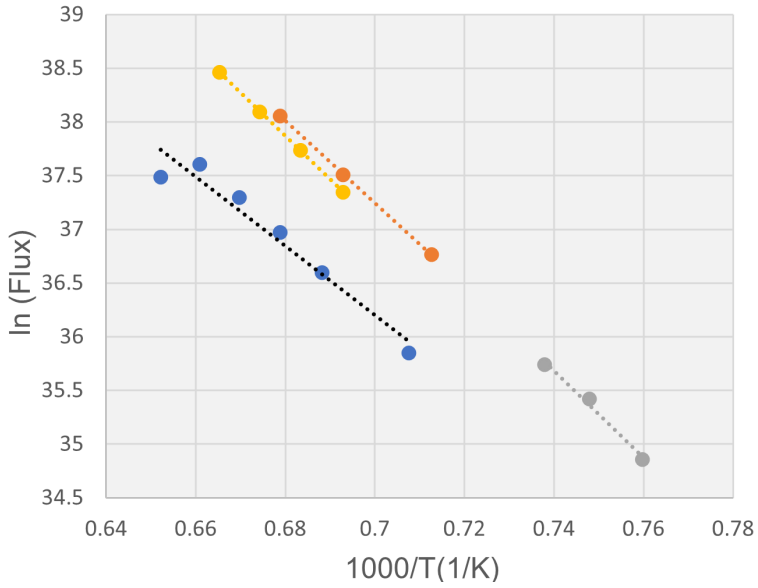

Figure 2.4: Flux calibrations of a Ge effusion cell over the period of 2021 to 2024. Different colors correspond to different calibration runs.

Ex situ flux calibration

In this work, flux from a given cell at a given temperature is generally *ex situ* calibrated by Rutherford backscattering spectrometry, which gives a very precise measurement of absolute atomic density of each elemental species on the sample. X-ray reflectivity gives good measurements of total film thickness, but the absolute atomic density is not well known. The density measured in X-ray Reflectivity (XRR) is only the equivalent X-ray density, not the true density of the film. In addition, XRR requires electron density contrast between the film and substrate. There is no such contrast in Sn/InSb, so it cannot be used. Profilometer measurements of the total grown film thickness (usually by shadowing a portion of the substrate during growth) give a rough estimate of atomic fluxes, but this method also has issues with different phases and varying densities. Spectroscopic ellipsometry gives reliable results on very well-known materials deposited in a very consistent matter. It is typically used for dielectric layers deposited by atomic layer

deposition.

A high resolution *ex situ* technique to calibrate fluxes when Rutherford backscattering spectrometry is not available is X-ray diffraction. For materials that grow as high-quality thin films, an on-axis out-of-plane reflection will show Pendellösung fringes corresponding to the film thickness. Again atomic flux must be derived from an assumed density, but this technique can be used on the actual epilayer rather than a reference sample to calibrate the equivalent compound/alloy growth rate.

For well-known materials with low lattice mismatch and good interface quality, a superlattice of the materials of interest may be grown instead. The superlattice diffraction profile gives access to two degrees of freedom, the average out-of-plane lattice constant of one period and the total period thickness. Therefore the layer composition of a binary (AlAs/GaAs) or ternary/binary (InGaAs/GaAs) superlattice can be extracted on the order of a monolayer. The latter case is only possible if the ternary shares a flux source with the binary.

In situ flux calibration

Flux calibrations can be entirely based on effusion cell temperature, but stability of the effusion cell must be trusted. This trust must be verified as source depletion and redistribution during heating/cooling cycles will shift the equivalent fluxes for a given cell temperature. For day-to-day flux checks and measurements of flux transients and drift, an *in situ* method is preferable. Relative *in situ* measurements of flux are usually calibrated against absolute *ex situ* measurements. In select cases where films grow in a layer-by-layer mechanism, the intensity of the reflection high energy electron diffraction profile of the surface oscillates according to the layer-basis growth rate (Sec. 2.3.2). Other *in situ* flux probes are discussed below.

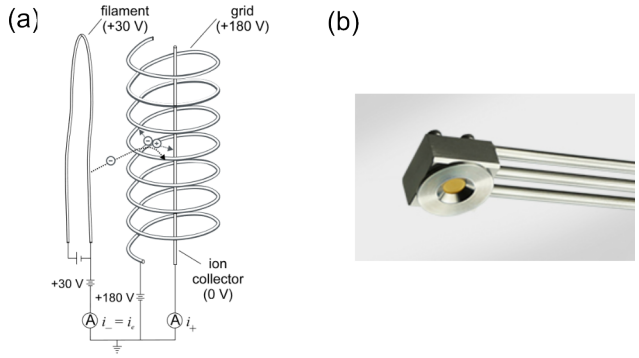

Figure 2.5: *In situ* flux measurement instruments. (a) A hot cathode Bayart-Alpert ionization gauge. Copyright Granville-Phillips. (b) A quartz crystal microbalance. Copyright MBE-Komponenten.

Beam flux gauge The beam flux gauge works on the same principle as a conventional ion gauge (Fig. 2.5(a)). A resistively heated tungsten wire produces electrons via thermionic emission. These electrons are accelerated toward the grid and create ions via collisions with residual atoms and molecules. The ions are then collected by the unbiased collector filament and read as a current proportional to flux. The low flux limit of the gauge is the X-ray limit: electrons emitted by the filament strike the grid or other metal in the system to produce X-rays which, when incident on the collector, generate a photoelectric current. Fluxes resulting in reasonable growth rates are well above this lower limit. The current produced by equivalent true incident fluxes of different atoms will vary by the ionization efficiency of those atoms. Ratios of absolute measured collector current or pressure then do not correspond directly to true atomic flux ratios, but the two ratios are linearly correlated.

In a typical ion gauge or beam flux gauge, this process is controlled by an ion gauge controller which sets the emission current of electrons between the filament and the grid. Since this emission current will modify the collector current (more electrons → more collisions → more ions → higher current), stable control of this parameter is essential. Ion gauge controllers also convert the measured ion current into pressure, calibrated for

N_2 [142]. Different manufacturers calibrate in slightly different ways and the calibration for different gauge designs varies. To solve these issues, we control beam flux gauges with external electronics and a LabVIEW based control algorithm (including stable PID loops for emission current).

Use of beam flux gauges is also complicated by experimental geometry and methods. The flux gauge is quite sensitive, so small changes in the flux gauge location and orientation due to human variation or gear backlash can easily add percent level unreliability to measured currents. Beam flux gauges are usually not mounted on high precision UHV rotation/translation stages. These geometric effects are convoluted with effusion cell geometry; certain elements will show high sensitivity to position, others low. The history of the flux gauge is also an important factor. For example, a measurement of arsenic flux before a measurement of gallium flux will be different than one after since the gallium will pump on the arsenic. Logical choice of elemental order is essential and must be consistent. A series of flux gauge measurements, one atomic flux at a time, is performed with only the later measurements (after at least two cycles) used for actual calibration. The time of each flux gauge measurement should also be comparable run to run. Consistent measurement of the background signal before and after each cell flux calibration is also essential, as the background chamber pressure (unless it is below the X-ray limit, in which case the X-ray induced current) generates some "dark" current.

Flux gauges are unsuitable for certain scenarios. Electron beam sources generate electrons which can interfere with operation. These sources also include magnetic fields which can bend the thermionic electrons and ionized gas particles in the flux gauge away from their intended path. Certain elements like titanium or cesium will modify the work function of the filament leading to wildly varying emission currents. Flux gauge measurements of titanium, for example, lead to negative equivalent collector currents. Other elements, for example boron, will react with the components of the flux gauge and

are then also incompatible.

Quartz crystal microbalance The quartz crystal microbalance (QCM) works on a similar principle as a quartz watch. A quartz crystal is set to oscillate with an applied voltage, and then oscillates at its resonant frequency. This resonant frequency depends of the mass of the oscillator. In the QCM, a disk-shaped surface of the quartz is exposed to the beam flux (Fig. 2.5(b)). The frequency of oscillation is damped by the deposition of material. Conversions based on the density and acoustic impedance of the deposited material provide an equivalent thickness of deposited material from a given change in frequency. This equivalent thickness is correlated to the true material flux, but needs to be corrected by a geometric factor accounting for the location of the QCM in the UHV chamber with respect to that of the sample surface during growth.

The QCM provides a suitable alternative to beam flux gauges. For systems with different classes of materials, such as alternating depositions of oxides and metals, delamination of material can be an issue. There is also a finite amount of material that can be deposited on a QCM before it ceases to oscillate entirely and needs to be replaced. The resonant frequency is also sensitive to coupled vibrations which are unavoidable from certain vacuum pumps or from operations such as the opening and closing of shutters. The radiative heat transfer from the high temperature effusion cell changes the temperature of the quartz crystal which then modifies the oscillation frequency independent of mass damping. Temperature effects are somewhat offset by active water cooling of the QCM. Due to these effects, QCM growth rates are only reliable some time after the shutter is opened, and the reported growth rate is generally an average of measurements over a few minutes.

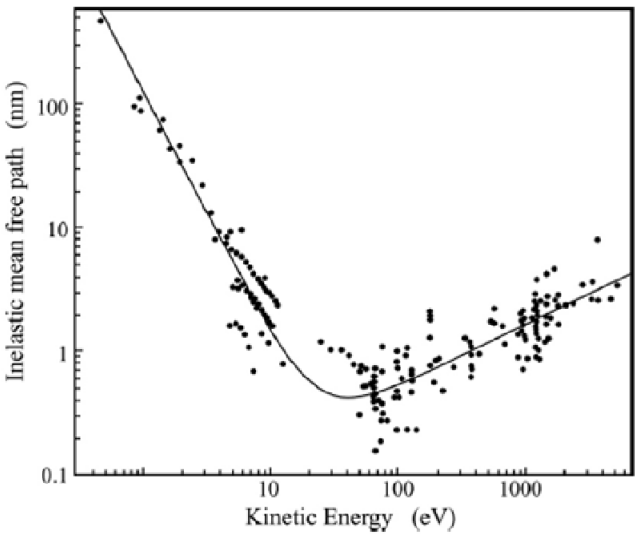

Figure 2.6: The universal curve of photoemission. Reprinted from [143] with permission from Wiley.

2.3 *In situ* characterization

2.3.1 Photoemission spectroscopy

Photoemission spectroscopy is used in this dissertation to describe both the chemistry and electronic structure of materials. Both the excitation from core levels and the excitations from delocalized valence electrons are studied. The photoelectrons are exciting using incident light in the vacuuum ultraviolet (VUV) and X-ray regimes. This results in photoelectrons with short mean free paths defined by the universal curve (Fig. 2.6). Due to this, these techniques are very surface sensitive and require a pristine surface. For the films investigated in this dissertation, all films are directly transferred between the growth chamber and the photoemission chamber without leaving the UHV environment.

Angle-resolved photoemission (ARPES) gives an (almost) direct measurement of the occupied band structure of a material (Fig. 2.7). This allows topological phase identification to proceed relatively easily compared to other techniques which give either indirect measurements of the band structure or direct measurements at only certain k points. In

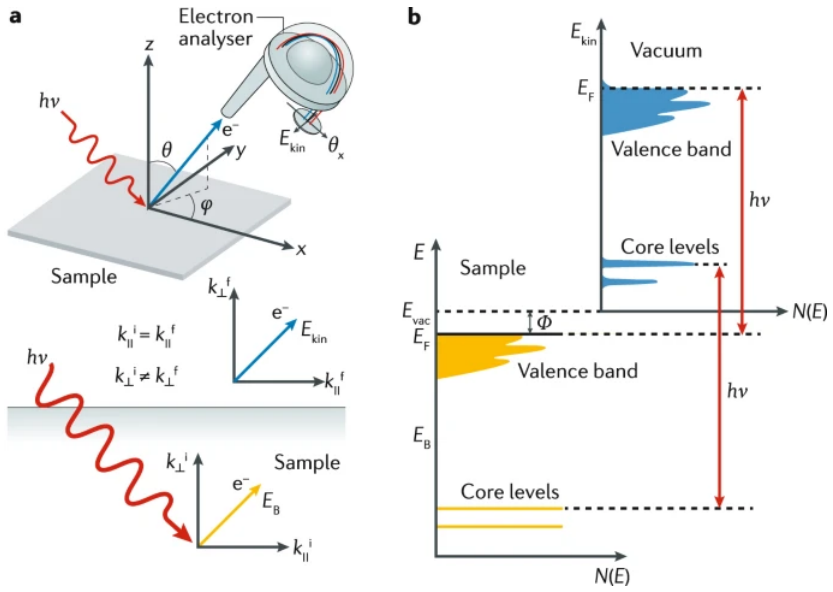

Figure 2.7: (a) Schematic of the photoemission process in ARPES. The electron analyzer disperses electron in exit angle and in kinetic energy. (b) The conservation of energy in photoemission. Reproduced from [144] with permission from Springer Nature.

addition, spin-resolved ARPES allows for the identification of spin-polarized topological surface states.

Mathematical formulation of the technique

The following derivations follow from Refs. [145–147]. The generation of photocurrent may be described by Fermi's golden rule

$$w \propto \frac{2\pi}{\hbar} |\langle \psi_f | H_{int} | \psi_i \rangle|^2 \delta(E_f - E_i - \hbar\omega) \tag{2.4}$$

where f and i subscripts correspond to the final and initial states, E corresponds to the energy of these states, ψ corresponds to the N electron states involved in the transition, $\mathbf{p}$ is the photoelectron momentum, and $\mathbf{A}$ is the vector potential corresponding to the incident light. The δ function enforces the conservation of energy in the system. The

H_{int} term has the general form

$$H_{int} = \frac{e}{2mc}(\mathbf{A}\cdot\mathbf{p} + \mathbf{p}\cdot\mathbf{A}) - e\phi + \frac{e^2}{mc^2}\mathbf{A}\cdot\mathbf{A} \tag{2.5}$$

where $\mathbf{A}$ and ϕ are the vector and scalar potential from the electromagnetic field of light. The Weyl gauge is used which sets the scalar potential to zero. The third term corresponds to two photon processes which are irrelevant to the current discussion. From the commutation relation $[\mathbf{p},\mathbf{A}] = -i\hbar\nabla\cdot\mathbf{A}$ the first term may be simplified to $2\mathbf{A}\cdot\mathbf{p} + i\hbar\nabla\cdot\mathbf{A}$. The latter term here may be set to zero by the *dipole approximation*, which states the spatial variation of the photon beam's electromagnetic field is negligible. This is equivalent to translational symmetry in the system. These excitations are usually described in terms of the three step model of photoemission (Chapter 1) so that they are more tractable, but the one step model should give the best agreement with experiment.

Under the *sudden approximation*, hole relaxation processes can be neglected such that the total wavefunction may be factored and the transition rate between initial and final states, w, becomes

$$w \propto \left|\langle\phi_f|\,\mathbf{A}\cdot\mathbf{p}\,|\phi_i\rangle\right|^2 \left|\langle\Psi_s^{N-1}|\Psi_i^{N-1}\rangle\right|^2 \delta(E_f - E_i - \hbar\omega) \tag{2.6}$$

where the first factor represents the one-electron matrix element ($M_i^f(k)$, discussed in detail in Chapter 5) and the second factor gives, essentially, the effects of electron interactions due to the final state s. The total photoemission intensity is proportional to the sum of Eq. 2.6 over all i, f, s. The sum of the second factor over these states encodes all many-body interactions into the spectral function $A(k,\omega)$. The spectral function is equivalent to the imaginary part of the one-electron removal Green's function such that

it can be described by

$$A(k,\omega) = \frac{-1}{\pi}\frac{\Im(\mathbf{\Sigma})}{(\omega - \epsilon_k - \Re(\mathbf{\Sigma}))^2 + (\Im(\mathbf{\Sigma}))^2} \tag{2.7}$$

where $\mathbf{\Sigma}(k,\omega)$ represents the particle self energy and ϵ_k represents the one electron bare band dispersion. The imaginary portion of the self-energy manifests as changes to the linewidth of a Lorentzian-like function. The real portion of the self-energy manifests as renormalization of the band dispersion. Fits to the energy or momentum distribution of ARPES data are performed with Voigt profiles, where the Lorentzian represents the band dispersion and the Gaussian represents the resolution function of the measurement.

In core-level photoemission analysis, k dependence is not present since the core-level electrons are localized. Core-hole relaxation and electron interactions are ignored as well, which allows the binding energy of photoelectrons to be written as $E_B = E_{kin} - E_F$ or $E_B = \hbar\omega - E_{kin} - \phi$ (where $\mathrm{E_F}$ is the kinetic energy of photoelectrons at the Fermi level), which is the orbital binding energy. This is equivalent to Koopman's theorem in quantum chemistry.

In valence band photoemission, the bare band dispersion and one electron matrix element $M_i^f(k)$ have momentum dependence and. By treating the initial and final states as Bloch states, the photoemission intensity without interactions can be written as

$$I \propto M_i^f f(E)\delta\left(k_{f||} - k_{i||} + G_{||}\right)\delta\left(k_f - k_i + G\right)\delta\left(E_f - E_i - \hbar\omega\right)\delta\left(E - E_f + \phi\right) \tag{2.8}$$

where ϕ is the work function of the material, G is the reciprocal lattice vector of the Bloch state, and $f(E)$ is the Fermi-Dirac distribution (equivalent to stating only occupied states may be photoexcited). The first δ function corresponds to the in-plane momentum being conserved. This is required by the preservation of translational symmetry in-plane. The

total momentum must also be conserved, represented by the second δ function. The photon momentum is ignored here as it is small at photon energies below the soft X-ray regime. The third δ function corresponds to total energy conservation, while the fourth states that only photoelectrons with energies above the surface work function may escape the material. The single-electron matrix element can give information about the orbital symmetry of the initial state using linear or circular dichroism measurements (Chapter 5 and Ref. [145]).

The conservation of energy in the photoemission process is shown by the schematic in Fig. 2.7(b). The energy in this work is not converted to binding energy, E_B, but is instead referenced to the kinetic energy of photoelectrons at the Fermi level ($\mathrm{E} - \mathrm{E_F}$). Momentum conservation, in the simple case of the surface normal aligned to the center of the detector slit, gives the in-plane momentum of the electron in the material

$$k_{||} = \sqrt{\frac{2mE_{kin}}{\hbar^2}}\sin\theta \tag{2.9}$$

where θ is the exit angle difference from the surface normal. As mentioned earlier, this equation derives from the preservation of translational symmetry between vacuum and the material. The out-of-plane momentum, on the other hand, is not conserved as the surface of the sample breaks translational symmetry. This also violates the dipole approximation at the surface.

If the final state is precisely known, then the photoemission spectrum may be directly simulated. Usually this is not the case and the final state is assumed to be free-electron like with a zero energy level of E_0. This allows definition of a parameter called the inner potential

$$V_0 = E_0 - e\Phi \tag{2.10}$$

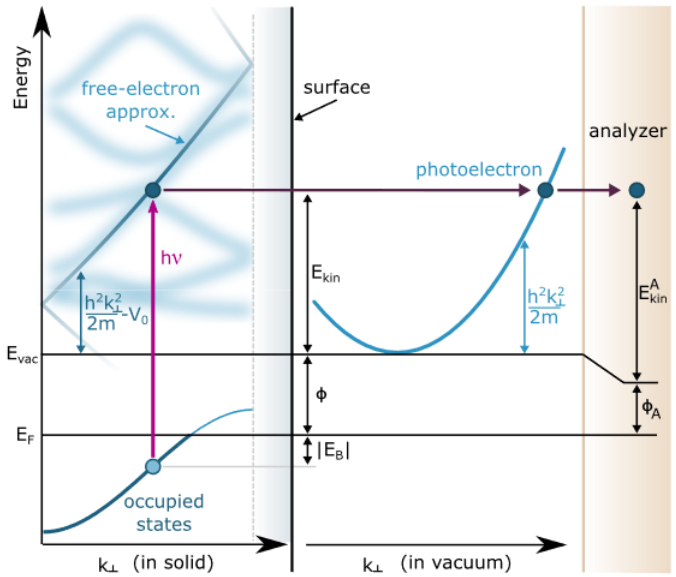

Figure 2.8: Schematic of the inner potential model. Reprinted with permission from [146]. Copyright 2021 by the American Physical Society.

where Φ is the materials work function (Fig. 2.8). The out-of-plane momentum is then defined as

$$k_z = \sqrt{\frac{2m}{\hbar}\left(E_{kin}\cos^2\theta + V_0\right)} \tag{2.11}$$

While the inner potential can be calculated, it is usually found experimentally by sweeping the photon energy in an ARPES measurement. The measured spectrum should repeat with photon energy according to the Brillouin zone periodicity in the k_z direction. The value for V_0 is then back calculated from the periodicity. V_0 is usually $5-20$ eV, but only measured with $\approx$0.5 eV resolution. Bulk-derived bands in three-dimensional (not 2D or layered) materials with no flat bands have dispersion in all directions. Surface-derived bands only have dispersion in directions in the surface (i.e. no k_z dispersion). Photon energy sweeps then allow identification of surface states versus bulk bands, but care must be taken as the intensity of surface states is modulated by photon energy as well [148].

From the above equations it seems that the energy at a δ profile of k can be pre-

cisely measured, but there is intrinsic broadening that limits resolution. The in-plane momentum resolution is dominated by propagated angular resolution and scales with $\sqrt{h\nu}$. In a measurement at a given photon energy, photoelectrons have a finite inelastic mean free path (Fig. 2.6). By the Heisenberg uncertainty principle this introduces uncertainty broadening into k_z by $\Delta k_z \propto \frac{1}{\lambda_{IMFP}}$ [149]. This broadening manifests as an energy broadening $\Delta E \propto \Delta k_z \times v_z(k_{||})$ where $v_z(k_{||})$ is the band velocity in the out-of-plane direction at the measured in-plane momentum. For the VUV photon energy range Δk_z is generally on the order of 0.1 Å^{-1} or about 5% of the Brillouin zone in α-Sn. This energy broadening can be quite large and typically dominates the linewidth of bulk bands. Since surface states have $v_z = 0$ they do not suffer from these effects.

Instrumentation

The instrumentation involved in an ARPES experiment can be broken down into three main components: (1) the light source, (2) the sample holders (manipulator) and (3) the photoelectron detector. The sample holder and manipulators involved in this study were designed and upkept by beamline scientists at the various facilities. The ARPES manipulator in the Palmstrøm lab was a modified VacGen design.

Most of the ARPES work in this dissertation makes use of synchrotron radiation as a light source. Electrons are generated and accelerated to extremely high energies (GeV) before being injected into the storage ring. In the storage ring electrons orbit at speeds very close to the speed of light. Synchrotron radiation is emitted from these electrons as their acceleration is modified. For the endstations used in this work, an undulator is used to produce light at continuously tunable energy. The electrons are directed through a magnetically poled structure where the gap between the poles determines the energy of emitted photons (Fig. 2.9). The light is then passed through a diffraction grating and series of slits to improve the resolution, spot size, and focus. The resolution at a

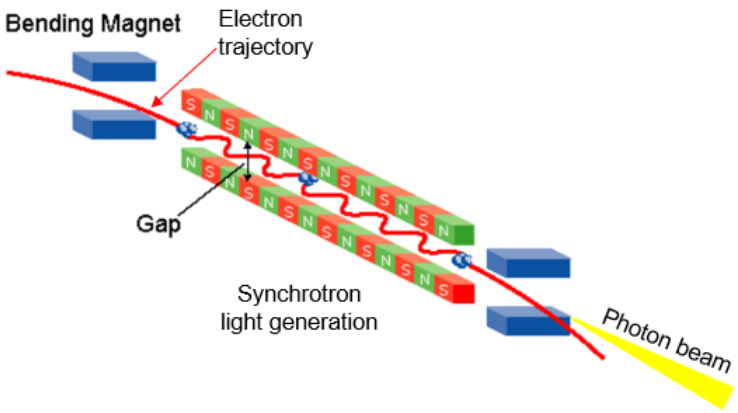

Figure 2.9: Undulator operating principle. Adapted from [150].

given photon energy is determined by the details of the undulator and the diffraction grating, as well as by the (usually tunable) slit apertures. To obtain focused light with high resolution at all photon energies, the optics are all mounted on translation stages to achieve a Rowland circle geometry. Synchrotron light sources are billion dollar facilities with limited experiment time. To still perform measurements, "offline" light sources are necessary as well, discussed below. These sources can only be used at one or two fixed photon energies.

Some of the measurements performed in this work make sure of a helium discharge lamp as a light source. Discharge lamps only emit light at discrete emission lines. Multiple emission lines are excited simultaneously—a monochromator is usually used to separate out these contributions. The linewidth is generally <1 meV, but the spot size is quite large (on the order of 1 mm). The emitted light is mostly unpolarized, but can be polarized through gratings (See Chapter 5). The light intensity is also relatively low, especially when the lamp is equipped with a capillary tube to reduce spot size and gas load. Since it is a gas-based system, these light sources are usually differentially pumped to maintain the excellent vacuum conditions necessary in the measurement chamber. Lasers are another common light source which provide high intensity, narrow bandwidth, good po-

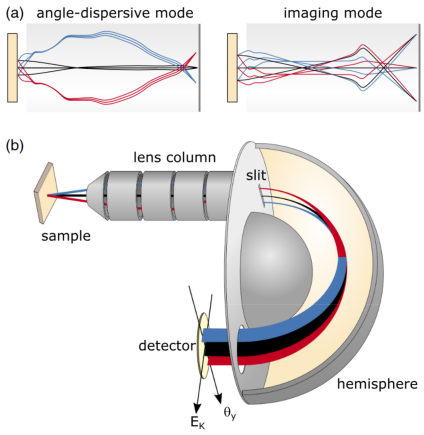

Figure 2.10: (a) Trajectories of photoelectrons in the lensing section in angle-dispersive mode and imaging mode. (b) Trajectories of photoelectrons in the hemispherical section. Reprinted with permission from [146]. Copyright 2021 by the American Physical Society.

larization control, and high timing precision (for time-resolved studies). Currently lasers are limited to low (<20 eV) photon energies which limit the range of the Brillouin zone mapped in a single shot measurement. These low energies result in good momentum resolution and good bulk sensitivity.

Most modern ARPES detectors are either time of flight or a hemispherical analyzer. Only the latter is used in this dissertation. Photoelectrons are emitted from the sample and collected into an aperture (the "nose cone"). There is no intentional applied field between the sample and the analyzer. There is a small unintentional electric field arising from the difference in work function between the sample and analyzer [146]. The photoelectrons are then accelerated or retarded according to the pass energy. At the same time, the photoelectrons are sorted according to their incoming angle (Fig. 2.10(a)). The photoelectrons pass through a slit between the lensing section and the detector section, where the energy resolution is limited by the width of the slit. The length of the slit is the direction along which angular information is stored. Certain slits have an additional aperture which removes stray photoelectrons at unusual energy/angle combinations.

The photoelectrons that travel through the slit are directed electrostatically between the inner and outer shells of the hemispherical detector (Fig. 2.10(b)). The pass energy is the photoelectron energy at which the center trajectory is followed. The pass energy is determined by the potential applied between the inner and outer shell of the hemisphere, weighted by the inner and outer radii of the detector. After the electrons have travelled through the hemisphere, they have been sorted by both angle and incident kinetic energy in perpendicular directions. Lower pass energies correspond to better energy resolution, as a set photoelectron can be dispersed across a larger physical distance on the detector. Smaller slit widths also correspond to better energy resolution.

The electrons are then directed through a wire mesh at ground (to provide a uniform electron field) and then a multichannel plate (2D electron amplifier). The electrons finally collide with a phosphor screen, where a CCD camera captures a picture of the $E-\theta$ dispersion which can be converted to a band structure measurement through Eqs. 2.9 & 2.11. Only a small section of photoelectron kinetic energies can be measured at a time (larger pass energies give larger windows). In these fixed mode measurements, the grid pattern is still usually visible. To remove detector asymmetries and the grid pattern, measurements are swept over all kinetic energies of interest (every kinetic energy is averaged over every energy channel on the detector). The step size of this sweep, number of camera frames per energy step, and total number of sweeps may all be chosen by the user. The latter two time constants have slightly different effects on the signal-to-noise ratio, but the difference is rarely relevant for the measurements performed in this work. The lens modes used to operate the analyzer determine the angular resolution and collected photoelectron angle range. Smaller angle ranges result in better angular resolutions but reduced count rates.

Modern detectors, such as the Scienta Omicron DA30-L used in this work, provide electrostatic deflectors. With the application of an additional applied bias near the nose-

cone, the center of the photoelectron beam incident on the detector can be shifted in the angle parallel to the slit and perpendicular to the slit. This allows rapid mapping of the Fermi surface of the sample of interest. Previously, sample alignment proceeded by a series of $E - k$ cuts which were compared to the expected band structure. For example in a III-V, the valence band maximum can be investigated at a series of angles until its kinetic energy is maximized—the sample is then aligned to the Γ point. With rapid Fermi mapping, few band structure details other than the core symmetries of the system are required (although they are certainly beneficial). The shape of the measured Fermi map can be aligned onto the detector for rapid crystal alignment. It is important to align by shape rather than intensity as matrix element effects can modify the intensity distribution.

In an ARPES measurement, it is optimal to maximize the signal to reduce noise in the measurement. The desire for higher intensity has a trade-off with reduced resolution. This trade-off is true for both incident light and measured photoelectron intensity. The analyzer resolution exists in discrete steps determined by the pass energy and analyzer slit. These are usually chosen such that the energy linewidth of bands in the system of interest are not dominated by the Gaussian resolution function. In cases where this is not possible, the resolution is adjusted to the best value where the intensity is such that the measurement can be performed in a reasonable amount of time. The light resolution is chosen in a similar manner. It is essential to measure with a resolution reasonable for the system of interest. If the resolution is much better than the intrinsic linewidths of the sample, counts are being thrown away. If there is a large mismatch in resolution between the light and the detector, counts are being thrown away. The measurements will then take a longer time, unnecessarily. During the limited time available at beamtime experiments, this intensity/resolution tuning is essential. It becomes even more important for spin-resolved ARPES measurements, where the cross-sections are orders of magnitude

lower and there is an additional aperture resulting in poorer resolution.

Spin- and angle-resolved photoemission spectroscopy (spin-ARPES)

From the above derivations, the spin of the initial state of the photoelectrons is preserved to a first approximation. This allows measurement of the spin polarization of the initial state bands in spin-resolved ARPES (spin-ARPES). However, other effects can produce spin polarization during the photoemission process [151, 152, and references therein]. First, the transportation and emission steps of photoemission can act as spin filters, which modulate the initial spin degenerate photoelectrons and generate a net spin polarization. Matrix element effects in the absorption step (such as those discussed for III-V photocathodes (Chapter 1)) can also produce spin-polarized photoelectrons. This can be true for any system with any polarization of light including unpolarized light. Matrix elements can modify the magnitude and direction of the initial state spin polarization vector, including generating non-zero spin polarization where the initial state had zero spin polarization. These matrix element effects depend sensitively on the final state and are thus modulated by photon energy. Care must be taken in spin-resolved measurements that the spin polarization measured truly corresponds to the initial state spin polarization— one or both of light polarization-dependence and photon energy-dependence of the spin polarization should be investigated. Further discussion of these effects are found in Chapter 5. In spin-ARPES, instead of the photoelectrons being directed onto the 2D detector in the hemispherical analyzer, they are bypassed through an aperture into a 0D spin detector. There are multiple methods of measuring the spin polarization magnitude and direction including Mott detectors and VLEED (very low energy electron diffraction) detectors. ALS beamline 10.0.1.2, where spin-resolved photoemission measurements were performed, is equipped with VLEED-based detectors (Fig. 2.11).

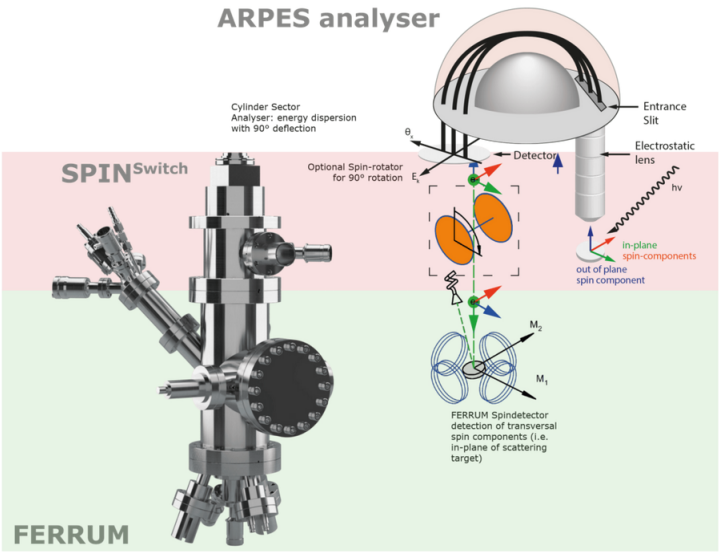

Figure 2.11: Schematic of the VLEED detectors equipped on the ARPES analyzer. Copyright Ferrum.

In VLEED, low energy electrons are directed at near normal incidence onto a magnetic thin film. For the Ferrum detectors used in this work, this consisted of an Fe film grown on W(001) oxidized to form the Fe(001)-p(1×1)-O surface termination [153]. This termination is robust and allows the VLEED target to be used without degradation for weeks in a UHV environment. The incident electrons are then scattered depending on the magnitude and direction of their spin polarization with respect to the magnetization vector of the Fe film. The scattered electrons are counted by a channeltron detector. A measurement consists of photoelectrons of a specified photoelectron kinetic energy and exit angle, convoluted with the spin aperture size, directed into the spin detector. This beam is accelerated or decelerated to the specified scattering energy (6.3 eV at BL 10.0.1.2) before impinging on the magnetic film. The magnetization vector is held constant at this time. Counts are collected for a time specified by the user before the magnetization is switched. The magnetization of the film is switched $+ \; - \; - \; +$ along the direction of interest by Helmholtz coils. The measurement then proceeds to the next

kinetic energy/exit angle pair. Usually, measurements are collected at fixed angle while sweeping kinetic energy so that any systematic variation in detector efficiency or deviation in sample alignment can be corrected. When the polarization vector is aligned with magnetization vector, the intensity of electrons scattered into the channeltron detector increases.

One pair of magnets measures one spin direction and two orthogonal pairs can be integrated quite easily. Two sets of orthogonal paired spin detectors are used to simultaneously measure the $\hat{x}, \hat{y}, \hat{z}$ dependence of the polarization vector with the $\hat{z}$ component being doubly measured. VLEED detectors are more commonly used than Mott detectors as they scatter more total photoelectrons (more efficient process) while having a similar Sherman function (correspondence between measurement asymmetry and true spin polarization).

The spin polarization in a direction is calculated from the difference in intensity between the magnetization parallel and antiparallel to that direction via

$$P_{x,y,z} = \frac{1}{S_{eff}} \frac{I^{+}_{x,y,z} - I^{-}_{x,y,z}}{I^{+}_{x,y,z} + I^{-}_{x,y,z}} \tag{2.12}$$

where S_{eff} is the Sherman function which describes the relationship between the measured asymmetry and the true spin polarization of photoelectrons in that direction. In other words if an incident beam is fully polarized, the detector will only measure a polarization equal to the Sherman function [151]. The Sherman function can be calculated using relativistic simulations such as GEANT, but is generally calibrated against a material with known polarization. The gold-standard calibration is an activated strained superlattice GaAs photocathode, but this is not usually technologically feasible in a real ARPES system and only commonly used by the manufacturer. Instead, the Sherman function is calibrated based on systems with well-known spin polarization: Au(111)

Rashba surface states, Bi(111) surface states, and, more recently, Bi_2Se_3 surface states. The Sherman function is usually not known with a high degree of precision. In this work the Sherman function was not precisely calibrated as it had previously been found not to vary. The sense of spin polarization direction and the approximate Sherman function were checked on Bi(111) thin film samples.

Sometimes instead of working with spin-polarized ARPES data in terms of the polarization vector, it is easier to compare to the spin population of the measured spectrum. This spin population is defined by

$$S^{\uparrow\downarrow}_{x,y,z} = \frac{I^{+}_{x,y,z} + I^{-}_{x,y,z}}{2}(1 \pm P_{x,y,z}) \tag{2.13}$$

While the efficiency of VLEED detectors is comparatively high, the spin detection process is still overall inefficient. The overall process results in intensities several orders of magnitude lower than a typical ARPES measurement. Due to this, the uncertainty in the measured spin polarization or spin population must be taken into account for correct conclusions about the presence/absence of spin polarization. These are derived using propagated error in the intensity terms in the above equations. Any uncertainty in the Sherman function is ignored.

$$\Delta P = P \cdot \sqrt{\frac{(\Delta I^{+})^2 + (\Delta I^{-})^2}{(I^{+} + I^{-})^2} + \frac{(\Delta I^{+})^2 + (\Delta I^{-})^2}{(I^{+} - I^{-})^2}} \tag{2.14}$$

and

$$\Delta S^{\uparrow\downarrow} = S^{\uparrow\downarrow} \cdot \sqrt{\frac{(\Delta P)^2}{(1 \pm P)^2} + \frac{(\Delta I^{+})^2 + (\Delta I^{-})^2}{(I^{+} + I^{-})^2}} \tag{2.15}$$

where $\Delta I = \sqrt{I}$ by assuming Poisson statistics. These calculations must be performed for each direction along which spin polarization is measured.

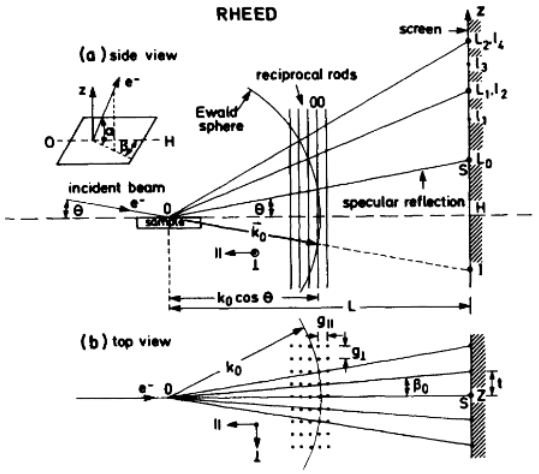

Figure 2.12: Schematic of the diffraction condition in RHEED observed (a) from the side of the sample and (b) top down of the sample. Reprinted with permission from [154]. Copyright 1983 by the American Physical Society

2.3.2 Reflection high energy electron diffraction

Most molecular beam epitaxy systems are equipped with reflection high energy electron diffraction (RHEED) systems. A high energy beam of electron (10 to 20 keV) is directed at grazing incidence onto the surface of a sample. The grazing incidence makes RHEED a very surface sensitive technique only probing the first 1–2 monolayers of the surface. The diffracted electrons impinge on a phosphor screen and the luminescence is measured by a CMOS camera. Since the surface is 2D, the reciprocal lattice appears as rods perpendicular to the surface. The intersection of the Ewald sphere with the reciprocal space rods is projected onto the phosphor screen (Fig. 2.12). In Fig. 2.12 integer order Laue rings are always present. The surface reconstruction is a probe of the chemistry at the surface according to well-calibrated surface reconstruction phase diagrams, especially for III-V semiconductors.

The surface sensitivity of RHEED allows measurements of the surface morphology by changes to the shape of the diffraction pattern. A high quality surface has a pattern

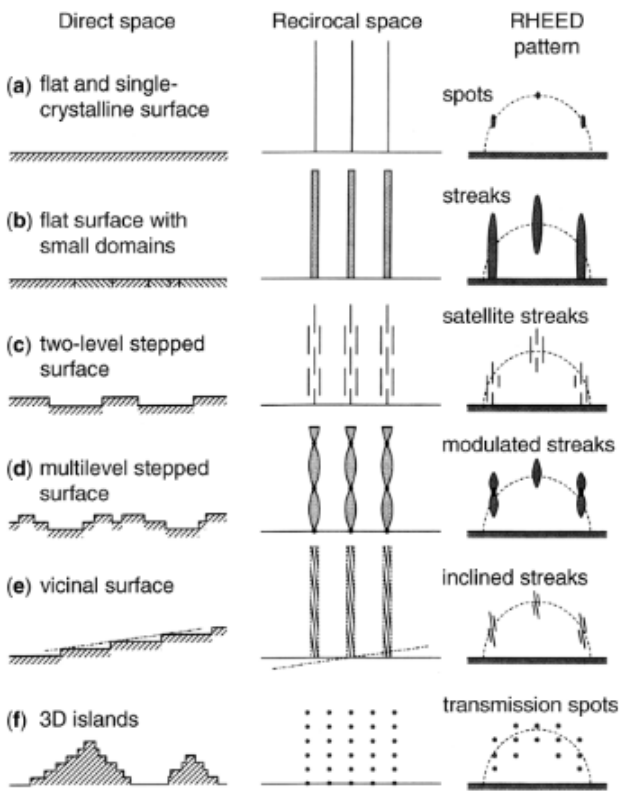

Figure 2.13: Relationship between real space, reciprocal space, and observed RHEED pattern for different surface morphologies. Reprinted from [155] with permission from Wiley.

characterized by elongated spots, corresponding to a very low radius reciprocal space rod. When surfaces have more disorder the rods broaden and the spots become streaks. Misinclination of the surface such as faceting projects as chevrons. Islands on the surface (typically indicative of poor growth) gives transmission of the electron beam and thus appears as a more typical Laue diffraction pattern. The RHEED patterns for different surface morphologies are given in Fig. 2.13. In this manner, quick feedback on changes to growth conditions can be achieved. This closing of the feedback loop ensures valuable resources are not spent characterizing poor quality films. The RHEED pattern can also be monitored during growth to see changes in morphology from effects such as segregation or film relaxation.

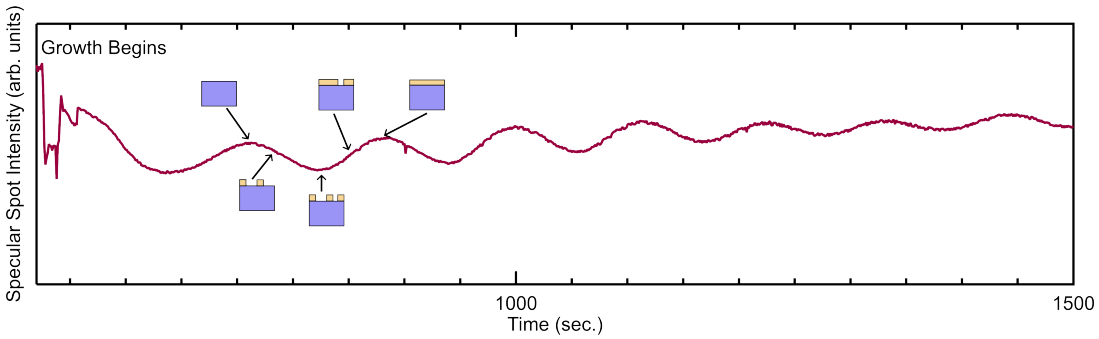

Figure 2.14: RHEED oscillations during growth of α-Sn on InSb(001). A schematic shows the effect of layer-by-layer growth on the specular intensity.

Finally, if a film grows in the layer-by-layer growth mode then the RHEED intensity oscillates with a frequency equal to the layer-basis growth rate (Fig. 2.14) [156]. The phase of this oscillation differs for different order reflections in each Laue zone [157]. There is still debate over the exact origin for this effect, but the simple explanation is based off of a surface with oscillating smoothness as the layer grows giving oscillating specular reflection. In III-V semiconductors, the oscillation period corresponds to the growth of one III-V monolayer (an atomic layer of III and an atomic layer of V). In Group IV semiconductors, RHEED oscillations can proceed on either a monolayer (one atomic layer) or bilayer (two atomic layer) basis depending on growth temperature and surface preparation [158].

2.4 *Ex situ* characterization

2.4.1 X-ray diffraction

X-ray diffraction allows for a deeper understanding of both the composition and structure of a material. In this work X-ray diffraction was used to calculate structural ordering, confirm layer thicknesses, and extract stoichiometry in GeSn and InAlGaAs thin films (provided a model can be built for lattice constant vs. composition, usually

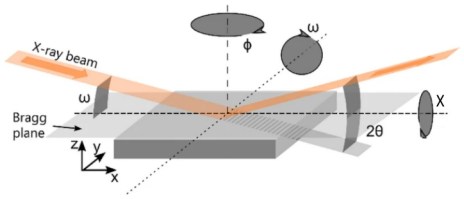

Figure 2.15: Typical geometry of an X-ray diffractometer. Reproduced from [159] with permission from Springer Nature.

the only model necessary is Vegard's law). The geometry discussed in this work is given in Fig. 2.15. Full calculations and discussions of the following can be found in the cited works. Here we review some aspects most relevant to this thesis. Structure factor measurements are discussed in the context of Heusler alloys in Chapter 3, but can also be applied in III-V and group IV alloys as well (although this is less common, as alternative techniques are available to measure the same properties).

Out-of-plane measurements

Simple out-of-plane $\theta/2\theta$ measurements are used to identify the out-of-plane lattice constant of the material. Unstrained alloy lattice constants are assumed to follow Vegard's law, however most of the films studied in this dissertation are strained. In this case the elastic tensor components that give the relationship between in-plane and out-of-plane strain must be mixed according to Vegard's law as well

$$\epsilon_{zz}(x) = -2\frac{C_{12}(x)}{C_{11}(x)}\epsilon_{xx}(x) \tag{2.16}$$

where x is the composition being varied. For high resolution determination of the lattice constant, the absolute position of the film diffraction peak is not used. Instead, it is referenced to the substrate peak. If tilt of the epilayer with respect to the substrate is suspected, performing a reciprocal space map around the out-of-plane Bragg reflection gives a direct measurement of this tilt.

X-ray diffraction measurements essentially measure the Fourier transform of the structure. Because of this when films have finite (not infinite) thickness in the out-of-plane direction the peak intensity can be described by a sinc function centered on the Bragg reflection where the oscillation period corresponds to the film thickness. A more robust version of this effect can be calculated from kinematical and dynamical diffraction modelling. These oscillations are called Pendellösung fringes. These fringes have constant phase on either side of the Bragg peak. For α-Sn films, the phase of the Pendellösung fringes shifts on either side of the Bragg peak. The origin of this effect is as-yet not understood.

Rocking curves (ω measurements at fixed 2θ) are frequently used to assess the quality of films via the Scherrer equation [160]. However due to the aforementioned Fourier transform effect, there is a finite linewidth associated with the thickness of the film. A 50 nm film having a narrower linewidth than a 25 nm film does not necessarily correspond to it being higher quality, but if it had a broader linewidth it would certainly be lower quality.

In-plane measurements

Out-of-plane measurements are typically measured with a 0D detector and at fixed offset between ω and 2θ. In-plane measurements can be performed in such a manner as well, but because the epilayer Bragg reflection is not required to lie on a certain high symmetry line it is difficult to perform measurements this way. These asymmetric coupled scans are only possible when working with materials with very similar lattice constants and symmetries to their substrate. Instead, in-plane measurements are performed with the reciprocal space map method where an entire region of ω-2θ space is measured. These reflections are indicated in Fig. 2.16(a).

This is very time-consuming with a 0D detector (although when combined with an

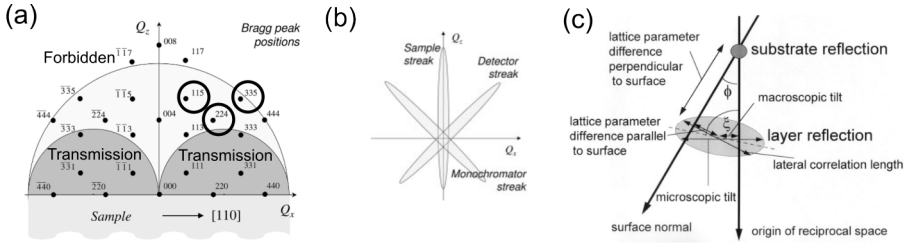

Figure 2.16: (a) Accessible Bragg reflections for Si with Cu Kα radiation. (b) Experimental artifacts in a reciprocal space map. (c) Schematic of some of the information accessible in an in-plane reciprocal space map. (a) and (b) are reprinted from [160], Copyright Springer. (c) is reprinted with permission from [161]. Copyright IOP Publishing.

analyzer crystal this gives very good resolution), so a 1D detector that collects intensity across a range of 2θ values at each ω is used instead. The Bragg reflection gives the in-plane and out-of-plane component of the spacing of the reflection ((220) and (004) for the (224)) geometry. The in-plane and out-of-plane lattice constant can the be calculated by the hkl relationship to that spacing. Both grazing incidence and grazing exit configurations are possible for each Bragg reflection. Grazing incidence gives lower resolution but higher intensity so it is used for the weak Heusler reflections in this work. Grazing exit gives higher resolution but lower intensity so it is used for all other materials investigated. In addition, better in-plane resolution is achieved by using Bragg reflections closer to the $Q_{||}$ line. The (224) reflection is used for Heuslers and III-Vs. The (115) and (335) reflections are used for α-Sn and α-$Sn_{1-x}Ge_x$.

Much more information about the structure of the film can be extracted from the reciprocal space map, but is convoluted with streaks that appear due to the monochromator crystal, sample, and, if an analyzer is used, the analyzer crystal. These streaks are summarized in Fig. 2.16(b). Strain gradients, microscopic tilt, and lateral domain size can be extracted (Fig. 2.16(c)). In III-V semiconductors, partial relaxation of strained films proceeds anisotropically. The in-plane lattice constant must be investigated in both the $\langle 110 \rangle$ and $\langle 1\bar{1}0 \rangle$ directions.

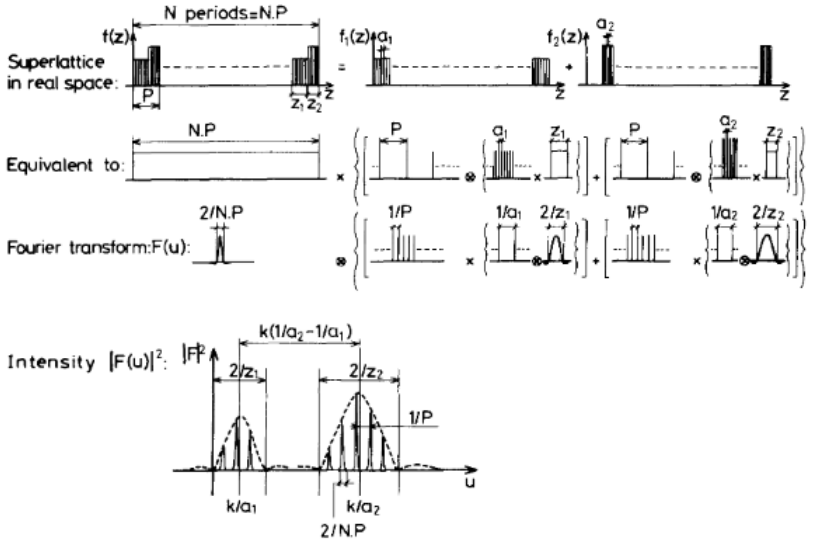

Figure 2.17: Schematic description of the diffracted profile of a one-di- mensional superlattice in the kinematical theory. If the lattice parameters are different enough, the profile shows two separate sets of peaks. In that case, the spatial correlation of the two materials has little influence on the profile. Reprinted from [162] with permission of AIP publishing.

Superlattice diffraction

In diffraction of a superlattice, the measurement is no longer directly sensitive to the lattice spacing of the component elements. The integer Bragg reflection corresponds to the average out-of-plane lattice constant of the period of the unit cell. Other integer order reflections are somewhat analogous to Pendellösung fringes. Instead the spacing corresponds to the thickness of the superlattice period. Higher order fringes correspond to the total thickness of the superlattice. The intensities of these fringes is related to the structure factor through both constructive and destructive interference. The Fourier transform relationship between the measured spectrum and the real space periodicity is shown schematically in Fig. 2.17.

Quality of a superlattice is typically judged by the number of fringes visible in the XRD measurement. Sometimes linewidth analysis is used, but again it must be treated

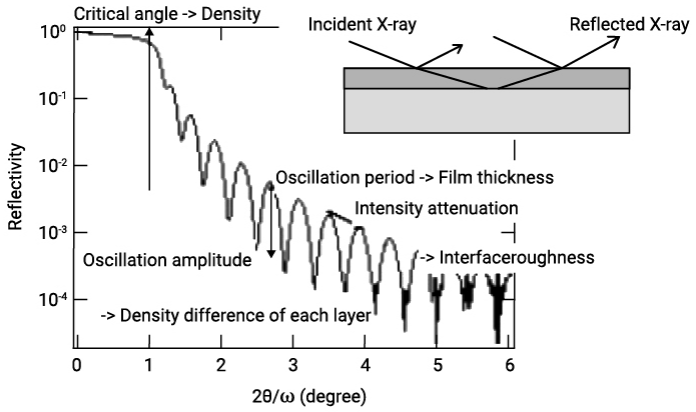

Figure 2.18: Schematic of the XRR measurement for a single film. Correspondence between each feature in the measurement and its associated material parameter are given. Copyright Rigaku.

with caution. The superlattice peak linewidths are related to the structure of the superlattice in addition to the quality of the superlattice.

X-ray reflectivity

Another X-ray technique that can be used in an X-ray diffractometer is X-ray reflectivity. Here incident X-rays are directed at grazing incidence onto a sample surface. The 2θ scattering angle is then swept through low angles $<10°$. The incident X-rays reflect off of surfaces and interfaces and constructively or destructively interfere depending on the exit angle. The measured signal produces an oscillation (Kiessig fringes) with a frequency corresponding to the thickness of the film. In multilayer systems the complexity of the problem quickly increases and the data must be directly fit to a model produced via the Parratt formalism [160]. It is essential that prior to the XRR measurement, the diffractometer is aligned to the surface normal rather than the crystal normal. The relationship between material parameters and the XRR measurements are shown in Fig. 2.18. Alignment to the crystal plane normal, as in diffraction measurements, will give an unphysical quickly damped signal (false roughness measurement) and modified frequency

and amplitude (density and thickness).

2.4.2 Rutherford backscattering spectrometry

Rutherford backscattering spectrometry (RBS) can be used to find the absolute elemental fluence deposited on a substrate. A high energy (typically 2 MeV) beam of helium ions is directed onto a sample surface. By a billiard ball-like collision, the relationship between the scattered ion energy and incident ion energy or kinematic factor is

$$K = \frac{E_1}{E_0} = \left(\frac{\left(M_2^2 - M_1^2 \sin^2\theta\right)^{1/2} + M_1 \cos\theta}{M_1 + M_2} \right)^2 \tag{2.17}$$

where M_1 is the helium ion mass, M_2 is the mass of the element in the matrix involved in the collision, and θ is the scattering vector [163]. The cross section σ is proportional to Z by

$$\sigma \propto \left(\frac{Z_1 Z_2 e^2}{E} \right)^2 \tag{2.18}$$

where Z corresponds to the atomic number [163]. The ratio of measured cross-sections can be compared to the ratio of two elements. In other measurements, the ion beam can be directed along certain axial or planar channeling conditions to find the presence of interstitial impurities or assess the quality of the crystal. For flux calibration measurements, the sample is rotated randomly to average over any channeling effects. The absolute amount of the element of interest is found by (1) integrating the area under the curve for each elemental peak in the RBS spectrum and (2) fitting the data to a model of the measured spectrum with the elemental concentrations as inputs. Detailed procedures for the analysis of this data can be found in Ref. [164].

2.5 Tight-binding calculations

In this thesis, measurements of the band structure using angle-resolved photoemission spectroscopy are complemented with calculations of the band structure using the tight-binding method. This method, also known as the linear combination of atomic orbitals (LCAO) method, is a semi-empirical technique that is not very computationally complex, allowing for band structure calculations to be performed without the use of a computing cluster. Because tight-binding calculations are semi-empirical, parameters may be tuned to give better agreement with experiment without the calculation losing its physical robustness [165]. In other semi-empirical techniques like $k \cdot p$ it is difficult to correctly represent bands at symmetry points away from the Γ point. These features are quite easily observed in ARPES, and this calculation technique is thus not ideal for comparison. *Ab initio* calculations are valuable and currently the "gold standard" of band structure calculations of topologically non-trivial systems. These calculations have difficulty correctly representing the band structure of α-Sn (Chapter 5). Furthermore in the tight-binding method, the physical interpretation of individual parameters allows sensible alloying between two calculated band structures without building complex unit cells [166].

The tight-binding calculation is based on the assumption that the wave function of an atom in the lattice may be represented as

$$\psi = \sum_b c_b \phi_b \tag{2.19}$$

where ϕ_b are the individual atomic orbital wave functions for that atom, described by

$$\phi_b = R^b_{n,l}(\mathbf{r}) X^b_{l,c}(\Omega) \chi_\pm \tag{2.20}$$

where $R_{n,l}(\mathbf{r})$ is the radial component of the wave function, $X_{l,c}$ is the cubic harmonic representing the orbital, and $\chi_{\pm}$ is the spinor projection representing spin up/down states [167]. Orbitals located on the same atom are orthogonal to each other, so this is an orthogonal basis. To obey the periodicity of the system (i.e. represent a real crystal) the atomic orbital state must obey Bloch's theorem. This is achieved by instead representing the atomic orbital as

$$\phi_{b\mathbf{k}}(\mathbf{r}) = \frac{1}{\sqrt{N}} \sum_i e^{i\mathbf{k}\cdot\mathbf{R}} \phi_b(\mathbf{r} - \mathbf{R}_i) \tag{2.21}$$

where $\mathbf{R}$ is the lattice vector of the system. The summation is over all equivalent lattice atom position in the crystal. The dispersion (Energy) is calculated at each $\mathbf{k}$ point by

$$E(\mathbf{k}) = \int \psi^*_{\mathbf{k}} H \psi_{\mathbf{k}} d\mathbf{r} \tag{2.22}$$

where ψ is the total wave function in the crystal, which as we remember, is the sum of all atomic orbital wave functions. This can be equivalently written as

$$\sum_i (H_{i,j} - \delta_{i,j} E(\mathbf{k}) c_i \tag{2.23}$$

where $H_{i,j} = \int \phi^*_{i\mathbf{k}} H_{i,j} \phi_{j\mathbf{k}} d\mathbf{r}$. The energies are then found by the eigenvalues of the Hamiltonian matrix with the atomic orbital basis at each $\mathbf{k}$ [168].

When $i = j$, this can be termed a one-center integral. This is represented by the diagonal terms of the matrix with additional geometric terms. These non-geometric terms are named the onsite energies, These onsite energies are the unbound atom orbital energies, and thus the number of onsite energies matches the number of elements of the basis. Generally the onsite energies of all orbitals with equal l are equivalent (since there is no potential to lift the degeneracy between different m_l). The next integral is where two basis orbitals on different sites interact via the potential on one of these

sites. This is termed a two center integral. A three center integral is where two basis orbitals on different sites interact via the potential on a third, different site. These three center integrals are small and frequently ignored. The two center integrals are also called hopping terms.

In the Slater-Koster picture, there is a limited number of interactions between different orbitals. On nearest neighbors, p orbitals can form σ or π bonds, for example. These interactions can be linearly combined to fill out the matrix elements of the Hamiltonian weighted by the direction cosines for the atomic sites of interest. Instead of the integral on each matrix element being worked out, a much smaller number of integral computations is necessary. In addition, by tuning only these orbital terms or Slater-Koster parameters, a more universal model of electronic structure of solids may be obtained. The matrix element values may be directly modified to adjust relative band alignments at high symmetry points [169], but this results in a loss of the generality of the approach.

For the α-Sn tight-binding calculations presented in this thesis, the Slater-Koster parameters were fit to the band structure calculated in Ref. [94] by Rogalev *et al.* [170]. A sp^3d^5 basis was used, resulting in a basis with length 36 (2 atoms in the lattice, spin-up and spin-down). Commonly in semiconductors an anti-bonding s orbital is added to the basis [165]. The parameters, specifically the spin-orbit coupling strength, were modified slightly to result in better agreement with experimental band alignments. Second nearest neighbor interactions are included. For simulations of ARPES measurements in Chapter 5, the final state is assumed to be a free electron plane wave. For the calculations in Chapter 7, a scalar offset is added to the onsite potentials between the two Sn atoms in the basis (which are normally equivalent). This is a simple approximation to break the inversion symmetry of the Hamiltonian. However, the true form of inversion symmetry breaking in the system will likely break the inversion symmetry of the hopping terms in addition to the onsite terms. Details of all calculations are given in Appendix A.

Chapter 3

Growth and characterization of Heusler topological semimetal Co_2FeSn

3.1 Introduction

Due to the presence of nodes and nodal lines in their band structures (and the breaking of time reversal symmetry) magnetic topological semimetals generally host a large anomalous Hall effect (AHE) [40] in the energy vicinity of these band crossings. Via the Mott relation, this usually results in a large anomalous Nernst effect (ANE) at a nearby energy level as well [171, 172]. Materials exhibiting a large AHE have seen use in spintronic devices and magnetic sensing [71, 73, 74, 173]. A large ANE is desired for spin caloritronics, but even more exciting is their use in novel thermal cooling architectures [174–176]. However, most of these magnetic topological semimetals have low Curie temperatures, at or just above room temperature. Thus, while the "0 K" effects are large, the room temperature anomalous transport is relatively low (Fig. 3.1). Heusler

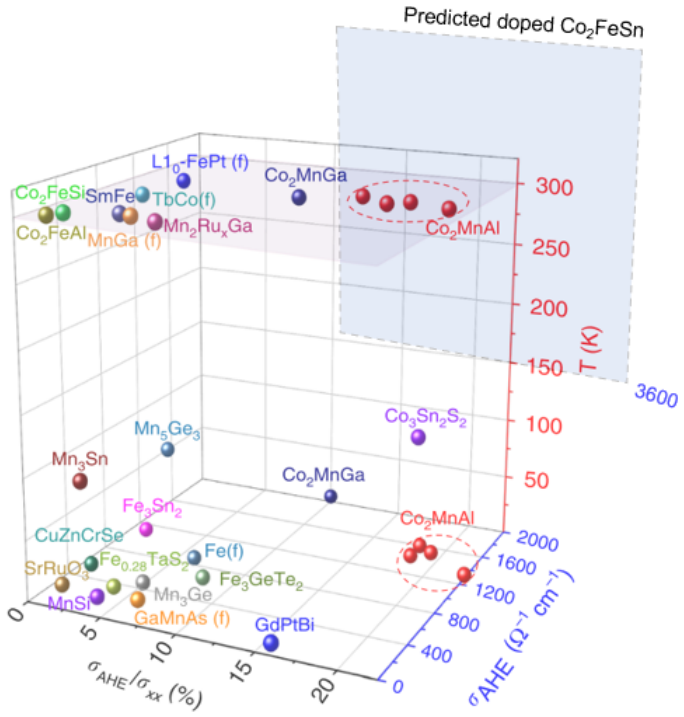

Figure 3.1: Comparison of the magnitude of the anomalous Hall effect for various typical, Heusler, and topological magnets at a range of temperatures. The predicted performance of Co_2FeSn is drawn schematically. Adapted from [179] via Creative Commons Attribution 4.0 International License.

alloys, a structure class hosting many topological semimetallic compounds, tend to have high Curie temperatures—essential for room temperature operation [80, 83, 177, 178].

The full Heusler compound Co_2FeSn is predicted to be a nodal line semimetal with the nodes only 120 meV above the Fermi level (Fig. 3.2(a)) [86]. At this point in the band structure the anomalous Hall conductivity (AHC) has been predicted to increase to 3600 S/cm, almost triple the maximum value recorded or theorized in a Heusler (Fig. 3.2(b)) [86]. The anomalous Nernst conductivity (ANC) is predicted to reach 11 A/Km at room temperature, which is more than double that of the maximum value previously measured or predicted in another Heusler [86]. These are all "intrinsic" values, defects, and disorder can both enhance and diminish these effects [55]. The Curie temperature for Co_2FeSn has not been directly predicted, but is likely near the Heusler compounds in

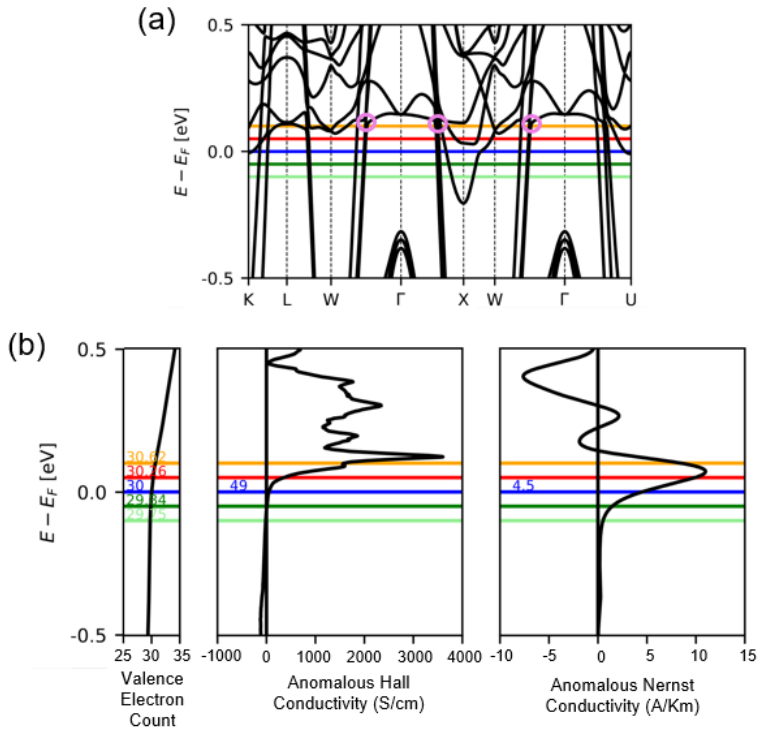

Figure 3.2: (a) Calculated band structure of Co_2FeSn. The locations of the nodal lines are circled. (b) The valence electron count necessary to shift the chemical potential and the energy-dependent anomalous Hall and anomalous Nernst coefficient, calculated from the Berry curvature of the band structure. Reproduced from [86] via the Creative Commons License.

the same family ($Co_2Fe(Si,Ge)$) [180,181], and thus greater than 700 °C. This large Curie temperature should result in better room temperature magnitudes of the ANC and AHC than typically seen in topological semimetals.

Unfortunately, Co_2FeSn is a metastable compound well-known to not be synthesizable in the bulk [182]. Using arc-melting, it phase segregates into CoFe and Co_3Sn_2 when attempted [183]. Molecular beam epitaxy (MBE) is an out of equilibrium technique and by using a substrate of similar symmetry and lattice constant to the material of interest, a metastable compound can be stabilized [136]. Co_2FeSn has been grown successfully on MgO by sputtering, but MBE growth has not been reported [182]. In addition, most applications of large AHC and ANC materials are as components in thin film-based

devices.

3.2 Methods

The general procedure for producing smooth, well ordered Heusler films is to perform growth at a substrate temperature 300 °C–500 °C followed by a high temperature anneal (>500 °C) after growth is completed [184]. Achieving full ($L2_1$) ordering is difficult for most Heusler compounds, with films usually being some combination of B2, A2, DO_3, and $L2_1$ ordering [80, 81]. In this study a series of Co_2FeSn(001) films were grown via MBE on MgO(001) substrates with the registry of MgO[100]$\|$$Co_2FeSn$[110] (Fig. 3.3). The equilibrium bulk lattice constant of Co_2FeSn is unknown, but generally measured to be within 2% with that of MgO in this registry [182]. MgO(001) (10 mm × 10 mm × 0.1 mm) substrates were purchased from CrysTec GmbH and were shipped vacuum packed to UCSB. They were stored in N_2 ambient until soon before growth. At this point, 9–18 substrates at a time were annealed in a tube furnace at 800 °C for 12–16 hours in 3 slm N_2 and 3 slm O_2. After loading out of the tube furnace (at 600 °C), the samples were allowed to cool for 10 minutes before being stored in a wafer carrier. The samples are then back-coated with 200 nm Ti. If very high temperatures are required, a Ta back-coating may be used instead. MgO substrates are generally mounted solder-free to eliminate any indium or gallium incorporation in the grown films. The back-coating serves as an absorber for the radiative heater in the MBE, allowing more direct heat transfer to the transparent substrate.

Before growth, substrates are stored in a vacuum desiccator. Since MgO is hygroscopic, this step is essential to ensure a pristine surface for film growth. Even in the dessicator, the surface degrades. Substrates older than ∼6 months are generally discarded. After substrates are mounted solder-free, they are loaded into the UHV system.

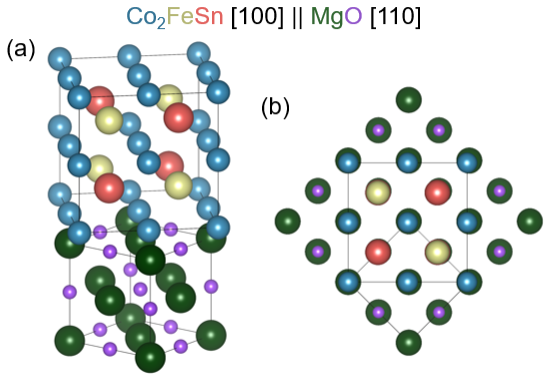

Figure 3.3: (a) Isometric view of $Co_2FeSn(001)/MgO(001)$ with the $MgO[100]||Co_2FeSn[110]$ registry. (b) Top-down view of the same.

The substrates are annealed *in situ* at 700 °C for 1 hour in a vacuum $< 1 \times 10^{-8}$ Torr. The substrate is then cooled to 630 °C, where a 20 nm MgO buffer layer is deposited at a rate of 1 nm/min by e-beam evaporation. The e-beam source material is generally outgassed heavily just before the initial substrate anneal. The samples are then cooled to room temperature and ready for growth.

Stoichiometric fluxes of Co:Fe:Sn 2:1:1 were calibrated via Rutherford backscattering spectrometry and generally checked with a flux gauge at the beginning of each day of growth. Growth and anneal temperature were varied to maximize ordering in the Co_2FeSn films. All Co_2FeSn films were nominally 13 nm thick. The sample was rotated during growth to improve sample-to-sample consistency and remove any compositional gradients on the sample, which can lead to unexpected magnetic responses. The PID control of the substrate setpoint temperature was disabled during growth/rotation (constant output powers). Growth was performed in a modified VG V80 MBE with a base pressure $< 4 \times 10^{-11}$ Torr. All Co_2FeSn was capped with 3–10 nm AlO_x deposited by e-beam deposition at a rate of 0.3 nm/min. If the cap is kept thin (<4 nm), low resistance contacts may still be made to the Heusler film and X-ray absorption measurements may still be performed.

Some Co_2FeSn was grown on Cr-buffered MgO, where 15 nm of Cr was deposited by MBE on an identically prepared MgO buffer at 100 °C. The initial RHEED showed a 3D morphology. The samples were then annealed at 450 °C for 1–3 hours, after which the RHEED became streaky. Interestingly, Cr buffers did not show any reconstruction after their initial preparation. After long term (>1 week) storage, a c(2×2) reconstruction appeared (potentially related to N_2 adsorption [185]). The contamination of the surface did not appear to adversely affect the growth of Co_2FeSn. Some attempts were made to grow on GdAs/InAlAs/InP(001) templates, as used in the past for other full Heusler growth [186]. While the initial results were promising, InAlAs has a much lower thermal conductivity than MgO, which makes Nernst measurements very difficult. Close lattice matching of the buffer layer with the Co_2FeSn also precluded extraction of the Co_2FeSn peak intensities, so reliable ordering calculations from XRD were not possible. This buffer layer route was not further pursued.

Magnetic measurements were performed using a Quantum Design MPMS XL. Due to the oxide substrate, much care must be taken during sample handling to ensure there are no spurious magnetic measurements [187, 188]. In particular, there is no contact between the MgO substrate and stainless steel tools. Cleaving of the sample post-growth, to prepare the correct size for magnetization measurements, is performed with a razor blade separated from the sample by VWR wipes. Diamagnetic MgO substrates have paramagnetic impurities which are active at low temperatures. In addition, the metal back-coat layer is paramagnetic. All magnetization measurements presented have a combined paramagnetic and diamagnetic background fit and subtracted.

Hall/Nernst measurements were made on devices such as that shown in Fig. 3.4. The design and fabrication of this device is discussed in detail in [189]. Resistive heaters were used to control the temperature and the applied temperature gradient, Nernst response, and Hall response are all measured via lock-in technique. Measurements were performed

at room temperature. The fabrication and measurement were both performed by Han Yu in the group of Paul Crowell at the University of Minnesota.

3.3 Nucleation and epitaxy

The registry of MgO[100](001)||Co_2FeSn[110](001) leads to only 1–2% lattice mismatch of the film during growth. The exact critical thickness is unknown, but likely around 10 nm. No matter the growth temperature used, initial nucleation of Co_2FeSn on MgO(001) leads to spotty RHEED indicative of 3D growth (Fig. 3.5). At higher temperatures, ($\geq$450 °C) the RHEED stays 3D throughout, while for low temperature growth the streaky RHEED indicates the film smooths out relatively quickly. From atomic force microscopy (AFM), at high temperature growth there is a cobble stone texture morphology. This is potentially evidence of the phase separation seen in XRD. At low and medium temperature growth the morphology is similar, although the sample grown at colder temperature is smoother. The RHEED pattern also indicates good epitaxy of Co_2FeSn/MgO(001), as expected from the close symmetry and lattice matching and from prior work [182].

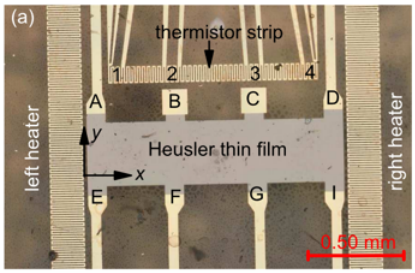

Figure 3.4: Example device that Nernst and Hall measurements are made on. Reprinted with permissions from [189]. Copyright 2022 by the American Physical Society.

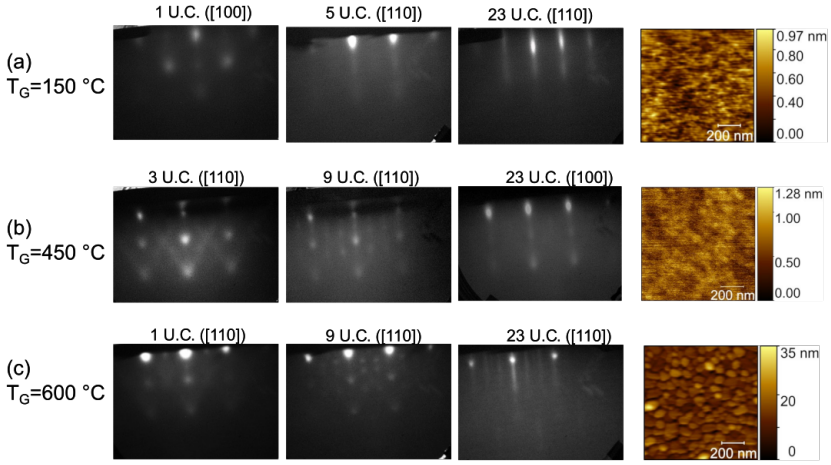

Figure 3.5: RHEED measurements taken during growth of Co_2FeSn with *ex situ* AFM measurements of the true morphology. Three growth condition are used (a) Low temperature growth (b) Medium temperature growth and (c) High temperature growth.

3.4 Ordering in Heusler alloys

While Heusler compounds are sometimes thought of as line compounds, they may actually sustain various amounts of off-stoichiometry while retaining the Heusler ($L2_1$) crystal structure. In real materials, it is even sometimes seen that an off stoichiometry is the ideal composition for optimal ordering in Heuslers [190]. This then begs the question of what is unoptimal ordering? Large concentrations of antisite defects in X_2YZ full Heusler alloys are typical, especially in thin films, and result in different symmetry-based crystal structures [80, 81]. The usual full Heusler $L2_1$ ordering has distinct lattice sites for the X, Y, and Z elements. The most typical case of disorder, Y-Z disorder, results in these elements being indistinguishable in their lattice sites. The crystal structure then becomes B2. If all of the atoms are indistinguishable on their lattice sites, then the crystal is A2 ordered (also known as the BCC crystal structure). When the X and Y sites are disordered, the structure is DO_3. These disordered crystal structures are summarized in Fig. 3.6.

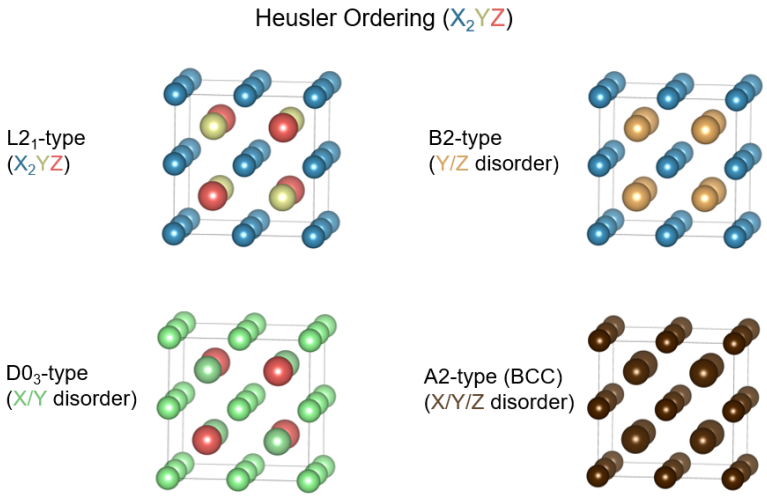

Figure 3.6: Heusler crystal structure and different disordered structures possible in this system

Since the symmetry of the crystal structure is changed from these different kinds of disordered, they can be detected using X-ray diffraction. There are three sets of allowed reflections in an $L2_1$ ordered crystal.

$$F_1 = 4(2f_x + f_y + f_z) \text{ where } h,\ k,\ l \text{ are even and } h + k + l = 4n \tag{3.1}$$

$$F_2 = 4(2f_x - f_y - f_z) \text{ where } h,\ k,\ l \text{ are even and } h + k + l = 4n + 2 \tag{3.2}$$

$$F_3 = 4(f_y - f_z) \text{ where } h,\ k,\ l \text{ are odd} \tag{3.3}$$

where $f_{x,y,z}$ corresponding to the average atomic scattering factor on each lattice site. F_1 is always allowed, no matter the chemical disorder, as the site scattering factors will still sum up to the same value. F_2, on the other hand, will be forbidden if there is complete disorder (A2) as f_x, f_y, and f_z will all be identical. F_3 will be forbidden if there is disorder between the Y and Z sites (B2) ordering. The presence of $L2_1$ ordering

is then generally determined by the presence of a (111) peak in an XRD measurement. The ratio of B2 ordering to A2 ordering is given by the relative intensity between the (002) peak and the (022) or (004) peak. DO_3 ordering is difficult to detect for most common full Heuslers; the similar $3d$ transition metal elements result in f_x and f_y being close to identical even without disorder. Using anomalous XRD, DO_3 ordering may be measured [191]. It can also tentatively be attributed to unexpected trends in magnetism or the anomalous Hall effect [192, 193].

Once the allowed reflections of the Heusler of interest have been measured, simple equations allow the calculation of the approximate absolute ordering. First given by Webster in 1973 [194],

$$S_{B2} = \sqrt{\frac{I_{002}^{meas}}{I_{004}^{meas}} \frac{I_{004}^{calc}}{I_{002}^{calc}}} \tag{3.4}$$

where S_{B2} is the percentage of B2 ordering and I is the measured integrated intensity or the calculated intensity assuming full ordering. For more precise calculation of the concentration of $L2_1$ ordering, an updated equation with the (111) rather than the (002) peak intensity should be used instead [195]. For relative trends *in the same system*, the ratio between measured (002) and (004) integrated peak intensities may be used as long as the exact same measurement conditions are used for each peak and for each sample. For a true estimation of the B2 or $L2_1$ ordering, Eq. 3.4 must be used very carefully.

The root of this calculation is the extraction of the structure factor from the measured XRD intensity. The integrated intensity in a $\theta/2\theta$ measurement is related to the structure factor by [160]

$$I = ECF \frac{1}{\dot{\theta}} G(\theta) C(\theta)^2 L(\theta) \frac{|F_h|^2}{V_{UC}^2} V \frac{A(\theta, t)}{2\mu} \tag{3.5}$$

where ECF encapsulates fundamental constants and experimental parameters, such as

slit width, $\dot{\theta}$ is the scan speed of the measurement, $G(\theta)$ is the geometric factor, $C(\theta)^2$ is the polarization factor, $L(\theta)$ is the Lorentz factor, F_h is the structure factor, V_{UC} is the volume of the unit cell, V is the volume illuminated, $A(\theta, t)$ is the absorption term which is scaled by the absorptivity μ. No multiplicity or texture terms are included, as we only consider the case of epitaxial films.

First, it is clear from ECF and $\dot{\theta}$ that measured intensities cannot be accurately divided to extract a true structure factor ratio unless the *exact* same measurement conditions are used to measure both peaks. This rule is not always followed, as the (002) and (111) peaks can be quite weak and a user may increase the slit size or decrease the measurement speed in order to improve the signal-to-noise and strength of this peak. However, if these updated parameters are then not used in the measurement of the peaks which they are being compared to, a quantitative extraction becomes impossible. The V_{UC} term is generally constant sample to sample, although disorder can have slight effects on the equilibrium lattice constant. These changes are generally negligible and can be ignored, but this must be confirmed on each sample measured. The geometric term $G(\theta)$ is generally given for the powder diffractometer case where $\chi = 0$ (where χ is traditionally the third Euler angle where the first two are ω in the measurement plane and ϕ the sample azimuth). However in epitaxial films, measurements of the (022) and (111) peaks require $\chi \neq 0$. This strongly modifies the geometric term and cannot be ignored. The illuminated spot on the sample no longer matches the measured spot received into the detector [196], which also changes the geometric term. The angle of incidence also changes the volume of the sample illuminated. These effects are rarely if ever taken into account for ordering calculations of thin films.

The difference in the absorption term at different geometries is also rarely taken into account, especially at $\chi \neq 0$. It can be somewhat simplified by the small thickness approximation (which gives a linear absorption as a Taylor expansion of the analytical

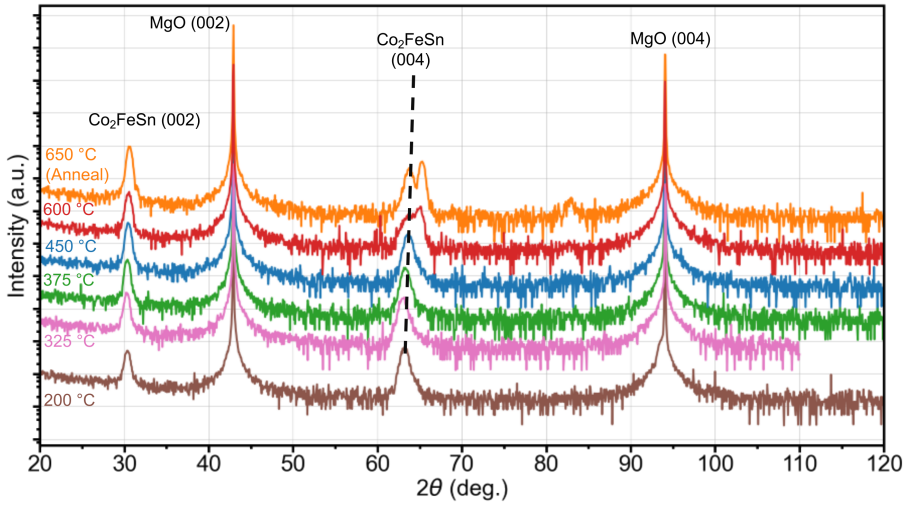

Figure 3.7: Wide range $\theta - 2\theta$ measurements as a function of growth temperature conditions for Co_2FeSn/MgO(001).

exponential absorption term). The absorptivity and the Lorentz factor can be taken into account in the usual fashion. Finally, the polarization term normally used in ordering calculations is that derived for unpolarized light incident on the sample of interest. Most modern diffractometers used for the study of epitaxial Heusler compounds use a monochromator, which partially polarizes the light. This changes the polarization term significantly as a function of incident light angle [197]. Clearly the calculation of absolute ordering in a film is a complex topic, but unfortunately it is rarely treated as such. Calculations of ordering concentrations in the literature must be interpreted with much care.

3.5 Structural quality and attempts to improve ordering in Co_2FeSn

Out-of-plane $\theta - 2\theta$ scans at a variety of growth conditions are summarized in Fig. 3.7. All films show the presence of both the (002) peak and the (004) peak, indicative of

significant B2 ordering. The (004) peak is used as the A2 reference rather than the (022) to remove associated issues with measuring at $\chi \neq 0$. Evidence of phase segregation at higher growth and annealing temperatures (>500 °C) is shown by the splitting of the Co_2FeSn(004) peak. From analysis of other off-axis reflections in Fig. 3.8—(224), (022), and (226)—we find that this splitting is indicative of segregation into a B2 phase (similar to the Co_2FeSn parent phase) and either a B2 CoFe phase or an A2 CoFe(Sn) phase. The B2 and A2 phases of CoFe are difficult to differentiate with lab-based XRD because they have almost identical atomic scattering factors. In any case, the "defect" phase with smaller lattice constant (higher 2θ peak) is probably CoFe-like [182]. Sn still can have a large solubility in a CoFe matrix [198, and references therein]. While the defect phases are only clearly evident in XRD at high temperatures, they likely nucleate at colder temperatures [182].

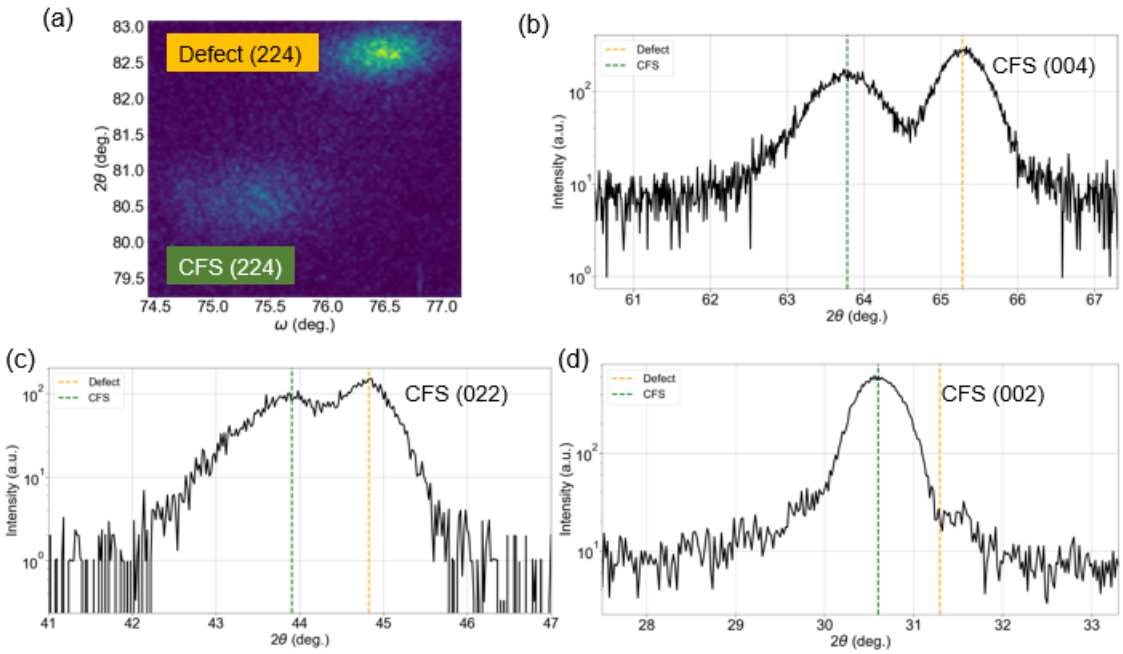

Figure 3.8: X-ray diffraction measurements of phase separation in Co_2FeSn grown at 130 °C and annealed at 650 °C. (a) Reciprocal space map in the vicinity of the (224) peak for Co_2FeSn. Out-of-plane $\theta - 2\theta$ measurements (b) near the (004) peak, (c) at $\chi \neq 0$ near the (002) peak, and (c) near the (002) peak.

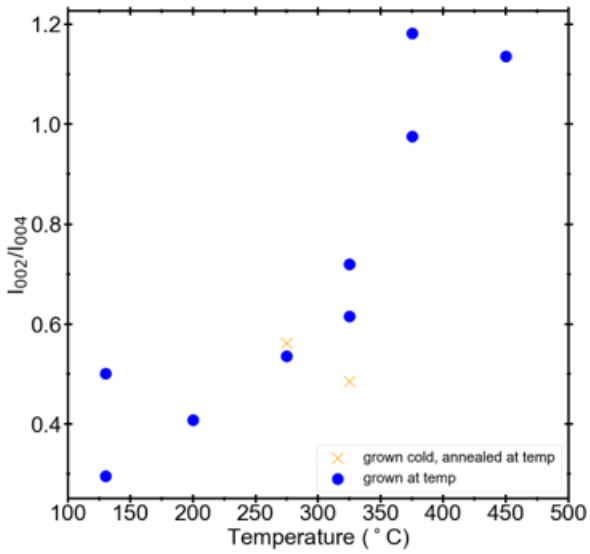

Figure 3.9: Ratio of integrated intensities of the measured (002) and (004) peaks of Co_2FeSn for various growth conditions.

An additional defect phase is also visible near the MgO(004) peak, at 83° in Fig. 3.7. No other peaks indicative of this phase are observed. There are too many possible structures to make a reasonable assignment of this phase as Co, Fe, and Sn have large mutual solubilities in a large number of various binary and ternary intermetallic compounds.

No tested combination of growth and annealing conditions produced films with a non-zero (111) peak in XRD, the hallmark of the $L2_1$ phase. Although there is no $L2_1$ ordering in the Co_2FeSn, there is a clear trend in the ratio of the integrated peak intensity of the (002) and (004) reflections as a function of growth temperature. This ratio is a stand-in for the B2/A2 ordering ratio via Eq. 3.4. Upon increasing growth temperature, a larger fraction of the film is B2 ordered (Fig. 3.9). This results in a tradeoff where to get the most ordered film, growth must occur at a temperature below the extrapolated phase segregation temperature. For our system, that appears to be around 375 °C. Recent results have shown that a rapid thermal anneal is capable of forming $L2_1$ ordering, but with a much lower ANC than expected [199]. Our lower temperature anneals did not appear to have any measurable improvement on B2 or $L2_1$ ordering.

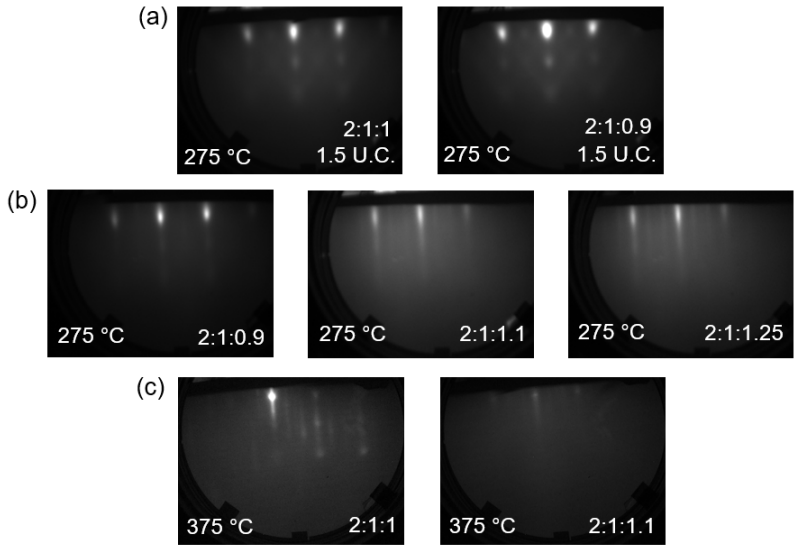

Figure 3.10: RHEED along the [110] direction of Co_2FeSn with varying Sn concentrations for (a) nucleation at 275 °C (b) 10 nm of growth at 275 °C and (c) 10 nm of growth at 375 °C.

Since most growth temperatures investigated here are above the melting point of Sn (232 °C), we also investigated the potential of incorporating excess Sn to serve as a surfactant and improve growth quality. During growth at low temperatures (comparable to or below the Sn melting point), a Sn deficiency led to slightly rougher nucleation (Fig. 3.10(a)). This deficiency also caused rougher films after growth had proceeded for an additional ∼10 nm than for the stoichiometric or Sn excess cases (Fig. 3.10(b)). Sn excess smoothened films slightly via streakier RHEED, but not significantly more than for the stoichiometric condition. At higher growth temperatures (Fig. 3.10(c)), excess Sn smooths the film but leads to much dimmer, hazier RHEED—potentially from molten Sn on the surface as growth proceeds. Varying the Sn concentration had little effect on the ordering or film quality. In one stack of four films with different Sn composition (Fig. 3.11), the full-width-at-half-maximum and ratio of B2/A2 ordering is comparable to that for stoichiometric growth. Thus it appears that film quality and ordering is not particularly sensitive to Sn composition.

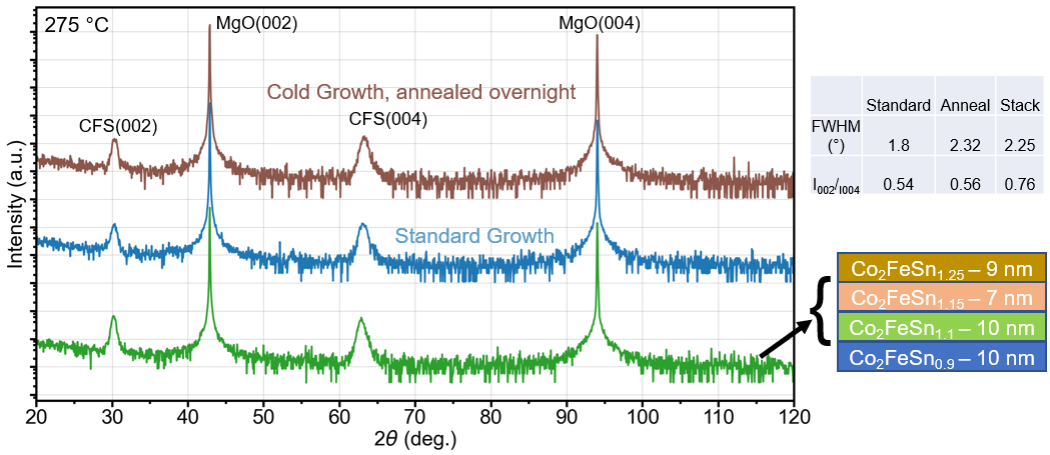

Figure 3.11: Wide range $\theta - 2\theta$ measurements of Co_2FeSn growth with varying Sn concentrations compared to stoichiometric conditions. All films are grown or annealed at 275 °C.

Chromium buffer layers between Co_2FeSn and MgO were also attempted to improve ordering, as has been reported in the past [182]. From RHEED it was found that Cr buffer layers grew rough, but smoothened after a 300 °C anneal (Fig. 3.12(a)–(c)). The Cr buffers were epitaxial to MgO with a Cr[110](001)‖MgO[100](001) ($2a_{Cr} \approx \sqrt{2}a_{MgO}$) and relaxed. However, we found that at growth temperatures above 130 °C, the Co_2FeSn reacts heavily with the Cr buffer layer (Fig. 3.12(d)). For the same nominal film thickness, the Co_2FeSn(004) peak intensity decreases strongly with increasing growth temperature. The $L2_1$ ordering still does not appear.

A comparison of all attempts to improve ordering are summarized in Fig. 3.13. Chromium buffer layers seem to drastically improve ordering at low temperatures. Unfortunately, Cr is conductive and reliable AHE and ANE measurements cannot be made.

Other attempts to improve ordering, such as changing the Fe composition in the film, did not appear to be successful. However, using a lower growth rate (13 nm/hr → 6 nm/hr) appeared to improve ordering significantly. It is unclear whether this was related directly to the growth rate or the increase in the effective annealing time at the growth temperature. Long anneals on cold-grown films at high temperatures did not appear to

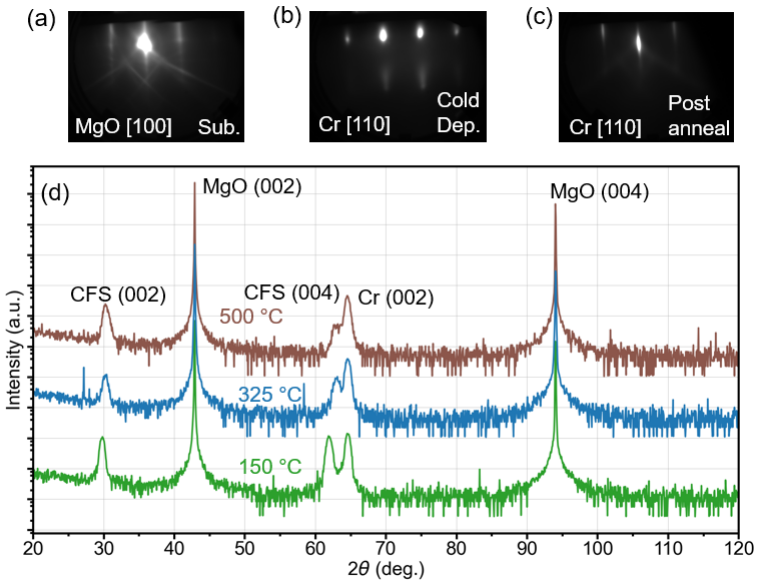

Figure 3.12: (a) RHEED along the [100] of MgO before the Cr buffer layer is grown. RHEED along the Cr[110] (a) after initial Cr deposition and (b) after a 300 °C anneal. (d) Wide range $\theta - 2\theta$ measurements of Co_2FeSn grown on Cr(001)/MgO(001).

significantly improve the ordering comparing to growing at that high temperature instead. Growing thicker films (30 nm vs. 13 nm Co_2FeSn) increased the ordering significantly. The usual explanation for this effect is that the thicker film is effectively annealed for a longer time. Since in Co_2FeSn annealing does not have a strong effect on ordering, the mechanism of ordering improvement is as-yet unclear. The main method of improving the B2 ordering in Co_2FeSn films is to grow with the highest substrate temperature possible before defect phases begin to form.

3.6 Ferromagnetism of $Co_2FeSn(001)$ thin films

Magnetic measurements confirmed the expected ferromagnetism in this system with the Curie temperature above room temperature. In addition, all films showed a <110> easy axis with four-fold symmetry. A four-fold symmetry is expected for the four-fold symmetric crystal structure. Growing with no substrate rotation resulted in only two-fold

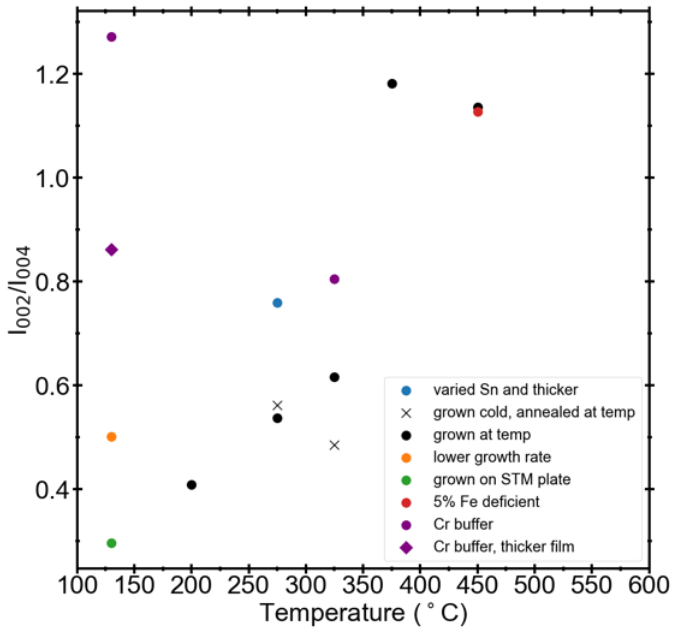

Figure 3.13: Ratio of integrated intensities of the measured (002) and (004) peaks of Co_2FeSn for various growth conditions including various growth schemes.

symmetry of the easy axis. On III-V substrates, interfacial bonding can also result in two-fold symmetry [200]. The <110> easy axis is expected if the film has $L2_1$ or B2 ordering. With DO_3 or A2 ordering, the <100> is the expected (but not required) easy axis. The in-plane easy axis is expected for all films, which should not show perpendicular magnetic anisotropy due to the shape anisotropy of the thin film. While growth on chromium improved ordering from XRD, it switched the easy axis of the Co_2FeSn to the <100> (Fig. 3.14). The mechanism for this change in anisotropy is unclear. The coercivity significantly decreased in both directions, indicative of improved sample quality. The antiferromagnetic Cr film could possibly apply an exchange bias to the magnetic Co_2FeSn film. No lateral offset is found in the hysteresis loop, so there is no significant exchange bias.

Studies of the magnetization of these films generally agree with the XRD ordering results, in that higher growth temperatures correspond to larger magnetic moments con-

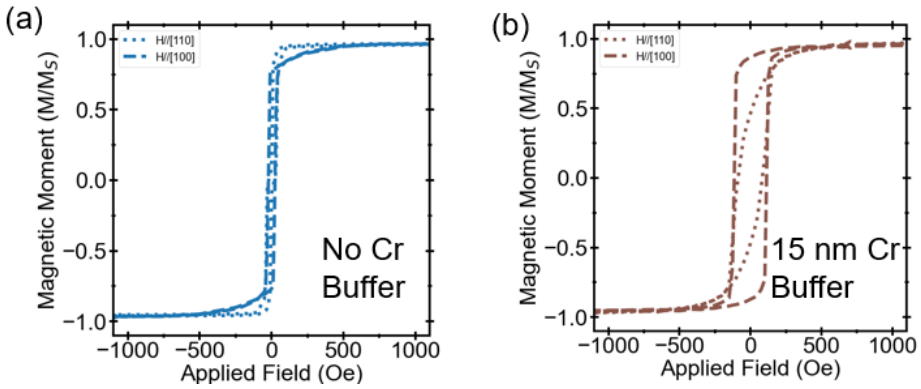

Figure 3.14: Hysteresis loops measured with the magnetic field parallel to the Co_2FeSn [110] and [100] directions for 13 nm Co_2FeSn grown at 150 °C on (a) MgO(001) and (b) 15 nm Cr(001)/MgO(001). Measurements were performed at 15 K.

sistent with higher B2 ordering (Fig. 3.15). The magnetic moment of Co_2FeSn is expected to be 6 μ_B/formula unit via the Slater-Pauling rule (a group theoretical calculation) [201] and 5.3 μ_B/formula unit via first principles calculations [86]. Our films showed a maximum of ∼5.1 μ_B/formula unit for a sample grown at 325 °C, which decreases at higher growth temperature. The deviation from calculated values could be due to the lack of $L2_1$ ordering. DO_3 ordering (undetectable in XRD) could also be competing with B2 ordering and lead to this reduction in ferromagnetism [192]. In Co_2-based full Heuslers the X-Y disorder is usually assumed to be low.

The coercivity along the easy axis has a non-monotonic dependence on growth temperature. This could be related to material quality issues such as phase segregation or other disorder in the films. In general the magnetization measurements of Co_2FeSn indicate the magnetic ordering is similar to the $L2_1$-ordered case, even if the films are only B2 ordered.

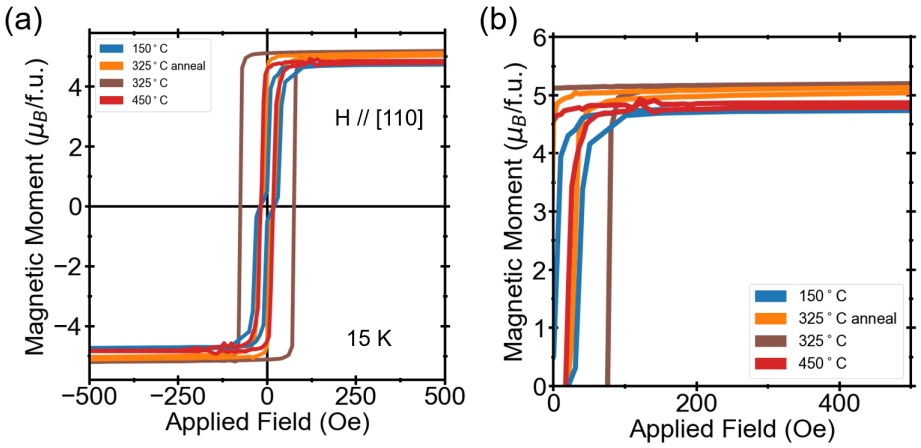

Figure 3.15: (a) Hysteresis loops measured with the magnetic field parallel to the Co_2FeSn [110] for 13 nm Co_2FeSn grown at a variety of temperatures. (b) Zoom-in of (a). Measurements were performed at 15 K.

3.7 Anomalous Nernst and Hall effect measurements

Since perfect $L2_1$ ordering is used in the calculations for giant ANC and AHC [86], yet not achieved here experimentally, we next study whether the B2 ordered Co_2FeSn has anomalous Nernst/Hall properties close to that calculated for the $L2_1$. Samples grown at a variety of temperatures were fabricated into modified Hall bars by Han Yu at the University of Minnesota, following previous work [189]. The applied temperature gradient, Nernst response, and Hall response are all measured via lock-in technique. The Nernst response of three samples is observed in Fig. 3.16(a). A clear decrease in Nernst voltage is seen as the growth temperature (B2/A2 ratio) increases. The value of the Nernst voltage is also only slightly better than Heuslers such as Co_2MnSi, which is known to have a low ANC. The anomalous Nernst effect is then much smaller than that calculated for the $L2_1$ structure. In Fig. 3.16(b), a similar trend is observed in the magnitude of the AHE, where ordering decreases the AHC. This trend is contrary to what is usually observed with other full Heuslers, where less disorder results in large ANE and AHC [202, 203]. The highest AHC value is in the coldest grown sample, 95

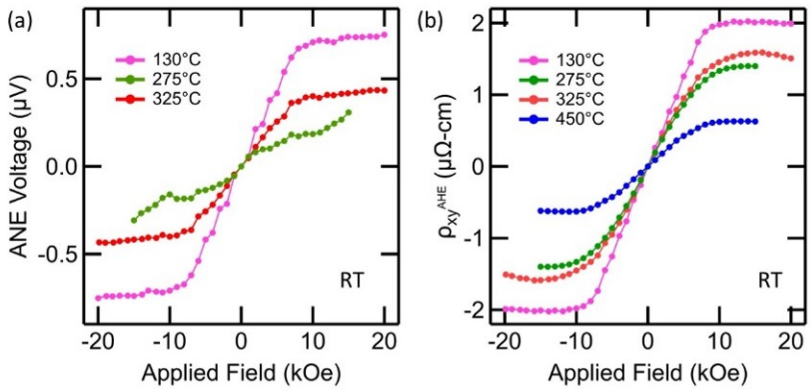

Figure 3.16: Anomalous room temperature transport of Co_2FeSn grown at various temperatures. (a) The anomalous Nernst effect. The size of the Nernst effect is much smaller than expected, likely from the lack of $L2_1$ ordering. (b) The anomalous Hall resistivity for the same set of samples. The small magnitude of the anomalous Hall effect is consistent with calculations [86]. Measurements were performed by Han Yu at University of Minnesota.

S/cm, while the $L2_1$ ordered structure is predicted to have an AHC of ∼50 S/cm [86].

While the ANC and AHC deviate from expected values, this result shows that disorder can enhance the properties sought after from these topological semimetals and could be desired, rather than avoided. This effect is not limited to this full Heusler—Co_2FeAl [204] and Co_2MnSi [205] and others [193] show similar trends, but this trend has not yet been rigorously characterized. The specific route to take to maximize the AHC and ANC likely depends heavily on the ordering and composition of the Heusler of interest.

3.8 Conclusion

Full Heusler Co_2FeSn has been predicted to have large ANC and AHC. Thin films were grown epitaxially by molecular beam epitaxy on MgO(001) substrates. The crystalline ordering of Co_2FeSn films was optimized through a variety of growth conditions. The maximum ordering found is B2 ordering, rather than the ideal $L2_1$. Growth at high temperatures results in phase separation and the creation of defect phases. The mag-

netic moment in highly B2-ordered films approaches the theoretically predicted magnetic moment.

The anomalous Nernst conductivity was measured to be lower than that expected from first principles calculations, but was surprisingly found to be inversely related to improved B2 ordering. The anomalous Hall conductivity was higher than predicted and followed the same reverse-ordering trend. This charts a path for further studies of defect-engineered topological semimetals as a source for large AHE and ANE. For $L2_1$ ordered Co_2FeSn, the anomalous Nernst and Hall conductivities slightly above the Fermi level are much larger than those at the Fermi level. Thus electron-doping Co_2FeSn films via Ni-alloying on the Co-site should increase drastically the magnitude of the anomalous Hall and Nernst effect in these defect-engineered Heusler films.

Chapter 4

Growth of α-Sn with reduced p-type doping

4.1 Introduction

α-Sn, the diamond structure allotrope of Sn, is a zero-gap semiconductor with an inverted electronic band structure at the Γ point [88].[1] Experiments have suggested that on InSb, α-Sn thin films go through multiple topological phase transitions between 2D TI, 3D TI, 2D DSM, 3D DSM, and normal insulator as a function of surface orientation, strain, and film thickness, generating much interest as a testbed for topological phase transitions [107, 108, 170, 207–213]. Exact results vary by research group and measurement technique. α-Sn is—to our knowledge—the only elemental material showing many of these phases. Due to its elemental nature, α-Sn should not suffer from the well-known antisite defect issues seen in many other multi-component topological materials. Bulk single crystals of α-Sn have been well studied in the past, where dopant concentration

[1] Some of the work presented in this chapter has previously appeared in Ref. [206]. Copyright 2024 by the American Physical Society.

could be better controlled and the inverted band structure was confirmed [90]. In thin film growth of α-Sn, InSb has been the primary substrate of choice for surface science studies. These growths of α-Sn are usually performed via molecular beam epitaxy (MBE) on sputter-anneal cleaned InSb leading to an In-rich surface. Indium is known to be a p-type dopant in α-Sn in the bulk [93] and has been seen to readily incorporate into α-Sn thin films from the InSb substrate [214, 215]. This effect even occurs when α-Sn is grown on a fresh *in situ* MBE-grown InSb buffer layer with an In-rich surface reconstruction [209]. The heavy p-type doping results in a Fermi level below the valence band maximum (VBM) and the surface Dirac point (near the VBM), making identification of the topological phase difficult via techniques such as angle-resolved photoemission spectroscopy (ARPES). In addition, the bulk mobility [93] and surface state mobility are both inversely dependent on carrier density [216], furthering the need for reduced unintentional p-type doping.

ARPES has been a key technique for fingerprinting topological materials due to the direct measurement of the filled-state band structure [36,144]. Fingerprinting via another common technique, magnetotransport, either requires extensive fitting of quantum oscillations via Lifshitz-Kosevich analysis to give indirect evidence of the topological phase or a gated device to map out a relevant portion of the Landau fan diagram for a more direct measurement of the topological phase [35]. In both cases, the filled bands must have high enough mobilities such that the cyclotron orbit time is shorter than the scattering time in the material [217]. For α-Sn, this condition is frequently not met: only the surface state oscillation is observed in low mobility films [208, 218], while high mobility films show two oscillation frequencies [207]. It is difficult to correctly identify the topological phase without measuring both the bulk and surface bands. The two key parameters to differentiate the possible topological phases are the presence (or absence) of a gap in the topological surface states and the presence (or absence) of a gap between the bulk

conduction and valence bands. Finally, the presence of parallel bulk transport in indium doped α-Sn (under conditions where the topological phase includes a bulk band gap) greatly reduces the applicability of the material both in fundamental physics studies and devices making use of the topological surface states.

Besides doping, incorporation of indium has been proposed to reduce the quality of α-Sn growth [108], similar to what has been suggested in α-$Ge_{1-x}Sn_x$ growth [219]. To reduce p-type doping and produce higher quality films, bismuth and tellurium are frequently used as compensatory dopants and/or surfactants [108, 212]. Bismuth and tellurium also possibly change topological signatures from α-Sn, modifying at least the band velocity of α-Sn's linear surface states [214]. The structural and electronic effects of incorporating Bi/Te in the α-Sn have not been investigated in detail. Another standard solution to limit indium incorporation is to use a low substrate temperature and high Sn growth rate [209, 214, 215]. However, a lower substrate temperature during growth was seen to be associated with lower structural quality of the epitaxial α-Sn [220].

Most reported growths studying the topologically non-trivial nature of α-Sn have been initiated on the In-rich InSb(001)-c(8×2) reconstruction of InSb(001) [107,108,170, 207–209, 212, 214, 218], depicted in Fig. 4.1(a). This reconstruction consists of a 0.5 monolayer (ML) of In and a 0.5 ML of Sb, with another 0.25 ML of In on top [221]. It is possible that the indium incorporating into the α-Sn films is sourced from this surface. On the other hand, the c(4×4) reconstruction, depicted in Fig. 4.1(b), has 1 ML of In on the surface, followed by 1 ML of Sb, and then an additional 0.75 ML of Sb [222]. The almost-double layer of Sb on the surface likely decreases the amount of indium that is available on the InSb surface for incorporation into the growing α-Sn film.

Here we find that by growing α-Sn on the Sb-rich InSb(001)-c(4×4), we drastically decrease indium incorporation without distorting the band structure of the epitaxial α-Sn films. We show that this reduction in In segregation persists through active heating of the

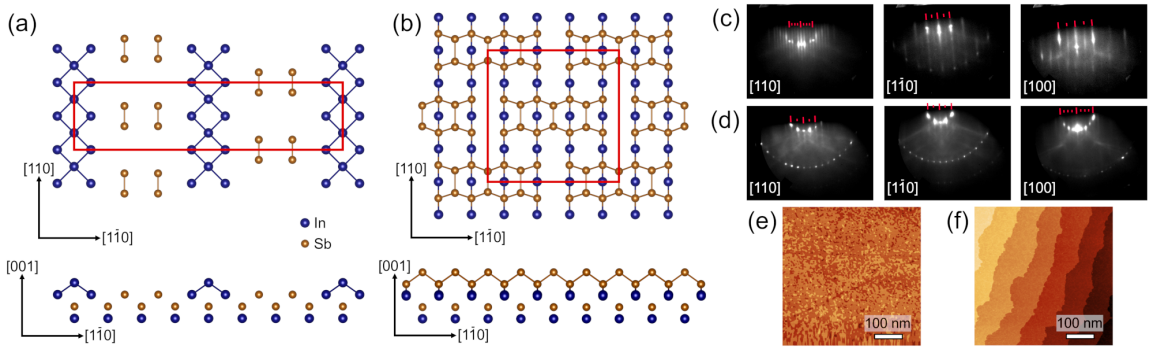

Figure 4.1: Surface reconstructions of InSb(001) surface. (a) Top and side view of the In-rich c(8×2) reconstruction following the model of [221]. (b) Top and side view of the Sb-rich c(4×4) reconstruction using the atomic positions determined in [222]. RHEED patterns along the [110],[1$\bar{1}$0], and [100] directions for (c) the c(8×2) reconstruction with a 4×, 2×, and 2× pattern, respectively, and (d) the c(4×4) reconstruction with a 2×, 2×, and 4× pattern, respectively. *In situ* STM images of (e) the c(8×2) surface directly after atomic hydrogen cleaning and (f) the c(4×4) surface after the Sb termination procedure.

substrate during growth. This method then allows an increase in total heat load that can be applied during α-Sn growth, potentially demonstrating a route toward higher mobility thin films. The decrease in indium incorporation is found using *in situ* angle-resolved photoelectron spectroscopy (ARPES), *in situ* ultraviolet photoelectron spectroscopy (UPS) and *ex situ* low temperature magnetotransport. This work offers a route for pure α-Sn growth where the features of interest are below the Fermi level, such that topological phase identification through techniques such as ARPES can proceed more readily.

4.2 Methods

4.2.1 Growth

The α-Sn films studied here were grown using a modified VG V80 MBE growth system. All samples were grown on undoped (001)-oriented InSb substrates (Wafer-Tech Ltd.). The native oxide was removed via atomic hydrogen cleaning using a thermal

cracker (MBE Komponenten) resulting in the In-rich c(8×2)/4×2 surface reconstruction, as determined by reflection high energy electron diffraction (RHEED) [223]. The Sb-rich samples were prepared with constant monitoring of the reconstruction via RHEED along the [110] while referencing the InSb(001) surface reconstruction phase diagram [223,224]. The substrate temperature was ramped continuously from 373 K through the following transitions to the final annealing temperature. Near 550 K, the c(8×2) surface was dosed with approximately 0.75 ML Sb until the c(8×2) just fades to the p(1×1) reconstruction. At higher temperatures the reconstruction transitions to the c(4×4) and, starting a few degrees below the c(4×4)/a(1×3) transition (approximately 643 K), was exposed to an Sb_4 flux continuously. The sample was then annealed under an Sb_4 overpressure 40-60 K above this transition point for at least 30 minutes. The sample was then cooled quickly down back through the a(1×3)/c(4×4) transition to achieve the final c(4×4) reconstruction. Both prepared surfaces show streaky RHEED, indicating relatively smooth surfaces (Fig. 4.1(c), (d)). The morphology of the substrates was confirmed using *in situ* scanning tunneling microscopy (STM) with the freshly hydrogen cleaned surface (Fig. 4.1(e)) containing a higher terrace density than after the Sb-termination/anneal procedure (Fig. 4.1(f)). Some samples with In-rich reconstructions were annealed at 623 K for 30 minutes to smooth the surface further.

A bilayer (BL) of α-Sn is defined here as 9.5×10^{14} at/cm^2, or $\frac{1}{2}$ of the diamond unit cell. Three different film thicknesses were studied: 13 BL, 50 BL, and 400 BL. The 13 BL films were grown at a rate of 0.25 BL/min at a substrate thermocouple temperature of 296 K under radiative backside heating. The real temperature is above the melting point of Ga (302.9 K). The 50 BL films were grown at a rate of 0.5 BL/min at a substrate thermocouple temperature of 253 K under passive radiative cooling from the liquid nitrogen cryopanel. The real temperature is significantly below the melting point of Ga. For the 13 BL and 50 BL films, the substrate thermocouple is between the

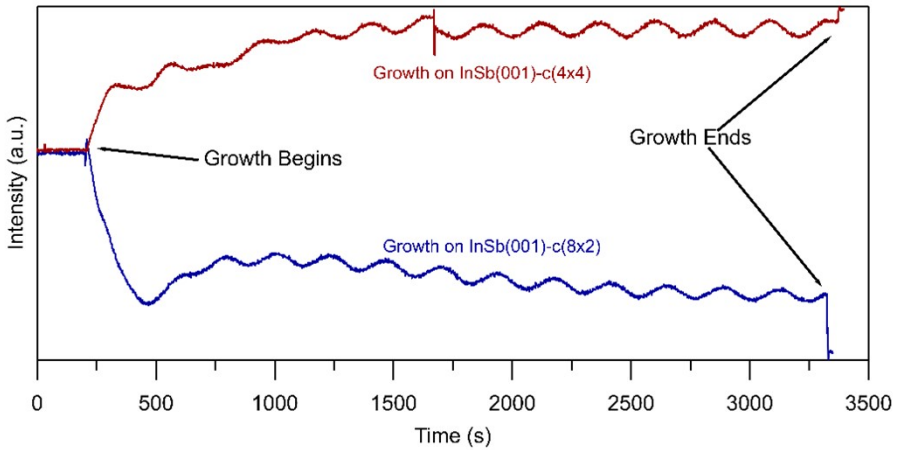

Figure 4.2: RHEED oscillations during growth of α-Sn on InSb(001) showing layer-by-layer growth. The electron beam is slightly unstable. Oscillations were recorded on the specular spot for the c(8×2) surface and the first order spot for the c(4×4) surface. The oscillation frequency is identical for the two samples.

substrate heater and the molybdenum block to which the substrate is indium bonded. The gallium references are performed by heating/cooling gallium in place of a sample and observing the melting/freezing by RHEED or visual inspection. The 400 BL film was grown at a rate of 1.25 BL/min in a separate chamber with active liquid nitrogen cooling on the sample. The sample is indium bonded to a tungsten block which is then clamped (in direct thermal contact) with an *in vacuo* liquid nitrogen filled stainless steel vessel. The substrate temperature remains around 80 K via thermocouple during growth. This thermocouple is clamped to the manipulator close to the tungsten block. Different growth temperatures and growth rates were used to investigate the effect of heat load on the effectiveness of the termination procedure. The growth rates are calibrated via bilayer oscillations in the RHEED intensity during growth (Fig. 4.2) and Rutherford backscattering spectrometry on Si reference samples.

4.2.2 Characterization

Angle-resolved and -integrated photoelectron spectroscopy measurements of the 13 BL films were performed at beamline 5-2 of the Stanford Synchrotron Radiation Lightsource (SSRL) using linear polarized light. Measurements of the 50 BL and 400 BL film were performed at beamline 10.0.1.2 of the Advanced Light Source (ALS) using p-polarized light. Spectra were collected with a Scienta-Omicron DA30L electron analyzer with variable energy resolution and angular resolution better than 0.1°. Samples were transferred *in vacuo* from the MBE system at UCSB to SSRL and ALS via a vacuum suitcase with base pressure better than 4×10^{-11} Torr. During the photoemission measurements the sample temperature was kept under 20 K and the pressure was better than 3×10^{-11} Torr.

In situ STM was performed in an Omicron VT-STM at room temperature with a bias of 3 V and a tunneling current of 100 pA. *Ex situ* magnetotransport measurements on 56 BL films with magnetic field up to 14 T were performed at 2 K in a ^{4}He cryostat (Quantum Design Physical Property Measurement System). The 56 BL films were grown under the same conditions as the 50 BL films and were not capped; the native oxide is expected to consume 3-6 BL [225]. Ohmic contacts were made with silver paint following the van der Pauw geometry. A standard four terminal, low frequency AC lock-in technique was used with a constant excitation current of 100 μA.

4.3 Film morphology and scanning tunneling spectroscopy

We observe the typical mixed $(2\times1)/(1\times2)$ reconstruction in α-Sn [220] characterized by a $2\times$ RHEED pattern in the $\langle110\rangle$ directions and a $1\times$ pattern in the $\langle100\rangle$ directions

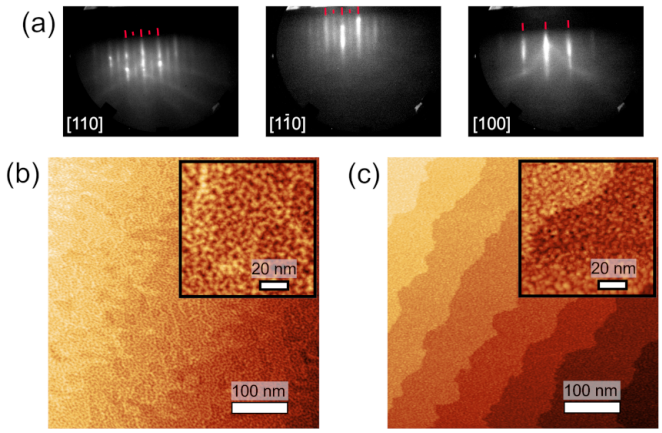

Figure 4.3: Surface structure of α-Sn(001). (a) RHEED patterns along the [110], [1$\bar{1}$0], and [100] directions showing a 2×, 2×, and 1× pattern respectively, indicative of a mixed (2×1)/(1×2) reconstruction. *In situ* STM of 13 BL α-Sn grown on (b) InSb(001)-c(8×2) and (c) InSb(001)-c(4×4). Insets are 100 nm x 100 nm measurements under the same conditions.

(Fig. 4.3(a)) for all growths less than 100 BL, irrespective of substrate surface termination. During growth all samples show oscillations in the RHEED intensity indicating a bilayer-by-bilayer growth mode for α-Sn (Fig. 4.2).

The overall surface morphology is roughly equivalent for both films (Fig. 4.3(b,c)). The structure consists of bilayer terraces which are then decorated with a grain structure as has been seen previously in α-Sn/InSb(001) [214]. The change in bilayer terrace structure between the two cases is likely due to the differences in the starting substrate morphology. The grains in α-Sn grown on the Sb-rich surface reconstruction were slightly (∼20%) smaller than the grains grown on the In-rich surface reconstruction (Fig. 4.3(b,c) insets). The RMS roughness on a single terrace also decreases from 2.04 Å to 1.75 Å.

The average step height of a terrace for the case of grown on InSb(001)-c(4×4) is given in Fig. 4.4(a). The step heights within the grains generally correspond to one atomic layer in Fig. 4.4(b). The grains are then likely stacks of atomic layers with an alternating (2×1) vs. (1×2) reconstruction, where each layer is partially visible. This then leads

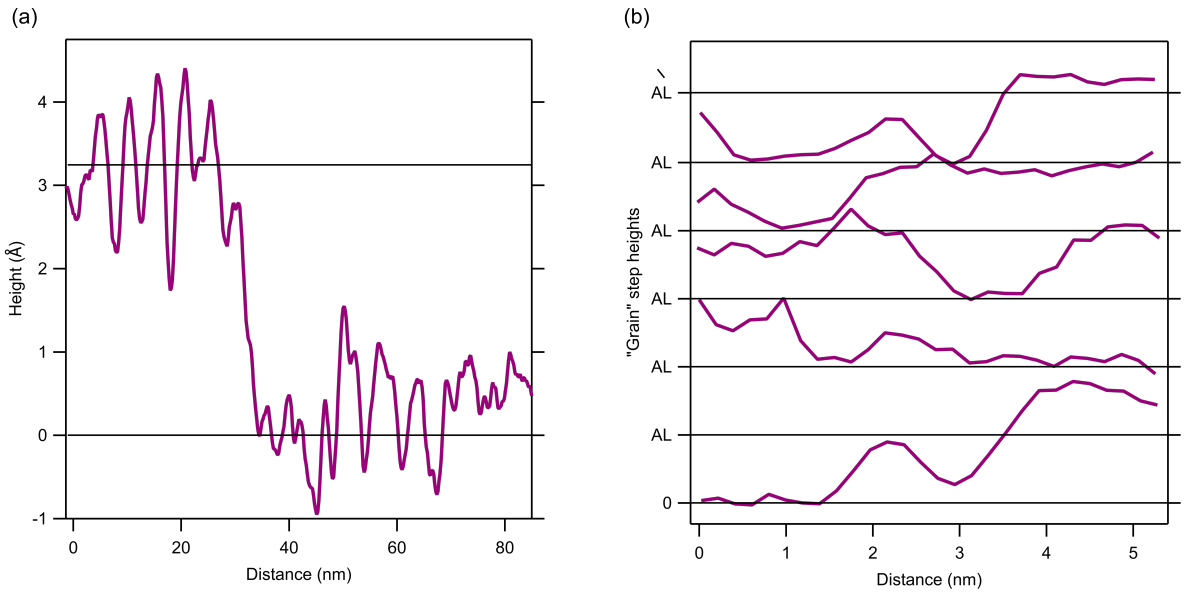

Figure 4.4: Line profile analysis of *in situ* STM of α-Sn(001). (a) Line profile over one terrace edge averaged over roughly 5 nm in the direction perpendicular to the edge. The height of one strained α-Sn bilayer is indicated. (b) Line profiles collected over several grains. Increments are in 1 atomic layer or 1.622 Å steps. The line profiles are artificially offset both vertically and horizontally for clarity.

to the observed mixed (2×1)/(1×2) reconstruction in RHEED. The alternate stacking structure has been directly observed before in α-Sn via STM [226], and is well-known for Si(001) surfaces.

In addition, scanning tunneling spectroscopy (STS) is potentially a useful tool for studying the density of states in this system. This could be useful to study the presence of a gap in both the surface and the bulk states—if the gap is larger than the experimental energy resolution and the band edges are sharp enough. In addition, it could be useful to study higher lying conduction bands (i.e. the L valley, which is potentially separated by $< kT$ from the Γ valley [227]). However, the nonuniformity of the (001) surface makes these measurements difficult. In the past, STS measurements have been averaged from individual measurements at similar heights. Because the "height" in STM is inherently convoluted with the density of states, this technique is not robust and unlikely to give

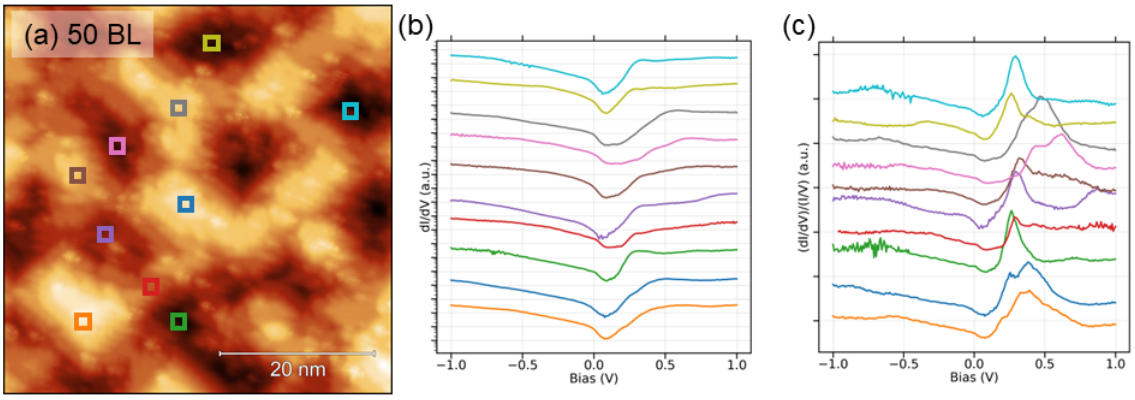

Figure 4.5: (a) 50 nm × 50 nm STM measurement on 50 BL α-Sn using the same scan conditions. The atomic layer steps are visible. (b) Constant tip height STS measurements performed at various locations across the sample surface. Each line scan is the average of 30 forward and 30 backward sweeps (c) STS measurements in (b) normalized to the point-by-point resistance for better band identification. All measurements were performed at 77 K. STS measurements courtesy of Connor Dempsey.

meaningful results [214].

We have measured STM/S on a 50 BL α-Sn, where the morphology is relatively similar to that in 13 BL α-Sn. The raw STS measurements are shown in Fig. 4.5, where there is clearly high variation. The usual normalization procedure [228] gives a potentially truer density of states for this semiconductor (Fig. 4.5(c)). However, the variation across the sample is still very clear and it is difficult to assess whether a feature is truly from the (001) surface of 50 BL α-Sn, or through some lateral confinement effect. As such future STS studies were discontinued. The (111) surface of α-Sn, which generally shows sharper atomic layers on each bilayer terrace [211, 229, 230] is potentially more fruitful for such detailed STS studies.

4.4 Film stoichiometry

The effect of substrate termination was first studied on the 13 BL films grown with active substrate heating at 296 K. Measurements were performed at photon energies of

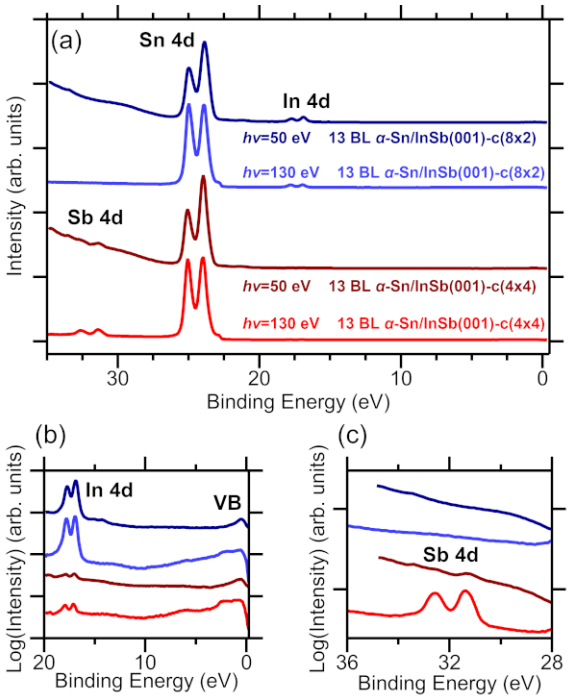

Figure 4.6: UPS measurements of 13 BL α-Sn films grown on the two different surface reconstructions of InSb(001) at 296 K. Measurements are offset for clarity. (a) Survey UPS measurements at photon energies of 50 eV and 130 eV, normalized to the integrated Sn 4*d* intensity. Zoom-in of (b) the valence band and indium core level region and (c) the antimony core level region with the same scan ordering.

50 eV and 130 eV to modulate the information depth, discussed later. Growth on the Sb-rich surface termination of InSb(001) resulted in no clear peaks corresponding to indium in a full-range UPS scan (Fig. 4.6(a)), indicating a large decrease in indium composition. We extracted the very weak intensity of the In 4*d* states and found a reduction in the indium concentration by over an order of magnitude. Extraction of exact concentration of indium and antimony in the films is problematic as the distribution of dopants is unknown and computed cross-sections and mean free paths under these experimental conditions are inaccurate.

Assuming homogenous composition, using the spectra taken at a photon energy of 130 eV, and using parameters computed by SESSA [231], we find the total concentra-

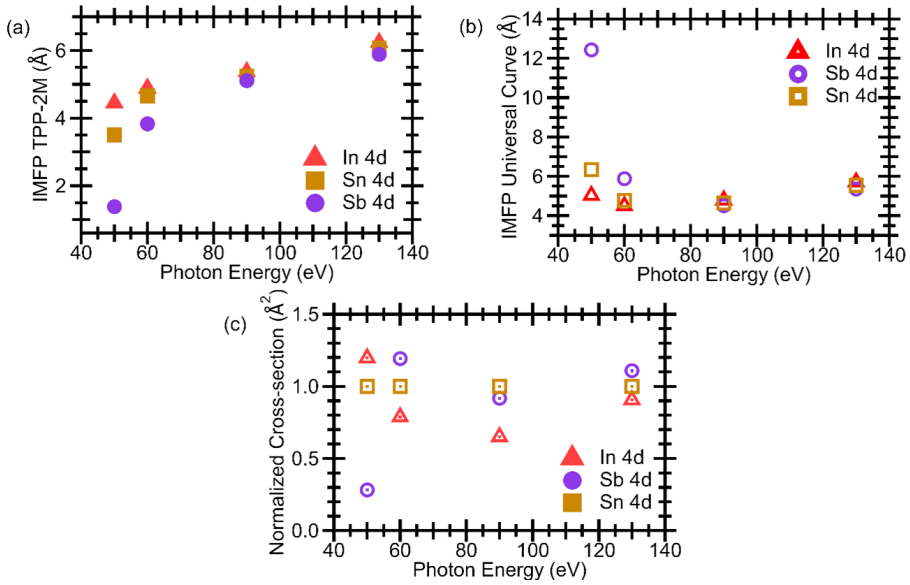

Figure 4.7: (a) Inelastic mean free paths calculated according to the TPP-2M equation. (b) Inelastic mean free paths calculated according to a modified fit to the universal curve. (c). Cross sections calculated by SESSA, normalized to the Sn 4d core level cross sections. All values (IMFPs & cross sections) are calculated for each spin-orbit split photoelectron peak and then averaged according to the theoretical branching ratio. The kinetic energies used are found directly from each UPS measurement. The binding energies of the 4*d* In, Sn, and Sb peaks are roughly 17 eV, 24 eV, and 32 eV.

tion of indium in the film decreases from approximately 2% to approximately 0.18% by changing the surface termination that α-Sn growth is initiated on. By increasing the signal amplification in the electron analyzer, the indium core levels could be resolved more clearly. With reference to the valence band intensity in Fig. 4.6(b), a similar sized reduction in the concentration of indium in the films is found. However, there is a concomitant increase in Sb concentration in the α-Sn films from growth on the c(4×4) reconstruction (Fig. 4.6(c)). There is no visible Sb signal when growth is initiated on the c(8×2) reconstruction, indicating all of the Sb observed is incorporated in the α-Sn film. This Sb incorporation is not necessarily a detraction; Sb is an established n-type dopant in α-Sn [90] which should further shift the Fermi level in the desired direction.

Using a combination of measurements at different photon energies (to modulate the

inelastic mean free path (IMFP)) and the angle (to modulate the escape depth at constant IMFP) we may extract more information about the distribution of In and Sb in the 13 BL α-Sn films. Inelastic mean free paths (IMFPs) were calculated using SESSA according to the TPP-2M equation (named for its proposers Tanuma, Powell, and Penn) [231] or according to a modified fit to the universal curve [143]. The cross-sections are computed via SESSA and a weighted average according to the expected branching ratio between the $4d^{\frac{3}{2}}$ and $4d^{\frac{5}{2}}$ peaks. Computed and experimental cross-sections are normalized to those of the Sn $4d$ core level. These results are summarized in Fig. 4.7.

Since the TPP-2M equation is ill-defined for photoelectron kinetic energies below 50 eV, we concentrate on IMFPs calculated via the universal curve. Peak area ratios are extracted from peak fits to the data in Fig. 4.6(a). Comparing the 130 eV to 50 eV measurement for Sb $4d$, the peak area decreases by a factor of about 2.5. Taking into account only cross-section ratios, we would expect the peak intensity to go down by a factor of 4. The Sb IMFP increases drastically from 5.2 to 12.5 Å, while the Sn IMFP increases slightly from 5.5 to 6.2 Å. This indicates that there is more Sb deeper in the Sn film and thus there is no spike of Sb concentration near the Sn surface.

For indium under the same measurement conditions, from 130 eV to 50 eV, the In $4d$ normalized peak area goes up by a factor of 2. The cross-section ratio should only go up by about 1.3. The Sn IMFP goes up from 5.5 to 6.2 Å, while the In IMFP goes down from 5.7 to 5.0 Å. This increase suggests that there is more indium closer to the surface of the Sn. For both the case of indium and antimony incorporation in α-Sn/InSb(001), there is no evidence of significant (on the order of magnitude of a monolayer of dopant) segregation to the surface, in contrast with bismuth dopants [108].

Angular dependent measurements were also performed to extract the doping profile and are summarized in Fig. 4.8. If the relative composition of an impurity increases with an increased exit angle in UPS, there is more of that impurity toward the surface

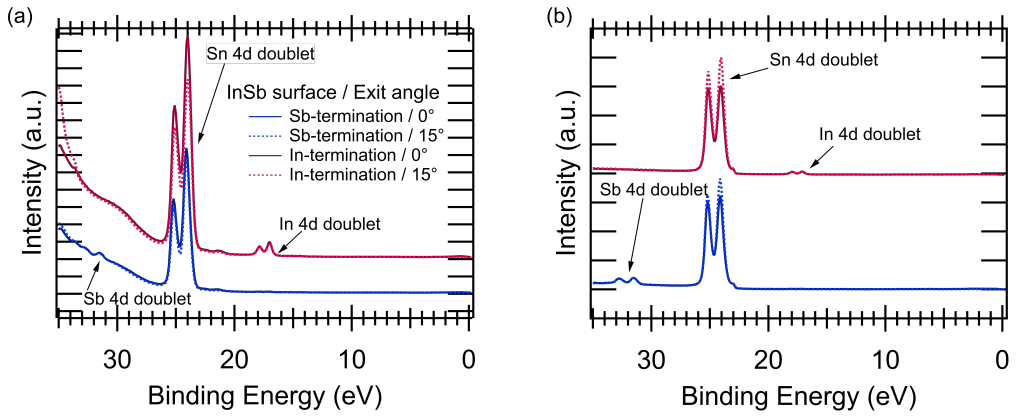

Figure 4.8: Survey UPS measurements (at normal exit and with a 15° exit angle) of 13 BL α-Sn grown on the two studied surface reconstructions of InSb(001) (a) taken with $h\nu = 50$ eV and (b) taken with $h\nu = 130$ eV

of the film rather than in the bulk. If the impurity is homogenously distributed along the growth direction of the film, the relative ratio should be constant with exit angle. First using $h\nu = 50$ eV (Fig. 4.8(a)), an increase in exit angle slightly increases the relative concentration of Sb. This could indicate some small preferential Sb segregation toward the film surface (but by relative intensities, it would still necessarily only be a small fraction of a monolayer). This conclusion is complicated by the large difference between the IMFPs for Sb 4d and Sn 4d at this photon energy. Turning to In, where the IMFPs are more similar, the In to Sn ratio increases when the UPS measurement is more surface sensitive, indicating again some segregation. These segregation effects conflict with the normal exit, photon energy dependent results. However, repeating these measurements at $hv = 130$ eV (Fig. 4.8(b)) leads to good agreement with the photon energy dependent results. The ratio of both In to Sn and Sb to Sn decrease with an increased exit angle, indicating these elements have a higher concentration closer to the film/substrate interface. The disagreement between the angle-dependent measurements at different photon energies could be from photoelectron diffraction effects. Although In and Sb are substitutional with α-Sn and the relative diffraction pattern will be similar,

since the core levels have different energies (and thus wavelengths) the angle scale of the diffraction pattern will be contracted or extended.

Next we investigated behavior of In and Sb incorporation when α-Sn films are grown thicker and with reduced heating during growth. Neither In nor Sb $4d$ peaks are visible in the survey UPS measurements in Fig. 4.9(a) for a 50 BL (0.5 BL/min) sample grown at 253 K on an Sb-rich surface nor for a 400 BL (1.25 BL/min) sample grown at 80 K on an In-rich surface. By the same method as earlier we enhanced the signal from the indium, as seen in Fig. 4.9(b). It is clear that the concentration of indium is reduced further by growing on an Sb-rich surface than by growing at ultracold temperature on an In-rich surface, resulting in a more than 50% decrease in indium incorporation. There is again an increase in the amount of Sb incorporation (Fig. 4.9(c)). Thus the concentration of indium in α-Sn can be reduced significantly at a range of growth temperatures and growth rates by growing on the Sb-rich c(4×4) reconstruction of InSb(001). This surface termination procedure is more effective than the conventional method of minimizing sample temperature and maximizing Sn growth rate.

4.5 Electronic structure

The persistent *p*-type indium doping in the α-Sn films results in the node of the surface states (and the valence band maximum) being above E_F (Fig. 4.10(a)), and thus not accessible by a filled state measurement such as conventional photoelectron spectroscopy. This is evident in growth of α-Sn on the In-rich surface reconstruction in Fig. 4.10(b), where the Dirac node is projected to be 32±7 meV above E_F via a linear fit to the surface states. Reducing the indium incorporation (with the concomitant increase in Sb incorporation) as observed in these same samples in Fig. 4.6(a), resulted in a Dirac node measured 36±10 meV below E_F (Fig. 4.10(c)). The group velocity of

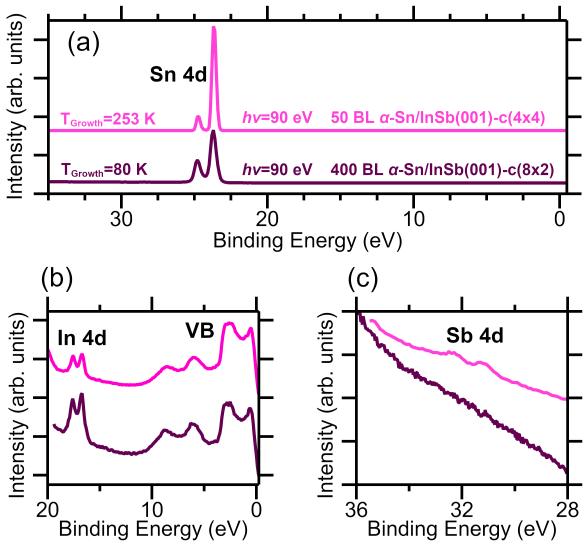

Figure 4.9: UPS measurements of 50 BL α-Sn on the c(4×4) reconstruction grown at 253 K and 400 BL α-Sn on the c(8×2) reconstruction grown at 80 K. Measurements are offset for clarity. (a) Survey UPS measurements at a photon energy of 90 eV, normalized to the integrated Sn 4*d* intensity. Zoom-in of (b) the valence band and indium core level range and (c) the antimony core level range with the same sample ordering.

the surface states ($\frac{1}{\hbar}\frac{dE}{dk}$ using the slope of the linear fit) in Fig. 4.10(b) is 4.1±0.1×10^5 m/s and in Fig. 4.10(c) is 4.0±0.2×10^5 m/s. The dopants/surfactants of Bi and Te commonly used in α-Sn growth result in a high group velocity near 7×10^5 m/s, while a lower group velocity is found in "phase pure" α-Sn (5×10^5 m/s) [108, 212, 214]. The low and unchanging band velocity we observe is thus consistent with the preservation of "phase pure" α-Sn even with the higher concentrations of Sb in the α-Sn film. We next turned to the bulk band structure to validate the absence of any band distortion.

The band structure of these 13 BL α-Sn films in the vicinity of the $\mathbf{\Gamma_{003}}$ high symmetry point was investigated using a photon energy of 127 eV, assuming an inner potential of 5.8 eV [170]. A schematic for the expected band structure of α-Sn in a 3D topological insulator-like phase is shown in Fig. 4.10(a) [170, 209, 212]. In growth on both the In-rich (Fig. 4.10(e)) and Sb-rich (Fig. 4.10(f)) reconstruction, the experimental data is

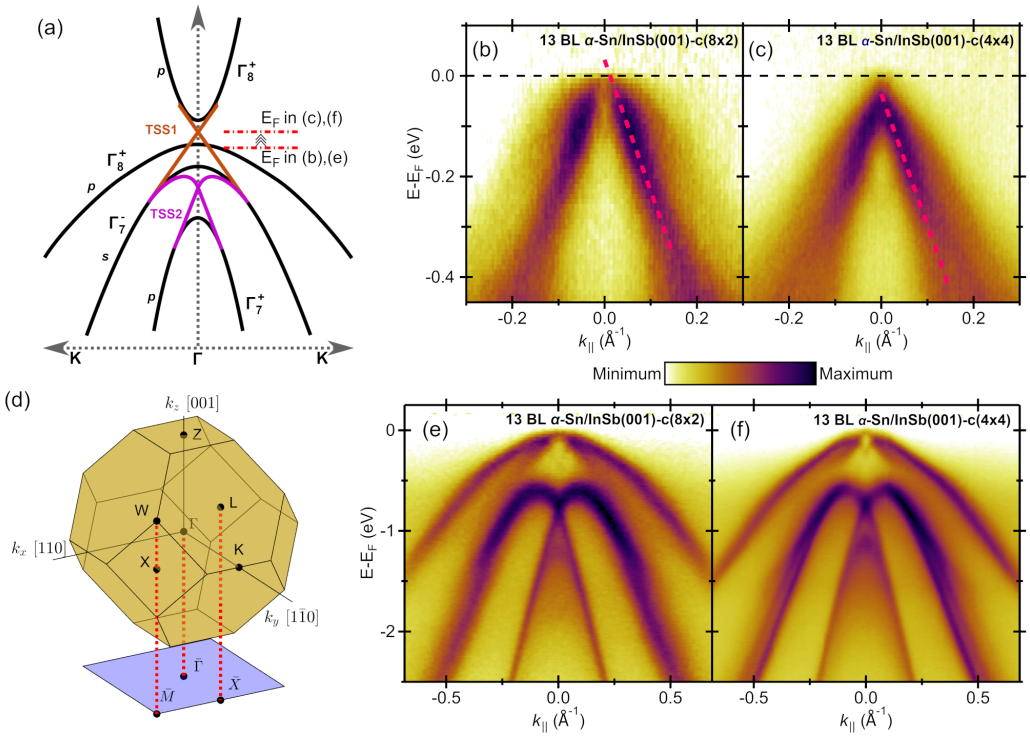

Figure 4.10: ARPES measurements of the 13 BL α-Sn films. (a) Band schematic of α-Sn in a 3D topological insulator-like phase. Surface state measurements at $h\nu$=21 eV in the $\bar{X}-\bar{\Gamma}-\bar{X}$ direction for 13 BL α-Sn grown on (b) InSb(001)-c(8×2) and (c) InSb(001)-c(4×4). Dashed lines corresponding to a linear fit of TSS1 are overlaid on the spectra. (d) Bulk and surface Brillouin zone schematic of α-Sn. Bulk band measurements at $h\nu$=127 eV in the $K-\Gamma-K$ direction in the vicinity of $\mathbf{\Gamma_{003}}$ for 13 BL α-Sn grown on (e) InSb(001)-c(8×2) and (f) InSb(001)-c(4×4).

consistent with the schematic. There is no evidence of the inverted p-like "light hole"-character conduction band (Γ_8^+) coming down to touch the VBM, therefore a bulk band gap exists. The topological surface state studied in prior works [106–108,170,208–214,232] (and which determines the topological phase) is labelled TSS1; its Dirac node is located approximately 80 meV above the valence band maximum. The valence band maximum consists of the uninverted "heavy hole" band with p-character (Γ_8^+). Below this is the inverted "conduction" band with s-like character (Γ_7^-). The lowest depicted band is the p-like split-off band (Γ_7^+). The distinctive M shaped feature between the split-off band and the "conduction" band is associated with a second topological surface state

TSS2, discussed in more detail elsewhere [170]. There is an additional cross-like state in between TSS2 and TSS1, which we attribute to a topological interface state and is discussed further in Chapter 6.

No discernible change to the bulk dispersion is observed, indicating the reduction of indium and addition of antimony can be treated as a rigid band shift from doping. While carrier density changes could be extracted from the knowledge of k_F, surface band bending is a non-negligible effect in topological insulators [233]. As ARPES (and UPS) are surface sensitive measurements, these observed carrier density changes do not reflect accurate changes in the carrier densities in the bulk of the crystal (i.e. an estimation of the doping). To ensure the reduction in indium incorporation is reflected in the bulk of the film, we turned to low temperature magnetotransport.

4.6 Magnetotransport

Magnetotransport measurements were performed on 56 BL α-Sn films to account for the native oxide consuming 3-6 BL [225]. The substrates were gallium bonded to avoid unnecessary post-growth sample heating. The topological surface state should be robust to oxidation, but the surface chemical potential will likely shift with respect to the Dirac node of the topological surface state [208]. Since the top surfaces are identical for these samples, any effect of oxidation should be identical between these samples as well. Longitudinal and transverse resistance measurements for the 56 BL α-Sn films grown on the two different InSb(001) reconstructions are shown in Fig. 4.11. Growth on InSb(001)-c(4×4) resulted in n-type behavior at high field while growth on InSb(001)-c(8×2) resulted in p-type behavior at high field in Fig. 4.11(a). Shubnikov-de Haas oscillations are visible in both the longitudinal and transverse geometry.

Additional low field Hall measurements in Fig. 4.11(b) clarify the presence of three

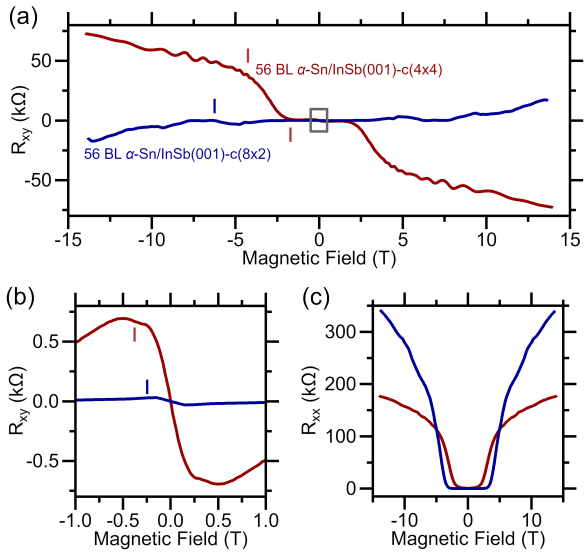

Figure 4.11: Magnetotransport measurements of 56 BL α-Sn films performed at 2 K. (a) Transverse resistance as a function of magnetic field for α-Sn films grown on the c(8×2) and c(4×4) surfaces of InSb(001). (b) Zoom-in of (a) showing an additional inflection point in each sample. (c) Longitudinal resistance vs. magnetic field for the two samples. Approximate inflection points in transverse geometry measurements are marked.

inflection points in the Hall effect in α-Sn on Sb-rich InSb and only two inflection points in α-Sn on In-rich InSb. This change is likely due to an increase in mobility of the bulk α-Sn carriers. The bulk mobility is sensitive to crystal quality, the carriers only being observable in quantum oscillations in high quality samples [207, 208, 218]. The onset of Shubnikov-de Haas oscillations occurs at a lower magnetic field value in films grown on Sb-rich InSb(001), indicating higher quantum mobilities [217]. We anticipate this initial onset to be indicative of the surface states, which have been found to have a higher mobility than the bulk heavy holes [207, 208, 218].

In the longitudinal geometry, we observe a sharp increase in the resistance at an applied field of around 4 T (Fig. 4.11(c)). This is a consequence of the established magnetic field induced metal-insulator transition in InSb [234]. The behavior of freeze-out in InSb is extremely sensitive to absolute dopant concentrations [235]. Carrier freeze-out complicates Hall analysis, as the response of the substrate in a transverse geometry

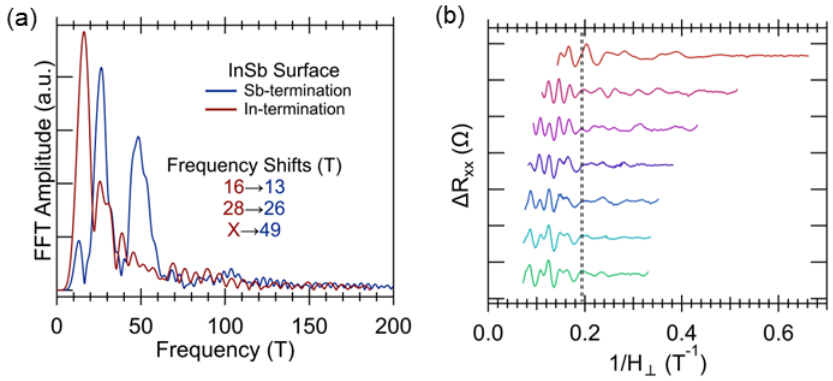

Figure 4.12: (a) Fast fourier transform of the R_{xx} data in Fig. 4.11. (b) Field angle dependence of oscillations for the sample grown on Sb-rich InSb(001). The angle of the field with the sample normal increases from 0° to 60° in 10° increments, from the bottom to the top of the plot.

is highly non-linear and has no simple analytical form. While quantitative analysis is difficult, we find that there is a clear, drastic change in the carrier concentrations in the α-Sn films when grown on different surface terminations of InSb(001).

A 3rd-order polynomial fit was subtracted from the R_{xx} curves of each sample to isolate the Shubnikov-de Haas oscillations. A fast fourier transform (FFT) is then performed on the background-subtracted data to extract the frequencies. Each frequency corresponds proportionally to the cross section of the Fermi surface of that band [217]. There are two clear frequency peaks in the FFT spectrum (Fig. 4.12(a)) for Sn/In-rich InSb located at 16 and 28 T, while for Sn/Sb-rich InSb there are three peaks at 13 T, 26 T, and 49 T. The carriers associated with the bands will be referred to as F1 (16/13 T), F2 (28/26 T), and F3 (XX/49 T). The addition of F3 is most likely from the increased mobility of the film grown on Sb-terminated InSb allowing oscillations to now be visible. The increased quality of the film allows the scattering time to be greater than the cyclotron orbit time for the bulk valence band carriers. By comparison to the literature [207, 208, 218], F1 can be attributed to the topological surface state. Thus, F2 originates from the InSb valence band. However, we note that neither our InSb-derived

band, nor the InSb-derived band of other work [207], agree with the nominal substrate carrier density of 10^{14} cm^{-3} which should have a frequency component less than 1 T.

We successfully observe a decrease in the F1 component when α-Sn is grown on the Sb-terminated InSb surface from 16 T to 13 T. The frequency of the F1 component also appears to be independent of tilt angle (Fig. 4.12(b)) which indicates that the band it originates from is 2D. This conclusion is limited in that the mean free path of the carriers is on the order of the film thickness, which can also produce this angle-independent effect. For clearer magnetotransport results, we began to collaborate with Stuart Holmes and Yilmaz Gul at University College London. For this substrate termination study, the magnetotransport concurs with both the UPS and ARPES measurements that growth on the Sb-rich InSb(001) surface reconstruction reduced p-type doping in α-Sn films by limiting indium incorporation.

4.7 Conclusion

Topologically non-trivial α-Sn thin films have been grown on the Sb-rich InSb(001)-c(4×4) and In-rich InSb(001)-c(8×2) surface reconstructions. Despite active substrate heating and lack of intentional surfactant or dopant species, the α-Sn films grown on the Sb-rich reconstruction show minimal indium incorporation. This method results in less indium incorporation than even growing α-Sn at cryogenic temperatures while on the In-rich c(8×2) reconstruction. The reduction in p-type doping was confirmed through UPS, ARPES, and magnetotransport. Our work facilitates more robust identification of the topological phase via angle-resolved photoemission and magnetotransport. Furthermore, it allows for a wider growth window of α-Sn thin films on InSb(001) and opens up a path for a similar methodology on other crystal orientations of interest in this materials system. Without this thin film growth process, the studies in Chapters 5, 6, 7, and 8

would not be possible.

Chapter 5

Clarifications to the surface and bulk electronic structure of α-Sn

5.1 Introduction

α-Sn, the diamond allotrope of Sn, has long been known to have an inverted band structure [88]. In contrast to similarly diamond structured group IV semiconductors Si and Ge, strong relativistic effects in α-Sn result in large $5p$-splitting from the spin-orbit interaction and large shifts of the $5s$ and $5p$ states via the mass and Darwin effects; this creates a band inversion between the $5s$ and $5p$ states [236]. The band inversion is between the second valence band and the conduction band analogous to HgTe. In the bulk α-Sn is a gapless semiconductor, where the quadratic touching point between the p-like $\Gamma^+_{8,c}$ and $\Gamma^+_{8,v}$ is assured by the symmetries of the system.

Bulk α-Sn is not stable at room temperature, transitioning to the topologically trivial, superconducting β-Sn above 13.2°C [87]. However, it was found that by growing thin films via molecular beam epitaxy on closely lattice- and symmetry-matched substrates, the transition temperature could be raised above room temperature [101]. The exact

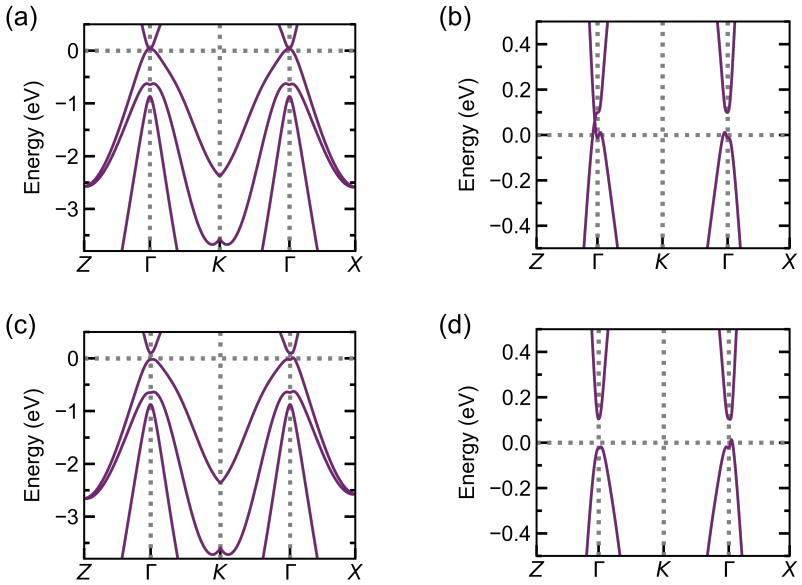

Figure 5.1: Topological phase transitions as a function of strain in α-Sn(001). (a) Tight-binding calculation of the bulk electronic structure under 1% biaxial compressive strain. (b) Zoom-in near the charge neutrality point. (c) Tight-binding calculation of the bulk electronic structure under 1% biaxial tensile strain. (d) Zoom-in near the charge neutrality point.

transition temperature varies significantly based on strain and film thickness [101, 237–239], but is typically greater than 50°C and can reach up to 200°C.

It is now generally accepted that compressive strain from epitaxial growth of α-Sn on the common substrates of InSb(001) (-0.15%) or CdTe(001) (-0.12%) results in the formation of a 3D Dirac semimetal (DSM) phase [109, 209, 210, 232, 240, 241]. The crossing is between the $\Gamma^+_{8,c}$ and $\Gamma^+_{8,v}$ bands in the [001] direction and is enforced by $C_4(z)$ symmetry [207, 209, 210, 232]. Tensile strain is expected to result in a 3D topological insulator (TI) phase [109,240], however (to our knowledge), this has not yet been realized experimentally due to the lack of an appropriate substrate. These strain-based transitions are shown through tight-binding calculation in Fig. 5.1.

Under compressive strain, the inverted conduction band (Γ^-_7) has its behavior near the K and Γ points slightly modified (Fig. 5.1(a)). A gap is created in all directions

other than the $\Gamma - Z$ direction, where a Dirac node is formed (Fig. 5.1(b)). Under tensile strain, the inverted conduction band (Γ_7^-) is modified as well (Fig. 5.1(c)). A global band gap opens, forming a 3D topological insulator (Fig. 5.1(d)). Strain also induces some warping at the valence band maximum ($\Gamma_{8,v}^+$). In general, increasing the magnitude of biaxial strain in α-Sn(001) increases the size of the band gap (TI) or spacing between bulk Dirac nodes (DSM).

The effect of quantum confinement on α-Sn thin films has also been of much interest. Compressive strained ultrathin films have been suggested to be a 3D TI [106–108] or 2D TI [207] when grown on InSb(001), a 2D DSM [213] or 2D TI [211, 242] when grown on InSb(111), or a 2D TI phase coexistent with unconventional superconductivity when grown on PbTe(111)/Bi_2Te_3(0001) [243]. Many of these studies involve either surface dosing or bulk doping with Te or Bi to improve surface quality and electron-dope the (usually degenerately p-type doped) films [107, 108, 212], which could have unexpected effects on the surface electronic structure and has been consistently measured to modulate at least the band velocity of the topological surface states [206, 209, 214].

The tunability between these phases in α-Sn make it an interesting testbed for topological phase transitions. There are a limited number of topological materials which may be grown as high quality thin films, especially at the ultrathin limit where quality usually degrades. The most comprehensive work is on HgTe, an inversion symmetry broken analogue to α-Sn, where multiple phase transitions as a function of confinement and strain (analogous to α-Sn) have been observed [34, 244–249]. In addition to HgTe, the effect of confinement and/or strain has been studied to a lesser degree in $(Cd,Zn)_3As_2$ [250, 251], Na_3Bi [252], and $(Sb,Bi)_2(Se,Te)_3$ thin films [253–255], each with their own intricacies. These, typically compound, materials are prone to point defects (specifically anti-site defects) and it can be difficult to achieve the desired stoichiometry or chemical potential, which can sometimes be solved via alloying, doping, or electrostatic gating. α-Sn, as an

elemental semimetal/semiconductor, should not suffer from issues with alloy disorder, off-stoichiometry, or other related issues seen in compound and alloy topological materials. Particularly interesting for spintronic applications, α-Sn has shown very efficient spin-charge conversion at room temperature (Chapter 1).

Although there has been much interest in α-Sn, there are still open questions in the band structure which we seek to answer here. In early band structure measurements of α-Sn thin films via cyclotron resonances in magnetotransport and magnetotransmission [227] and angle-resolved photoemission spectroscopy [256–259], the presence of topological surface states was not observed. More recent studies have observed the presence of one [107, 108, 208], two [212], or three [209] surface states in the region where the topological surface state is expected to appear. These results involve the use Bi [108,208] or Te [107,170,212] as a dopant/surfactant. Only one of these surface states has been measured to have non-zero spin polarization consistent with a topological surface state [108, 212]. The location of the Dirac node of the topological surface state in α-Sn(001) is subject to disagreement as well. The crossing is commonly calculated to be in the middle of the $\Gamma_{8,v}^{+}$-Γ_{7}^{-} gap, independent of film thickness [107, 209, 260], while many experiments find the crossing to be significantly closer to the valence band maximum, if not above the valence band maximum [170, 206, 209]. There are limited direct measurements of the distance between the surface state Dirac node and the valence band maximum at the $\mathbf{\Gamma}$ point.

Our primary focus in this chapter is to investigate the number, the nature, and the dispersion of surface states of compressive strained α-Sn/InSb(001) via spin- and angle-resolved photoemission spectroscopy (SARPES and ARPES). We first investigate the relationship between the dispersion of the surface states and the bulk bands in ultrathin films where confinement effects are strong. The existence of only two surface states near the valence band maximum is confirmed, both of which terminate in the confinement-

induced bulk band gap. Only these two surface states are present across a large range of film thicknesses investigated here. We further measure an additional band inversion and topological surface state deep below the Fermi level, consistent with the work of Rogalev *et al.* [170]. Interestingly, *both* of the observed surface states near E_F are revealed to be spin-polarized with the expected ideal orthogonal spin-momentum locking and opposite helicities. Furthermore, the growth procedure used (Chapter 4) results in high quality α-Sn films without additional extrinsic dopants, emphasizing that the features observed here are intrinsic to α-Sn. Our results clarify the surface and bulk electronic structure of α-Sn and challenge the results of many calculations. The presence of two surface states with opposite polarization has an important bearing on future spin-charge conversion measurements as the position of the surface Fermi level can drastically change the spin polarization of the Fermi surface and thus the spin-charge conversion efficiency.

5.2 Methods

Thin films of α-Sn were grown on both the indium rich c(8×2) and the antimony rich c(4×4) reconstruction of InSb(001) as discussed in our earlier work [206]. Variable growth temperature and rates were used, as described in Chapter 4. In this chapter, a single 13 BL film and a single 50 BL film are studied. Four different 400 BL films labelled 400 BL-A,B,C,D are studied as well. The surface reconstruction of α-Sn films as measured by reflection high energy electron diffraction generally showed the mixed (2×1)/(1×2) reconstruction, except 400 BL-B which showed a (2×2) reconstruction. Tight-binding calculations were performed in the Chinook framework [167] with parameters slightly modified from those reported in Ref. [170] which were themselves extracted from Ref. [94].

Strain was incorporated using Harrison's d^2 rule and a modified Harrison's rule for group IV semiconductors [169]. The tight-binding calculation gives good agreement in

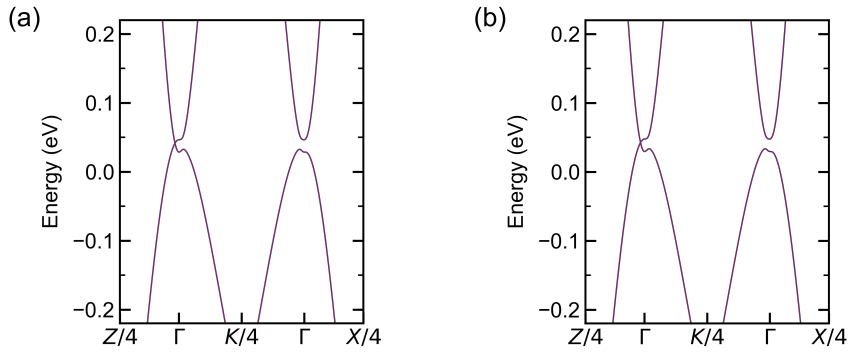

Figure 5.2: Tight-binding calculations near the charge neutrality point using (a) Harrison's d^2 rule and (b) a version of Harrison's rule with modified exponents scaling the hopping parameters.

Dirac node spacing with experimental results [241], as shown in Fig. 5.2. α-Sn on InSb(001) has much smaller compressive strain than that shown in Fig. 5.1. Under the 0.15% compressive strain in this system, the spacing between Dirac nodes is small ($\Delta k_z = 0.016$ Å^{-1} in Fig. 5.2(a)), close to that found experimentally [241] and half of that found via first principles [209].

Strain was incorporated using Harrison's d^2 rule which has been shown to fail for Ge and Si where higher order exponents are more accurate; the exact exponent depends on the hopping term [169]. While the exponents for a modified Harrison's rule have not been explicitly worked out for α-Sn, we estimate they will be at least as large as those for Ge. Using the exponents for Ge found in Ref. [169], as shown in Fig. 5.2(b), there is no significant change in the calculated band structure (Δk_z increases by <1%). Since higher order exponents do not measurably modify the computed band structure, for simplicity Harrison's d^2 rule is used for the remainder of this work.

Structural characterization of some α-Sn films showed high quality films fully strained to the InSb(001) substrate is given in Fig. 5.3. While the critical thickness of α-Sn/InSb(001) has been shown to be much greater than the thicknesses investigated here (on the order of 500 nm [101]), the growth of high quality α-Sn is very sensitive to sub-

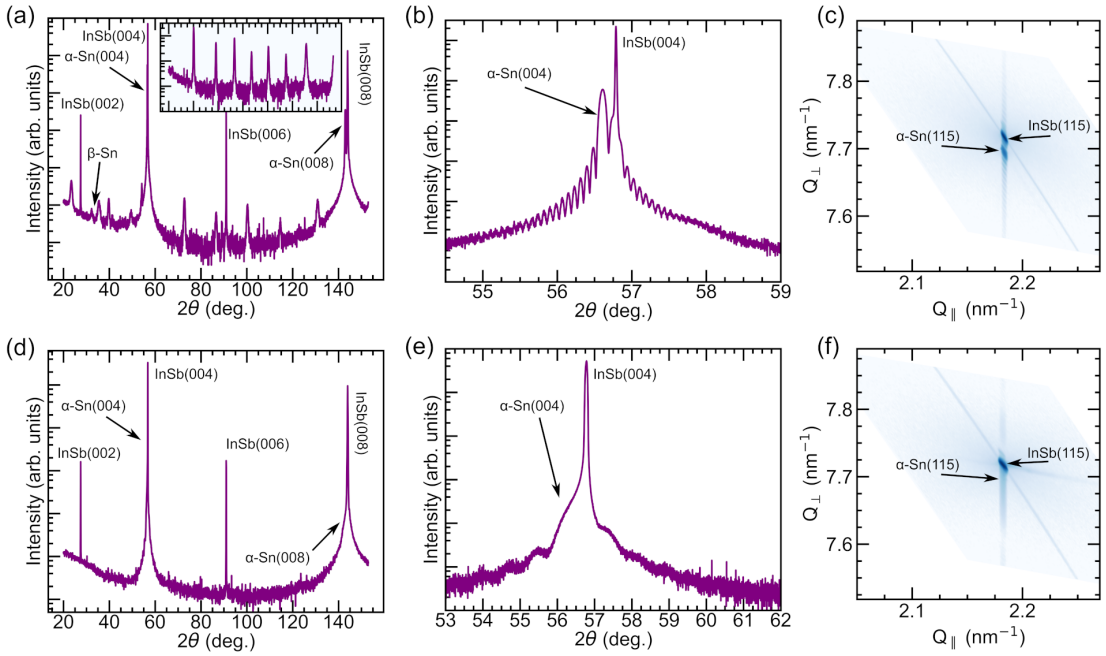

Figure 5.3: X-ray diffraction of α-Sn/InSb(001) taken using Cu Kα1 radiation. Measurements on sample 400 BL-D (a) a large range on-axis $2\theta/\omega$. Inset: Identical measurement of the sample holder used for this measurement. (b) A zoom in of the region near the InSb(004) peak. (c) Reciprocal space map in the region of InSb(115). (d)–(f) the same measurements as (a)–(c) but on a 54 BL α-Sn film.

strate preparation and growth conditions and thus must be verified. Investigating first the structure of 400 BL α-Sn in the sample 400 BL-D (Fig. 5.3(a)), the α-Sn peaks are clear. There are numerous peaks visible from the tungsten sample holder, shown in the inset. There is a small β-Sn(101) peak visible near 32°. No other orientations of β-Sn or subphases indicative of major interreactions between Sn and InSb are visible. This sample was indium bonded to the tungsten sample holder, so it could not be removed without converting the α-Sn to β-Sn (melting the indium).

In Fig. 5.3(b) a zoom-in near the α-Sn(004) peak is shown. The out-of-plane lattice constant is found to be 6.4984 Å, in excellent agreement with other work using computed elastic tensors for pseudomorphic growth of α-Sn/InSb(001) [240]. In the reciprocal space map in Fig. 5.3(c), it is clear that the film is fully strained to the InSb substrate with

the reference lattice constant of 6.479 Å. For the 54 BL film, there is no evidence of any β-Sn formation or other subphase formation (Fig. 5.3(d)). The 54 BL film, as expected, remains fully strained to the InSb substrate (Fig. 5.3(f)).

ARPES measurements were taken at beamline 5-2 at Stanford Synchrotron Radiation Lightsource (SSRL) with s- or p-polarized light or taken at beamline 10.0.1.2 at the Advanced Light Source (ALS) with p-polarized light or He1α light (21.2 eV) using a monochromatized helium electron cyclotron resonance (ECR) plasma source. Light was directed along the $\langle 1\bar{1}0 \rangle$ direction for all measurements. At both beamlines, data were taken using a Scienta Omicron DA30L detector. The sample temperature was kept below 20 K and the base pressure during measurement was lower than 3×10^{-11} Torr. The samples were transferred from the growth systems at UCSB to SSRL and ALS using a custom designed ultrahigh vacuum suitcase with base pressure lower than 4×10^{-11} Torr.

Spin-resolved measurements were performed at beamline 10.0.1.2 using Ferrum spin detectors [153]. The spin texture is measured in three orthogonal directions $(\hat{x}, \hat{y}, \hat{z})$ which are parallel with our (k_x, k_y, k_z) axes. The spin polarization was calculated from measured spin-resolved energy distribution curves (EDCs) by the usual equation $P = \frac{1}{S}\frac{I_\uparrow - I_\downarrow}{I_\uparrow + I_\downarrow}$, where the Sherman function $S = 0.22$. The error bars in polarization are calculated from propagated error in the polarization equation assuming Poisson statistics and neglecting error in the Sherman function. The sign of P_Y and the Sherman function were validated on bismuth thin film calibration samples. The angular acceptance window and energy window of the spin-resolved measurements is variable, but typically set at 1° and 40 meV.

5.3 Results

5.3.1 Dispersion near bulk Γ

The bulk-like electronic structure is calculated via tight-binding in Fig. 5.4(a). The slight compressive strain from growth of α-Sn on InSb(001) does not modify the dispersion strongly other than the behavior near the quadratic touching point (Fig. 5.1). The band structure is consistent with the expected gapless semiconductor with band inversion.

The highest energy band depicted is the p-like $\Gamma_{8,c}^{+}$ band. This band is inverted from its usual character (in the parlance of the Ge band structure, it is the light hole band). It is degenerate at the $\mathbf{\Gamma}$ point with the first valence band, the $\Gamma_{8,v}^{+}$ band, which has the p-like heavy hole (HH) character. The second valence band is the s-like Γ_{7}^{-} band, the inverted conduction band. The band inversion in α-Sn is between the $\Gamma_{8,c}^{+}$ and the $\Gamma_{8,v}^{+}$ band. The third valence band is the p-like Γ_{7}^{+} split-off band. The band shapes agree with other calculations [88, 209, 261]. However, there is still some slight contention in the shape of Γ_{7}^{-} band near its maximum. Some calculations [107, 209, 261, 262](in addition to Fig. 5.4(a)) suggest a dimple-like warping away from the parabolic-like dispersion while others [88, 94] do not. The presence of this warping has important ramifications for critical point measurements and excitonic effects in this material [240]. The shape of this band is very sensitive to spin-orbit splitting in the system [240], and thus sensitive to how spin-orbit coupling is taken into account in the given calculation.

Since the features of interest in α-Sn are near the $\mathbf{\Gamma}$ point, we first clarify the band dispersion of both the bulk bands and surface states here, summarized in Fig. 5.4(c)–(e). These measurements are performed on a 13 BL film which is expected to be in a 3D TI or 2D TI phase [106–108, 207]. In order to deconvolute any matrix element effects in the band structure we investigate the $\mathbf{\Gamma_{003}}$ and $\mathbf{\Gamma_{002}}$ points with both s- and p-polarized light. Matrix elements are usually defined within both the sudden and the

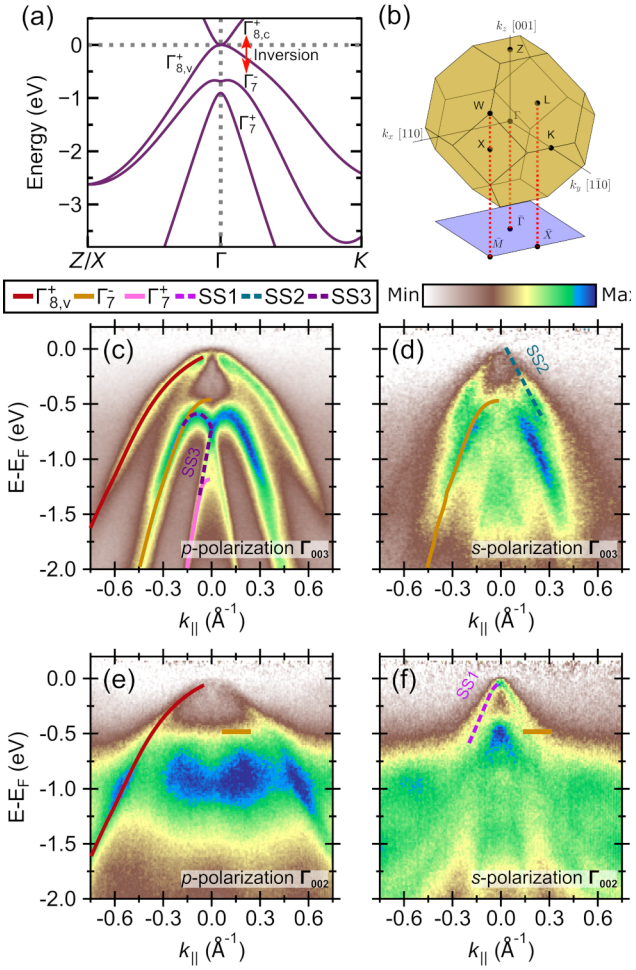

Figure 5.4: (a) Electronic structure of α-Sn as calculated by the tight-binding model modified from [170]. The band inversion is indicated. (b) Bulk and surface Brillouin zone for the (001) orientation of α-Sn. ARPES measurements on 13 BL of α-Sn at (c) $\mathbf{\Gamma_{003}}$ with p-polarized light (d) $\mathbf{\Gamma_{003}}$ with s-polarized light (e) $\mathbf{\Gamma_{002}}$ with p-polarized light and (f) $\mathbf{\Gamma_{002}}$ wth s-polarized light. $\mathbf{\Gamma_{003}}$ corresponds to $h\nu$=127 eV and $\mathbf{\Gamma_{002}}$ corresponds to $h\nu$=55.8 eV. Guides to the eye for surface states and valence bands are indicated. Horizontal lines correspond to the maximum of the associated band. All measurements are along the $\overline{X}-\overline{\Gamma}-\overline{X}$ direction.

dipole approximations and assuming noninteracting electrons [145, 146]. This results in the one electron dipole matrix element

$$M_{f,i}^{\mathbf{k}} = \langle \phi_f^{\mathbf{k}} | H_{int} | \phi_i^{\mathbf{k}} \rangle \tag{5.1}$$

where $\phi_f^{\mathbf{k}}$ is the final state of the photoelectron, $\phi_i^{\mathbf{k}}$ is the initial state of the photoelectron, and H_{int} is the Hamiltonian representing the electron-photon interaction [146]. The intensity of the measurement is proportional to the squared matrix element $I(k, h\nu) \propto |M_{f,i}^{\mathbf{k}}|^2$ while the initial state $\phi_i^{\mathbf{k}}$ is the feature of interest in our measurements [146]. The final state $\phi_f^{\mathbf{k}}$ of the photoelectron is usually assumed to be free electron-like with even symmetry; the symmetry of H_{int} varies by the polarization of light being used; the symmetry of the initial state depends on the geometry of the measurement and orbital character of the excited band [145]. From these arguments, tuning the polarization of incident light in the ARPES measurement elucidates the character of a given band [145].

Tight-binding calculations of matrix element effects in α-Sn for p- and s-polarized illumination are shown in Fig. 5.5. The same tight-binding model discussed earlier was used as the initial state, while a free electron final state was assumed. The calculation replicates the measured high intensity of the heavy hole valence band ($\Gamma_{8,v}^{+}$) band with p-polarized light in Fig. 5.4, in contrast with other calculation/experiment [170]. The conduction band has low intensity no matter the polarization of incident light. There is a vanishing intensity of the heavy hole valence band near the Γ point for p-polarized light, indicating that the similar feature observed in the measured ARPES data is due to a matrix element effect rather than a hybridization effect.

The photon energies corresponding to the $\mathbf{\Gamma_{003}}$ and $\mathbf{\Gamma_{002}}$ points are derived from the relation

$$k_z = \frac{\sqrt{2m_0}}{\hbar} \sqrt{E_k - \frac{\hbar^2}{2m_0} k_{||}^2 - V_0} \tag{5.2}$$

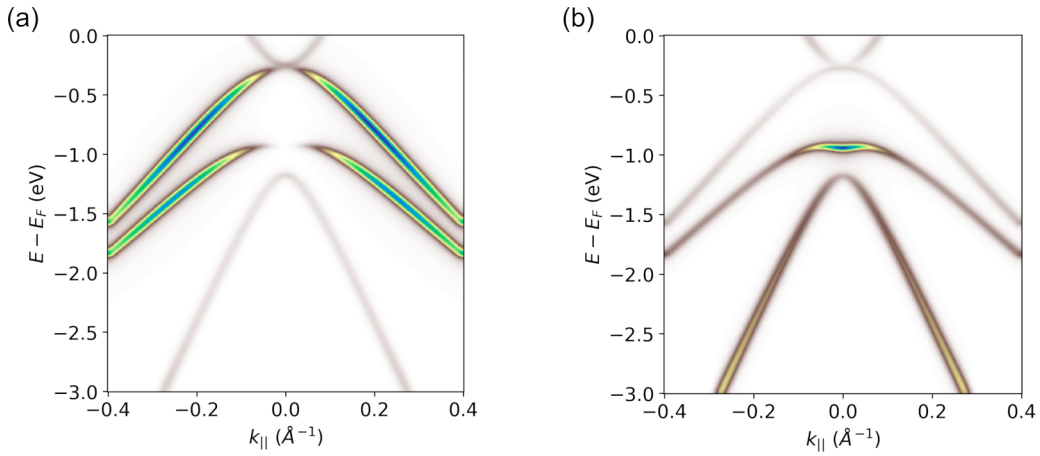

Figure 5.5: Representative calculated ARPES measurements along $K - \Gamma - K$ with a free electron-like final state using (a) p-polarized light and (b) s-polarized light. The Fermi level is artificially offset to show polarization effects on the conduction band. Tight-binding alculations were performed in *chinook* [167] with the assistance of Paul Corbae.

using the inner potential model which assumes free electron-like final states (Chapter 2) [145, 146]. The inner potential, V_0, used currently is 5.8 eV [170], but another derived inner potential of 9.3 eV [209] does not change the expected dispersion significantly. Since all data in Fig. 5.4(c)–(e) were taken at the $\mathbf{\Gamma}$ point, the dispersion of the bands in Fig. 5.4(c)–(e) is identical but matrix element effects shift the relative intensity of certain bands. The linear dichroism between s- and p-polarized light is not consistent between measurements at $\mathbf{\Gamma_{003}}$ (Fig. 5.4(c) vs. Fig. 5.4(d)) and at $\mathbf{\Gamma_{002}}$ (Fig. 5.4(e) vs. Fig. 5.4(f)). The only shared feature is increased intensity of the $\Gamma^+_{8,v}$ heavy hole band using p-polarized light. This indicates that at these photon energies, linear dichroism cannot be treated as a direct probe of orbital characters for the valence bands in α-Sn. Since the initial state ($\phi_i^{\mathbf{k}}$) and H_{int} are unchanged, only a change in the final state can then explain the varying matrix element behavior at different photon energies. Final state effects are then likely significant in ARPES measurements of this system.

In Fig. 5.4(c), all of the valence bands are visible and agree with their expected dispersion from the calculations (Fig. 5.4(a)). Starting from high binding energy, the

split-off band has its maximum 1.1 eV below the Fermi level. There is an additional band inversion in between the split-off band Γ_7^+ and the inverted conduction band Γ_7^-, discussed in detail in Ref. [170] which results in an additional surface state deep below the valence band maximum. This topological surface state, the **M**-shaped SS3, (labeled TSS2 in prior work [170, 209]) arises from the split-off band and joins the inverted conduction band near $k_{||} = \pm 0.15$ Å^{-1}.

The maximum of the inverted conduction band is not visible here due to matrix element effects. Past the $k_{||}$ extent of SS3, an additional surface state arises from the inverted conduction band. This surface state then disperses up to the valence band maximum, where it is difficult to distinguish the surface state from the heavy hole band. The heavy hole band ($\Gamma_{8,v}^+$) is then visible as the outermost band. The maximum of the heavy hole band is indicated and notably around 90 meV below the Fermi level. By keeping the measurement at $\mathbf{\Gamma_{003}}$ and switching to *s*-polarization (Fig. 5.4(d)), the linear-like surface state (SS2) arising from the inverted conduction band is visible. It disperses up to the Fermi level as indicated. The maximum of the inverted conduction band (Γ_7^-) is also now clearer. No warping of any kind is visible. The difference between the Γ_7^- and $\Gamma_{8,v}^+$ band maxima is 390 meV in close agreement with the 410 meV measured by other techniques [240].

We next move to a measurement with *p*-polarized light at $\mathbf{\Gamma_{002}}$(Fig. 5.4(e)). Only the heavy hole band is clear here. A faint intensity corresponding to the inverted conduction band can be seen. Switching to *s*-polarization at the $\mathbf{\Gamma_{002}}$ point (Fig. 5.4(f)), a surface state again disperses toward the Fermi level from the inverted conduction band (Γ_7^-). This surface state (SS1) is not the same surface state measured in Fig. 5.4(d) (SS2), investigated in more detail in the next paragraphs. The inverted conduction band is visible, perhaps with a slightly lower effective mass near the band maximum than expected from the $\mathbf{\Gamma_{003}}$ measurement. This could be the result of a narrowing of this band near

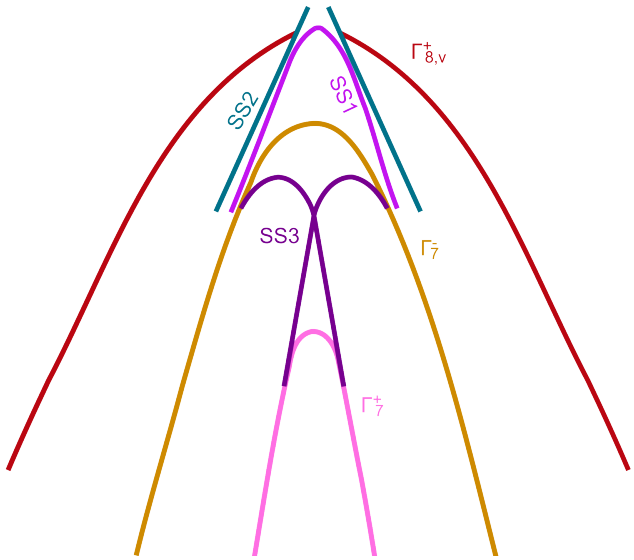

Figure 5.6: Schematic summarizing the measured bulk and surface bands in the $\overline{X} - \overline{\Gamma} - \overline{X}$.

its maximum as is seen in the analogous HgTe band structure [249]. A schematic of the measured bulk bands and surface states is given in Fig. 5.6.

To have a clearer picture of the surface state and bulk dispersion near the Fermi level (and valence band maximum) measurements were performed in the same conditions as Fig. 5.4 but in a smaller binding energy range (Fig. 5.7). In Fig. 5.7(a) the dispersion of the heavy hole band and surface states is shown using p-polarized light at $\mathbf{\Gamma_{003}}$. The guides to the eye shown here are derived from later panels. By keeping the same polarization and switching to $\mathbf{\Gamma_{002}}$ in Fig. 5.7(b), only the heavy hole band has high intensity. A guide to the eye is shown to indicate the parabolic-like dispersion. The valence band maximum is roughly 90 meV below the Fermi level. A summary of the various band positions derived for the 13 BL film is given in Table 5.1.

There is a vanishing intensity of the heavy hole band at $\mathbf{\Gamma}$, which is visible in films of comparable thickness to ours in Ref. [170] and films of unknown thickness in Ref. [107]. We do not observe the heavy hole band with measurable intensity using s-polarized light so it is unclear whether this is a matrix element effect specific to the use of p-polarized

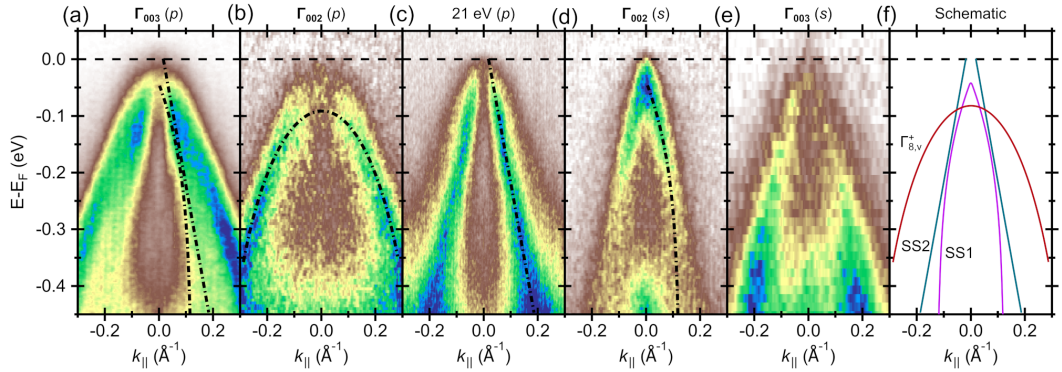

Figure 5.7: ARPES measurements close to E_F at (a) $\mathbf{\Gamma_{003}}$ with p-polarization (b) $\mathbf{\Gamma_{002}}$ with p-polarization (c) $h\nu$=21 eV with p-polarization (d) $\mathbf{\Gamma_{002}}$ with s-polarization (e) $\mathbf{\Gamma_{003}}$ with s-polarization. Guides to the eye are drawn in black. A schematic summarizing the guides to the eye is shown in (f). All measurements are along the $\overline{X}-\overline{\Gamma}-\overline{X}$ direction. $\mathbf{\Gamma_{003}}$ corresponds to $h\nu$=127 eV and $\mathbf{\Gamma_{002}}$ corresponds to $h\nu$=55.8 eV.

light, or a feature pertaining directly to the initial state. Changes to the initial state away from the expected parabolic-like band could be from strain-induced distortions calculated via tight-binding and $k\cdot p$ models [170, 240], however in our calculations we find—for the moderate strains induced by the -0.15% strain in this system—the bowing is quite small compared to experiment (Fig. 5.2). A tight-binding calculation of the ARPES spectra, including matrix element effects partially replicates this missing intensity feature (Fig. 5.5). Furthermore, quantum well states derived from the heavy hole band (discussed further in Section 5.3.4) retain this missing intensity at $\overline{\mathbf{\Gamma}}$. It is thus likely the missing intensity derives mostly from matrix element effects.

Table 5.1: Energies corresponding to band maxima at $\mathbf{\Gamma}$(for bulk bands) and surface state crossings (for surface states) referenced to E_F in the 13 BL film.

	SS1	SS2 (fit)	SS3	$\Gamma^+_{8,v}$	Γ^-_7	Γ^+_7
$E-E_F$ (eV)	-0.05	0.04	-0.72	-0.09	-0.48	-1.17

In order to investigate the surface state structure of α-Sn in more detail, photon energies in the range of 17-23 eV are frequently used. We use $h\nu$=21 eV (Fig. 5.7(c))

in order to better compare to reports in the literature at similar photon energies. This photon energy results in a k_z value either halfway between the $\mathbf{\Gamma_{001}}$ and $\boldsymbol{Z}$ points (using an inner potential of 5.8 eV [170]) or an additional ∼10% closer to the $\boldsymbol{Z}$ point (using an inner potential of 9.3 eV [209]). Referencing the tight-binding calculations in Fig. 5.4(a) and the heavy hole maximum (Table 1), the highest lying bulk band in a $h\nu$=21 eV measurement should be the heavy hole band ($\Gamma^{+}_{8,v}$), which should have its maximum ∼1.5 eV below the Fermi level. As Fig. 5.7(c) only probes 500 meV below the Fermi level, no bulk bands should be visible in this measurement. This measurement is dominated by a linear surface state (SS2) which has a crossing ∼37 meV above the Fermi level.

In Fig. 5.7(d) at $\mathbf{\Gamma_{002}}$ with s-polarization, a different surface state (SS1) has significant intensity. SS1 has a crossing ∼50 meV below the Fermi level (and thus ∼40 meV above the valence band maximum). We do not see any evidence of an upper branch to this surface state as would be expected in a Dirac-like topological surface state, however this could arise from the proximity of the crossing to the Fermi level. There does not appear to be any significant anticrossing-like behavior as the surface states disperse through the heavy hole band. Finally, at the $\mathbf{\Gamma_{003}}$ point with s-polarization (Fig. 5.7(e)), the linear SS2 can be seen with a dispersion closely matching the guide to the eye in Fig. 5.7(c).

A schematic summarizing the dispersion of the bands observed in 13 BL α-Sn is given in Fig. 5.7(f). Importantly, we observe only two surface states in ultrathin α-Sn(001); both states disperse into the bulk band gap transitioning from surface resonances to true surface states. Of these two surface states, the dispersion of SS2 is more consistent with that of a Dirac-like topological surface state.

5.3.2 Clarification to the number of surface states in α-Sn(001) films

Generally VUV measurements far from the $\mathbf{\Gamma}$ point in α-Sn(001) show evidence of three states which are associated with either three surface states [209] or two surface states and a bulk band [212]. These observations span a large range of film thicknesses such that quantum confinement effects are likely not in play. While three bands are visible in our $\mathbf{\Gamma_{003}}$ measurement with p-polarization in Fig. 5.7(a) (SS1, SS2, and HH), only SS2 is readily visible with p-polarization in Fig. 5.7(c). A series of momentum distribution curves (MDCs) taken from the measurement in Fig. 5.7(c) are plotted in Fig. 5.8(a). The lineshapes are consistent with those presented in Ref. [212] and indicative of three bands. The two innermost states correspond to SS1 and SS2, but the identification of the outermost state is unclear. These MDCs are then plotted against MDCs taken from Fig. 5.7(b) where primary intensity is due to the heavy hole band. The outermost peak in the MDCs from the $\mathbf{\Gamma_{002}}$ measurement, which corresponds to the heavy hole band, lines up with the outermost peak in the MDCs from the $h\nu$=21 eV measurement. This indicates the third and outermost peak seen in these VUV measurements could actually be the heavy hole band.

This is verified by performing a three band fit to the MDCs of the $h\nu$=21 eV data and a two band fit to the MDCs of the $\mathbf{\Gamma_{002}}$ data, summarized in Fig. 5.8(b). The peaks are fit to a Voigt lineshape where the Gaussian component is fixed at the experimental momentum resolution. The fit is constrained such that there is approximate symmetry of the peak locations, amplitudes, and FWHMs across $\overline{\Gamma}$. The magnitude of the error bars for the peak locations in the three band fit are typical for the fits to peak location in the rest of this chapter. We exclude the error bars (always less than 0.01 Å) from other plots for clarity. The outermost state in the two fits in Fig. 5.8(b) lines up almost

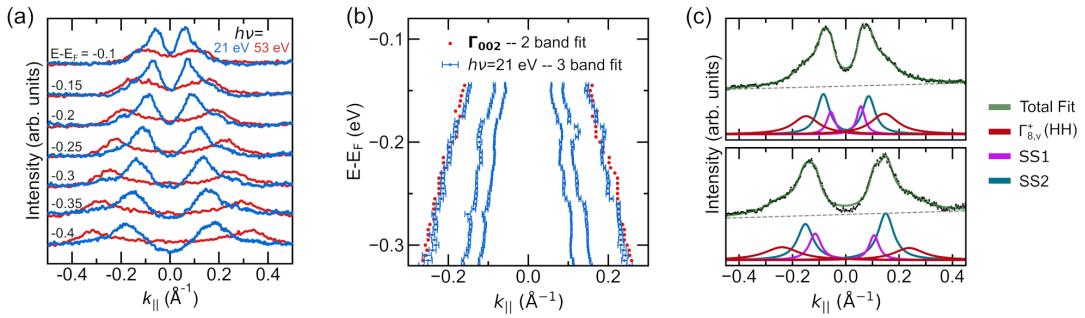

Figure 5.8: Detailing the number of surface states in ultrathin α-Sn. (a) Representative momentum distribution curves (MDCs) from the $h\nu$=21 eV measurement in red and the $\mathbf{\Gamma_{002}}$ measurement in blue. MDCs are integrated over 10 meV. (b) Fit peak locations for a 3 band fit for the $h\nu$=21 eV measurement (red) and a 2 band fit for the $\mathbf{\Gamma_{002}}$ measurement (blue). (c) Representative three band fits to the MDCs from the $h\nu$=21 eV measurement corresponding to *top*: E-E$_F$=150 meV and *bottom*: E-E$_F$=305 meV.

exactly, confirming that the three states seen in our VUV measurement are SS1, SS2, and the HH band. Repfresentative three band fits to the $h\nu$=21 eV measurement, showing its suitability for the given system are given in Fig. 5.8(c) for 150 meV and 305 meV binding energy. While these identifications have been confirmed in ultrathin films, we would like to show this is a global effect for the α-Sn(001) surface independent of film thickness.

In order to clarify this point further, 400 BL α-Sn films are investigated. At this thickness, there should not be significant confinement effects and the films are expected to be in the 3D DSM phase [207, 209, 210]. The measurement with p-polarization at $h\nu$=21 eV is shown in Fig. 5.9(a) on 400 BL-A where the presence of three tightly dispersing states can now be clearly seen, all crossing the Fermi level. The surface state crossings and valence band maximum are 50–100 meV above E$_F$.

In Fig. 5.9(b) the dispersion at the $\mathbf{\Gamma_{002}}$ point is shown. The heavy hole band is clearly resolved, while the surface states are broad and difficult to observe. Fits are performed on the MDCs of these measurements to more precisely compare their shapes.

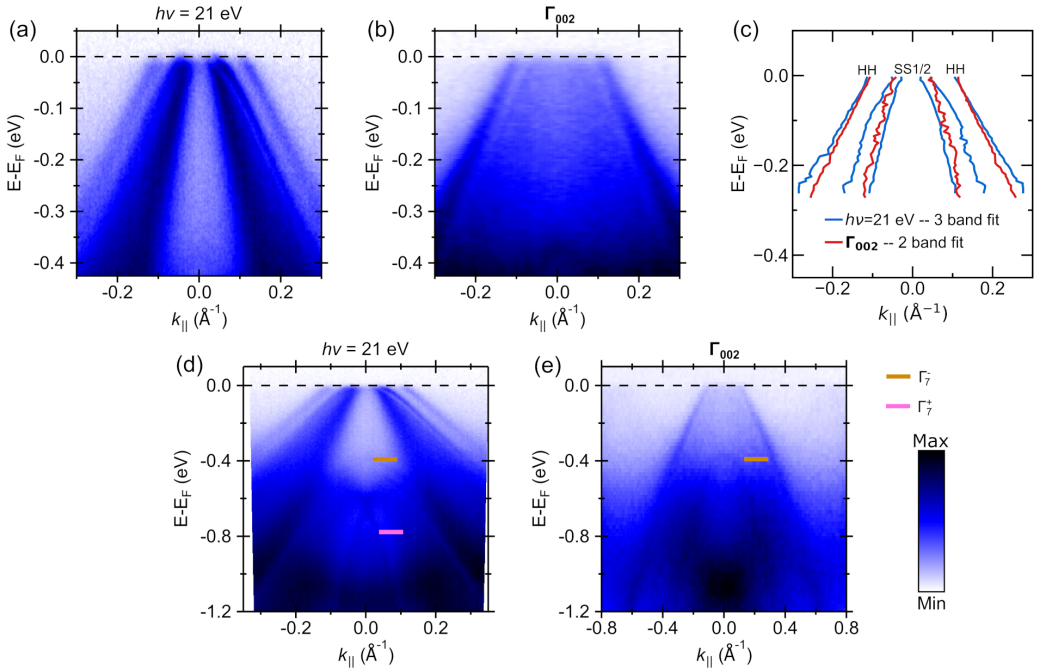

Figure 5.9: Detailing the number of surface states in thick α-Sn. ARPES measurements at (a) $h\nu$=21 eV and (b) $\mathbf{\Gamma_{002}}(h\nu$=53 eV) for a 400 BL film (400BL-A) along the $\overline{X}-\overline{\Gamma}-\overline{X}$ direction (c) Fit peak locations for a 3 band fit for a $h\nu$=21 eV measurement (red) and a 2 band fit for the $\mathbf{\Gamma_{002}}$ measurement (blue). (d) Wider binding energy range of the measurement in (a). (d) Wider binding energy/momentum range of the measurement in (b). Horizontal colored lines correspond to bulk band maxima. All measurements were performed with p-polarized light.

A three band fit is performed for the $h\nu$=21 eV measurement. We could not perform a robust three band fit to the $\mathbf{\Gamma_{002}}$ data due to the lack of sharpness of the bands. Instead, we perform a two band fit with the expectation one of the bands will essentially average SS1 and SS2.

The fit dispersions are summarized in Fig. 5.9(c) where this assumption is shown to be correct. The outermost band in both fits lie almost directly on top of each other. Thus, the outermost state measured in ARPES of both thin and thick films of α-Sn(001) using VUV light is likely the heavy hole band at $\mathbf{\Gamma}$ rather than a third surface state, even though the k_z value estimated using the inner potential model disagrees quite strongly with this explanation.

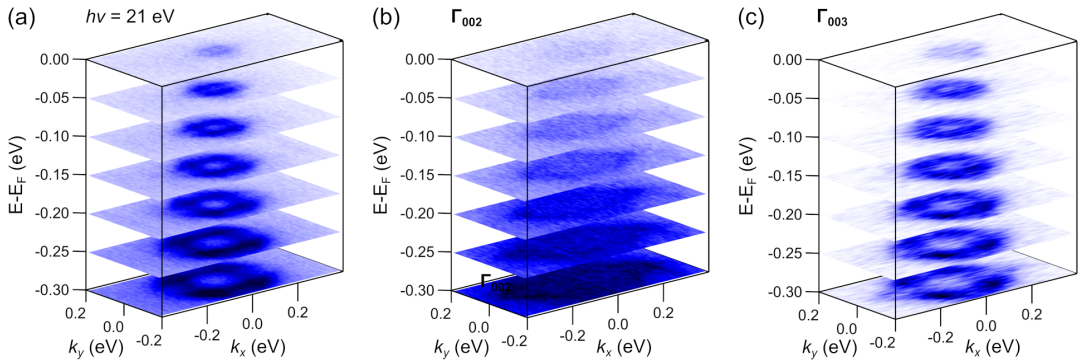

Figure 5.10: Constant energy countours taken at (a) $h\nu$=21 eV, (b) $\mathbf{\Gamma_{002}}$ ($h\nu$=53 eV) and (c) $\mathbf{\Gamma_{003}}$ ($h\nu$=127 eV)for a 400 BL film (400BL-B) with p-polarized light. Contours were integrated over a 10 meV window.

If the $h\nu$=21 eV measurement is sampling the heavy hole at $k_z = 0 \times \frac{4\pi}{c}$, ostensibly it should sample the other bulk bands at $k_z = 0 \times \frac{4\pi}{c}$ as well. A wider energy range of the $h\nu$=21 eV measurement is shown in Fig. 5.9(d). The maximum of the inverted conduction band is hazily visible 390 meV below E_F. This location agrees with a more direct measurement of the Γ_7^- band maximum at the $\mathbf{\Gamma_{002}}$ point in Fig. 5.9(e). Using the Γ_7^--$\Gamma_{8,v}^+$ spacing derived earlier for the 13 BL film, the valence band maximum would be only 20 meV above the Fermi level. Likewise, the inverted conduction band (Γ_7^-) is visible with its expected $\mathbf{\Gamma}$ point dispersion. The node of SS3 is approximately 630 meV below the Fermi level. A gap in intensity can be seen in between the node of SS3 and the maximum of the split-off band (Γ_7^+). The maximum of the split-off band is 385 meV below the maximum of the Γ_7^- band. The dispersion of the Γ_7^- band agrees with that shown in Fig. 5.4(d), appearing parabolic-like with minimal warping.

So far we have only investigated the appearance of the unexpected $\mathbf{\Gamma}$ point dispersion using $h\nu$=21 eV along the $\overline{X} - \overline{\Gamma} - \overline{X}$ direction. In Fig. 5.10, constant energy contours of 400 BL-B α-Sn are plotted. In Fig. 5.10(a) for $h\nu$=21 eV, SS1 and SS2 have the highest intensity. SS1 appears to nearly isotropic. The exact dispersion of SS2 is difficult to resolve, but it appears less isotropic with maximum intensity along the $\overline{M} - \overline{\Gamma} -$

$\overline{M}$ direction (four-fold symmetry). Finally the heavy hole band appears as a broad background at higher k than SS1 and SS2. It also appears four-fold symmetric, as would be expected for the heavy hole band. In Fig. 5.10(b) for the $\mathbf{\Gamma_{002}}$ measurement, only the heavy hole band is visible, matching the broad background in Fig. 5.10(a). This contour retains the expected four-fold symmetry. Finally in the measurement at $\mathbf{\Gamma_{003}}$(Fig. 5.9(c)), SS1 and SS2 have the same contours as in Fig. 5.9(a), but here the intensity of the heavy hole band is greater. The contour of the heavy hole band agrees with the $\mathbf{\Gamma_{002}}$ and $h\nu$=21 eV measurements as well. The measured contours for the heavy hole band in Fig. 5.10 The measured constant energy contours of the heavy hole band also show good agreement with tight-binding calculations of the predicted constant energy contours using p-polarized light in Fig. 5.11.

Calculations of the constant energy contours using p-polarized light (Fig. 5.11(a)) show that the conduction band can appear two-fold symmetric from matrix element effects even when the band itself if four-fold symmetric. The heavy hole valence band shows the expected four fold symmetry with matrix element effects modulating the intensity to be two-fold symmetric. A weaker version of this intensity modulation is observed in Fig. 5.10. Using s-polarization, as shown in Fig. 5.11(b), removes the intensity modulations.

Thus, the ARPES measurements of α-Sn(001) with VUV light deviate strongly from the inner potential model using the generally accepted values of the inner potential. Possible origins for this discrepancy are discussed further in Section 5.4.1.

5.3.3 Spin-polarized ARPES of the surface states near the valence band maximum in α-Sn(001)

To help identify the character of the surface states (SS1 & SS2) we performed spin-resolved ARPES measurements on the same sample 400 BL-A. Spin polarization was

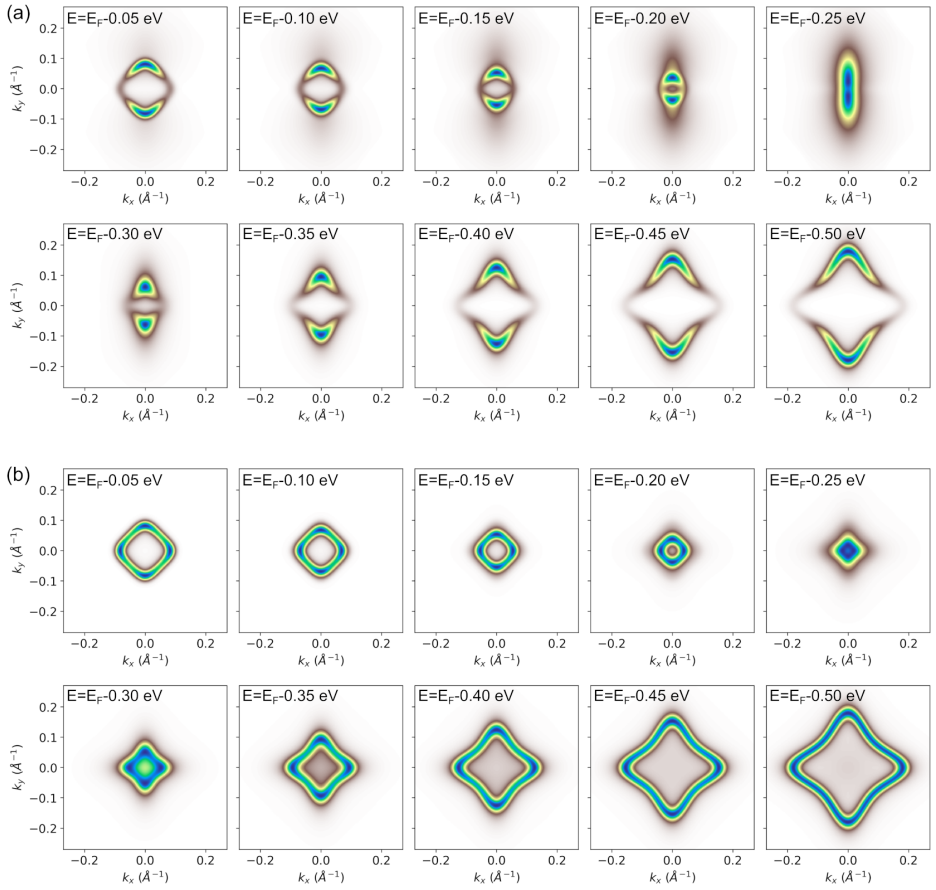

Figure 5.11: Representative calculated constant energy contours with a free electron–like final state using (a) *p*-polarized light and (b) *s*-polarized light. The Fermi level is artificially offset to the level in Fig. 5.5. The geometry is the same as depicted in Fig. 5.4. Calculations were performed in *chinook* [167] with the assistance of Paul Corbae.

investigated in the $(\hat{x}, \hat{y}, \hat{z})$ directions summarized in Fig. 5.12. The EDCs along which spin polarization was measured are indicated in Fig. 5.12(a). A constant energy contour corresponding to E-E_F = −0.1 eV in Fig. 5.10(b) is shown in Fig. 5.12(b). At large k_x (Fig. 5.12(c)) there is negligible spin polarization in the $\hat{z}$ direction. There is a very slight spin polarization at high binding energy at positive k_x, but the spin polarization does not obey time reversal symmetry so it is unlikely to be an initial state effect. At smaller k_x (Fig. 5.12(d)), there is no spin polarization in either the $\hat{x}$ or $\hat{z}$ directions. At the smallest k_x (Fig. 5.12(e)), there is no polarization in the $\hat{z}$ direction. There is a slight increase of spin polarization near E_F at negative k_x, but as before it does not obey time reversal symmetry. Since P_X and P_Z are zero at all points measured, any non-zero P_Y then results in the ideal helical spin-momentum locked spin texture of the surface state as expected if it were a Dirac-like topological surface state or Rashba-split surface state.

Indeed in P_Y, a finite spin polarization is measured. Rather than the one spin state measured in past work [107,108,212], we see evidence of two spin states. At $k_x = \pm 0.163$ Å^{-1} there is a state with $P_Y \approx 10\%$ polarization peaked 400 meV below E_F, while the second spin state—with opposite spin polarization—is peaked 100 meV below the Fermi level with a small polarization. Both spin states obey time reversal symmetry. At $k_x = \pm 0.109$ Å^{-1} the spin polarization of the lower energy state is much larger, around 20%, and peaks near 300 meV.

The second spin state shifts in binding energy by a similar amount and retains its much smaller spin polarization. Finally at $k_x = \pm 0.054$ Å^{-1}, where the heavy hole band is above E_F, the spin polarization due to the lower binding energy state is no longer visible. There appears to be a constant shift in P_Y by about −5% across these measurements (k-independent), which is likely due to the spin-dependent photoemission matrix elements (SMEs) that have been observed in Bi_2Se_3 [263, 264]. In addition, the measured P_Y decreases at large k_x values. In Fig. 5.13, P_Y measurements of a 400 BL

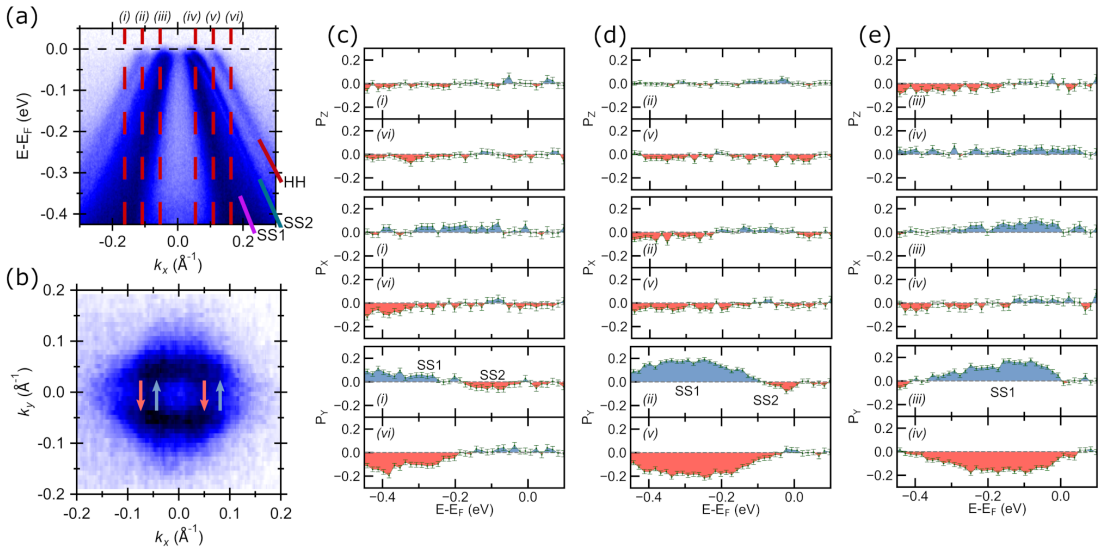

Figure 5.12: Determination of the spin texture of the surface states. (a) ARPES measurement of 400 BL-A with the energy distribution curves (EDCs) along which spin polarization was measured indicated with the red dashed line. (b) A constant energy contour taken from Fig. 5.10(a) at $E - E_F = 100$ meV. Spin polarization measured in ($\hat{x}$,$\hat{y}$,$\hat{z}$) at (c) $k_x = \pm 0.163$ Å^{-1}, (b) $k_x = \pm 0.109$ Å^{-1}, and (c) $k_x = \pm 0.054$ Å^{-1}. All measurements were made at $h\nu$=21 eV with p-polarization.

sample (400 BL-D) are shown across a larger and finer spaced k range.

The spin polarization of SS2 decreases at larger k. The spin polarization of SS1 decreases as well, but to a smaller degree. For now, we attribute the larger spin polarization peak to SS1 and the smaller spin polarization peak to SS2. This attribution (that the smaller peak corresponds to SS2 rather than the heavy hole band) is shown more rigorously in the next paragraphs. SS1 and SS2 are thus spin-polarized, having the ideal orthogonal spin-momentum locking and opposite helicities (Fig. 5.12(b)).

The magnitude of the spin polarization in SS1 is roughly half that of the spin polarization measured for α-Sn(001) in Barfuss *et al.* [107] and roughly equal to that measured in Scholz *et al.* [212], but the value of the polarization measured in Ohtsubo *et al.* [108] is unknown. The three prior SARPES measurements give overall similar results where only one spin state was visible and said spin state was associated with a Dirac-like topological

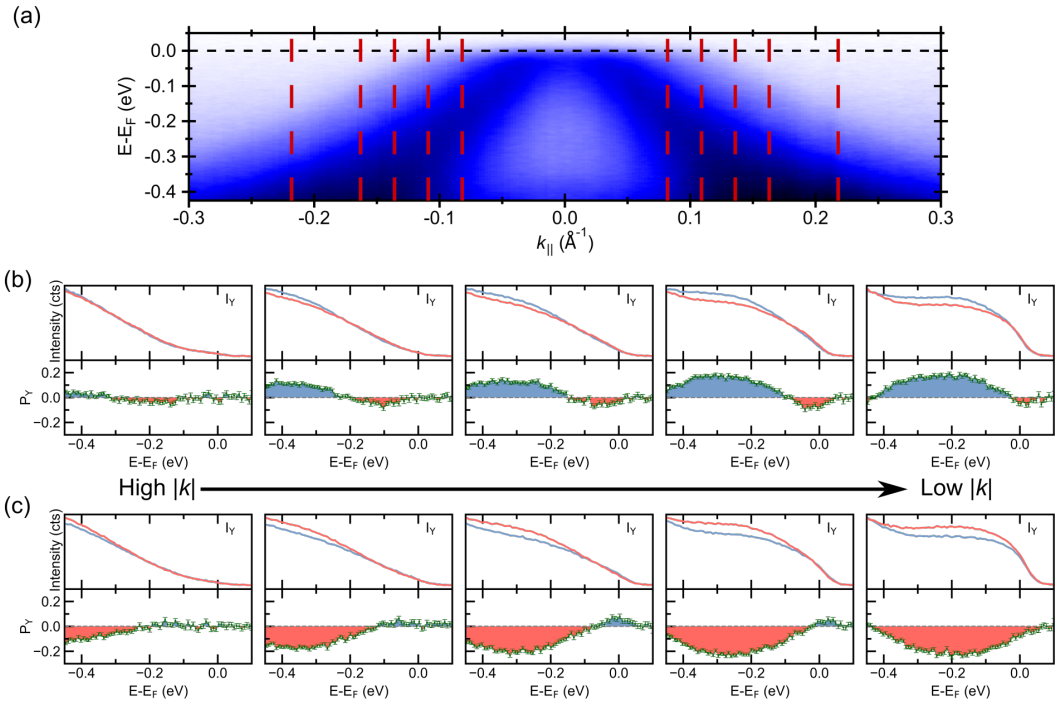

Figure 5.13: SARPES of 400 BL-D better showing the dispersion of the spin polarization of SS1 and SS2. (a) ARPES measurement showing the cuts along which P_Y was measured. (b) SARPES measurements at $-k_x$. (c) SARPES measurements at $+k_x$. All measurements are performed at $h\nu = 21$ eV with p-polarized light.

surface state.

The sign of the helicity of SS1 measured in Fig. 5.12 agrees with that found in Ohtsubo *et al.* [108], but has opposite helicity to that found in Barfuss *et al.* [107] and Scholz *et al.* [212]. While our work, Barfuss *et al.* [107], and Ohtsubo *et al.* [108] all report a perfect spin-momentum locking in SS1, Scholz *et al.* [212] reports some canting with a finite spin polarization in the $\hat{x}$ direction.

One possible root of these discrepancies is the experimental geometry. The polarization of light has been found to be a tool to manipulate the spin vector of the topological surface states in Bi_2Se_3-based systems [264,265]. In Ohtsubo *et al.* [108], which measures an equivalent helicity of SS1 to that in Fig. 5.12, the experimental geometry is equivalent to ours other than a $C_2(z)$ rotation of the two-fold symmetric substrate. This should not

have a large effect on these measurements as the measured electronic structure of the α-Sn film is four-fold symmetric (Fig. 5.10).

Moreover, modification of the SS1 spin texture by p-polarized light (as used here), should it follow the mechanism found in Ref. [264] and Ref. [266] for Bi_2Se_3-based systems, should show strong deviations from orthogonal spin-momentum locking at k other than those measured here. However, further measurements away from high symmetry lines found the ideal orthogonal spin-momentum locking indicating that the polarization of light does not have a strong effect on the measured spin texture of these samples.

The spin polarization previously shown was only measured along the $\overline{X}-\overline{\Gamma}-\overline{X}$ high symmetry direction. In $(Bi,Sb)_2(Sb,Te)_3$-based topological insulators, the light polarization tunes the spin texture of the topological surface by sensitivity of the matrix elements to the orbital texture [266]. If these effects are significant, the use of p-polarized light would not change the spin polarization along the symmetry line measured previously, but would cause significant changes of the spin texture away from orthogonal spin momentum locking at $k_y \neq 0$ [264, 266].

In an ARPES measurement at $h\nu = 21$ eV with p-polarized light at $k_y = +0.073$ Å^{-1} three bands are visible (Fig. 5.14(a)). Only one spin state is measured here, which due to its magnitude is likely SS1. The spin polarization at negative k_x (Fig. 5.14(d)) shows polarization in $\hat{x}$ and $\hat{y}$ as expected with orthogonal spin-momentum locking. At $k_x = 0$ (Fig. 5.14(e)), P_Y goes to zero, showing preservation of orthogonal spin-momentum locking. Finally at positive k_x (Fig. 5.14(f)), the spin polarization is inverted from Fig. 5.14(d) preserving time reversal symmetry. The angle of the spin vector in Fig. 5.14(d) and Fig. 5.14(f) is canted roughly 25° away from pointing fully in $\hat{x}$. This corresponds to perfect orthogonal spin-momentum locking within the limits of the measurement as from the ratio of k_x to k_y an angle of 30° is expected. The measured spin polarization vectors are drawn on the SS1 contour in Fig. 5.14(c).

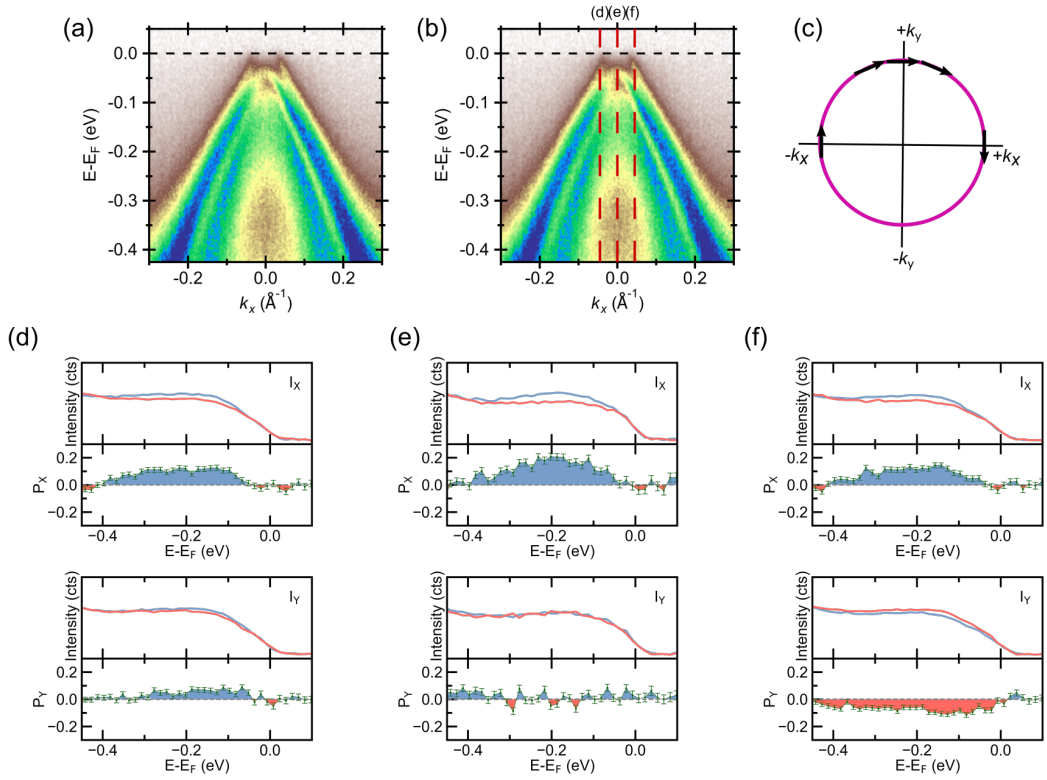

Figure 5.14: Measurement of spin polarization at $h\nu = 21$ eV with p-polarized light on 400BL-A at $k_y = +0.073$ Å^{-1}. (a) ARPES measurement (b) EDCs along which spin polarization was measured. (c) Measured spin texture of SS1. The arrows on the k_x axis are derived from Fig. 5.12. The other arrows are from these measurements. Spin polarization in $\hat{x}$ and $\hat{y}$ for the lines at (d) $k_x = -0.045$ Å^{-1}, (e) $k_x = 0$ Å^{-1}, and (f) $k_x = -0.045$ Å^{-1}.

Since using p-polarized light we measure the ideal orthogonal spin-momentum locking at these k, the photoelectron spin texture manipulation seen in (Bi,Sb)$_2$(Sb,Te)$_3$-based systems is not present in α-Sn. This is consistent with the calculation that α-Sn's topological surface state derives almost entirely from p_z orbitals [170], was opposed to (Bi,Sb)$_2$(Sb,Te)$_3$ where the surface state is a mixture of p_x, p_y and p_z orbitals [266].

The geometries used in [107] and Scholz *et al.* [212] are not directly reported. The spin canting in the $\hat{x}$ direction in Scholz *et al.* [212] could also potentially result from interference of spin-momentum locked textures of SS1 and SS2 if the intrinsic linewidths of these states overlap [267].

Finally, the prior SARPES measurements of α-Sn(001), did not find the presence of any spin polarization in SS2. This discrepancy between our measurements and the literature could arise from the good energy resolution of our measurements which is generally 3× better than that of other work on this material system. In addition, in all prior spin-resolved ARPES measurements the surface and/or the bulk of α-Sn is doped with Te or Bi to improve the surface quality and electron-dope the (generally degenerately p-type doped films) films. These treatments could strongly modify the measured surface electronic structure and have already been seen to renormalize the velocity of the surface states [206, 209, 214]. Impurities on the surface have also been calculated to potentially lead to a non-orthogonal spin-momentum locking [268]. The films used in our study are free from these treatments, and thus the effects measured here are intrinsic to α-Sn(001).

Now we investigate our attribution of the spin polarization as arising from the initial states of SS1 and SS2 by varying both the polarization of light and the resolution of the measurement. These measurements were performed at $k_x = \pm 0.109$ Å^{-1} where the intensity and bandwidth of the SS2 peak in P_Y is maximal.

A representative $h\nu$=21 eV ARPES measurement for these samples is shown in Fig. 5.15(a). The resolutions for the following spin-resolved measurements are indicated in Fig. 5.15(a) as well and correspond to an energy resolution better than 100 meV for Fig. 5.15(b,c), 63 meV for Fig. 5.15(d,e), and 33 meV for Fig. 5.15(f,g) and an angular acceptance of ±0.5°, ±0.5°and ±0.25°, respectively.

Spin-resolved photoemission measurements can sometimes measure a finite spin polarization for a feature that does not have a spin-polarized initial state [151]. These features generally arise from strong spin-orbit coupling related matrix elements and the details of the final state, but other mechanisms such as spin-dependent emission and spin-dependent photoelectron transport can have an effect as well [151, 152]. Fig. 5.15(b,c) probe the spin polarization of SS1 and SS2 using the He1α line isolated from the emit-

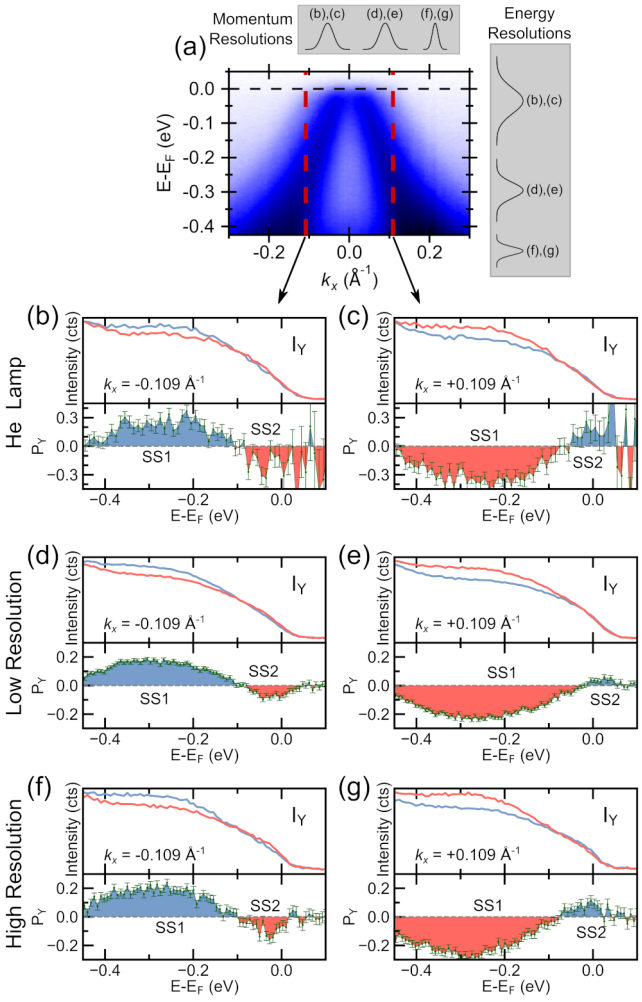

Figure 5.15: Verifying spin polarization in SS1 and SS2. (a) ARPES measurement of 400 BL-D using p-polarized light at $h\nu$=21 eV with the EDCs along which spin polarization was measured indicated with the red dashed line. P_Y measurement performed using He1α light on 400 BL-C at (b) $k_x = -0.109$ Å^{-1} and (c) $k_x = +0.109$ Å^{-1}A. P_Y measurements on 400BL-D using p-polarized synchrotron light at $h\nu$=21 eV taken at (d) $k_x = -0.109$ Å^{-1} and (e) $k_x = 0.109$ with low energy/momentum resolution. P_Y measurements taken immediately afterward on 400 BL-D at (f) $k_x = -0.109$ Å^{-1} and (g) $k_x = +0.109$ with high energy/momentum resolution.

ted spectrum of a helium ECR plasma source with a monochromator. This light is not entirely unpolarized as a) the light generated in an ECR plasma could have some slight polarization [269] and b) passing the light through a monochromator will partially polarize it. The geometry of the monochromator results in partially linearly polarized light with the polarization vector roughly 45° from the incidence plane. Even so, the total p-polarization using the He1α line should be less than that using the p-polarized synchrotron light and any features induced by the use of p-polarized should show a strong reduction. The matrix element effect of partially polarized light is a combination of the matrix element effects for the unpolarized and polarized contributions of the light [270]. Neither of these matrix element effects should obey time reversal symmetry [270]. In Fig. 5.15(b,c) the spin polarization of SS1 and SS2 are still clear and show time reversal symmetry; The use of the He1α line actually increases the maximum spin polarization of each state by $\sim$50%.

Since the heavy hole band (the outermost band measured at $h\nu$=21 eV, discussed in Section 5.3.2) is spin degenerate it cannot produce this measured spin polarization; we find that the low binding energy spin polarization is likely from SS2. The helicities of the spin textures of SS1 and SS2 agree with that measured using p-polarized light; the spin texture depicted in Fig. 5.12(b) (opposite to that typically measured for Dirac-like surface states) seems to then truly be the initial state spin texture, unmodified by matrix element effects from the use of p-polarized light, in agreement with the earlier discussion regarding Fig. 5.14.

In these measurements and those in Fig. 5.12, there is no region of null spin polarization in between the SS1 and SS2 peaks. There is therefore an overlap in the measured spin polarization from the Gaussian resolution function of the measurement. The dependence on the measured polarization on experimental resolution is investigated further using synchrotron light. Referencing Fig. 5.10(a), at $k_x = \pm 0.109$ Å^{-1} (neglecting the

angular acceptance window of the spin-resolved measurement) there is an energy spacing of 150 meV between SS1 and SS2 and 230 meV between SS1 and the HH band. Since the distance between SS1 and the HH band is so much larger than the energy resolutions used in Fig. 5.15(d)–(g), this change in energy resolution should not have an effect on the measured spin polarization. The angular acceptance window and thus the momentum resolution was varied in this measurement as well. Treating SS1, SS2, and the HH as parallel, the spacing between SS1 and SS2 is roughly 0.05 Å^{-1}, while the spacing between SS1 and the HH band is roughly 0.1 Å^{-1}. The angular acceptance windows correspond to a momentum resolution of 0.036 Å^{-1} and 0.018 Å^{-1} for Fig. 5.15(d,e) and Fig. 5.15(f,g), respectively. Similar to the argument with energy resolution, the SS1-HH momentum spacing is large enough that the change in momentum resolution between the two measurements should have a negligible effect if the HH band gave rise to the spin polarization nearer to the Fermi level.

In Fig. 5.15(d,e) spin polarization data at moderate energy and momentum resolution is shown. At negative k_x the inflection point between the spin states is 80 meV below E_F and at positive k_x it is 20 meV below E_F. By improving the resolution of the measurement, the reduced breadth of the resolution function should reduce overlap in the measured spin polarization. High energy/angle resolution spin-resolved measurements at the same k_x values on the same sample, immediately after the prior measurements, are shown in Fig. 5.15(f,g). Here at negative k_x the spin inflection point is 100 meV below E_F, while at positive k_x it is 75 meV below E_F. At negative k_x the inflection point shifts 20 meV downward with improved resolution, while at positive k_x the inflection point shifts 55 meV downward. The discrepancy between these values is likely from the constant offset of -5% in P_Y or a slight asymmetry in the experimental geometry. In addition, the spin polarization of SS1 and SS2 is increased. These large changes do not reflect the small changes expected if the spin polarization near E_F is from the heavy hole band: the

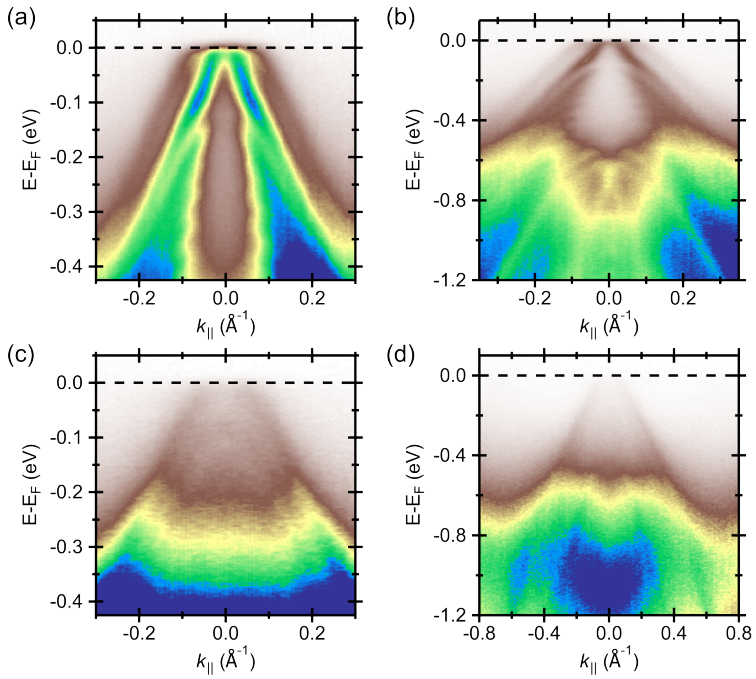

Figure 5.16: ARPES spectra using $h\nu = 21$ eV in a narrow (a) and wide (b) binding energy range. ARPES spectra at the $\mathbf{\Gamma_{002}}(h\nu = 53$ eV) in a narrow (c) and wide (d) binding energy range. All measurements use p-polarized light and are taken in the $\overline{X} - \overline{\Gamma} - \overline{X}$ direction.

measured spin polarization arises from SS1 and SS2 rather than SS1 and the heavy hole band ($\Gamma^{+}_{8,v}$). The origins of spin-polarized SS1 and SS2 is discussed further in Section 5.4.2.

5.3.4 The effect of confinement on spin polarization

Most studies of α-Sn with topology in mind have been on films much thinner than 400 BL where quantum confinement plays a stronger role. We investigate this effect in a $h\nu$=21 eV ARPES measurement of 50 BL of α-Sn (Fig. 5.16(a)). SS1 is clearly visible here, but SS2 and the HH band are not. The film is slightly electron-doped with respect to the 400 BL films. The linewidth of SS1 in this film is comparable to the linewidth of SS1 in the 13 BL film (Fig. 5.7), but noticeably narrower than the linewidth in the

400 BL film (Fig. 5.9). The linewidth of SS1 in the thin films is also relatively constant with binding energy (consistent with prior work [212]), while the linewidth of SS1 in the 400 BL film strongly increases with larger binding energy. This linewidth dependence could be due to enhanced electron-electron scattering, electron-hole scattering, impurity scattering, or a rougher surface [271–273] in the 400 BL film. 400 BL films are expected to be a 3D DSM compared to a 3D TI or 2D TI for the 13 and 50 BL films [106,207,209,210].

A series of quantum well states is apparent with the highest lying subband 150 meV below the Fermi level. These quantum well states have the same missing intensity at the $\mathbf{\Gamma}$ point observed in 13 BL films (Fig. 5.4). This indicates the missing intensity is intrinsic to the heavy hole band. However, this feature in the quantum well states still does not clarify whether the missing intensity is due to a matrix element effect or a hybridization effect—the quantum well states should have the same orbital character as the band it is derived from.

However, tight-binding calculations including matrix elements of the photoemission process imply that the missing intensity is a matrix element effect (Fig. 5.5). The inheritance of this missing intensity from the heavy hole band also confirms that these are in fact quantum well states, as opposed to Volkov-Pankratov states, which are spin-degenerate and disperse similarly to quantum well states [274]. A comparison of $E - k_{||}$ cuts slightly away from the $\mathbf{\Gamma}$ point ($k_y = 0.073$ Å^{-1}) for the 50 BL and 400 BL films, along with a $\mathbf{\Gamma_{002}}$ measurement of a 50 BL film is necessary to confirm the correspondence between the bands of 13 BL, 50 BL, and 400 BL films.

In Fig. 5.16(b), a wider energy range than in Fig. 5.16(a), quantum well states do not disperse at lower energies than the inverted conduction band. The Γ-like dispersion of the inverted conduction band and split-off band are visible as expected, as is SS3. At $\mathbf{\Gamma_{002}}$ in a narrow binding energy range (Fig. 5.16(c)), the heavy hole band and surface states in the bulk continuum are visible, but it is difficult to assign these as SS1/2 or

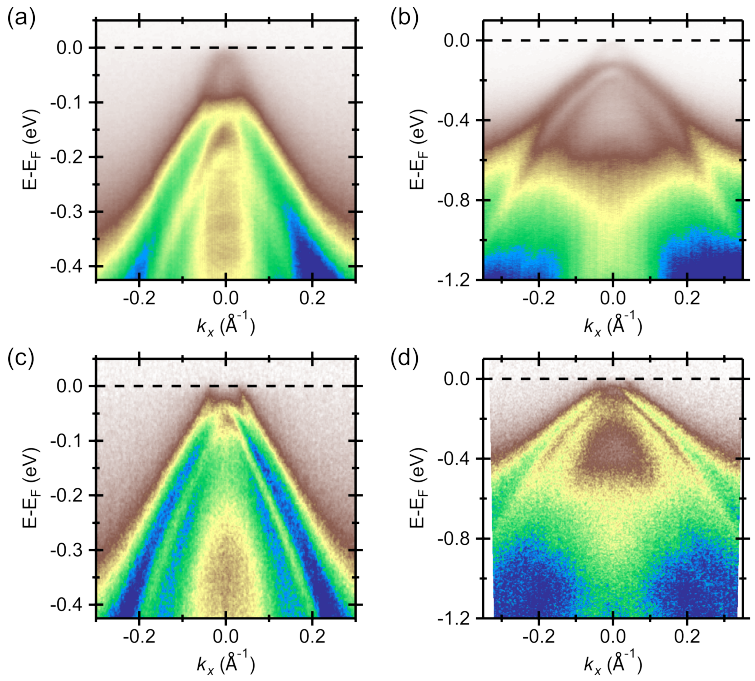

Figure 5.17: ARPES spectra at cuts slightly away from $\overline{\Gamma}$ ($k_y = +0.073$ Å^{-1}) at $h\nu = 21$ eV with p-polarized light. ARPES spectra on 50 BL α-Sn in a narrow (a) and wide (b) binding energy range. Measurements on 400 BL-A in a narrow (c) and wide (d) binding energy range.

quantum well states.

In a wider binding energy range (Fig. 5.16(d)), the shape of the outermost band is consistent with the heavy hole band, as expected at $\mathbf{\Gamma_{002}}$. In addition the parabolic-like inverted conduction band is visible. Using the bulk band spacings extracted in Table 5.1, we find that the valence band maximum in this 50 BL film is within 10 meV of E$_F$, implying that SS1/2 seen in Fig. 5.16(a) have their crossings above the valence band maximum (as is seen in 13 BL films).

Due to the presence of quantum well states with small subband spacing, it is difficult to perform the fitting procedure for band identification on the $h\nu = 21$ eV measurement of 50 BL films. Instead we turn to a cut slightly away from $\overline{\Gamma}$. In Fig. 5.17(a) for a 50 BL film, the quantum well states are visible at high binding energy. The highest energy

state here is then the heavy hole band which those quantum well states are derived from. Two states are degenerate (within the resolution of the measurement) before one has a cusp 100 meV below the Fermi level and the second has a cusp just below the Fermi level.

A wider binding energy measurement in Fig. 5.17(b) shows that other than the bands in Fig. 5.17(a), there is a band slighlty visible 600 meV below E_F corresponding to either SS3 or the inverted conduction band. For the 400 BL α-Sn film off-$\overline{\Gamma}$ cut measurement in Fig. 5.17(c), only 3 bands are visible. These correspond to the same bands as in Fig. 5.17(a), but without the presence of any quantum well states. In addition, the top most states cusp is now above E_F. In the wider binding energy measurement (Fig. 5.17(d)), the correspondence to Fig. 5.17(b) is also clear in that SS3 or the inverted conduction band is now visible a few hundred meV below the bands visible in Fig. 5.17(c).

Measurements of P_Y are shown in Fig. 5.18(b,c) where a similar spin polarization is seen as for the 400 BL films. The lineshape of the spin polarization in SS1 is much more asymmetric, possibly from the reduced linewidth of SS1 in this film as compared to the 400 BL films. The peak of the SS2 polarization is slightly below E_F, compared to the same k_x in 400 BL films where it is at or above E_F. This is due to the difference in chemical potentials between the two samples (the thinner film is more electron-doped). As with the 400 BL films, there is no spin polarization in the $\hat{x}$ and $\hat{z}$ directions. The quantum well states do not appear to be spin-polarized, as expected. SS1 and SS2 retain their ideal orthogonal spin-momentum locking and have a clockwise and counterclockwise, respectively, helicity as is the case in 400 BL films. Quantum confinement then does not strongly change the spin texture of SS1 and SS2, but does induce quantum well states and appears to modify the self-energy of SS1.

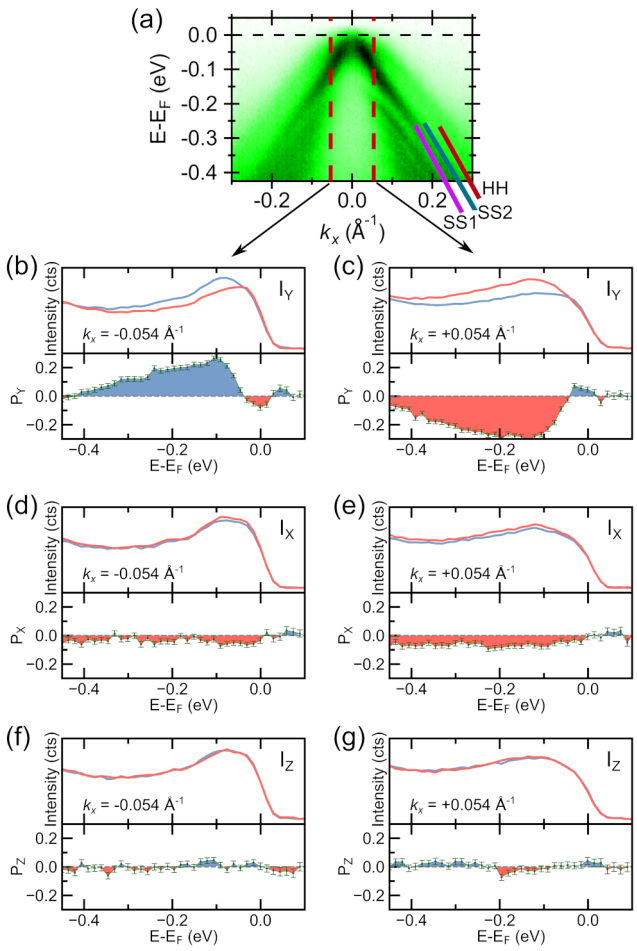

Figure 5.18: Spin polarization measurements on 50 BL α-Sn(001). (a) ARPES measurement with the EDCs along which spin polarization was measured indicated with the red dashed line. P_Y measurement at (b) $k_x = -0.054$ Å^{-1} and (c) $k_x = +0.054$ Å^{-1}A. P_X measurement at (d) $k_x = -0.054$ Å^{-1} and (e) $k_x = +0.054$ Å^{-1}A. P_Z measurement at (f) $k_x = -0.054$ Å^{-1} and (g) $k_x = +0.054$ Å^{-1}. All measurements were made at $h\nu$=21 eV with p-polarization.

5.3.5 Spin polarization in the topological surface state from double band inversion in α-Sn

We previously discussed disagreement over the exact shape of the inverted conduction band (Γ_7^-) in Section 5.3.1, leading to uncertainty as to the true nature of SS3. While our spin-integrated ARPES measurements agree with the proposed model in Ref. [170], here we seek to measure the spin polarization of this state to further confirm the secondary band inversion and show that SS3 is indeed topologically non-trivial. The EDCs along which spin polarization was measured are shown in Fig. 5.19(a), where the coexistence of $\mathbf{\Gamma}$ point-like bulk bands and SS3 is clear (Section 5.3.2). The innermost cuts cross the upper branch of the surface state, just touching the lower branch. The middle cuts cross only the upper branch of SS3, while the outermost cuts should mostly interact with the Γ_7^- band (the cuts are past the k_x extent of SS3 estimated in Fig. 5.4 and Ref. [170]). At the innermost cuts (Fig. 5.19(b,c)) there is no meaningful spin polarization in the $\hat{x}$ or $\hat{z}$ directions. In Fig. 5.19(d), a non-zero spin polarization is clearly evident in P_Y, centered 600 meV below E_F. This spin polarization then has the ideal orthogonal spin-momentum locking expected of a true topological surface state. The SS1 spin polarization is visible at binding energies lower than 400 meV. The upper branch of SS3 has an inverted polarization compared to the lower branch of SS3, implying the lower branch of SS3 has the same spin helicity as SS1 (again inverted from that typically associated with a Dirac-like surface state). In SS1, this helicity (inverted from that expected in a Dirac cone) was shown to not be a function of polarization of light in contrast to what is seen in Bi_2Se_3 where the polarization controls the spin texture [263, 264]. However, we have not performed SARPES measurements of the spin texture of SS3 using other polarizations of light or unpolarized light and thus cannot make this same attribution.

The spin polarization decreases slightly farther from the node of SS3 (Fig. 5.19(e))

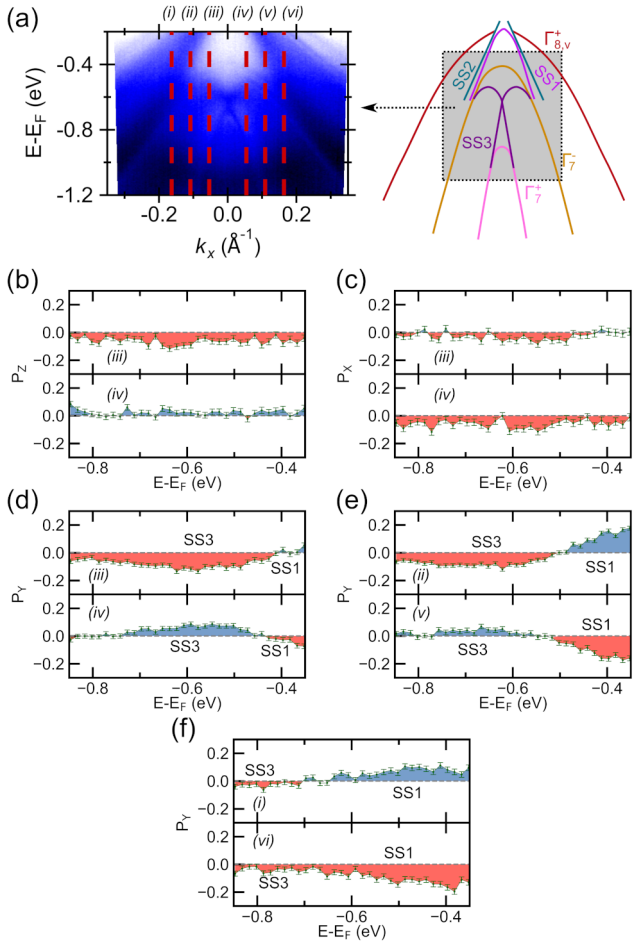

Figure 5.19: Spin polarization measurements of SS3. (a) ARPES measurement near SS3 of 400 BL α-Sn(001) (400 BL-A) with the EDCs along which spin polarization was measured indicated with the red dashed line. (b) P_Z and (c) P_X measured at $k_x = \pm 0.054$ Å^{-1}. P_Y measured at (d) $k_x = \pm 0.054$ Å^{-1}, (e) $k_x = \pm 0.109$ Å^{-1}, and (f) $k_x = \pm 0.163$ Å^{-1}. (g) Measured P_Y for surface states 1, 2 and 3. All measurements were made at $h\nu$=21 eV with p-polarization.

and almost fully vanishes when the cut is centered far away from the node of SS3 (Fig. 5.19(f)). The measured spin polarization in Fig. 5.19(f) is dominated by SS1. The spin-polarized SS3 then has some finite k extent—close to that indicated by the outermost constant momentum slices in Fig. 5.19(a)—whereupon it joins the Γ_7^- band. The **M**-shaped SS3 is truly a spin-polarized topological surface state with the expected spin-momentum locked spin texture, in conjunction with the spin-polarized surface states SS1 and SS2 (Fig. 5.21).

5.4 Discussion

5.4.1 Disagreement with the inner potential model

In Section 5.3.2, we found major discrepancies with the inner potential model using experimental values of the inner potential. It is not yet clear from where this discrepancy rises. The inner potential V_0 (Eq. (5.2)), is defined as $V_0 = E_0 - e\Phi$, where E_0 is the zero energy of the (assumed) free electron final band with respect to the valence band maximum of the semiconductor and Φ is the work function of the semiconductor [275]. The simplest explanation for the discrepancy we measure is that the constant inner potentials found in prior work of 5.8 eV [170](measured using soft X-ray light) or 9.3 eV [209](measured using extreme UV light) are incorrect. However, our results in Fig. 5.4 & Fig. 5.7 agree nicely with these computed inner potentials (and our own photon energy dependence measurements). Furthermore, to produce a $\mathbf{\Gamma}$ point at $h\nu$=21 eV, V_0 would need to be near 40 eV, an unphysical value.

One potential explanation is that the assumption of a free electron final state with constant inner potential fails at these low photon energies. In photon energy dependent measurements of α-Sn in the VUV range in the past, a $h\nu$ dependent inner potential

term was adopted such that the final state is parabolic with an effective mass of $0.22m_0$, although this approach was *ad hoc* [258]. It has been well-established that for lower photon energy ARPES measurements of GaAs(001) ($h\nu < 50$ eV) the expected dispersion assuming a free electron final state with constant inner potential varies in its suitability as a function of photon energy and as a function of the band in the initial state, while for GaAs(110) the constant inner potential model can be quite robust [275]. Deviations from this model vary by material, crystalline orientation, band of interest, and photon energy range used. Failures are then not unexpected and disagreements between measured band structure via ARPES and calculated band structure could just as likely be from deviations in the final states as deviations in the initial states [275]. In fact, deviations from the free electron final state were already observed in α-Sn via the dichroism measurements in Section 5.3.1.

Even assuming the inner potential model holds as expected, prominent k_z broadening can be present in low photon energy measurements. k_z broadening is caused by the Heisenberg uncertainty principle between k_z and the inelastic mean free path [146, 276]. The typical constant photon energy $E - k_{||}$ measurement is then not truly a slice at some given k_z value (determined by Eq. (5.2)), but actually integrated over some Δk_z inversely related to the inelastic mean free path (IMFP) of the photoelectrons [149]. If the broadening (i.e. total k_z sampled) is very large, band features could show up in unexpected locations. The IMFP for photoelectrons near the Fermi surface in the $h\nu$=21 eV measurement (calculated via a modified fit to the universal curve [143]) is 4.3 Å, close to the 5.0 Å IMFP (calculated by the same method) for the bulk-sensitive $h\nu$=352 eV measurements in prior work [170].

Another possible explanation for the presence of these states is that they are indirect transitions. When the energy of the final state is low, the effect of the crystal potential cannot be neglected [277]. This perturbation can result in a dispersion expected from

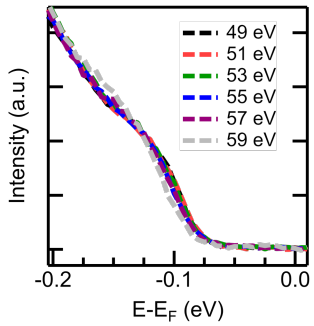

Figure 5.20: $h\nu$-dependent measurement of EDCs near the $\mathbf{\Gamma_{002}}$ point in 50 BL α-Sn. EDCs are integrated over ± 0.2 Å. Each EDC is normalized by its integrated intensity over the depicted energy range.

a high symmetry point to be seen at photon energies that do not correspond to that symmetry point [277]. In the similar system of CdTe(111) only indirect transitions are visible in ARPES measurements using photon energies in the 19-30 eV range; these indirect transitions reflect a Fourier sum of final states arising from high symmetry initial states corresponding to k_z=0 and 0.5 (center and edge of the Brillouin zone) [260, 278]. These indirect transitions show no photon energy dependence, the opposite of that which would normally be expected from direct bulk band transitions. If the presence of the $\mathbf{\Gamma}$ point like bulk band dispersion in the 21 eV measurements presented here is rooted in indirect transitions, any ARPES measurements in the VUV range where these indirect transitions are present would then be expected to show the HH band in close proximity to the set of two surface states.

Over a range of photon energies corresponding to $0 \pm 0.15 \times \frac{4\pi}{c}$ near $\mathbf{\Gamma_{002}}$ (Fig. 5.20), the valence band maximum and shape of the valence band did not change more than the uncertainty in the chosen Fermi energy (< 10 meV) except for the measurement at $h\nu = 59$ eV. Following the tight-binding band structure in Fig. 5.4, the measured valence band maximum *should* change by a few hundred meV over this k_z sweep. However the change in the $h\nu = 59$ eV measurement implies that there is some k_z dispersion of this

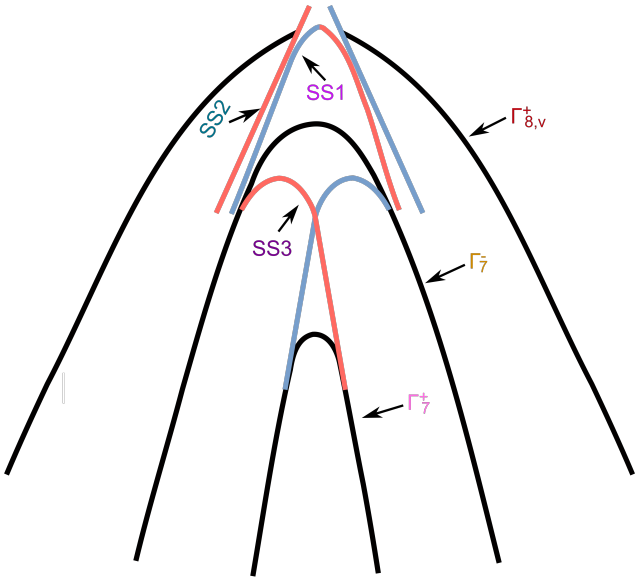

Figure 5.21: Spin polarization measured in this chapter mapped onto surface state dispersions of SS1, SS2, and SS3, where SS2 and SS3 are topological surface states.

band such that it is not an indirect transition. This change could also be due to a change in intensity of one of the surface states degenerate with the valence band maximum, as the intensity of these bands should oscillating with $h\nu$ [148]. Neither the situation of indirect transitions nor a failure of the free electron final state assumption can be clearly isolated in our current measurements, but both are reasonable explanations. Our results emphasize that the final states of α-Sn should be investigated in more detail such that better convergence can be reached between the predicted and measured initial state electronic structure of α-Sn.

5.4.2 Potential origins for the surface states observed

We observe the presence of two distinct surface states with opposite spin-momentum locked helical spin textures in α-Sn, independent of film thickness. We now discuss both the topologically trivial and the non-trivial potential origins of these surface states

(Fig. 5.21. Various surface states have been proposed to exist in this system including Dyakonov-Khaetskii states [279, 280] and Volkov-Pankratov states [274, 281]. In the work of Barfuss *et al.* [107], one topological surface state with the expected helical spin-momentum locked spin polarization of a Dirac-like surface state was observed while doping the films with percent levels of Te. Ohtsubo *et al.* [108] similarly measured the topological surface state, but with an opposite helicity for the spin texture and using an adlayer of Bi on the α-Sn(001) surface. More work on the (001) surface of Te-doped α-Sn thin films found the presence of a second, unpredicted surface state [212]. Building on this study, Chen *et al.* [209] found evidence of three surface states in undoped α-Sn(001), of which the state closest to $\overline{\Gamma}$ was attributed to be the typical topological surface state and the other two were associated with a Rashba-split surface state with a large Rashba coefficient. In addition, trivial surface states associated with the surface reconstruction of α-Sn(001) have been proposed [282] of which there is reasonable experimental agreement via surface core level shifts in ultraviolet photoelectron spectroscopy measurements [283].

Zeroth order Volkov-Pankratov states are equivalent to the Dirac-like topological surface state [274]. Higher order Volkov-Pankratov states are spin degenerate and outside of the bulk continuum, and thus cannot be the origin of the spin-polarized SS2 [274, 281]. Surface states derived from the reconstruction of α-Sn are spin degenerate, and thus cannot be attributed to SS1 or SS2. The quantum well states visible in the 50 BL film could potentially be attributed to Volkov-Pankratov states; The measured states are in the bulk continuum and thus surface resonances rather than surface states, disagreeing directly with the Volkov-Pankratov predictions [274]. As already discussed, these quantum well states also share band features with the heavy hole band they are derived from.

Dyakonov-Khaetskii states are spin-polarized, as we observe in SS1 and SS2, however they too exist outside of the bulk continuum rather than inside [279, 280]. These states modify the dispersion of the linear spin-polarized topological surface state and

are sensitive to coupling with the heavy hole band in α-Sn, epitaxial strain, band offsets, and film thickness [280, 284]. They connect directly from the bulk heavy hole band ($\Gamma^{+}_{8,v}$) to the bulk conduction band whereas we observe direct connection of SS1 and SS2 to the inverted conduction band (Γ^{-}_{7}) (Fig. 5.4). However, because these Dyakonov-Khaetskii states are sensitive to so many material parameters, tuning these parameters in the calculation may then result in a picture consistent with the measurements presented here [284].

The proposed origin most consistent with the dispersion and spin-texture observed here is the presence of electron-like and hole-like Rashba-split surface states which hybridize to form a Dirac-like topological surface state [209]. This picture is also consistent with the lack of an upper branch to SS1 in Fig. 5.7(c) as the outer branches of the Rashba states would form the Dirac-like surface state (SS2), while the inner states would form a lower spin resonance (SS1). However in Chen *et al.* [209], the Rashba-split states are calculated/measured to coexist with a topological surface state, which should result in three spin-polarized surface states rather than the two spin-polarized surface states observed here. The helicity of spin-momentum locking in SS1 and SS2 is also inverted from that expected in the minimal model in Chen *et al.* [209]. In a slightly different mechanism of Rashba-split surface state hybridization, a *single* pair of Rashba-split bands hybridize and result in only two sets of spin-polarized bands (one spin resonance and one Dirac-like surface state), rather than three. On the other hand, electron- or hole-like Rashba-split surface states could hybridize *with* a pre-existing topological surface to form the observed spin polarization as well (similar to the case of $MnBi_2Te_4$ [285]).

The measured spin polarization from the initial state of both SS1 and SS2 rules out that either band could be a trivial surface state from the surface reconstruction of the film. However if the Rashba effect is significant, it is possible that the Rashba splitting is acting on such a trivial surface state. The dispersion of surface bands derived from the

surface reconstruction of α-Sn(001) has been calculated under a number of bonding and domain configurations, but these bands generally switch from a surface resonance at low k to a surface state at high k [282]. This effect is not observed in the various $E-k$ slices or constant energy contours presented in this chapter for SS1 and SS2. Surface states derived from the surface reconstruction are not calculated to have connection to the inverted conduction band (Γ_7^-), while this direct connection is observed in all of the films studied here. However it has been shown that Rashba splitting can effect the connection between surface and bulk states [286]. Finally, in the α-Sn/InSb(111)B system, SS1 or SS2 is observed to disperse from the inverted conduction band (Γ_7^-) toward the valence band maximum [213]. SS1/2 can therefore not originate from any particularity of the (001) surface studied here. To our knowledge no present calculation or minimal model fully matches the dispersion and spin polarization of surface states observed in this chapter, although some form of a hybridized Rashba surface state picture [209, 285, 287] is the most consistent. In this picture SS1 is a lower spin resonance, while SS2 is a Dirac-like topologically non-trivial surface state.

5.5 Conclusion

Through detailed spin- and angle-resolved photoemission spectroscopy measurements, we have found several essential clarifications to both the bulk and surface electronic structure of Compressive strained α-Sn/InSb(001). By excluding the use of extrinsic surface and/or bulk dopants, we isolated the behaviors observed to be intrinsic to α-Sn. We have confirmed the presence of a spin-polarized surface state deep below the valence band maximum and found that there is no significant warping of the inverted conduction band, in contrast to many calculations. We have also observed the presence of only two surface states near the valence band maximum across a range of film thicknesses, both of

which have their crossing points above the valence band maximum in ultrathin films; the third state sometimes seen in low photon energy ARPES measurements, for our films, was consistent with the heavy hole dispersion at the $\mathbf{\Gamma}$ point for both 13 and 400 BL α-Sn films. Most importantly, both of these near-VBM surface states were observed to be spin-polarized with the ideal orthogonal spin-momentum locking but opposite helicities. We find that the inner spin-polarized surface state is likely a lower spin resonance (from a form of hybridization with Rashba states [209]), while the outer spin-polarized surface state is the topologically non-trivial Dirac-like surface state.

Our results exemplify the complexity of not only the electronic structure of α-Sn, but also the measured photoemission spectra. Few calculations predict the dispersion of the inverted conduction band or the dispersion and spin textures of the surface states observed in this chapter. A better agreement between theory and experiment would help with the understanding of α-Sn such that a more deterministic control of the topological phase is possible. As is, the clarification to the electronic structure of α-Sn reported here sheds light on the results of other measurement techniques which are not sensitve to the full band dispersion. This clarification allows us to further explore the details of surface state hybridization (Chapter 6), inversion symmetry breaking (Chapter 7), and the effect of alloying Ge for tensile strain (Chapter 8). Furthermore, the existence of oppositely spin-polarized surface states terminating above the valence band maximum could allow gate or dopant controlled tuning of the chemical potential in α-Sn to increase the already remarkable spin-charge conversion efficiency in this system, while also minimizing the contributions of the parasitic bulk channel.

Chapter 6

Film-substrate hybridization in α-Sn/InSb heterostructures

6.1 Introduction

Bulk α-Sn, the inversion-symmetric anologue of HgTe, possesses a band inversion between its conduction band $\Gamma_{8,c}^{+}$ and second valence band Γ_{7}^{-}—through the intervening $\Gamma_{8,v}^{+}$ first valence band [88]. Compressive strained thin films of α-Sn are in a 3D Dirac semimetal (DSM) phase which under the effect of quantum confinement transitions to a 3D topological insulator (TI), 2D TI, and 2D normal insulator (NI) phase [108, 109, 207, 210, 232].

α-Sn has also shown numerous promising results for spin-charge conversion and other spintronic and magnetoelectric applications [103, 111, 112, 288]. As an elemental material, α-Sn should not have the stoichiometry, anti-site defect, and other defect issues seen in other compound thin film topological materials systems.

Because the topological surface states disperse across the inverted $\Gamma_{8,c}^{+}$-Γ_{7}^{-} gap through the $\Gamma_{8,v}^{+}$ band, there should be some interaction between the topological surface state and

the $\Gamma_{8,v}^{+}$ band. This hybridization and its modification of the TSS dispersion can both direcly modify the topological phase and/or change the influence of thin film confinement effects on the topological phase.

In addition, the role of the substrate or barrier (to the α-Sn well) is essential. The preservation of a topological surface state when interfaced with a material has been of interest in topological systems since their inception. Different types of interface states have been calculated for zero-gap inverted semiconductors [274,279–281,284,289]. These interface states sometimes hybridize to have a different dispersion [290,291]. The chemical potential at opposite interfaces (with the top interface being vacuum or a capping layer) do not have to be the same [292–294], which can lead to individual quantum Hall signals from each interface [295] and large spin splitting in hybridized quantum well subbands [296]. The effect of the substrate/film interface could help explain the variations in topological phase identification in the literature for α-Sn.

In this chapter, we demonstrate the importance of the substrate in determining the topological phase of ultrathin α-Sn/InSb(001) thin films using angle-resolved photoemission spectroscopy paired with tight-binding and $k \cdot p$ models. We observe weak hybridization of the topological surface state with the $\Gamma_{8,v}^{+}$ band at the top surface. In these measurements, we also observe the presence of the topological surface state at the α-Sn/InSb interface, TSS_{bott}. The energy level, hybridization with $\Gamma_{8,v}^{+}$, and band velocity of TSS_{bott} appear to be a sensitive function of the film/barrier valence band alignment, which is itself very sensitive to the interface chemistry. This better understanding of hybridization and substrate effects in α-Sn allows better deterministic control of the topological phase of this system.

6.2 Methods

Thin films of α-Sn were grown on both the indium rich c(8×2) and the antimony rich c(4×4) reconstruction of InSb(001) [206]. Film thicknesses are referred to in bilayers (BL) where 1 BL corresponds to half of the conventional diamond cubic unit cell (1 BL = 9.5×10^{14} at/cm^2). The surface reconstruction of α-Sn films was a mixed (2×1)/(1×2) reconstruction, as measured by reflection high energy electron diffraction.

ARPES measurements were performed at beamline 5-2 at Stanford Synchrotron Radiation Lightsource (SSRL) or beamline 10.0.1.2 at the Advanced Light Source (ALS). At both beamlines, data were taken using a Scienta Omicron DA30L detector. The sample temperature was kept below 20 K and the base pressure during measurement was lower than 3×10^{-11} Torr. The samples were transferred from the growth systems at UCSB to SSRL and ALS using a custom designed ultrahigh vacuum suitcase with pressure lower than 4×10^{-11} Torr. All calculations were performed by George de Coster at the Army Research Laboratory.

6.3 Results and Discussion

Slab calculations of α-Sn show confinement-induced topological phase transitions to different topological phases when Sn is bounded by vacuum on both surfaces [207] or by CdTe on both surfaces [210]. Most α-Sn growths are performed on either CdTe or InSb substrates and are studied either *in situ* with ARPES (where the top barrier is vacuum) or *ex situ* by magnetotransport (where the top barrier is a native Sn oxide). CdTe capping layers for α-Sn have been demonstrated but are not typically used [297].

For α-Sn growth on CdTe ($E_{gap}^{0K} = 1.6$ eV), the valence band of α-Sn aligns approximately midgap [259,298,299]. As we will show, this situation approximates a vacuum-like

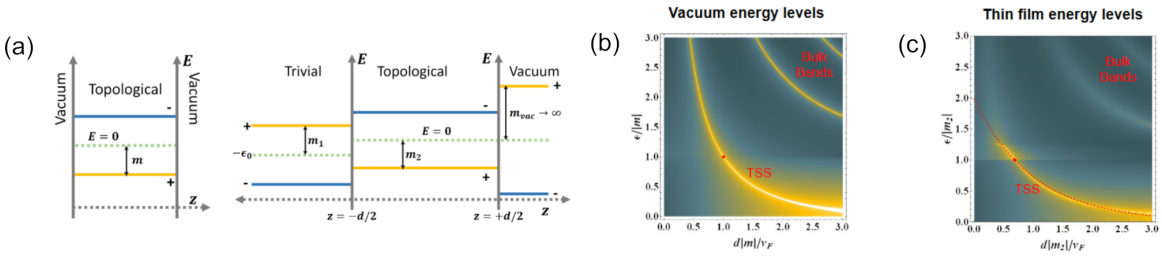

Figure 6.1: (a) Band alignments of α-Sn bounded by a combination of vacuum, CdTe, or InSb barriers. Hybridization of topological surface states with a slab of α-Sn bounded by (b) vacuum on both sides and (c) InSb on one side and vacuum on the other. An InSb substrate reduces the thickness at which surface state hybridization proceeds. Relative band alignments are discussed in the text. Calculations were performed by George de Coster of the Army Research Lab.

barrier. For growth of α-Sn on InSb ($E_{gap}^{0K} = 0.24$ eV), the valence band of α-Sn aligns either midgap [300] (Type I alignment) with a 100 meV valence band offset (VBO) or with a 400 meV VBO [301] (Type III alignment). For InSb barriers, the assumption of a vacuum-like barrier is weak.

In α-Sn grown on both CdTe and InSb, the epilayer is under compressive strain and is thus in a 3D DSM phase [109, 210, 232]. Confined films are expected to be in a 3D TI, 2D TI, or 2D NI phase [107, 108, 207, 210, 211], where the exact phase depends on the hybridization between the top and bottom topological surface states and the thickness of the film. Using a 6 band $k \cdot p$ model to capture the TSS and bulk bands nearest E_F, we may calculate the degree to which the TSS are strongly hybridized by calculating the gap in the surface state Dirac node. The thickness at which critical hybridization (ξ_C) occurs corresponds to the thickness below which surface states will only exist at energies occupied by bulk states in the continuum limit. For vacuum barriers on the top and bottom surfaces, and using parameters for α-Sn found in Ref. [210], we find $\xi_C = 19$ Å (Fig. 6.1(b)). In Ref. [210] using the full Kane model for a CdTe/α-Sn/CdTe quantum well results in $\xi_C = 24$ Å. The good agreement points toward the validity of the assumption that CdTe barriers can be considered vacuum-like. The band gap is still

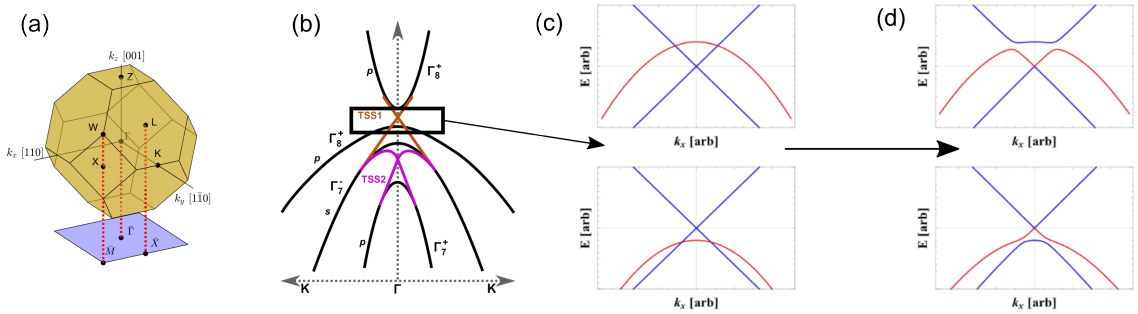

Figure 6.2: (a) Surface and bulk Brillouin zone for (001) oriented α-Sn. (b) Band schematic for α-Sn in the topological insulating phase. (c) The dispersion of the topological surface state through the $\Gamma^+_{8,v}$ band with no interaction for the case of the surface state Dirac node above and below the valence band maximum (d) The same as (c), but with hybridization turned on.

finite, leading to the slight deviation between the two cases.

However for growth of α-Sn/InSb, topological surface states are found to persist, gapless, to thicknesses as low as 20 Å via ARPES [209, 211]. Using new boundary conditions for a InSb/α-Sn/Vacuum stack, the hybridization between the top and bottom topological surface states are strongly frustrated (Fig. 6.1(c)). The value of ξ_C is now much less than 20 Å, in agreement with ARPES measurements [209, 211]. The effect of the VBO of the α-Sn film with the substrate has a strong effect on the topological phase of the confined thin film.

In α-Sn, the presence of $\Gamma^+_{8,v}$ band inside of the inverted band gap can modify the effect of topological surface state hybridization, since it will itself hybridize with the topological surface states. The VBO tunes this hybridization, as does the thickness of the film. Following the Kane Hamiltonian in Ref. [104], a minimal model can be written to understand the hybridization between the topological surface state and $\Gamma^+_{8,v}$ band.

A schematic of the band structure of α-Sn in the 3D TI phase, with the associated surface and bulk Brillouin zone is given in Fig. 6.2(a,b). In the schematic there is no hybridization between $\Gamma^+_{8,v}$ and the TSS. In addition, the Dirac node of the TSS is above the valence band maximum based off of experimental work [206,212] and contrary to first

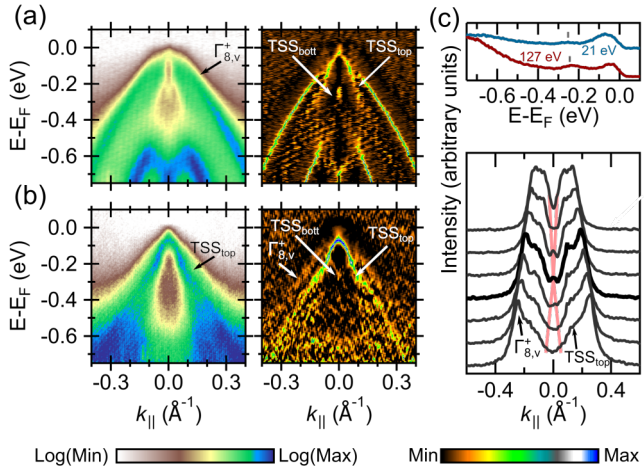

Figure 6.3: Measurements of 13 BL α-Sn/InSb(001)-c(4×4). (a) ARPES measurement and its second derivative at $\mathbf{\Gamma_{003}}$ with $h\nu = 127$ eV, where the heavy hole band has high intensity. (b) ARPES measurement and its second derivative at $h\nu = 21$ eV, where the TSS has high intensity. (c) Energy distribution curves at $\overline{\Gamma}$. The peak from the bottom TSS appears at the same energy in both. Momentum distribution curves in 30 meV increments. The bolded MDC is taken at the center of the node at $\mathrm{E - E_F} = 270$ meV.

principles calculations [107,207,209]. Prior calculations have shown the energy location of the TSS Dirac node may be tuned by a potential, such as from a surface reconstruction or heterojunction interface [302]. In Fig. 6.2(c), a zoom-in of the topological surface state in the vicinity of the valence band maximum is shown. Particle-hole symmetry is assumed. When hybridization between the topological surface state and the $\Gamma^+_{8,v}$ band is turned on (Fig. 6.2(d)), hybridization proceeds differently depending on the Dirac node location, although in both cases the TSS gaps out. When the Dirac node is above the valence band maximum, the system is gapless, but the upper branch of the TSS meets the valence band maximum. However, when the TSS Dirac node is below the valence band maximum a full gap (3D gap and 2D gap) forms. In both cases, the existence of spin-polarized surface states in a 3D band gap persists.

The penetration depth of the topological surface state, a measure of the localization of the state to the surface, can be defined as $\hbar v_F/\Delta$, where v_F is the Fermi velocity of

the topological surface state and Δ is the inverted band gap. For the topological surface state of α-Sn, the penetration depth is ~ 30 Å [210]. In α-Sn thin films that are near this thickness, the topological surface state at the substrate/film interface should be measurable in ARPES. This measurement could be complicated by the hybridization between the top and bottom surface states, but as shown earlier (Fig. 6.1) this hybridization is frustrated in the InSb/α-Sn/Vacuum system.

To observe the interface state, we study 13 BL (42 Å) α-Sn thin films grown on the Sb-rich c(4×4) reconstruction of InSb(001). In a measurement at the $\mathbf{\Gamma_{003}}$ point, the $\Gamma_{8,v}^{+}$ is the outermost band, while the topological surface state (TSS_{top}) at the vacuum/Sn interface disperses up from the Γ_7^- band at $k_{||} = \pm 0.18$ Å toward the valence band maximum (Fig. 6.3(a)). The surface Dirac node is just visible at $\mathrm{E_F}$, 120 meV above the valence band maximum. The surface Dirac node is thus in the bulk band gap, as in Fig. 6.2(b). In addition to the expected bands, there is a V-shaped band with its vertex at $\mathrm{E} - \mathrm{E_F} = 270$ meV. These features are made clearer in the curvature of the ARPES data, where there is no visible anticrossing between TSS_{top} and the $\Gamma_{8,v}^{+}$ band. This indicates that the hybridization (such as in Fig. 6.2(d)) is not strong at the vacuum/α-Sn interface, consistent with linewidth analysis of ARPES measurements of α-Sn(001) films of a similar thickness [212].

We identify the V-shaped band as the topological surface state at the α-Sn/InSb interface, TSS_{bott}. In measurements at $h\nu = 21$ eV (where the dispersion is Γ-like but the spectral intensity is weighted toward TSS_{top} over the $\Gamma_{8,v}^{+}$ band (Chapter 5)), the intensity of TSS_{bott} is reduced as much as the intensity of the $\Gamma_{8,v}^{+}$ (Fig. 6.3(b)). In the curvature it can be seen that the TSS_{bott} and $\Gamma_{8,v}^{+}$ are still present with the same dispersion as in Fig. 6.3(a). The location of the vertex of the V-shaped TSS_{bott} is at the same energy location in both cases, extracted from energy distribution curves (EDCs) at the $\overline{\Gamma}$ point (Fig. 6.3(c)). In momentum distribution curves (MDCs) taken around the

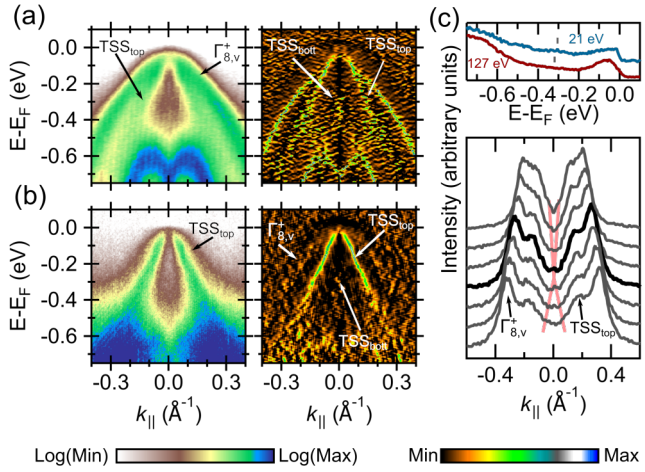

Figure 6.4: Measurements of 13 BL α-Sn/InSb(001)-c(8×2). (a) ARPES measurement and its second derivative at $\mathbf{\Gamma_{003}}$ with $h\nu = 127$ eV, where the heavy hole band has high intensity. (b) ARPES measurement and its second derivative at $h\nu = 21$ eV, where the TSS has high intensity. (c) Energy distribution curves at $\overline{\Gamma}$. The peak from the bottom TSS appears at the same energy in both. Momentum distribution curves in 30 meV increments. The bolded MDC is taken at the center of the node at $E - E_F = 330$ meV.

vertex, it becomes clear that TSS$_{bott}$ has a lower branch as well. The upper and lower branches of TSS$_{bott}$ are visible as small shoulders at lower $|k_{||}|$ than the TSS$_{top}$ peak (Fig. 6.3(c)). This state then has a dispersion consistent with the strong hybridization case in Fig. 6.2(d). The Dirac node of TSS$_{bott}$ is ∼110 meV below the valence band maximum.

For heterovalent interfaces, the charge at the interface is very sensitive to the interface chemistry [303]. This has been validated for numerous heterovalent semiconductors, such as Ge/GaAs [26, 304–308] where the measured band offset can vary by more than 100% dependent on growth conditions. We also studied 13 BL α-Sn grown on the In-rich c(8×2) reconstruction of InSb(001) to tune the interface chemistry.

In measurements at $\mathbf{\Gamma_{003}}$ of 13 BL α-Sn/InSb(001)-c(8×2), the shapes and approximate locations of TSS$_{top}$ and the $\Gamma^+_{8,v}$ bands are the same as for growth on InSb(001)-c(4×4) (Fig. 6.4(a)). There is a rigid band shift of these bands (and the Γ^-_7 band) from enhanced indium p-type doping in this film [206]. The projected location of the Dirac

node of TSS_{top} is 130 meV above the valence band maximum, in good agreement with the 120 meV spacing found for 13 BL α-Sn/InSb(001)-c(4×4). The band velocities of TSS_{top} in the two cases is identical within the margin of error as well [206]. The node of TSS_{bott} is not clear, but the upper and lower branches are visible in the gap between $\Gamma^{+}_{8,v}$ and Γ^{-}_{7}. When switching to $h\nu = 21$ eV, the intensity of $\Gamma^{+}_{8,v}$ and TSS_{bott} is again suppressed. The node is visible in the curvature of these measurements, where the node of TSS_{bott} is at $E - E_F = 330$ meV, 240 meV below the valence band maximum. This spacing is double that found for growth on InSb(001)-c(4×4). The upper and lower branches of TSS_{bott} are drawn schematically in Fig. 6.4(c), as the peak intensities are too weak to fit robustly. The TSS_{bott} band velocities appear to be modified in the two cases. This is consistent with the change in Dirac node location. The endpoints of the upper and lower branches ($\Gamma^{+}_{8,v}$-Γ^{-}_{7} gap) remain the same, so if the node location within this gap changes the linear band velocities must change.

Since these two films have equivalent thicknesses (13 BL) and equivalent top surfaces (α-Sn/vacuum), the change in interface chemistry, as expected, must lead to the change in TSS_{bott} The band velocities, Dirac node location, and thus hybridization of TSS_{bott} appear to then be very sensitive to the interface chemistry at the α-Sn/InSb(001) interface. A schematic for this behavior is given in Fig. 6.5(a) for the c(4×4) interface and Fig. 6.5(b) for the c(8×2) interface. The TSS_{top} and $\Gamma^{+}_{8,v}$ bands remain unmodified (although the chemical potential is slightly changed), while TSS_{bott} is modified strongly. We are likely able to observe TSS_{bott} (and changes to it) since it has a finite penetration depth (∼30 Å) toward the vacuum/α-Sn interface. This penetration depth is also likely increased (i.e. reduced surface localization) from hybridization with the bulk valence band. The ARPES measurements also have an information depth of > 10 Å via a modified fit to the universal curve [143]. It is then not too surprising that we can observe TSS_{bott} in our 42 Å (13 BL) films. This measurement is shown schematically in Fig. 6.5(c).

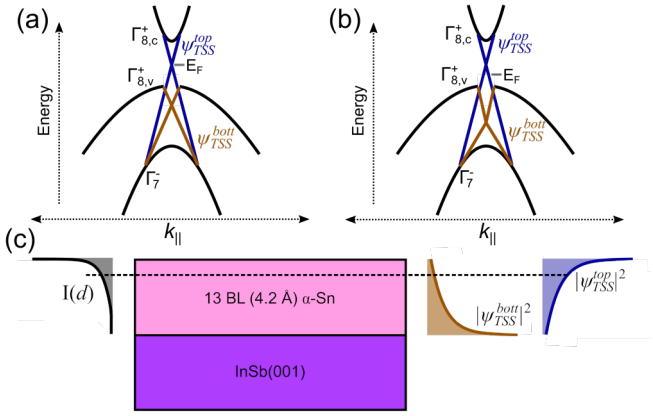

Figure 6.5: Schematic representation of the measured ARPES spectrum of the top and bottom surface states for (a) 13 BL α-Sn/InSb(001)-c(4×4) and (b) 13 BL α-Sn/InSb(001)-c(8×2). (c) Representation of the ability of ARPES to measure the bottom surface state.

In order to confirm that this attribution is correct, we also perform the same ARPES measurements on 400 BL (130 nm) α-Sn/InSb(001)-c(8×2) (Fig. 6.6). Here the dispersion of TSS_{top} and $\Gamma^+_{8,v}$ is similar to that found in Fig. 6.3 and Fig. 6.4, although the chemical potential in this case is farther below the valence band maximum. The energy range over which the TSS_{bott} would be expected to appear is indicated in Fig. 6.6(a). The TSS_{bott} state is absent in both the $\mathbf{\Gamma_{003}}$ measurements (Fig. 6.6(a)) and its curvature (Fig. 6.6(b)), and in the $h\nu = 21$ eV measurement (Fig. 6.6(c)) and its curvature (Fig. 6.6(d)). The existence of TSS_{bott} has also not been found in other ARPES measurements of thick (> 10 nm) α-Sn films on InSb [209] and on CdTe [241]. Since we see (1) no evidence of TSS_{bott} in thick films and (2) a change in TSS_{bott} from a change in interface chemistry, we confirm that TSS_{bott} is indeed the hybridized topological surface state at the bottom interface.

The measurement of an ungapped topological surface state at both the top and bottom interface of α-Sn/InSb(001) is consistent with the frustrated hybridization shown earlier through a toy model. Now we take a more realistic model of the vacuum/Sn/InSb stack and incorporate it into a slab-based $k \cdot p$ model. From here we can model the

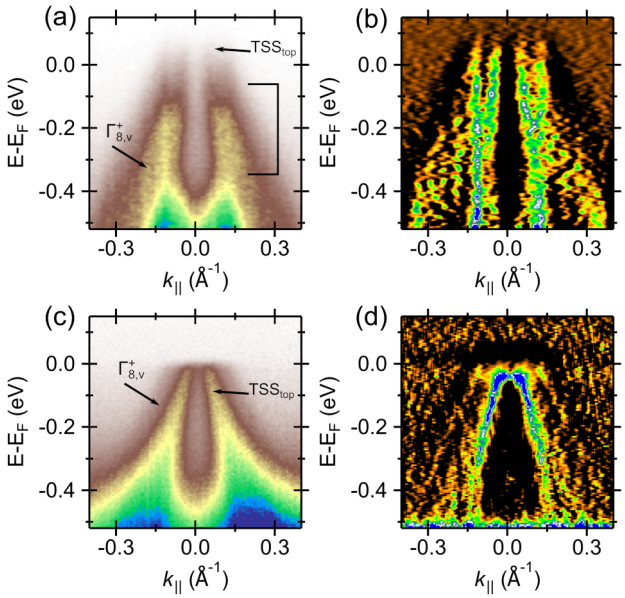

Figure 6.6: ARPES measurements of 400 BL α-Sn/InSb(001)-c(8×2). Measurement at (a) $h\nu = 127$eV and (b) its second derivative. The range at which TSS$_{bott}$ should appear is indicated. Measurement at (c) $h\nu = 21$ eV and (d) its second derivative.

surface spectral function of these slabs to simulate the measured ARPES measurements. Summarized in Fig. 6.7, TSS$_{top}$ is below the valence band maximum in all cases. This is likely because the surface potential is passivated in the calculation, rather than reflecting the true surface charge due to the surface reconstruction of α-Sn(001). The valence band offset clearly effects the presence of a bulk band gap and the dispersion of the topological surface states. This shows that the valence band offset of the substrate with the film tunes the degree of hybridization between the $\Gamma^{+}_{8,v}$ and the TSS. When the interface chemistry is modified for the two 13 BL films, the VBO is changed; this VBO shift modifies the hybridization of the TSS as well. The measured ARPES spectra for thin films of α-Sn should then be very sensitive to the substrate preparation prior to α-Sn growth.

Knowledge of the valence band offset between the film and the substrate is also essential to explain magnetotransport, magnetoabsorption, and other more indirect measurements of the α-Sn band structure. Band offset measurements could be performed *in situ*

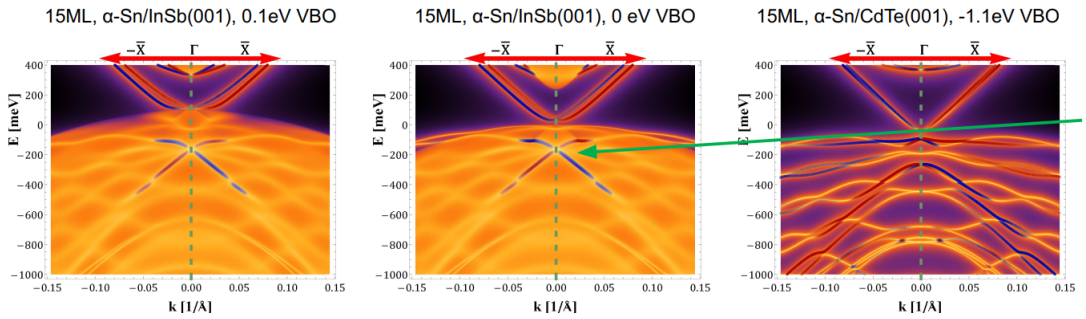

Figure 6.7: Calculated ARPES spectra of 15 BL α-Sn with two possible band alignments with an InSb(001) substrate or known VBO with a CdTe(001) substrate. The topological surface state is indicated. Calculations courtesy George de Coster.

with XPS, but growth interruptions could possibly modify the band offset and interdiffusion makes robust extraction of the offset difficult. Alternatively, capacitance-voltage profiling of a vertical diode would allow measurement of the band offset [304].

6.4 Conclusion

In this chapter, we clarified the effect of the substrate and of the surface state-bulk band hybridization for determining the topological phase of thin films of α-Sn. We found that hybridization at the α-Sn/InSb interface can frustrate hybridization between top and bottom topological surface states. Both the top and bottom topological surface states have been directly measured, with their Dirac nodes above and below the valence band maximum, respectively, and each with different hybridization strengths with the valence band.

Our work allows a path forward for deterministic control of the topological phase of α-Sn for device applications. It also points toward a potential confounding variable in different experimental results: the topological phase under thin film confinement is sensitive to substrate preparation, surface capping, and growth conditions.

Chapter 7

Inversion symmetry breaking in α-Sn/InSb

7.1 Introduction

α-Sn, the diamond allotrope of Sn (Fig. 7.1(a)), is a well-known zero-gap semiconductor with band inversion [88]. The α-phase is a low temperature phase, above -13 °C a semimetallic superconducting β-phase is stable [87]. The crystal structure and electronic structure of α (or grey) Sn were investigated thoroughly in the 1950s and 1960s using single crystals formed from Hg flux or by cooling filaments or powders of the β-phase [89, 90, 94, 309–312]. These crystals were generally small and the transition temperature to the β-phase was still under room temperature. In the 1980s, Farrow *et al.* were able to synthesize large area singe crystal α-Sn thin films on closely symmetry and lattice matched CdTe and InSb substrates [101]. The substrate stabilization effect raised the $\alpha \rightarrow \beta$ transition temperature above room temperature, increasing the accessibility of α-Sn experiments.

With band inversion, a zero band gap, and an inversion-symmetric diamond crystal

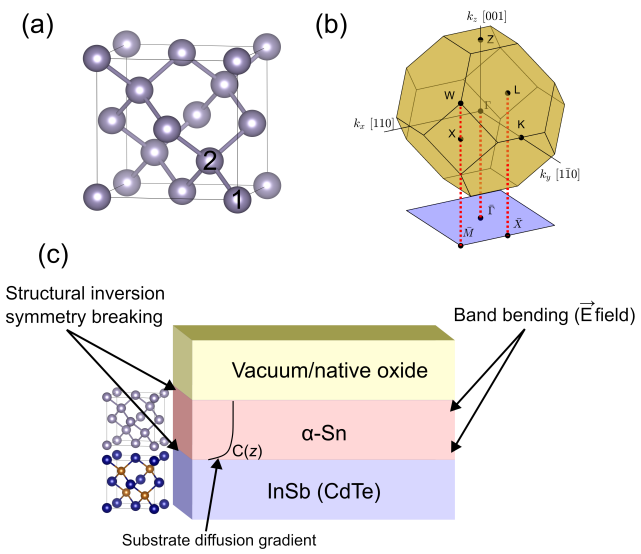

Figure 7.1: (a) Crystal structure of inversion-symmetric diamond lattice α-Sn. The two atom basis is shown. (b) Bulk and surface Brouillin zone of α-Sn(001). (c) Layer schematic of α-Sn thin films showcasing potential origins of inversion symmetry breaking.

lattice, α-Sn can be thought of as a parent phase to many other topologically non-trivial systems such as HgTe (its inversion-asymmetric analogue), ternary half-Heusler compounds, Li_2AgSb-based semiconductors, and more [110]. A better understanding of α-Sn thus provides a better understanding of the systems to which it is adiabatically connected. The zero gap degeneracy is ensured by the symmetry of the crystal (equivalent to a light hole-heavy hole degeneracy in other Group IV and III-V semiconductors). With perturbations such as strain or quantum confinement, the zero gap phase in the bulk is expected to transform into a 2D topological insulator (quantum spin Hall insulator), a 3D topological insulator, a 2D Dirac semimetal, or a 3D Dirac semimetal [107, 109, 210, 213, 229, 230, 232, 240, 242]. Other perturbations such as a magnetic field or circular polarized light can generate a 2D or 3D Weyl semimetal phase [109]. In addition, α-Sn is the only elemental material showing many of these phases.

The breaking of inversion symmetry in α-Sn should then change the spectrum of

topological phases in this system. Typical thin film growth of α-Sn on heteropolar semiconductor substrates is assumed to preserve the inversion symmetry found in bulk α-Sn, however there are many mechanisms by which this symmetry may be broken.

Inversion symmetry breaking may be loosely grouped into two categories: structure-based and electric field-based (Fig. 7.1(c)). The presence of an electric field across the film inherently breaks inversion symmetry. In thin films this may be applied through a gate effect, through surface alkali dosing [313], surface band bending, or heterojunction band bending (i.e. substrate charge transfer). At surfaces and interfaces, the breaking of translational symmetry leads to a local breaking of inversion symmetry, typified by the Rashba effect acting on surface states. The global inversion symmetry is broken from the asymmetric nature of this α-Sn film with an InSb bottom barrier and a vacuum or tin oxide top barrier providing the asymmetry. The bulk inversion symmetry could also be broken through some modification of the Sn crystal structure (Fig. 7.1(a)), typified by the Dresselhaus effect in III-V semiconductors [20]. Defect concentration gradients and inhomogenous strain gradients have also been shown to break inversion symmetry [314, 315].

Here we present evidence of inversion symmetry breaking in α-Sn thin films grown on zincblende InSb(001) substrates. This symmetry breaking is found by observing fingerprints in the electronic structure using angle-resolved photoemission spectroscopy. We discuss the potential origins and ramifications of this symmetry breaking.

7.2 Methods

Thin films of α-Sn were grown on InSb(001) as discussed in Chapter 4. Growth proceeded on different reconstructions of InSb(001), namely the In-rich c(8×2) and the Sb-rich c(4×4), to tune the interface charge transfer effect. Reflection high energy elec-

tron diffraction of α-Sn films showed the mixed $(2 \times 1)/(1 \times 2)$ surface reconstruction typical for this system.

ARPES measurements were performed at beamline 5-2 at the Stanford Synchrotron Radiation Lightsource (SSRL) or at beamline 10.0.1.2 at the Advanced Light Source with p-polarized light. At both beamlines the sample temperature was kept below 20 K and the base pressure was lower than 3×10^{-11} Torr. Data were collected using a Scienta Omicron DA30L detector. The samples were transferred between growth systems at UCSB and the beamlines at SSRL and ALS using a ultrahigh vacuum suitcase with base pressure lower than 4×10^{-11}.

Slater-Koster tight-binding calculations were performed using the *chinook* Python package [167]. Tight-binding terms were adapted from those listed in Ref. [170]. Inversion symmetry was broken by offsetting the on-site potentials of the two atoms in the α-Sn basis by a constant value, Δ. This approach is essentially equivalent to breaking the bulk inversion asymmetry, but likely does not accurately reflect electric-field or surface-based inversion symmetry breaking.

7.3 Results

The tight-binding band structure of bulk α-Sn with inversion symmetry preserved is given in Fig. 7.2(a). The $\Gamma_{8,c}^{+}$ conduction band in this system has p-character and is degenerate at Γ with the p-like $\Gamma_{8,v}^{+}$ valence band. Below this is the s-like Γ_{7}^{-} band. This inversion between the p-like Γ_{8}^{+} and s-like Γ_{7}^{-} is the band inversion that determines the non-trivial topology in this system. Beneath Γ_{7}^{-} is the Γ_{7}^{+} split-off band. The Γ_{8}^{+} and the Γ_{7}^{-} bands are degenerate at the X point (X_5), as expected in a homopolar diamond structure semiconductor.

Inversion symmetry breaking in the tight-binding model is qualitatively shown by

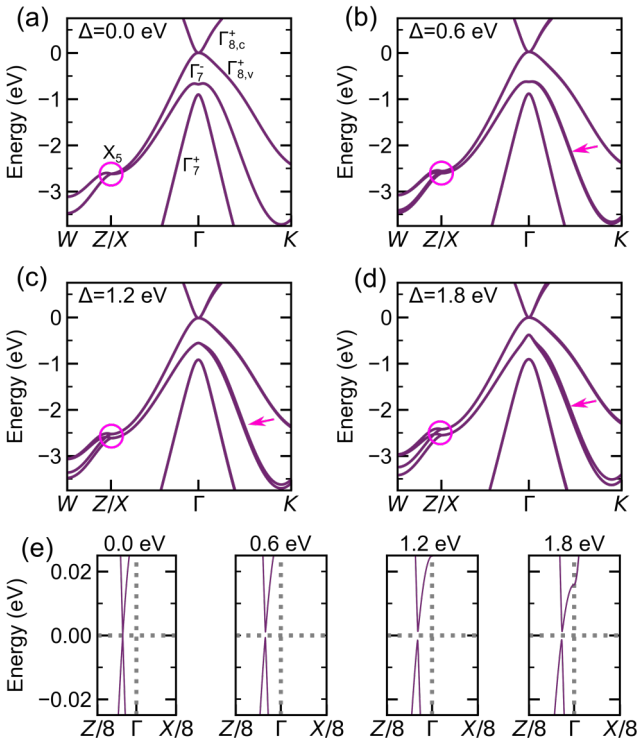

Figure 7.2: Unstrained α-Sn band structure with (a) inversion symmetry preserved and inversion symmetry broken by a potential offset of (b) Δ=0.6 eV (c) Δ=1.2 eV and (d) Δ=1.8 eV. Gap openings and spin-splitting are indicated in pink. (e) The effect of inversion symmetry breaking on the Dirac node in α-Sn with 1% biaxial compressive strain for inversion symmetry preserved and broken by the potentials used in (b)–(d).

offsetting the on-site energies of the two Sn atoms in the α-Sn basis (Fig. 7.1(a)). In its simplest form, the breaking of inversion symmetry in α-Sn converts the unstrained (strained) space group of $Fd\bar{3}m$ ($I4_1/amd$) to $F\bar{4}3m$ ($I\bar{4}m2$). For unstrained (strained) point groups this corresponds to O_h (D_{4h}) converting to T_d (D_{2d}). This symmetry lowering will open up a gap at any degeneracy ensured by the higher symmetry.

In the case of strained (or unstrained) α-Sn, this is the band degeneracy at the X or Z point (Fig. 7.2(b)). As Δ is increased, the gap at X is widened (Fig. 7.2(c,d)). The breaking of inversion symmetry leads to spin-splitting of the bands, most pronounced in the Γ_7^- band in the $K-\Gamma-K$ direction. We seek to identify the breaking of these

degeneracies by measuring the electronic structure of α-Sn thin films using angle-resolved photoemission spectroscopy.

α-Sn grown under biaxial compressive strain on InSb ($\epsilon_{xx} = -0.15\%$), results in a 3D Dirac semimetal phase [109,209,210,232,241]. By breaking inversion symmetry in a Dirac semimetal, a Weyl semimetal phase should form—as in the inversion-asymmetric HgTe system under compressive strain [316]. However, in Fig. 7.2(e) we instead find that a gap opens in the Dirac node. Since band inversion is preserved from the breaking of inversion symmetry, a compressive strained α-Sn thin film with broken inversion symmetry is in a 3D topological insulator phase. This transition is seen in another topological semimetal Cd_3As_2 as well [317]. Tensile strained α-Sn (with inversion symmetry preserved) forms a 3D topological insulator phase as well [109, 318]. The breaking of inversion symmetry does not close this gap, and thus preserves the 3D topological insulator phase.

We search for spin-splitting in the $K - \Gamma - K$ direction in α-Sn thin films using angle-resolved photoemission spectroscopy. These measurements are performed at $\mathbf{\Gamma_{003}}$ ($h\nu = 127$ eV [170]) with p-polarized light to enhance sensitivity to the bulk bands of α-Sn. In a 13 BL film grown on the Sb-rich c(4×4) reconstruction of InSb(001), there is significant spin-splitting of the Γ_7^- band along the $K-\Gamma-K$ direction (Fig. 7.3(a)). The magnitude of the splitting is clearer in the second derivative of the spectrum and increases with higher k. In another 13 BL film grown instead on the In-rich c(8×2) reconstruction of InSb(001), the splitting is still present, but the signal from the spin-split bands are weaker (Fig. 7.3(b)). For a thick 400 BL film, no splitting is readily apparent in the photoemission spectrum or its second derivative (Fig. 7.3(c)).

Momentum distribution curves (MDC) taken 2 eV beneath the valence band maximum from each spectrum in Fig. 7.3 are given in Fig. 7.4. Although the splitting was not very clear for the 400 BL sample in the spectrum, the peak shapes of all three samples are equivalent. This indicates that any spin-splitting seen in Fig. 7.3(a) is present with

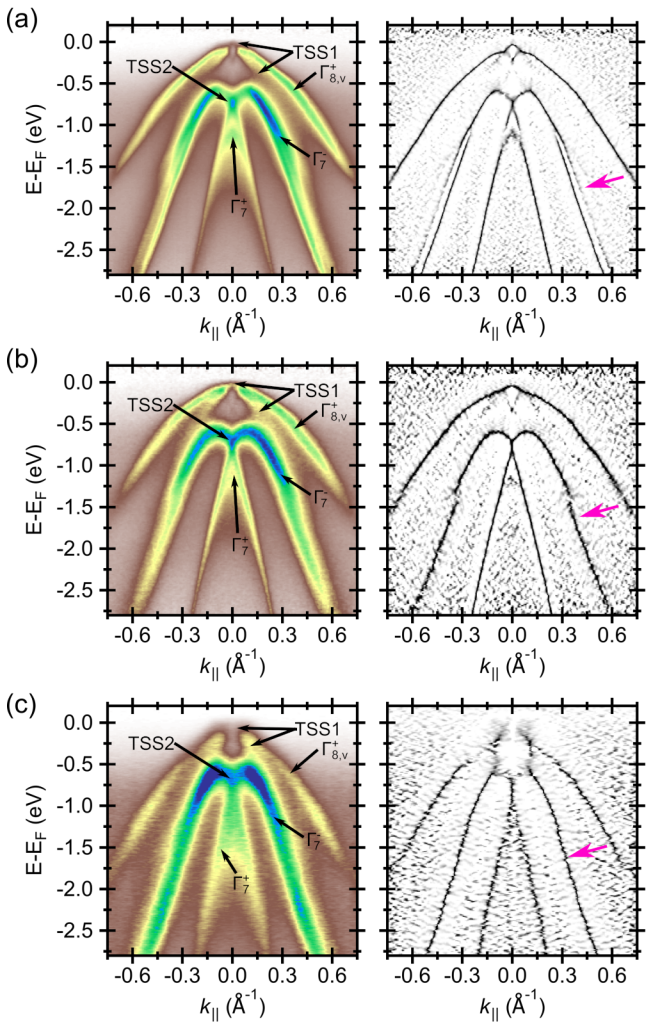

Figure 7.3: spin-splitting observed in ARPES measurements and second derivatives of the data along the $K-\Gamma-K$ direction for (a) 13 BL α-Sn/InSb(001)-c(4×4), (b) 13 BL α-Sn/InSb(001)-c(8×2), and (c) 400 BL α-Sn/InSb(001)-c(8×2). Measurements are performed at $\mathbf{\Gamma_{003}}$ using a photon energy of 127 eV and assuming an inner potential of 5.8 eV [170].

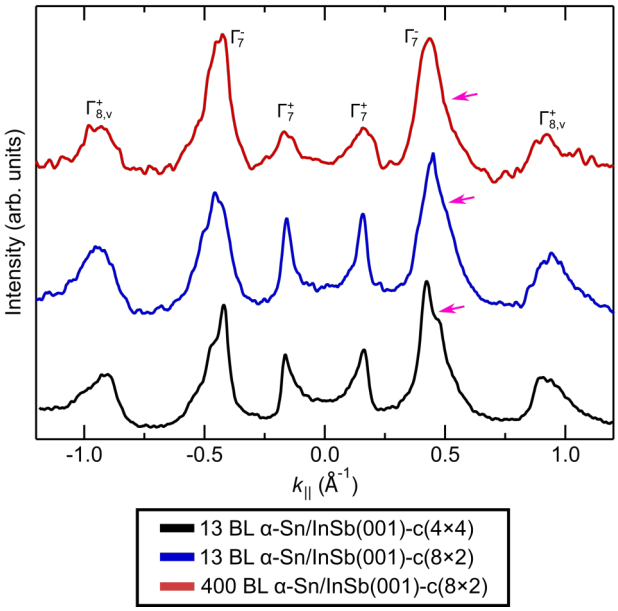

Figure 7.4: Momentum distribution curves (MDCs) for the samples studied in Fig. 7.3. The MDCs are taken from 2 eV below the valence band maximum and integrated over a 5 meV energy range.

an identical magnitude in Fig. 7.3(b,c), but is washed out in the raw spectra potentially from lower surface quality. The MDC peaks corresponding to the $\Gamma_{8,v}^{+}$ and Γ_{7}^{-} also appear asymmetric, potentially arising from spin-splitting in these bands as well. The magnitude of the spin-splitting is largest for the Γ_{7}^{-} band, consistent with our tight-binding model in Fig. 7.2.

In addition to spin-splitting, inversion asymmetry should manifest as a breaking of degeneracies at the Z point. The degenerate $\Gamma_{8,v}^{+}$ and Γ_{7}^{-} bands and the degenerate Γ_{7}^{+} and Γ_{6}^{+} bands are each split with a nonzero Δ (Fig. 7.5(a)). The opening of this gap in α-Sn/InSb(001) was previously investigated and not found to be present [258]. However, these measurements were performed at low photon energies where the inner potential model required *ad hoc* modifications in order to faithfully reproduce the α-Sn band structure along the $Z - \Gamma - Z$ direction [258]. We instead investigate the Z point

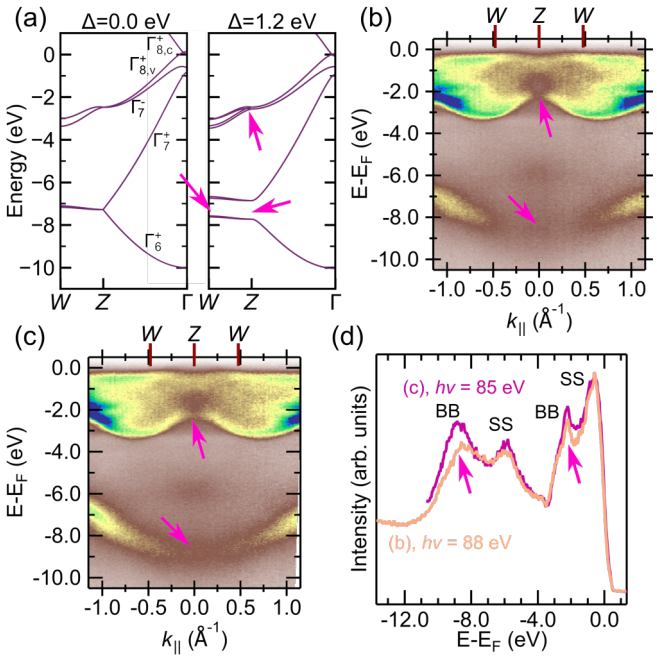

Figure 7.5: Degeneracy breaking at the Z point in 400 BL α-Sn. (a) Tight-binding calculation of the effect of inversion symmetry breaking at Z. Measurements in the $W-Z-W$ direction at the Z point at (b) $h\nu = 88$ eV ($V_0 = 9.3$ eV [170]) and (c) $h\nu = 85$ eV ($V_0 = 5.8$ eV [209]). (d) Energy distribution curves taken at the Z point integrated over ± 0.01 Å^{-1}. Bulk bands and surface states are indicated.

in between $\mathbf{\Gamma_{002}}$ and $\mathbf{\Gamma_{003}}$.

We investigate this Z point using two published inner potentials for α-Sn. In Fig. 7.5(b), for an inner potential $V_0 = 5.8$ eV ($h\nu = 88$ eV) [170] there is a surface state near E_F. Below this, the expected dispersion in the $W-Z-W$ direction is visible. However, the distinction between the two spin-degenerate bands dispersing between the W and Z points is not clear, indicated by the upper pink arrow. There is a matrix element effect strongly reducing the intensity of these bands near the Z point. There is another surface state visible near $E - E_F = 6$ eV. The second set of bulk bands is visible at energies below this, again indicated by a pink arrow. Using an inner potential $V_0 = 9.3$ eV ($h\nu = 85$ eV), the same bands with slightly shifted energies are present (Fig. 7.5(c)).

Energy distribution curves (EDCs) taken at the Z point of Fig. 7.5(b,c) are given in

Fig. 7.5(d). The two surface state peaks do not change with photon energy, consistent with their 2D nature. The lower energy bulk band shifts in energy deeper below E_F with the lower photon energy (higher inner potential). The higher energy bulk band does not appear to shift. These relative shifts are consistent with the $Z-\Gamma-Z$ dispersion of these bands. The lower energy bulk bands have a higher band velocity near Z than the higher energy bulk bands, and as such should shift more in energy with a fixed $h\nu$ (equivalent to a k_z) change.

While the increased linewidth of the lower energy bulk bands could be consistent with the increased splitting of these bands at the Z point (Fig. 7.5(d)), this effect could also have its origin in k_z broadening of the two sets of bands with very different band velocities. The results of multipeak fits to the bulk band peaks are also difficult to address physically due to this issue with k_z broadening. Instead, we investigate the X point near the $\mathbf{\Gamma_{002}}$ and $\mathbf{\Gamma_{003}}$ points, where the band velocity in the Z direction is smaller.

The calculated dispersion in the $X-\Gamma-X$ direction with broken inversion symmetry is reproduced in Fig. 7.6(a), where pink arrows point toward where a gap has opened. No significant spin-splitting is visible in this direction. An ARPES measurement along this direction of a thick film at the $\mathbf{\Gamma_{003}}$ is shown in Fig. 7.6(b), where the three bulk bands $\Gamma^+_{8,v}$, Γ^-_7, and Γ^+_7 have high intensity. The dispersion matches that expected from the tight-binding calculations. At the X point there is a surface state ~600 meV above the X minimum.

At $\mathbf{\Gamma_{002}}$, only the $\Gamma^+_{8,v}$ has high intensity (Fig. 7.6(c)). However, the same surface state at the X point is still visible. This is more visible in Fig. 7.6(d), centered at X, where the expected splitting from the inversion symmetry breaking would occur is indicated with a pink arrow. Should this surface state be interpreted as the $\Gamma^+_{8,v}$-Γ^-_7 gap, the gap size would be over 600 meV; this is an unphysically large value compared to similar zincblende III-V and II-VI semiconductors (usually much less than 500 meV).

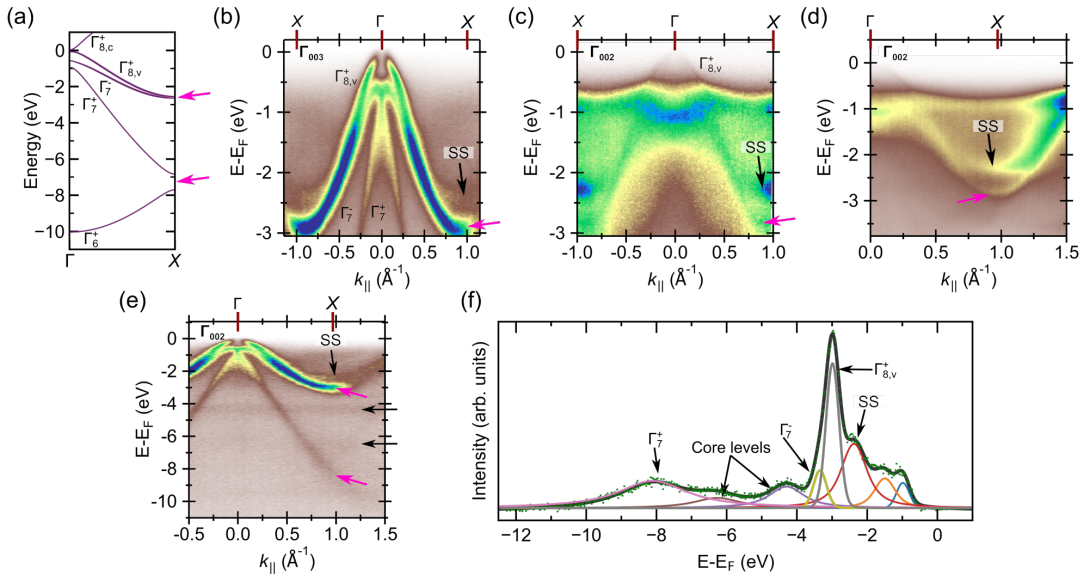

Figure 7.6: Degeneracy breaking at the X point in 400 BL α-Sn. (a) Tight-binding calculation of inversion-asymmetric α-Sn with $\Delta = 1.2$ eV. Pink arrows indicate broken degeneracies. ARPES measurements in the $X - \Gamma - X$ direction at (b) $\mathbf{\Gamma_{003}}$ ($h\nu = 127$ eV) and (c) $\mathbf{\Gamma_{002}}$ ($h\nu = 53$ eV). Measurements in the same direction, centered near the X point for (d) $\mathbf{\Gamma_{002}}$ and (e) $\mathbf{\Gamma_{003}}$. (f) Multipeak fit to an EDC at X near $\mathbf{\Gamma_{003}}$. See the text for details of the fit.

In the $\mathbf{\Gamma_{003}}$ measurement—where the $\Gamma^+_{8,v}$ and Γ^-_7 both have high intensity—if inversion symmetry is preserved, then these bands should only be degenerate at the X point. In Fig. 7.6(b), the splitting between the $\Gamma^+_{8,v}$ and Γ^-_7 approaches a constant, non-zero value near $k_{||} = 0.25$ Å^{-1} and retains this splitting *with negligible decrease in magnitude* through the X point. This indicates the degeneracy at X is indeed broken.

In Fig. 7.6(e) we attempt to observe the degeneracy broken between the Γ^+_6 and Γ^+_7 bands at the X point as well. There is no measurable intensity from the Γ^+_6 band. The critical points of transitions involving the first three valence bands in α-Sn are well established, but those corresponding to the Γ^+_6 band to our knowledge have not been found. On the other hand, measurements of the Γ^+_6 band have been reported in ARPES under similar experimental conditions to those used in this work [258]. Changing the polarization of light to s or circular does not reveal this feature. The origin of the

missing band is unclear, but likely arises from matrix element effects.

A multipeak fit is performed on an EDC taken at the X point in Fig. 7.6(d). Here peaks corresponding to each of the bulk bands ($\Gamma_{8,v}^{+}$, Γ_{7}^{-}, and Γ_{7}^{+}), as well as two core level peaks, are observed. The multipeak fit was performed with 8 Voigt profiles with the same Gaussian resolution component and variable Lorentzian linewidth. Since there is no visible Γ_{6}^{+} band, it is difficult to say whether the low energy ($E - E_F = 8$ eV) peak has a broken degeneracy or not. There is, on the other hand, a splitting at X of 260 ± 76 meV between the $\Gamma_{8,v}^{+}$ and Γ_{7}^{-} bands, indicating again that inversion symmetry is broken in α-Sn thin films.

7.4 Discussion

From these results, we find that inversion symmetry is broken in α-Sn thin films grown on InSb(001) that are both thin (13 BL/4.2 nm) and thick (400 BL/130 nm). Because the magnitude of spin-splitting in the Γ_{7}^{-} band (Fig. 7.3, Fig. 7.4) is not modified by either adjusted interface charge or adjusted film thickness, the role of the substrate and the substrate/film interface appears to be minimal. Heterojunction and/or surface potentials are, at maximum, around ∼300 meV. This value is inserted into the usual depletion width equation

$$W = \sqrt{\frac{2\epsilon_r \epsilon_0}{q} \frac{V_{bi}}{n}} \tag{7.1}$$

where we set the dielectric constant of α-Sn to be $\epsilon_r = 22$ [240] and assume $n \approx 10^{18}$ cm^{-3} (Chapter 4 & Chapter 5). We find the depletion width under these conditions to be roughly 30 nm. Thus any net electric fields applied to the surface or interface of the film should be screened heavily in the 400 BL (130 nm) film. The effect of inversion symmetry breaking is also just as strong in the 400 BL film as in the 13 BL film. The

inversion symmetry breaking is then either a bulk crystalline symmetry breaking or an effect localized to the surface (where ARPES probes only the first $\sim$1 nm of the film).

The abrupt termination of the film at the surface and interface results in the Rashba effect, however the Rashba effect should only act on the surfaces states as is typically seen in high Z semiconductors like Bi_2Se_3 [319]. In these α-Sn films, the bulk bands are susceptible to the inversion symmetry breaking potential. The Rashba effect is then not likely.

This then only leaves structural origins to the inversion symmetry breaking in this system, which also come in a few different manners. One cause could be some distortion of the crystal structure of α-Sn such that it approximates the heteropolar zincblende semiconductors, the bulk inversion asymmetry. This is a similar case to the conditions in the tight-binding approximation. This bulk crystalline symmetry breaking should be readily visible in X-ray diffraction of the normally forbidden $h+k+l = 4n+2$ reflections in a group IV system. However, due to the tetrahedral distortion of valence electron charge these reflections are actually not forbidden and have been observed in bulk single crystals of α-Sn [320]. This effect is independent of an azimuthal-dependent forbidden reflection intensity from multiple reflections, known as $Umweganregung$, which also occurs at these forbidden reflections [320, 321]. Since the lattice constant of α-Sn is also within 0.2% of InSb and CdTe, its most common substrates, it would be difficult to isolate these weak peaks in any case. A measurement such as second harmonic generation could potentially observe this change in basis, provided the intensity of the incident light is kept low to avoid β-Sn formation.

This change in crystal structure to break inversion symmetry could also shift the film from nonpolar to polar. Growth of polar/nonpolar/polar stacks is well-studied in the Ge/GaAs system, among other semiconductors, where the polarity of the top layer may be inverted from that of the bottom layer by masking the bottom layer polarity with the

nonpolar layer [322]. This effect is sensitive to the thickness of the nonpolar interlayer and interfacial bonding between the nonpolar and polar layers [323, 324]. In α-Sn/InSb(111) this effect seems to be very sensitive to Sb incorporation in the α-Sn film [325], indicating that perhaps there is competition with a potential due to inversion symmetry breaking. These trilayer structures have not yet been grown on the (001) surface. A gradient of dopants or defects in the film may also enhance an inversion symmetry breaking potential in the crystal structure [315]. A dopant gradient from diffusion with the InSb substrate is well-known for α-Sn/InSb heterostructures [108, 206, 209, 212, 215, 220, 326, 327].

Inhomogenous strain gradients—such as could be generated from a Sn native oxide or partial relaxation/dislocation generation—have also been suggested to break inversion symmetry [314]. Our α-Sn films are fully strained to the substrate within the resolution of our X-ray diffraction measurements (Chapter 5), but potentially have nuclei of β-Sn generating this inhomogenous strain field. However, the lack of observation of β-Sn in X-ray diffraction implies they are not large or numerous enough to have a significant effect. The application of inhomogenous strain to break inversion symmetry was originally proposed and has mainly been studied in silicon. This symmetry breaking has recently come into question; most of the measured effects are more consistent with defect-induced electric field effects rather than bulk inversion symmetry breaking [272, 328, 329].

Finally, the inherent asymmetry of the Vacuum/α-Sn/InSb stack could break inversion symmetry. A similar effect has recently been seen in our group in Bi/InSb(111) [330]. This effect is only strong if there is also strong hybridization between the film and the substrate [331]. The degree of hybridization between α-Sn and InSb has been calculated [211] and appears to be strong, in agreement with the discussion in Chapter 6. This effect is then the most likely origin of inversion symmetry breaking in α-Sn/InSb(001). Hybridization with the CdTe substrate appears to be weaker [210] and would potentially not show this inversion symmetry breaking. The nature of this hybridization has been

discussed in detail in Chapter 6.

7.5 Conclusion

In this chapter we investigated inversion symmetry breaking in α-Sn thin films on InSb(001). A simple tight-binding approach allowed us to find the observed fingerprints of this symmetry breaking, including degeneracy breaking at the X point and spin-splitting of the bulk bands. Using angle-resolved photoemission spectroscopy we identify the presence of these fingerprints in both thin 13 BL (4.2 nm) and thick 400 BL (130 nm) α-Sn films. Many electronic and structural causes of this inversion symmetry breaking exist, but we find that the most likely causes are either the strong hybridization between α-Sn and InSb leading to an inversion-asymmetric layer stack or a change to the crystal structure of the α-Sn film. This inversion symmetry breaking modifies the topological phase diagram of α-Sn and potentially explains discrepancies in topological phase identification in the literature.

Chapter 8

Topological phase transitions in α-$Sn_{1-x}Ge_x$

8.1 Introduction

Compressive strained α-Sn thin films are well studied, as discussed extensively in previous chapters. Tensile strained films, which can host a different spectrum of topological phases, have not been studied in detail experimentally. Of most interest with this perturbation is the relatively wide band gap (>100 meV) 3D topological insulator phase [104, 109]. We achieve tensile strain by alloying α-Sn with isovalent isostructural Ge (Fig. 8.1(a)) to reduce the film lattice constant.

The bulk band structure of α-Sn has been discussed in detail in previous chapters, but is briefly summarized here. There are three valence bands, the Γ_7^+ split-off band, the Γ_7^- inverted conduction band, and the $\Gamma_{8,v}^+$ heavy hole band. The heavy hole band is, in the bulk, degenerate with the $\Gamma_{8,v}^+$ inverted conduction band at Γ only. The bulk band structure is replotted in Fig. 8.1(c). Calculations do not accurately show the location and dispersion of the surface states.

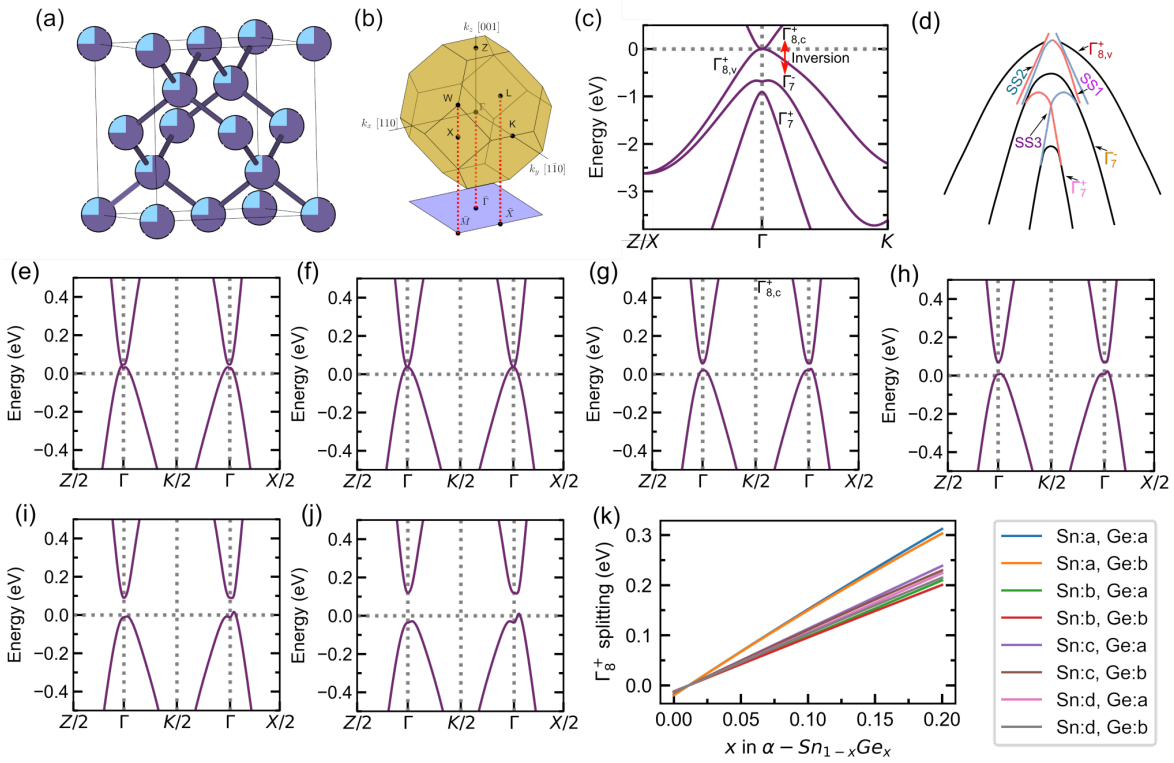

Figure 8.1: (a) Crystal structure of α-$Sn_{1-x}Ge_x$. (b) Brillouin zone schematic for this system (c) Tight-binding calculated band structure of α-Sn. (d) Schematic band diagram including surface states derived in Chapter 5. Calculations of the region near the Γ point with the application of strain of (e) -0.15%, (f) 0%, (g) 0.2%, (h) 0.5%, (i) 0.8% and (j) 1.2%. Positive strain corresponds to biaxial tensile strain. (k) Calculated band gap vs. Ge incorporation using a range of deformation potentials for pseudomorphic growth on InSb(001). Sn:a our work, Sn:b [318],Sn:c [332], Sn:d [241], Ge:a [332],Ge:b [318].

In Chapter 5, we mapped out two spin-polarized surface states, SS1 and SS2 near the valence band maximum. We proposed that SS2 was the Dirac-like topological surface state in this system. There is a secondary band inversion [170] which results in another spin-polarized topological surface state well below the valence band maximum. This double band inversion state is far enough below the Fermi level such that it does not have any bearing on the electronic properties of α-Sn. These measured spin-polarized surface states are schematized in Fig. 8.1(e).

The bulk band degeneracy at Γ is broken by any symmetry breaking in this system,

including epitaxial strain in the (001), (111), (011), and (211) orientations. For (001) films, biaxial (i.e. thin film) compressive strain induces a 3D Dirac semimetal phase while biaxial tensile strain induces a 3D topological insulator phase (Chapter 5). The former does not yet have clear direct experimental demonstration [207, 209, 213, 241] but is generally accepted. The latter has not yet been experimentally demonstrated at all. We seek to show direct proof of the 3D TI phase in α-Sn.

The main limitation for the study of tensile strained α-Sn is the lack of a suitable substrate. The common substrates already used for α-Sn growth, InSb and CdTe, have a lattice constant smaller than α-Sn leading to compressive strain. These are the largest lattice constant conventional (i.e. semiconductor and oxide) substrates. There are likely niche complex oxide substrates with larger lattice constants, but it is unlikely the α-Sn phase would be able to be stabilized. To our knowledge, no growth on large lattice constant complex oxide substrates has been attempted. A more complex lattice matching scheme [333] ($2a_{substrate} \gtrapprox a_{film}$, $a_{substrate} \gtrapprox 2a_{film}$, $\sqrt{2}a_{substrate} \gtrapprox a_{film}$ (45° rotation)) could also allow for application of tensile strain, should that substrate allow for the stabilization of the α-Sn phase over the β-Sn phase.

Another option is the use of an $InSb_{1-x}Bi_x$ alloy (a metamorphic virtual substrate or a single crystal wafer), since bismuth serves to increase the lattice constant of the semiconductor. However, bismuth is not very soluble InSb. The record Bi incorporation in this system is 5% [334] for strained thin films and 2% for bulk crystals [335], much less than the ∼7% necessary for *lattice-matching* to α-Sn (assuming Vegard's law with the InBi lattice constant given in Ref. [335]), let alone application of tensile strain. It also remains to be seen whether the relaxation process of $InSb_{1-x}Bi_x$ thin films results in Bi segregation, reducing the equilibrium lattice constant and the film quality of the metamorphic buffer for α-Sn growth.

Instead of engineering the substrate lattice constant to apply tensile strain, we instead

tune the film lattice constant by alloying α-Sn with isovalent, isostructural Ge. GeSn alloys on the Ge-rich side of the phase diagram (<15% Sn) have been well studied due to an indirect-to-direct band gap transition [166] allowing for infrared optoelectronic devices to be grown directly on Ge and Si substrates in an all group IV system [336–338]. The Sn-rich side of this alloy is less well-studied, but briefly summarized in Ref. [102]. Ge and Sn are almost entirely immiscible in the bulk with about 1% solubility of Sn in Ge and less than 1% of Ge in Sn [339]. Generally concentrations greater than these solubility limits can be achieved in high quality thin films grown by molecular beam epitaxy (MBE) or chemical vapor deposition (CVD).

In thin films of α-$Sn_{1-x}Ge_x$ grown by MBE on InSb, up to 6% Ge has been achieved [318]. Older work was able to claim a large range of Ge concentrations up to 10%, but it is difficult to assess the quality of these films from the published data [101, 238, 340–342]. Since α-Sn is metastable at room temperature, alloying Ge is expected to change the β-Sn transition temperature. In the bulk, the $\alpha \rightarrow \beta$ transition temperature is increased by alloying Ge in the α phase near the solubility limit [89, 343]. However, it is unclear whether this is (a) a dilute solute thermodynamic effect (b) a true Ge alloying stabilizing effect or (c) a kinetic effect [89, 343]. Part of the confusion stems from disagreement over the exact mechanism of the phase transition [344, 345].

In thin films, strain serves to reduce the stability of the metastable α-Sn phase. Only considering this effect, exact lattice matching (1.2% Ge) should result in the highest transition temperature. Because Ge serves as a stabilizing force independent of strain, the thermal stability should be higher for strained α-$Sn_{1-x}Ge_x$ than Sn with equal and opposite sign of strain. In addition, since it is the total strain energy that determines the thermal stability of the α-$Sn_{1-x}Ge_x$ film, the thickness of the epitaxial film will modify the temperature at which the $\alpha \rightarrow \beta$ transition occurs. This results in a complex thermal stability diagram [101, 237, 238].

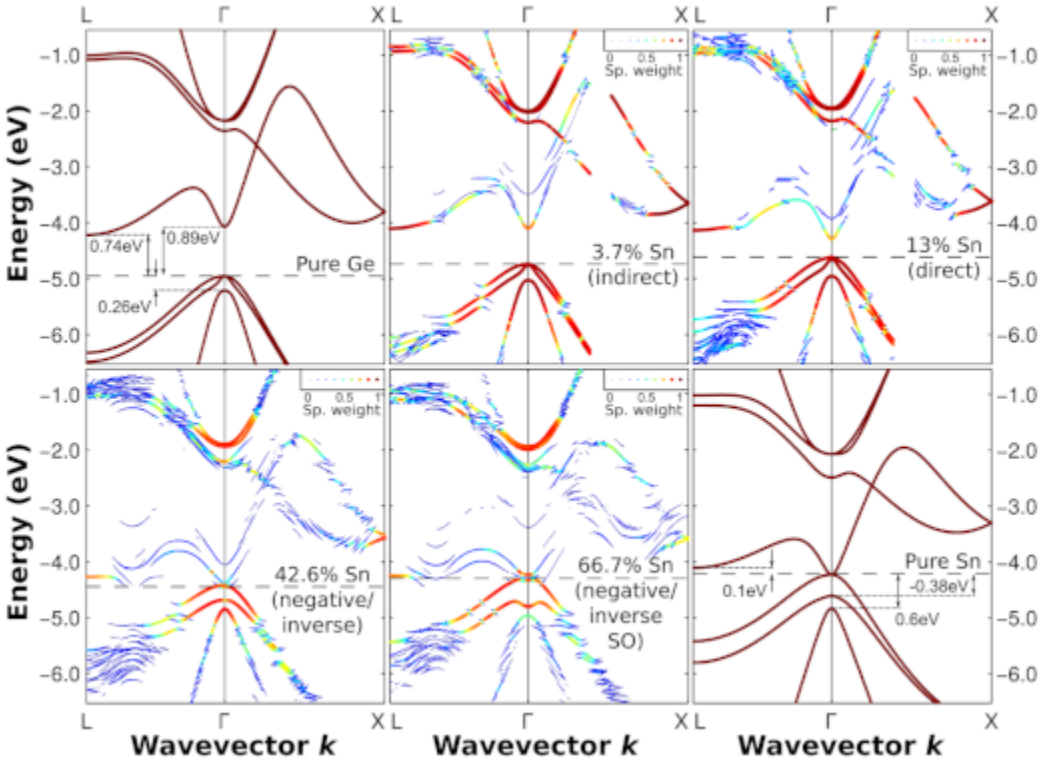

Figure 8.2: The band structure of parent compounds Ge and α-Sn and examples of unfolded band structure at a few selected ratio of Sn to Ge with different band orderings. Copyright IOP Publishing. Reproduced with permission from [356].

Experimental results for the $\alpha \rightarrow \beta$ transitions vary in the literature, likely due to varying measurement technique. Raman spectroscopy may be used as a sensitive probe of β-Sn formation [346, 347], but it also appears to have only slightly higher sensitivity to β-Sn formation as on-axis XRD [237]. Grazing incidence XRD gives much better sensitivity to the nucleation of β-Sn [348].

In thin film growth of Ge-rich GeSn, Sn tends to segregate to the sample surface to minimize strain energy [337, 349–354]; this segregation can also be reduced by the use of a surfactant during growth [355]. Segregation of Sn is also strongly temperature dependent, increasing rapidly above the Sn melting temperature (232 °C). Even at moderate temperatures (∼150 °C), when Ge is deposited on a few monolayers of Sn, the Sn will partially segregate above the growing Ge film [349, 350].

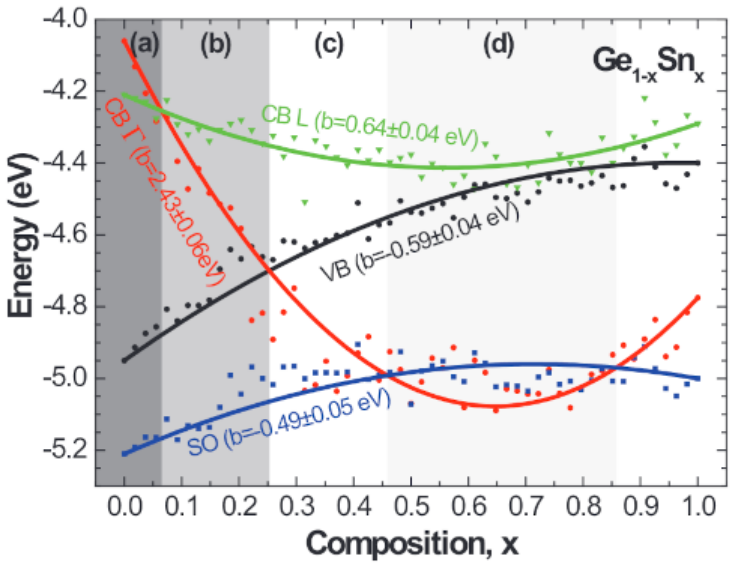

Figure 8.3: The band ordering from alloys between parent compounds Ge and α-Sn. Regions of different band ordering are indicated. Copyright IOP Publishing. Reproduced with permission from [356].

While Ge is topologically trivial, along the Sn-Ge alloy line (without the consideration of strain) the band inversion proceeds at relatively low concentrations of Sn. The exact critical concentration for band inversion varies by calculation technique and group, as bowing parameters across the composition range for this system are still not well agreed upon. The critical concentration for band inversion varies between 35% to 50% Sn [94,166,356,357]. The effect of compressive strain (to form a 3D DSM) and tensile strain (to form a 3D TI) should be identical across the entire composition range where the bands are inverted. The critical thicknesses at which confinement-based transitions occur will vary—these transitions are related to the new effective masses and new relative band positions of the alloy. Band diagrams calculated using an *ab initio* supercell approach have produced reasonable agreement with the available (Sn $<\sim$ 10%) literature [356]. This results in the band dispersion summarized in Fig. 8.2, with the band line ups as a function of Ge concentration summarized in Fig. 8.3.

The alloying of Ge into Sn will also modify the k_z spacing of the Dirac node (for

compressive strain) or the band gap size (for tensile strain). The strain-induced gap at the Γ point is given by

$$\Delta\Gamma_8^+ = 2b(\epsilon_{zz} - \epsilon_{xx}) \tag{8.1}$$

where ϵ_{xx} is the misfit between the epitaxial film and the substrate, ϵ_{zz} is the misfit in the growth direction (related to ϵ_{xx} by the ratio C_{12}/C_{11}, elements of the elastic tensor) and b is the shear deformation potential [358]. The value of b derived here is -3.7 eV from Fig. 8.1(e)–(j), quite larger than that calculated by DFT (-2 eV – -2.5 eV) [332, 359, 360] and that measured experimentally in the bulk (-2.4 eV) [91]. Our calculated deformation potential does give good agreement with the experimental Dirac node spacing (see Chapter 5). This larger deformation potential results in a larger band gap of α-$Sn_{1-x}Ge_x$ at a given x. Using a range of reasonable deformation potentials, the expected band gap size for various Ge concentrations of α-$Sn_{1-x}Ge_x$/InSb(001) is given in Fig. 8.1(k). Confinement effects will modify this gap size. It is important to note that the size of the Γ_8^+ band gap is zero across the entire Ge-Sn composition range, unless there is epitaxial strain or some other symmetry breaking.

α-$Sn_{1-x}Ge_x$/InSb(001) should form a 3D topological insulator with a reasonable band gap. The presence of random alloy disorder should not modify the topological phase (as long as band inversion is preserved) as has been seen for a very large number of topological material systems, a few of which are summarized in Refs. [361, 362]. While the bulk properties of α-$Sn_{1-x}Ge_x$ have been the subject of a few experimental reports [227,318,340], there has not yet been a clear identification of the topological phase in this system. We concentrate here on ultrathin films, which have shown promising spin-charge conversion [78].

We first identify the topological phase of ultrathin α-Sn to be that of a confinement-induced 3D topological insulator, clarifying an outstanding disagreement in the literature.

This 3D TI phase should then have its bulk band gap widened by alloying Ge. Instead, we observe an unexpected phase transition away from the 3D TI phase at Ge concentrations greater than 3%. Spin-resolved ARPES measurements show the presence of multiple spin-polarized surface states in addition to the topological surface state allowing a more unified model of this system to be devised.

8.2 Methods

8.2.1 Growth

Thin films of α-$Sn_{1-x}Ge_x$ were grown on both the indium rich c(8×2) and the antimony rich c(4×4) reconstruction of InSb(001) as discussed in Chapter 4. Film thicknesses are referred to in bilayers (BL) where 1 BL corresponds to half of the conventional diamond cubic unit cell (1 BL = 9.5×10^{14} at/cm^2).

In order to minimize (1) segregation effects and (2) the nucleation of β-Sn, the lowest growth temperature achievable was used. In the modified VG V80 system used for growth, this was -23 °C. The cooling was provided passively by radiative heat transfer with the liquid nitrogen cryoshroud. For growth of pure α-Sn in previous chapters, nucleation of β-Sn was less of a concern. However the additional heat load of the Ge effusion cell is not negligible and increases the sample temperature during growth to nucleate β-Sn. Other groups have found that increasing the sample-to-source distance can reduce the heat load on the sample. For our system and growth conditions, this was not necessary. For long growths (>15 nm), growth was paused in 15 nm increments for ∼30 minutes or until the thermocouple temperature decreases by 10 °C.

Growth is performed with Sn and Ge effusion cells. The Sn flux is kept constant at the equivalent flux of 1 bilayer of α-Sn every 2 minutes. The Sn effusion cell temperature

is fixed at 1064 °C, while the Ge effusion cell temperature varied between 1030 °C and 1082 °C. The Ge cell temperature and total growth time are varied. Growth rates are calibrated by RHEED oscillations at the beginning of every growth run and show good agreement with less frequent RBS calibrations. Samples are loaded out after growth without an intentional capping procedure. This procedure is typical for this system, but could result in a change in stoichiometry near the surface from selective oxidation [363]. A CdTe cap may be used to protect the surface but likely needs to be grown under Cd-rich conditions [297]. This generally necessitates both a CdTe compound source and separate Cd source, with which few systems are equipped. Care must also be taken to avoid the formation of SnTe [364].

The surface reconstruction of α-$Sn_{1-x}Ge_x$ films, as measured by reflection high energy electron diffraction, showed the mixed (2×1)/(1×2) reconstruction. Intensity oscillations of the RHEED pattern, indicative of a layer-by-layer growth mechanism, were found to persist through 30 nm of growth.

8.2.2 Characterization

X-ray diffraction measurements were taken in a double-crystal geometry using a Rigaku SMARTlab equipped with a two-bounce Ge(110) monochromator. Atomic force microscopy measurements were taken with a Bruker Dimension ICON. Photoemission data were taken at beamline 5-2 at Stanford Synchrotron Radiation Lightsource (SSRL) with p-polarized light. Other photoemission data were taken at beamline 10.0.1.2 at the Advanced Light Source (ALS) with p-polarized light or He1α light (21.2 eV) using a monochromatized helium electron cyclotron resonance (ECR) plasma source. Light was directed along the $\langle 1\bar{1}0 \rangle$ direction for all measurements. At both beamlines, data were taken using a Scienta Omicron DA30L detector. The sample temperature was kept

below 20 K and the base pressure during measurement was lower than 3×10^{-11} Torr. The samples were transferred from the growth systems at UCSB to SSRL and ALS using a custom designed ultrahigh vacuum suitcase with pressure lower than 4×10^{-11} Torr.

Spin-resolved measurements were performed at beamline 10.0.1.2 using Ferrum spin detectors. The spin texture is measured in three orthogonal directions $(\hat{x}, \hat{y}, \hat{z})$ which are parallel with our (k_x, k_y, k_z) axes. The spin polarization was calculated from measured spin-resolved energy distribution curves (EDCs) by the usual equation $P = \frac{1}{S}\frac{I_\uparrow - I_\downarrow}{I_\uparrow + I_\downarrow}$, where the Sherman function $S = 0.22$. The error bars in polarization are calculated from propagated error in the polarization equation assuming Poisson statistics and neglecting error in the Sherman function (Chapter 2). The angular acceptance window and energy window of the spin-resolved measurements is variable, but typically set at 1° and 40 meV. The sign of P_Y and the Sherman function were validated on bismuth thin film calibration samples.

Tight-binding calculations were performed using *chinook* [167] with parameters slightly modified from those reported in Ref. [170] which were themselves extracted from Ref. [94]. Strain was incorporated using Harrison's d^2 rule [169]. The tight-binding calculation gives good agreement in Dirac node spacing with experimental results [241].

8.3 Structural characterization

Most *ex situ* characterization was performed on 54 BL films; 4–6 BL is expected to oxidize [225]. High resolution X-ray diffraction in the vicinity of the InSb(004) reflection depicted in Fig. 8.4(a) shows high quality films with strong Pendellösung fringes. There is slight thickness variation from keeping the number of bilayers constant as c, the out-of-plane lattice constant, changes.

We are able to sustain high Ge concentrations, likely as our films are thinner than

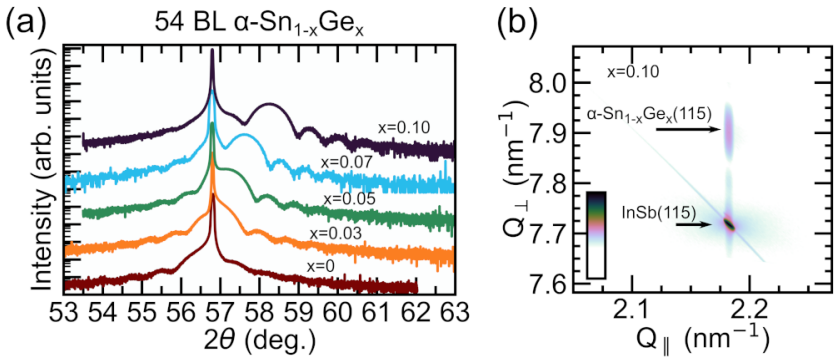

Figure 8.4: Structural characterization of α-$Sn_{1-x}Ge_x$ films. (a) On-axis HRXRD measurements in the vicinity of the InSb(004) reflection. (b) Reciprocal space map around the InSb(115) reflection for α-$Sn_{0.8}Ge_{0.1}$ shows the film is fully strained to the substrate.

what is usually investigated (minimizing strain energy) [238, 340, 341]. Ge concentration calibrated by RHEED oscillations and RBS calibrations are confirmed by X-ray diffraction measurements assuming Vegard's law holds without bowing. The presence of bowing in the lattice constant for this system has been debated since its inception. Recently it has been found that many studies reporting bowing suffer from poor material quality via segregation effects or from poor composition control and the bowing parameter should be set to zero [365]. All films are fully strained up to 10% Ge, as evidenced by reciprocal space maps near the InSb(115) and (335) reflections (Fig. 8.4(b)). Above this thickness, film quality degrades quickly.

Rocking curves performed on the 54 BL samples at the α-$Sn_{1-x}Ge_x$(004) reflection show narrow full-width-at-half-maximum (FWHM) (<540") for 0%, 3%, and 5% Ge, summarized in Fig. 8.5. A very thick 400 BL sample has a FWHM of <200". Ge alloying of 10% in a 54 BL doubles the FWHM of the rocking curve, indicating reduced film quality. Additional radiative heating from the effusion cell nucleating β-Sn is the likely cause of this reduction in film quality. However, no β-Sn was observed in these 54 BL samples through $\theta - 2\theta$ measurements. Magnetotransport of films grown under similar conditions also did not show superconductivity above 2 K, indicating there is not

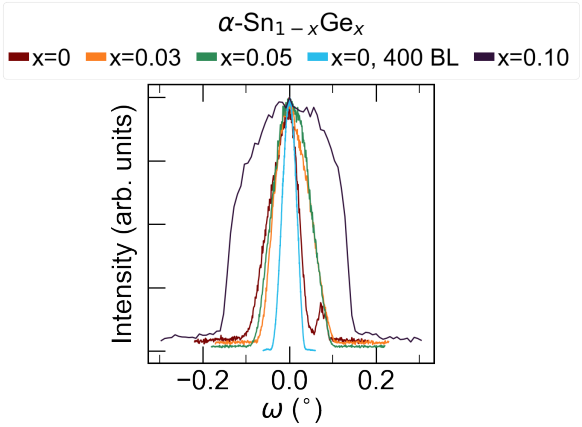

Figure 8.5: Rocking curves for selected 54 BL α-$Sn_{1-x}Ge_x$ samples around the (004) peak. In the x = 0 measurement there is a small peak from the substrate due to an experimental artifact. These rocking curves are compared to that of a pure α-Sn 400 BL film. Rocking curve width is related to both film thickness and film quality.

enough β-Sn to reach the percolation threshold (at 2 K).

Atomic force microscope measurements show smooth surfaces with visible bilayer terraces for 0% Fig. 8.6(a) and 10% Ge Fig. 8.6(b). Both samples have sub-nm roughness, with the RMS roughness being 0.5 nm vs. 0.3 nm for 0 and 10% Ge. The improved smoothness with the high Ge alloying is likely from increased sample heating during growth.

In Chapter 4 we benchmarked the Sb-termination procedure as a pathway to reduce In incorporation into α-Sn, even while heating the sample during growth (which normally enhances In incorporation). This procedure is even more important for α-$Sn_{1-x}Ge_x$, as the Ge effusion cell results in more sample heating during growth. Indium doping will prevent the ability to see the Dirac node of the topological surface state, and thus must itself be prevented.

Ultraviolet photoelectron spectroscopy was used to measure changes in indium and antimony incorporation as Ge was alloyed into the α-Sn, summarized in Fig. 8.7. In Fig. 8.7(a) for 50 BL films, there is a small increase in indium incorporation with increased

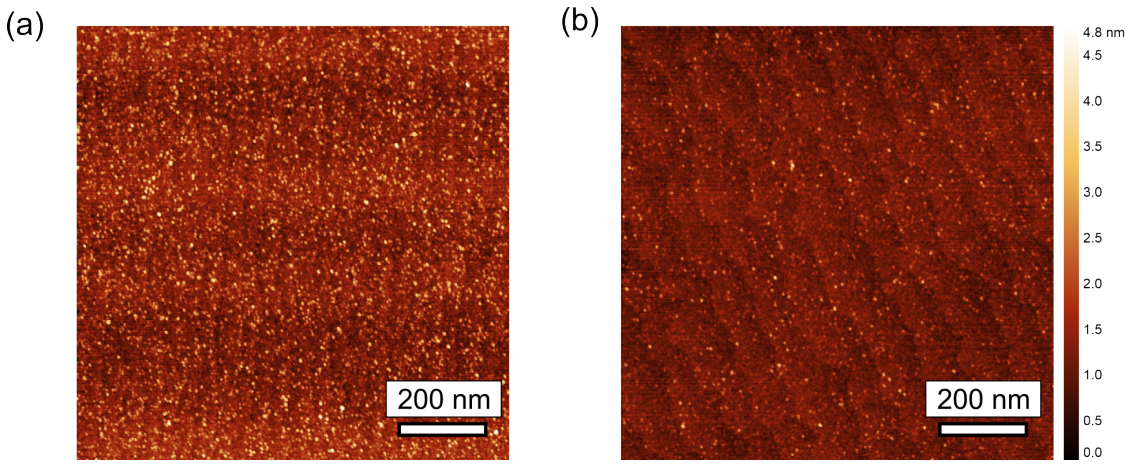

Figure 8.6: 2μm $\times$ 2μm atomic force microscope images of the surface of 54 BL (a) α-Sn and (b) α-$Sn_{0.9}Ge_{0.1}$. Bilayer terraces are clear in both samples.

germanium alloying. This could technically be from In having a higher solubility in Ge than Sn, but In in fact has a lower solubility in Ge than in α-Sn [366, 367]. This indium incorporation trend is present in 13 BL films as well, where the equivalent indium incorporation (In to Sn ratio) is higher. The incorporation should be higher in 13 BL films, as the source is the substrate and the indium does not appear to segregate to the surface.

There is also Sb incorporated into all studied films, but there is no available reference peak with which to benchmark trends in the ratio of Sb to Sn. Both dopant concentrations are small enough that they are not visible in survey UPS measurements for any of these films (Fig. 8.7(b)). A zoom-in of the Sn $4d$ core level for some samples is shown in Fig. 8.7(c). The branching ratio appears to vary as a function of the details of the sample thickness and Ge concentration, which could be due to final state effects.

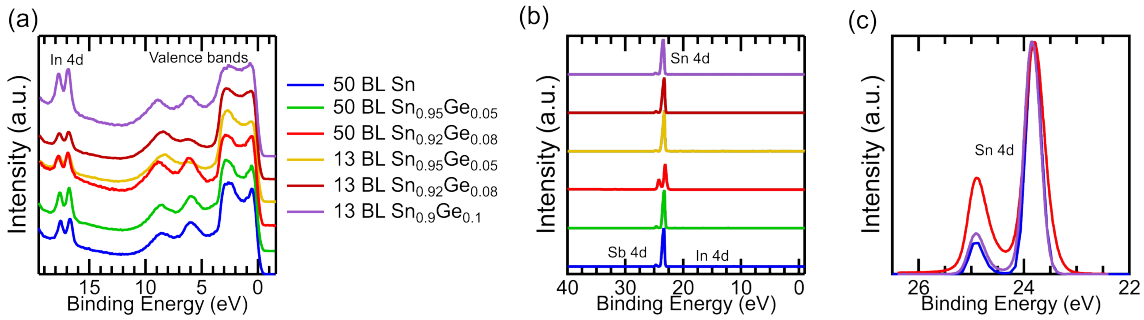

Figure 8.7: Ultraviolet photoelectron spectroscopy measurements on α-$Sn_{1-x}Ge_x$. (a) measurements in the vicinity of the In 4*d* core levels and the valence bands, normalized to the 2nd valence band intensity (the peak that has a binding energy near 3 eV). (b) Full range UPS of the same samples. (c) Zoom-in of the Sn 4*d* peaks for a subset of the samples.

8.4 Topological phase identification of 13 BL α-Sn

While in prior chapters we made numerous clarifications to the electronic structure and the understanding of measured ARPES spectra in α-Sn, we have not yet directly determined the topological phase of the films investigated. Ultrathin α-Sn thin films (10-15 BLs) have shown remarkably high spin-charge conversion efficiency [78], but the topological phase of these films is unknown. There is a lack of consensus over the range of topological phases in compressive strained α-Sn as a function of thickness and orientation. It is generally agreed that very thick (bulk-like) compressive strained α-Sn is a 3D DSM [109, 207, 209, 210, 232, 240, 241]. With quantum confinement, it has been calculated to go from 3D DSM→3D TI→2D TI→2D NI (for both (001) and (111) orientations) [210], 3D DSM→2D TI→2D NI (for (001) orientation) [207], and 3D DSM→ 2D DSM→2D TI (for (111) orientation) [213, 242]. Which transitions occur and at what thicknesses they occur is not generally agreed upon, possible due to the hybridization effects discussed in Chapter 6. There are also limited conclusive experimental demonstrations of the topological phase, as most ARPES experiments only study the surface states in α-Sn rather than the bulk bands [107, 108, 208]. In particular, there is not yet direct experimental demonstration of

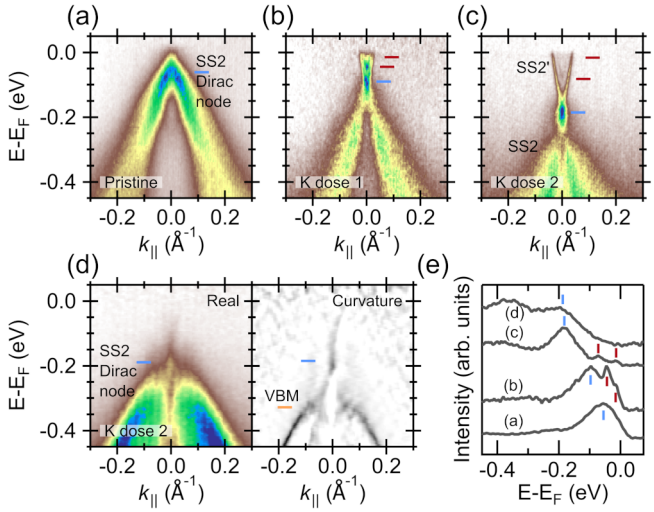

Figure 8.8: Confirming the topological phase of ultrathin (13 BL α-Sn. $h\nu$=21 eV ARPES measurement, sensitive to the surface states, for (a) pristine α-Sn (b) dosed with low K dosing (2 minute deposition) and (c) and high K dosing (5 minute deposition). There is a continuous crossing between the surface states. (d) $\mathbf{\Gamma_{003}}$ ($h\nu$=53 eV) measurement for the same film. All measurements are along the $\overline{X}-\overline{\Gamma}-\overline{X}$ direction with p-polarized light. (e) Energy distribution curves at the $\overline{\Gamma}$ point for (a)–(d). The blue lines indicate the peak corresponding to the crossing of the surface state. The red lines indicate downward band bending derived quantum well states induced from the K deposition.

the 3D TI phase in compressive strained ultrathin α-Sn. First we measure the topological phase of this ultrathin α-Sn before alloying with Ge. We work with 13 BL α-Sn films similar to those discussed in prior chapters.

In Fig. 8.8, $h\nu$ = 21 eV measurements on a 13 BL α-Sn film grown on an Sb-rich reconstruction of InSb(001) are shown. While SS1 and the bulk heavy hole band are present in measurements using this photon energy (Chapter 5) the majority of the photoelectron intensity comes from SS2 (Fig. 8.1(k)) the topological surface state. The Dirac node of this state is approximately 50 meV below the Fermi level, but the upper branch of the Dirac-like surface state (SS2') is not visible (Fig. 8.8(a)). Although we do not directly observe the full SS2', there is no evidence of a gap in the topological surface state. Since the topological phase is determined partially by the presence/absence of a

gap in the Dirac-like surface state (i.e. a gap between SS2 and SS2'), observing SS2' clearly is essential.

We attempt to observe SS2' more clearly by alkali dosing the surface with potassium. This procedure effectively electron dopes the surface by inducing downward band bending at the surface [368]. SS2' is more clearly visible here (Fig. 8.8(b)). There is still no measurable gap in the topological surface state, although the Dirac node is somewhat broader in energy than seen in the $(Bi,Sb)_2(Se,Te)_3$ family [369, 370]. This could be inherent to the system (as it is equivalent to what has been seen in other measurements of the α-Sn topological surface state [108, 209, 212]), or a result of the surface disorder in this system from the atomic-layer island grain morphology. Surface disorder has been shown to renormalize the linewidth of the Dirac node in $(Bi,Sb)_2(Se,Te)_3$ [369, 370].

The electric field at the surface due to the potassium-induced dipole can affect the topological phase and open a gap in the surface state [371]. The downward band bending also induces surface quantum well states [326], marked in Fig. 8.8 in red. Further potassium dosing causes a reduction in intensity below the surface state Dirac node, but still does not appear to cause a gap to open (Fig. 8.8(c)). The Dirac node is now broader in energy, as would be expected from the enhanced surface disorder that potassium dosing provides. The spacing between the Dirac node and the quantum well states increases, as does the spacing between the quantum well states. More potassium results in a larger confinement potential, increasing the subband spacing. Thus we have an ungapped Dirac-like topological surface state in 13 BL α-Sn, but do not observe the $\Gamma_{8,c}^{+}$ conduction band. The presence or absence of a gap in the bulk bands is also necessary to identify the topological phase of 13 BL α-Sn.

To help answer the question of the bulk band gap, we shift instead to investigate the $\mathbf{\Gamma_{003}}$ point, where the $\Gamma_{8,v}^{+}$ heavy hole band has high intensity (but this does not necessarily result in the same matrix elements as the $\Gamma_{8,c}^{+}$ band, see Chapter 5). The

measured surface state Dirac node in Fig. 8.8(c) is at the same energy as in Fig. 8.8(b), although the intensity of the surface states is very weak. The valence band maximum here is found to be 140 meV below the Dirac node, in excellent agreement with the extrapolated spacing (130 meV) between the SS2 Dirac node and the valence band maximum in Chapter 5. The surface state band locations at the $\overline{\Gamma}$ point are summarized in Fig. 8.8(e). In the $\mathbf{\Gamma_{003}}$ measurement, there is no evidence of the $\Gamma^+_{8,c}$ conduction band. There is thus no direct connection between the valence band and conduction band—a bulk band gap is present. The bulk band gap is at least 320 meV. The gap of ultrathin α-Sn has been calculated many times over the years [207, 210, 299, 372], resulting in gap sizes as low as 20 meV to greater than 450 meV in this thickness range. As-of-yet there is one measurement of the band gap of ultrathin α-Sn films grown on CdTe(111), which indicates a gap >400 meV for films thinner than 5 nm (13 BL = 4.2 nm), as measured by electron energy loss spectroscopy [299]. Thus the size of the bulk band gap here is reasonable.

It is also possible that matrix elements cause the $\Gamma^+_{8,c}$ conduction band to have vanishing intensity, but have its minimum between the surface Dirac node and the Fermi level. In order to remedy this, future experiments can vary the polarization of incident light. Even without polarization-dependent measurements, this vanishing intensity argument is unlikely. The MDC width of SS2' should increase as it approaches and hybridizes with the band from which it arises [272]. The MDC width of SS2' is approximately constant from the Dirac node to the Fermi level, so there is little to no change in surface-bulk hybridization. Thus there is a bulk band gap which at minimum is greater than 130 meV, but is likely greater than 320 meV. The next step is to verify that—at the current 13 BL thickness—the bulk bands are indeed 3D-like rather than 2D-like.

If a band is 3D, it shows a dependence on k_x, k_y, and k_z in its electronic structure. k_z is inherently linked to the photon energy used in the measurement (Chapter 2). If a band

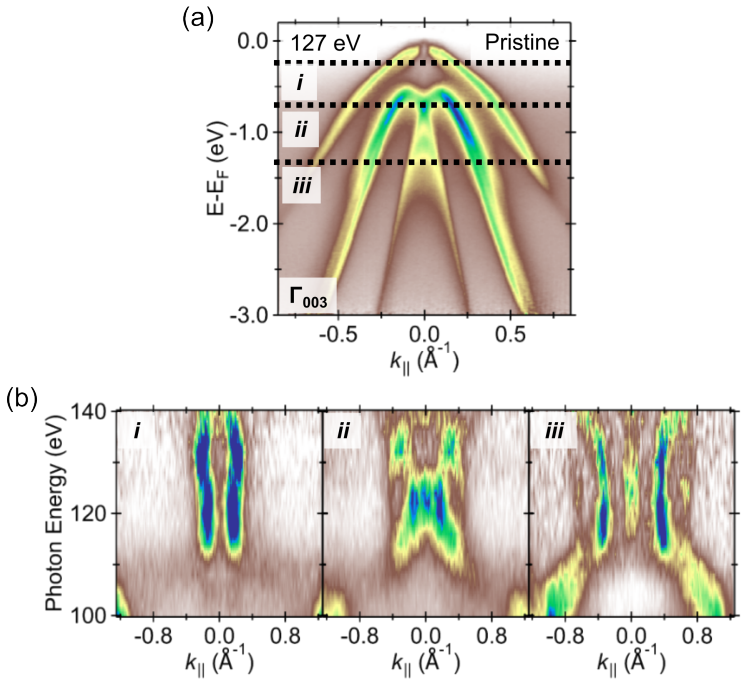

Figure 8.9: Photon energy dependence ARPES of 13 BL α-Sn/InSb(001). (a) Measurement at $h\nu$ =127 eV ($\mathbf{\Gamma_{003}}$) depicting the binding energy at which $h\nu$ dependence is studied (b) $h\nu$ dependence integrated over 5 meV in binding energy, centered at the indicated binding energies. The photon energy is swept in 2 eV steps, and interpolated into 1 eV steps.

disperses with photon energy, it is 3D like. If a band has an identical shape (although intensity may vary significantly) at different photon energies, it is 2D like. k_z dependence must still be analyzed carefully, as it has been shown for metal thin films that final state effects (depending on the character of the band) and interaction with the substrate can lend a k_z dependence even at the monolayer limit [373–376]. Since past measurements of α-Sn/InSb have demonstrated the lack of k_z dependence in films thinner than those studied here [213], we can conclude that these effects are not present in this system.

We perform photon energy dependence measurements in the vicinity of $\mathbf{\Gamma_{003}}$ such that the failure of the inner potential model observed in Chapter 5 can be disregarded. In this range, the three valence bands $\Gamma_{8,v}^{+}$, Γ_{7}^{-}, Γ_{7}^{+}, all show strong photon energy dependence and are thus all 3D (Fig. 8.9). With this information, we can finally confirm the topo-

logical phase of 13 BL α-Sn. Since the electronic structure is 3D-like, with a bulk band gap and 2D Dirac-like surface states crossing the 3D gap, 13 BL α-Sn is a 3D topological insulator. Thus the confinement-induced 3D TI phase in compressive strained α-Sn must be present in *ab initio* calculated results in order to expect these calculations to reproduce experimental thickness-induced topological phase transitions accurately. One important caveat is that inversion symmetry breaking in α-Sn, as discussed in Chapter 7, could potentially modify the topological phase diagram compared to calculations which generally obey preserved inversion symmetry. Since the direct origin of the inversion symmetry breaking is still unknown, this updated topological phase diagram cannot be determined well.

In addition, the observed k_z dependence implies that all films thicker than 13 BL on InSb(001) are 3D-like, since the 13 BL film is above the 3D-to-2D transition. The 3D-2D critical thickness has been observed before on the (111) surface to be between 10 BL and 30 BL. The topological surface states on opposite surfaces have been suggested to hybridize strongly with each other on InSb(001) under 6 BL [209]. In addition, if hybridization and 3D-2D transition effects are sensitive to the band alignment (Chapter 6), then different groups with varying substrate preparation and growth conditions will likely generate different heterovalent interfaces with different effective valence band offsets, leading to many conflicting experimental results.

8.5 Surface state band gap opening in ultrathin α-$Sn_{1-x}Ge_x$

Now that we have benchmarked the confinement-induced 3D TI phase in 13 BL α-Sn, we may begin to alloy Ge into the α-Sn. The switch to tensile strain should increase the

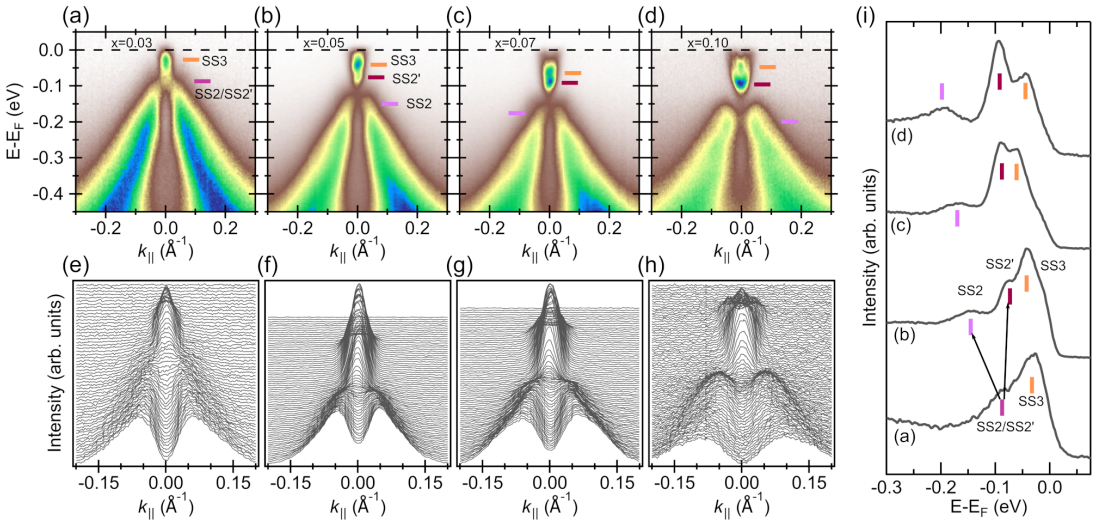

Figure 8.10: Topological phase transition by a gap opening in the surface states of 13 BL α-$Sn_{1-x}Ge_x$. ARPES measurements at $h\nu$=21 eV, sensitive to the surface states, for (a) $x = 0.03$ (b) $x = 0.05$ (c) $x = 0.07$ (d) $x = 0.10$. (e)–(h) corresponding momentum distribution curves. All measurements are along the $\overline{X} - \overline{\Gamma} - \overline{X}$ direction with p-polarized light. (i) Energy distribution curves at the $\overline{\Gamma}$ point for (a)–(d). At $x > 0.03$ the surface state crossing is gapped, indicating a topological phase transition away from the 3D TI phase. The crossing and band edges of the gapped crossing are indicated in purple (SS2/SS2'). The orange marker indicates the location of a second surface state (SS3) in the upper branch.

band gap of the 3D TI phase. Alloying 3% Ge (0.2% tensile strain, Fig. 8.10(a)) shifts the surface Dirac node further below the Fermi level than in the case of pure α-Sn. This effect has a few potential origins. Sb, which is incorporated as a dopant in all the films, could have a higher ionization efficiency in α-$Sn_{1-x}Ge_x$ than Sn, leading to a change in the surface band bending. The addition of Ge could also affect the band alignment of the surface states and bulk bands, without drastically modifying the surface point-defect density that determines the surface chemical potential. In addition, the opposite could be true where the surface state density (and thus surface chemical potential) is varying, but the relative band positions are identical. There is no clear way to identify which case is valid, but we do find that the higher the Ge concentration, the farther the Dirac node shifts below the Fermi level.

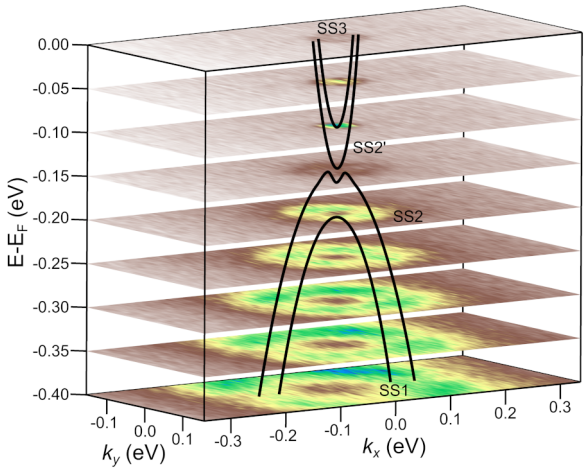

Figure 8.11: Constant energy contours of 13 BL α-$Sn_{1-x}Ge_x$ where $x = 0.10$ measured at $h\nu$=21 eV. A schematic of the dispersion of SS1, SS2, SS2', and SS3 are drawn.

For 13 BL α-$Sn_{0.97}Ge_{0.03}$, there is another surface state, SS3, above the Dirac node and SS2'. When more Ge is alloyed, the surface Dirac node forms a gap (Fig. 8.10(b)–(d)), indicating a transition away from the expected 3D TI phase. With increasing the Ge concentration, we have found that the size of the gap between SS2 and SS2' increases. In addition, the difference between the "Dirac node" (average between SS2 and SS2') and the location of SS3 is tuned by Ge concentration. These relative changes are summarized in EDCs at $\overline{\Gamma}$ in Fig. 8.10(i). Thus both the gap in the topological surface state (SS2) and the "new" state (SS3) are intrinsically related to the Ge content in the film. The gap is present at all Ge concentrations over 3%. The appearance of this gap is surprising, as all Ge concentrations should lead to a 3D TI phase. The gap indicates the transition to a new phase which could be either a 2D TI, 2D NI, or 3D NI, but we do not have experimental evidence to identify which topological phase is present.

This gap may be seen as well in constant energy contours of α-$Sn_{0.9}Ge_{0.1}$ in Fig. 8.11. The expected shape of the bands along the $k_y = 0$ line is drawn schematically. However, narrower energy slices are necessary in order to more clearly see the gap between SS2 and SS2'. These constant energy contours are summarized in Fig. 8.12. From Fig. 8.12(a)–

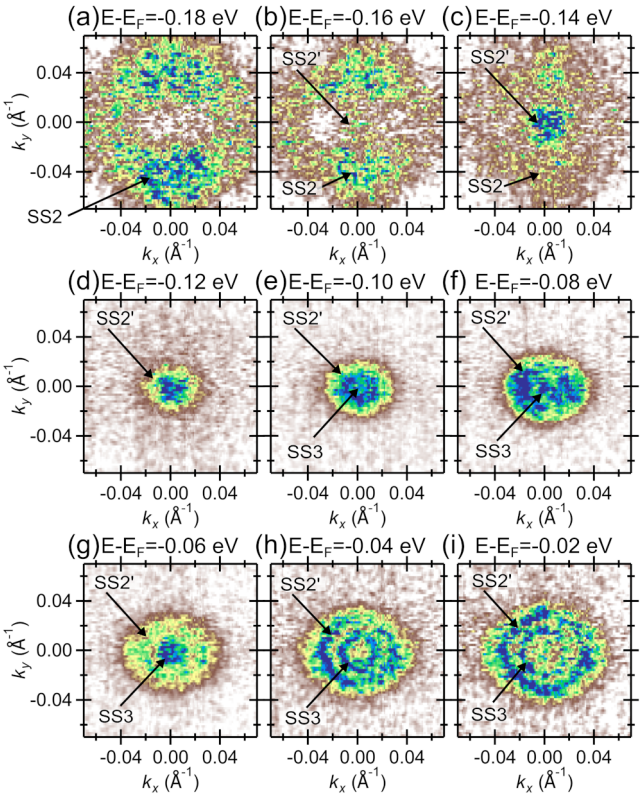

Figure 8.12: Constant energy countours of 13 BL α-$Sn_{1-x}Ge_x$ where $x = 0.10$ measured at $h\nu$=21 eV with a finer energy scale, further showing the presence of a gap in the surface states.

(c), SS2 and SS2' are both visible, but never connect. In Fig. 8.12(d), 20 meV higher in energy, only SS2' is present. The elliptical contour of SS2' is clear in Fig. 8.12(e). The minimum of SS3 is just visible in the center of this contour. In Fig. 8.12(f)–(h), the elliptical contour of SS2' continues to be present, while SS3 appears to be fully isotropic. The two-fold symmetric contour of SS2' is surprising, as α-Sn is four-fold symmetric. It is unlikely to result from the surface reconstruction of the film, as no other evidence of surface reconstruction-induced states (folded bands, surface states with the symmetry points of the reconstruction, etc.) were found. Potentially the α-$Sn_{1-x}Ge_x$ film is only two-fold symmetric, but the anisotropy is not clearly visible in the lower branches.

This two-fold symmetry could be related to the inversion symmetry breaking discussed

in Chapter 7. A bulk inversion symmetry breaking inherited from the InSb substrate would result in a point group of T_d instead of O_h, with only a two-fold rotational symmetry around the (001) axis. However, with the application of strain the inversion-symmetric point group should technically be D_{4h} and the inversion-asymmetric point group should be D_{2d}.

Regardless of inversion symmetry, the presence of a gap in the topological surface state of Ge-rich α-$Sn_{1-x}Ge_x$ is clear, indicating the topological phase transition away from the 3D TI phase. What phase the system ends up in is unclear, and depends on the details of what exactly is causing the surface states to open a gap. The most likely options are a transition to a 2D TI phase or a transition to a 3D NI phase. The latter is more likely as the bulk bannds in 13 BL films still show k_z dependence. More accurate calculations are necessary to answer this question.

8.6 Bulk band movement with Ge alloying

We have verified the topological phase transition in α-$Sn_{1-x}Ge_x$, but we still do not know the behavior of the bulk bands with Ge alloying. We map the Γ dispersion for all Ge concentrations studied and observe a downward shift of the valence band (Fig. 8.13). In order to quantify this shift, we extract MDCs from Fig. 8.13(a)–(d) at $E - E_F = -200$ meV and map these onto a parabolic fit to the heavy hole band of pure α-Sn in the direction investigated here (corresponding to an effective mass in the $K-\Gamma-K$ direction of $0.44m_e$, derived from the ARPES measurements for pure α-Sn in Chapter 5). This approximation is valid as Ge does not appear to shift the effective mass of the heavy band more than 5% in this Ge alloying range [318]. This approach leads to a total shift of the VBM of about 44 meV between 3% Ge and 10% Ge. Thus the distance between E_F and the VBM for 3%, 5%, 7%, and 10% Ge corresponds to 158 meV, 170 meV, 180

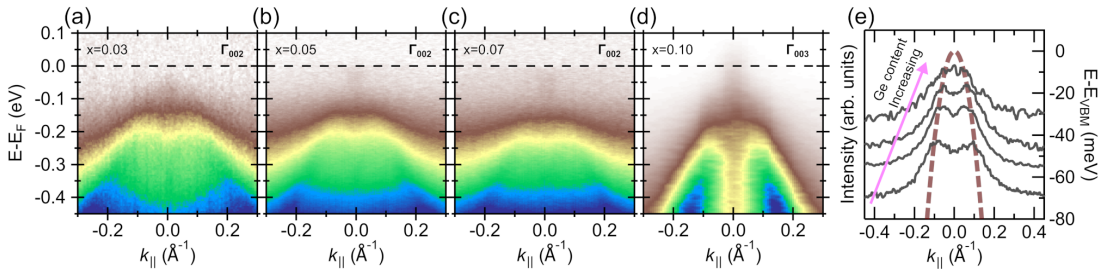

Figure 8.13: Movement of the valence band maximum with Ge alloying. The relative positions between the surface states and the valence band maximum shifts with Ge composition. Valence band measurements of 13 BL α-$Sn_{1-x}Ge_x$ at (a) $x = 0.03$ and $\mathbf{\Gamma_{002}}$, (b) $x = 0.05$ and $\mathbf{\Gamma_{002}}$, (c) $x = 0.07$ and $\mathbf{\Gamma_{002}}$, (d) $x = 0.10$ and $\mathbf{\Gamma_{003}}$. (e) momentum distribution curves extracted at $E - E_F = -0.2$ eV in $\mathbf{\Gamma_{002}}$ measurements. The MDCs are plotted against a parabolic fit to the heavy hole band in pure α-Sn with an effective mass of $0.44m_e$ to show the approximate energy level shifts.

meV, 192 meV, respectively.

These relative changes in VBM energy are very similar to the change in the location of the average of the minimum of SS2' and the maximum of SS2 (within 10%) in Fig. 8.10(i). Therefore the distance between the valence band maximum and the Dirac node is (within a window of a few meV) constant with Ge alloying. So if the bulk band gap is opening with Ge alloying, the distance between the conduction band maximum and the "Dirac node" is increasing. Since this trend is seen in SS3, we must confirm that SS3 is indeed a surface state and not the inverted light hole band ($\Gamma^+_{8,c}$ conduction band). Spin-resolved ARPES measurements can help identify the origin of this state.

8.7 Spin-resolved ARPES of α-$Sn_{1-x}Ge_x$ films

In order to have a more convincing identification of the surface states, we performed spin-resolved ARPES. Spin-polarized data is presented only in S_Y, the spin population, because there was no measurable spin polarization in $\hat{x}$ or $\hat{z}$. The spin population derivation is defined in Chapter 2, but is essentially the measured spin-integrated EDC weighted by the true spin polarization. In thicker films of α-Sn, we have previously shown that SS1

and SS2 are both spin-polarized with orthogonal spin-momentum locking and opposite helicities (Chapter 5). In spin-resolved ARPES measurements of 13 BL α-$Sn_{1-x}Ge_x$ at $x = 0.03$ (Fig. 8.14(a)), we first look at only the lower branches in slices (i) and (iv). We see two spin-polarized surface states, corresponding to SS1 and SS2, where the polarization of SS2 is much lower than that of SS1. This is in agreement with the work in Chapter 5 for pure α-Sn. Looking at slices (ii) and (iii), the spin polarization of SS1 is still measured, but SS2 is no longer visible. Instead there is a measured spin state above SS2, at SS2', with spin polarization opposite to that of SS2 (as expected of SS2'). With $x = 0.08$, SS3 is more visible. The outer slices (i) and (iv) primarily cross SS2'. We find that SS2' has spin polarization of the same sign and similar magnitude to SS1. It also appears that there is another spin state, closer to the Fermi level, likely from SS3. Asymmetry across k in the measured spin population is likely from slight alignment asymmetry in the collected spin-resolved EDCs.

In Fig. 8.14(g) for $x = 0.1$, slices (i) and (iv) are just touching the outer edge of SS2', where the angular acceptance window of 1 ° (resulting in a momentum acceptance of 0.036 $Å^{-1}$), should capture most of SS2' without any contribution from SS3. Indeed in these measurements, SS2' has the same sign of spin polarization as SS1. All measured spin populations obey time reversal symmetry. In slices (ii) and (iii), where the measurement is closer to SS3, the same spin polarization as earlier is measured. This spin polarization only consists of a few data points. To remedy this, another $x = 0.1$ sample was grown and measured. The spin polarization measurements are summarized in Fig. 8.14(k,l) and shows again the expected spin polarization. The measured spin polarization of SS3 implies that it is indeed a surface state and not the spin-degenerate bulk band. When we map the measured spin polarization onto the measured surface state dispersions, we end up with a schematic as depicted in Fig. 8.14(m). In another sample with $x = 0.1$, we used the He1α line of a He ECR plasma discharge lamp to confirm the origin of

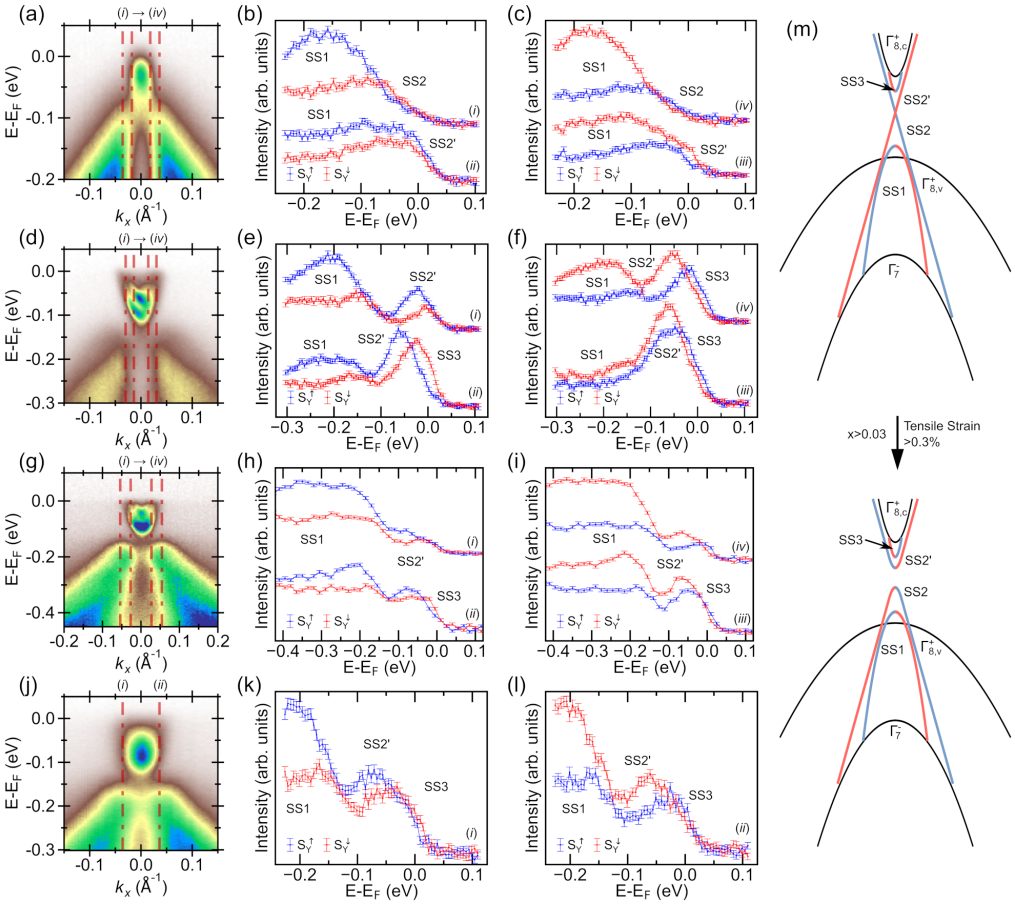

Figure 8.14: Spin polarization of the surface states in α-$Sn_{1-x}Ge_x$ measured at $h\nu$=21 eV. (a) Representative EDCs along which spin polarization is measured for $x = 0.03$. Spin population at (b) negative and (c) positive momentum values. (d)–(f) the same for $x = 0.07$. (g)–(i) the same for $x = 0.1$ (j)–(l) the same for a different sample at $x = 0.1$, showing the spin polarization measurement is robust. (m) A schematic mapping the measured spin polarization to the measured band dispersions.

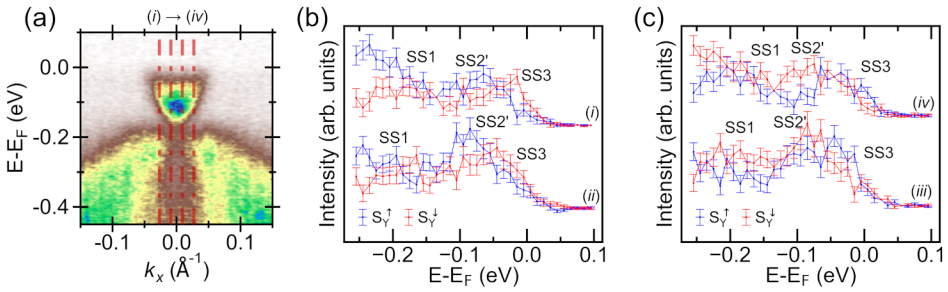

Figure 8.15: Spin polarization of the surface states in α-$Sn_{1-x}Ge_x$ at $x = 0.1$ measured with the He1α line. (a) Representative EDCs along which spin polarization is measured for $x = 0.03$. Spin populations at (b) negative and (c) positive momentum values.

the spin polarization (Fig. 8.15). This light is only partially polarized (the polarization vector points approximately halfway between s and p). The same three spin states are measured, showing that the initial state of SS2, SS2', and SS3 are spin-polarized, rather than the measured spin polarization being the result of a matrix element effect. Thus the spin polarization above SS2' in energy indeed comes from SS3, a spin-polarized surface state, rather than the spin-degenerate bulk conduction band $\Gamma^+_{8,c}$.

The schematic derived in this work is an amalgam of the model discussed in Ref. [287] and Ref. [209]. Two Rashba-split surface states—a hole-like pair and an electron-like pair—hybridize to form a topological surface state (SS2/SS2'), an upper spin resonance (SS3), and a lower spin resonance (SS1). Below $x = 0.03$, the confinement-induced 3D TI phase in α-$Sn_{1-x}Ge_x$ is preserved. At some critical Ge concentration between $x = 0.03$ and $x = 0.05$, a gap opens in the topological surface states. The distance between the average location of SS2 and SS2' and the valence band maximum is constant. The increase in energy of SS3 with Ge alloying is likely linked to the increase in energy of the $\Gamma^+_{8,c}$ conduction band, since the bulk band gap widens with Ge alloying.

8.8 Origin of the unexpected topological phase transition in ultrathin films of α-$Sn_{1-x}Ge_x$

The origin of the gap in SS2 and SS2' is still unclear. The most common case of a thin film topological insulator showing a gapped surface state is via hybridization between the surface state at the film/substrate interface and the film surface. This hybridization is related to the penetration depth of the surface state, which is itself inversely proportional to the inverted band gap by $\hbar v_F/\Delta$ [377,378]. The Fermi velocity v_F of the surface states (the linear portion of SS2) is constant. Since the inverted band gap is constant or increasing with Ge concentration [318], and the band velocity is constant with Ge concentration, the penetration depth should decrease with higher Ge alloying. A surface state hybridization gap should then decrease with higher Ge alloying, which is not observed. Thus hybridization between opposite surface states does not seem to be a plausible origin for the gap in TSS for α-$Sn_{1-x}Ge_x$ with $x > 0.03$.

Other mechanisms of hybridization could be present as well. While the penetration depths are similar for these films, the chemical potential in the top surface state may be different than that of the bottom surface state due to different band alignments. The more different the band alignment of the top and bottom surface states, the weaker the hybridization [284, Chapter 6]. It is then possible that the addition of Ge makes the surface state chemical potential at the InSb interface more similar to that at the surface, increasing the hybridization between top and bottom TSS at a set penetration depth (Chapter 6).

Finally, the topological insulator state in α-$Sn_{1-x}Ge_x$ has generally only been calculated to have one spin-polarized surface state. Our observation of an upper and lower spin resonance, generally not calculated by first principles, means that the calculations are missing a key component of this system. If *ab initio* or empirical (tight-binding, $k \cdot p$)

calculations could be performed that correctly predict all of the surface states present in this system, it would be possible to test whether the alloying of α-Sn with Ge opens the surface state gap, as suspected, or if "pure" tensile strain causes this effect.

8.9 Evidence for a 3D topological insulator phase in α-$Sn_{1-x}Ge_x$ films under weak confinement

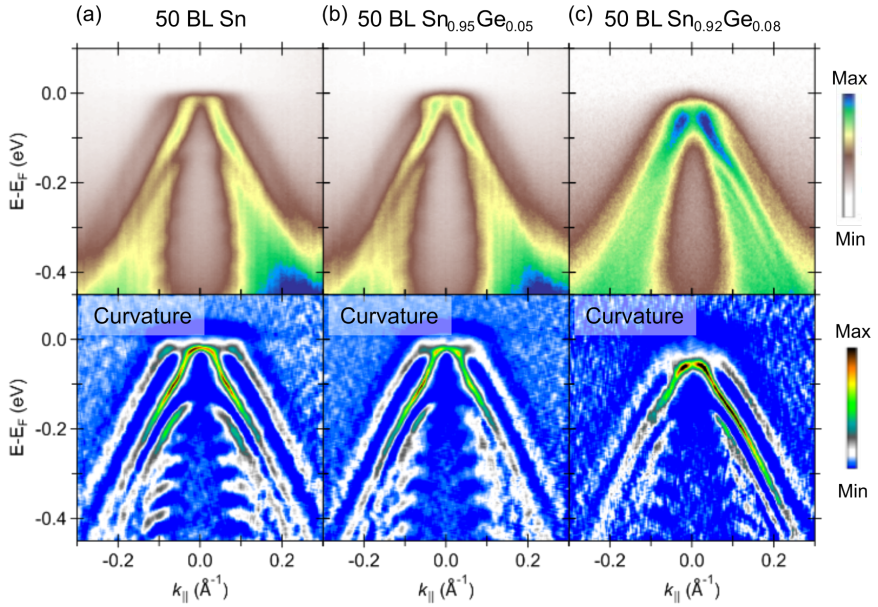

Figure 8.16: Measurements of the topological surface state in α-$Sn_{1-x}Ge_x$ at $h\nu = 21$eV for (a) 50 BL α-Sn, (b) 50 BL α-$Sn_{0.95}Ge_{0.05}$, and (c) 50 BL α-$Sn_{0.92}Ge_{0.08}$. The curvature enhances the locations of the bands. Measurements were taken along the $\overline{X} - \overline{\Gamma} - \overline{X}$ direction.

We also investigated the band structure of thicker 50 BL α-$Sn_{1-x}Ge_x$ briefly. Unfortunately, we were not able to observe the surface Dirac node for any of these samples, so topological phase identification was difficult (Fig. 8.16). The Dirac node does shift down closer to E_F as it does in the 13 BL films, but not below E_F. Quantum well states are visible in all three samples with near-equivalent spacing, indicating that the effective

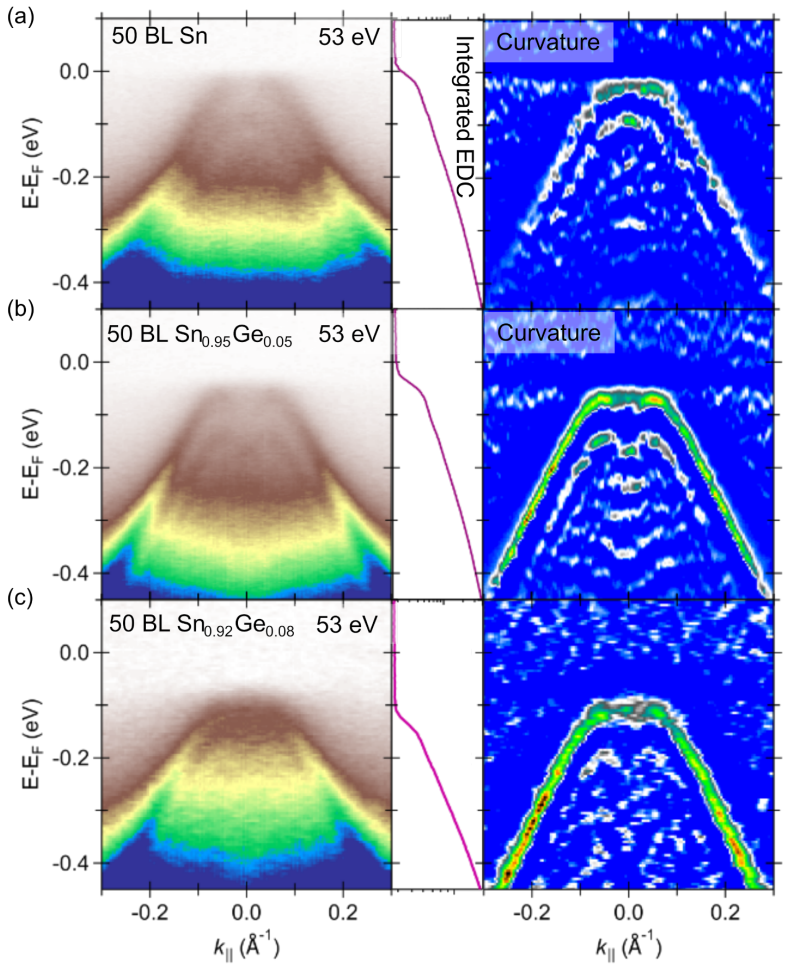

Figure 8.17: Measurements around the $\mathbf{\Gamma_{002}}$ point at $h\nu = 53$ eV for (a) 50 BL α-Sn, (b) 50 BL α-$Sn_{0.95}Ge_{0.05}$, and (c) 50 BL α-$Sn_{0.92}Ge_{0.08}$. The curvature is used to enhance the band locations. The EDCs are integrated over the full ± 0.3Å^{-1} momentum range. Measurements were taken along the $\overline{X} - \overline{\Gamma} - \overline{X}$ direction.

mass for all three samples is similar.

The total downward shift in the surface state dispersion is over 100 meV, much higher than the ∼50 meV for 13 BL films over a similar composition range. The relative band shift is then clearly a function of the film thickness. Changes to relative band alignment should not be a function of film thickness. The surface Fermi level position is related to bulk carrier density and the surface state density, where the bulk carrier density is tuned by Ge alloying and film thickness.

To study the bulk band structure, measurements around the $\mathbf{\Gamma_{002}}$ point were taken at a photon energy of 53 eV. The outermost band is the $\Gamma^+_{8,v}$ heavy hole band. The bands within the bulk continuum are quantum well states derived from the heavy hole band. For 50 BL α-Sn (Fig. 8.17(a)), the valence band maximum is slightly above E_F when investigating the $\mathbf{\Gamma_{002}}$ point. For α-$Sn_{0.95}Ge_{0.05}$, the valence band maximum (with expected vanishing intensity at the $\overline{\Gamma}$ point) is now approximately 50 meV below E_F (Fig. 8.17(b)). There appears to be some warping of the heavy hole band where the band velocity changes sign close to the $\overline{\Gamma}$ point. This is reflected in the dispersion of the quantum well states derived from the heavy hole band. In α-$Sn_{0.92}Ge_{0.08}$, the valence band maximum is now 100 meV below E_F (Fig. 8.17(c)). No sign change of the band velocity is visible, so the origin of this change in the α-$Sn_{0.95}Ge_{0.05}$ sample is unclear. However in both Fig. 8.17(b) and Fig. 8.17(c) we do not see evidence of the conduction band crossing the valence band, so it is unlikely that 50 BL α-$Sn_{0.95}Ge_{0.05}$ and 50 BL α-$Sn_{0.92}Ge_{0.08}$ are in the 3D DSM phase. As long as the surface states are not gapped at the surface Dirac node, at this thickness α-$Sn_{1-x}Ge_x$ is in a 3D TI phase as expected from calculations.

8.10 Conclusion

Tensile strained α-Sn has been proposed to be a topological insulator which may be integrated with III-V (InSb) and II-VI (CdTe) electronics, which also could demonstrate high spin to charge conversion efficiency. Using angle-resolved photoemission spectroscopy (ARPES), we first explore the electronic structure of ultrathin compressive strained α-Sn/InSb(001) grown by molecular beam epitaxy. We find evidence of the confinement-induced 3D TI phase in compressive strained α-Sn, clearing up a long-standing disagreement in the literature. With this phase benchmarked, we then alloy the

α-Sn films with Ge to decrease the bulk lattice constant and switch from compressive to tensile strained α-$Sn_{1-x}Ge_x$/InSb(001). The tensile strain induces a phase transition unexpectedly away from the 3D TI phase in ultrathin films, but appears to result in the expected 3D TI phase for thicker films. We supplement these measurements with spin-ARPES and show the presence of multiple spin-polarized surface states in addition to the previously measured topological surface state. The existence of these spin-polarized resonances in this system points toward tuning of the chemical potential being a key factor in improving the performance of α-$Sn_{1-x}Ge_x$ spintronic devices. Our results pave the way for a better understanding of the effect of strain and confinement on α-Sn's band structure.

Chapter 9

Development of InAlGaAs/AlGaAs spin-polarized photocathodes

9.1 Introduction

Spin-polarized electron beams are an essential tool in particle physics and have been used in nuclear and high energy physics research for decades [7, 379, 380]. New priority initiatives, such as the Jefferson Lab polarized positron source mentioned as a priority in the 2023 National Science Advisory Committee Long Range Plan for Nuclear Science, will require a high current polarized electron source with excellent lifetime [115,381]. The development of the vacuum and high voltage systems for a polarized positron source will require an ample supply of high polarization photocathodes for beam tests. The Electron Ion Collider at Brookhaven National Laboratory also requires a reliable and large supply of high polarization photocathodes capable of delivering a high bunch charge electron beam [116]. Since the only commercial vendor for high polarization strained superlattice photocathodes ceased production 10 years ago, there is no commercial supplier for high polarization photocathode material: re-establishing a robust domestic supply chain is a

priority.

Electron sources for accelerators have used tensile strained GaAs/GaAsP strained superlattices (SSL) as a source for high polarization electron beams for decades [7]. GaAs/GaAsP SSL photocathodes have been optimized through a series of SBIR awards to commercial semiconductor manufacturer SVT Associates in collaboration with both SLAC National Accelator Laboratory and Jefferson Lab. These GaAs/GaAsP SSL photocathodes were grown using molecular beam epitaxy (MBE) or gas source molecular beam epitaxy (GSMBE) and provide high electron spin polarization (ESP) over 85%, sufficient photocathode quantum efficiency (QE) up to 1.2%, and acceptable operational lifetime up to 300 Coulombs when used at Jefferson Lab's CEBAF injector [382]. These photocathodes have been used extensively at Jefferson Lab and elsewhere. They are uniform across the wafer surface, reproducible between production runs, and have minimal differences in QE as a function of laser polarization axis (low analyzing power) [383]. Unfortunately, SVT discontinued growing these high polarization GaAs/GaAsP photocathodes in 2014 and decommissioned their phosphide MBE system.

While GaAs/GaAsP photocathodes using MBE have been optimized and provide sufficient QE, high polarization and suitably long lifetimes, growing this structure has many challenges. Phosphorus is a dangerous and uncommon source element in MBE systems, limiting potential vendors and raising the production cost for phosphide-based photocathodes significantly. The alternative, a phosphine (highly poisonous) gas source, forms high vapor pressure byproducts when used with some gallium sources (triethyl gallium), additionally complicating growth. Phosphorus residue is toxic and flammable when performing routine maintenance on the growth chamber, leading to further increased production costs.

The stack used for state-of-the-art GaAs/GaAsP photocathodes is shown in Fig. 9.1. First there is GaAs a thick transition layer from the GaAs substrate to $GaAs_{1-x}P_x$

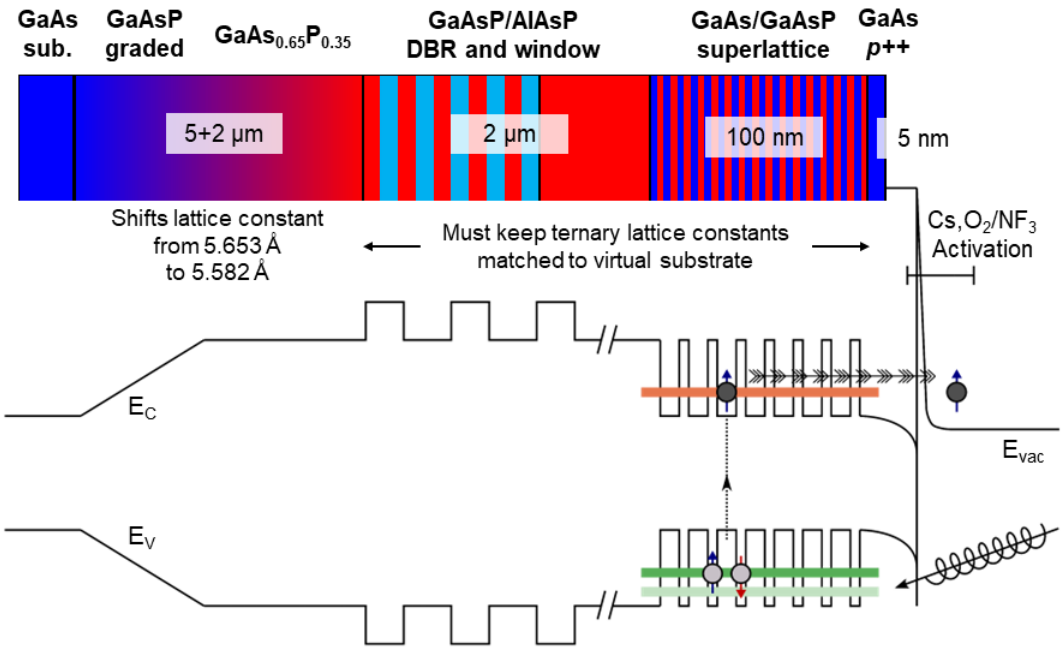

Figure 9.1: The photocathode design that is the current state of the art with its resultant band diagram, after [133]. The substrate and mirror sections are p-type doped at $\sim 5 \times 10^{18}$ doped while the superlattice region is p-type doped at $\sim 5 \times 10^{17}$ cm^{-3}. The window also serves to block any carriers generated beneath it from reaching the surface of the photocathode. The $p++$ region is doped to $\sim 5 \times 10^{19}$ cm^{-3}. The surface is activated to negative electron affinity with alternating Cs and NF_3 depositions until quantum efficiency is maximized.

[131, 384, 385] which serves as the lattice mismatched base (also known as a virtual substrate) for the SSL photocathode. Above this a superlattice mirror (Distributed Bragg Reflector (Chapter 1)) is grown. After that there is the photoemissive GaAs/GaAsP superlattice region. The total superlattice thickness is generally kept < 100 nm to reduce photoelectron depolarization during electron transport to the surface. Finally there is a highly doped GaAs layer, with a thickness near the depletion width, to reduce surface charge accumulation [382].

The GaAsP graded layer (Fig. 9.1) takes a long time to grow via MBE (more than 75% of total photocathode growth time) and is thus very expensive. One sample generally takes more than 12 hours to grow. Threading dislocations nucleated in the metamorphic

virtual substrate also propagate into the active region and are expected to degrade performance (lifetime, electron spin polarization, quantum efficiency), but to our knowledge the effect of dislocation density on photocathode performance has not been rigorously investigated. The ratio of As to P in GaAsP is also very sensitive to variations in substrate temperature and drifts in cell flux [386]. It is then quite difficult to ensure lattice matching to the virtual substrate throughout the entire active region of the device. Unintentional strain relaxation in the active region strongly degrades device performance and reduces the yield of successful photocathodes.

An alternative to MBE for growing GaAs/GaAsP SSL photocathodes is metal organic chemical vapor deposition (MOCVD). This technique uses much faster deposition rates, is less expensive and the use of phosphorus is more common, which solves some of the problems of growing GaAs/GaAsP with MBE. However, the thick transition layer between GaAs and GaAsP still needs to be grown for a MOCVD cathode, so the increased density of crystal defects is sustained. The surfaces of GaAs/GaAsP SSL photocathodes grown using MOCVD exhibit noticeable ripples due to lattice relaxation, which can lead to undesirable charge asymmetry effects (different QE depending on laser helicity) [383]. The Nagoya group has long found success with MOCVD [387], only recently replicated in the US [388]. While the best of the MOCVD GaAs/GaAsP photocathodes exhibit excellent QE and polarization, there are still significant variations in polarization across the sample, changes in the wavelength for peak polarization after heating the cathode, and significant sample to sample variation [389,390]. MOCVD-grown samples cannot be capped with amorphous arsenic *in situ*, a process used in MBE-grown samples, which drastically increases their heat cleaning temperatures after load in to a photogun (450 °C $\rightarrow$ 600 °C), reducing surface quality. This reduces the quantum efficiency and yield of successful photocathodes.

Finally, to enhance yield (QE), GaAs/GaAsP photocathodes have been grown with in-

tegrated Distributed Bragg Reflectors (DBRs) which improve quantum efficiency without reducing the phototelectron spin polarization [391, 392]. Both MBE [133] and MOCVD [388] have shown successful integration of photocathodes with DBRs. These DBRs use GaAsP/AlAsP or GaAsP/InAlP as the reflector layer and GaAsP as the window layer. As mentioned earlier, the As to P ratio is difficult to control in these structures, making the DBR structure for GaAs/GaAsP difficult to grow with consistent resonance peaks and lattice matching [133]. The GaAs/GaAsP DBR structure developed by SVT Associates and tested at Jefferson Lab is summarized in Fig. 9.1, after Ref. [133]. Clearly there are many issues with the GaAs/GaAsP system hindering consistent, inexpensive, high quality photocathodes.

By replacing the tensile strained GaAs wells with $In_xAl_yGa_{1-x-y}As$ (InAlGaAs) and the GaAsP barriers with $Al_zGa_{1-z}As$ (AlGaAs), photocathodes may be grown that only use commonly available sources. Many commercial vendors will be available to grow these photocathodes—reducing the supply chain issues that exist for GaAs/GaAsP. Following promising results in literature [393], we began to develop high polarization photocathodes in this materials system. InAlGaAs/AlGaAs superlattices can be grown directly on GaAs, removing the thick and defective graded buffer region. Wafer-to-wafer consistency and defect densities should be improved, as should affordability (total growth time is cut in half). Since only the group III site (In, Al, Ga) is alloyed rather than the group V site (As, P, Sb), wafer uniformity should improve as well as the sticking coefficients of group III atoms approach unity [394].

Finally, the InAlGaAs/AlGaAs structure allows greater capacity for tunable band alignments. In this system, the relative band alignment and total band gap of the superlattice can be tuned independently from each other, and both independently from the level of strain in the InAlGaAs layer (Fig. 9.2). In GaAs/GaAsP, the only tunable composition is the As to P ratio which tunes all three of these parameters simultane-

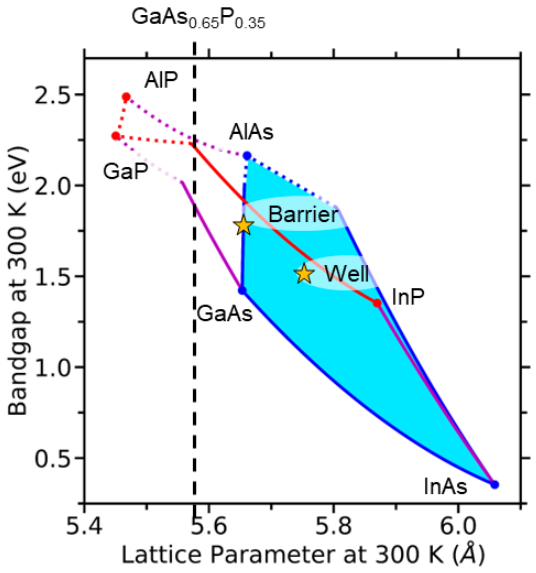

Figure 9.2: band gap vs. lattice parameter for various III-V's and their alloys at room temperature. The points correspond to the standard well and barrier composition referenced throughout the text.

ously. Many of the aforementioned issues can also be solved with InGaAsP/AlGaAs or InGaAsP/GaAsP heterostructures, but the use of phosphorous is still not ideal. For InAlGaAs/AlGaAs photocathodes, the wavelength for peak polarization can be adjusted freely and higher strain levels may be incorporated to improve spin polarization/quantum efficiency polarization further.

There are a few other avenues of band engineering that are possible in InAlGaAs/AlGaAs photocathodes that are not present in GaAs/GaAsP photocathodes. The topmost layer of the superlattice (sometimes called the active layer) is highly doped to decrease surface charge limit (SCL) effects in the photocathode under large bunch charges [129,130]. This layer, typically GaAs, dictates the chemistry and band alignment between the Cs-O/F functionalization layer and the semiconductor. Varying the composition of this active layer could potentially boost quantum efficiencies by reducing the surface barrier. A reduction of the surface barrier would also lead to a decrease in magnitude of the surface charge limit effect. In addition, the top GaAs layer is not band gap matched to

the InAlGaAs/AlGaAs superlattice—tuning the band gap of the highly doped region to match the superlattice band gap will improve measured photoelectron spin polarization.

Further quantum efficiency improvement could come from a chirped (graded InAlGaAs thickness) or graded aluminum composition superlattice which both generate an electric field that sweeps photoelectrons to the surface. This has been achieved in AlGaAs/GaAs photocathodes [395], but is not possible in the GaAs/GaAsP system. Varying the As to P ratio in the barriers at values below that in the metamorphic buffer will reduce the total superlattice thickness that can be grown (Fig. 9.2), reducing QE. Varying the As to P ratio in the barriers at values above that in the metamorphic buffer will result in tensile strained barriers (Fig. 9.2), reducing photoelectron spin polarization. Optimization of these schemes for InAlGaAs/AlGaAs photocathodes is possible due to the near lattice-matching between AlAs and GaAs. This approach could also reduce surface charge limit effects for high current and high bunch charge electron beams by increasing the tunneling rate of conduction electrons through the surface barrier. The InAlGaAs/AlGaAs system, with its higher average ionicity than GaAs/GaAsP, could potentially be less susceptible to ion damage and these photocathodes could thus have longer lifetimes than GaAs/GaAsP [396–398].

In this work we seek to demonstrate InAlGaAs/AlGaAs SSL photocathodes as a suitable alternative to GaAs/GaAsP. We develop a recipe for high polarization photocathodes that can be easily grown by many commercial semiconductor manufacturers using their standard MBE sources, thus providing a robust supply chain for these high polarization photocathodes. We also show the potential for InAlGaAs/AlGaAs photocathodes to show greater spin polarization, quantum efficiency, and lifetime than current GaAs/GaAsP photocathodes.

Our objective is to take a multifaceted approach to improving the performance of strained superlattice InAlGaAs/AlGaAs photocathodes to reach and then exceed the

level at which the current state-of-the-art GaAs/GaAsP system performs. These photocathodes can then replace those currently used for production beam at the Jefferson Lab polarized electron source. InAlGaAs/AlGaAs photocathodes allow for high strain (high polarization) and more complex layer designs. These photocathodes can be grown directly on GaAs with elements commonly found in both research- and commercial-grade MBE systems. In addition, they can be grown quickly and with lower cost compared to the phosphides—the designs optimized here can be sent to commercial vendors with minimal adjustments. These simplifications of the epitaxial growth process are expected to improve defect densities, wafer-to-wafer consistency, and wafer uniformity.

9.2 Methods

InAlGaAs/AlGaAs strained superlattices were grown by molecular beam epitaxy in a modified VGV80H solid source III-V system. Group III fluxes are calibrated by both RHEED oscillations and by XRD of calibration GaAs/AlGaAs and GaAs/InGaAs superlattices. We have found that XRD calibrations are required for compositions across growth runs to be consistent to within $\sim 1\%$. Unity V/III ratio is found by, during homoepitaxial GaAs(001) growth, setting the growth rate to the equivalent InAlGaAs growth rate at 520 °C. Then the As valve is closed, reducing flux, until the RHEED pattern transitions from a group V rich surface reconstruction to a group III rich surface reconstruction ($(2 \times 4) \rightarrow (1 \times 1)$ [399]). The flux was cycled back and forth across this transition to account for any hysteresis in a) the valved cracker or b) the surface transition. Relative changes in As flux are tracked with a beam flux gauge. *p*-type doping is achieved using solid source beryllium. Dopant density calibrations are performed by measuring the Hall carrier density on 1 μm GaAs calibration samples grown on semi-insulating GaAs(001) substrates using the same growth temperature and total growth

rate as used in the superlattice region. The growth rate of the superlattice region is roughly 0.5 ML/s. Ohmic contacts in the van der Pauw configuration are made to Hall samples by annealing pure In contacts for 1 hour at 400 °C in air.

Photocathode samples are all capped with a layer of amorphous As to protect the surface during transport to Jefferson Lab for measurements. After growth, the stack is exposed to an As_2 flux around 5×10^{-6} Torr for 30 minutes while the sample temperature is held below 50 °C. The spin polarization of photoelectrons is measured at Jefferson Lab using a microMott polarimeter, discussed in detail in Ref. [400]. Samples are installed in the polarimeter using a load-locked bellows system which is baked in between each sample change-over. A SuperK variable wavelength laser is used to illuminate the sample at wavelengths between visible and 810 nm. Software has been developed to automate measurement QE and polarization as a function of wavelength [400]. Photocathodes are activating using a SAES Cs dispsenser and a NF_3 leak valve via the usual yo-yo method. All photocathode measurements were performed at room temperature by Marcy Stutzman at Jefferson Lab.

9.3 Growth optimization of InAlGaAs/AlGaAs photocathodes

While GaAs/GaAsP SSL photocathodes have been the standard spin-polarized photocathodes, this has been partially a matter of convenience—SVTA was able to produce high performance GaAs/GaAsP spin-polarized photocathodes while InAlGaAs/AlGaAs photocathodes showed inconsistent results [401]. However, InAlGaAs/AlGaAs SSL photocathodes have produced spin polarization/quantum efficiency curves [393] comparable to GaAs/GaAsP SSL photocathodes [382] with similar hole splitting [402], albeit with

Reference	**Standard**	**High strain**	**Varied wells**	**Digital alloy**
6 nm GaAs	6 nm GaAs	6 nm GaAs	6 nm GaAs	6 nm GaAs
90 nm 12× (5.1 nm $In_{0.16}Al_{0.23}Ga_{0.61}As$ /2.3 nm $Al_{0.27}Ga_{0.73}As$)	60 nm 8× (5.1 nm $In_{0.16}Al_{0.23}Ga_{0.61}As$ /2.3 nm $Al_{0.27}Ga_{0.73}As$)	90 nm 12× (5.1 nm $In_{0.2}Al_{0.27}Ga_{0.53}As$ /2.3 nm $Al_{0.34}Ga_{0.66}As$)	90 nm 14× (3.8 nm $In_{0.2}Al_{0.2}Ga_{0.6}As$ /2.8 nm $Al_{0.24}Ga_{0.76}As$)	60 nm 8× (5.1 nm $In_{0.16}Al_{0.23}Ga_{0.61}As$ /3× (1 ML AlAs/ 2 ML GaAs))
500 nm GaAs	500 nm $Al_{0.3}Ga_{0.7}As$	500 nm $Al_{0.3}Ga_{0.7}As$	500 nm $Al_{0.3}Ga_{0.7}As$	500 nm $Al_{0.3}Ga_{0.7}As$
p-GaAs(001) sub.	*p*-GaAs(001) sub.	*p*-GaAs(001) sub.	*p*-GaAs(001) sub.	*p*-GaAs(001) sub.

Table 9.1: Layer designs for the different photocathodes investigated in this work.

optimal operation at wavelengths higher than desired for use at Jefferson Lab.

InAlGaAs/AlGaAs superlattices are not a commonly studied materials platform. As such, optimal growth conditions for defect-free, smooth, and fully strained superlattices with sharp interfaces are not well understood. InGaAs/GaAs superlattices are optimally grown at temperatures $\geq$ 520 °C, and the addition of aluminum usually increases optimal growth temperatures; See for example Refs. [403–405]. We first derived optimal growth conditions on InAlGaAs/AlGaAs test samples so that high quality photocathodes could be grown.

These test structures allowed for indirect optimization of the growth conditions of InAlGaAs/AlGaAs photocathodes. Growth temperature and V/III overpressure were both varied. First, the structural effect of varying these parameters was measured with X-ray diffraction. For superlattice diffraction, the 0^{th} order peak corresponds to the average out-of-plane lattice constant. The spacing between integer order reflections gives the total thickness of the period of the superlattice. The higher order fringes are related to the total thickness of the superlattice layer. In Fig. 9.3(a), the HRXRD near the GaAs(004) peak is shown for the sample series where growth temperature was varied.

The 0^{th} order peak, located near 65°, shifts very slightly to larger angles at higher growth temperatures. This indicates a slightly reduced superlattice period out-of-plane lattice constant, likely from reduced In incorporation in the film. The change between

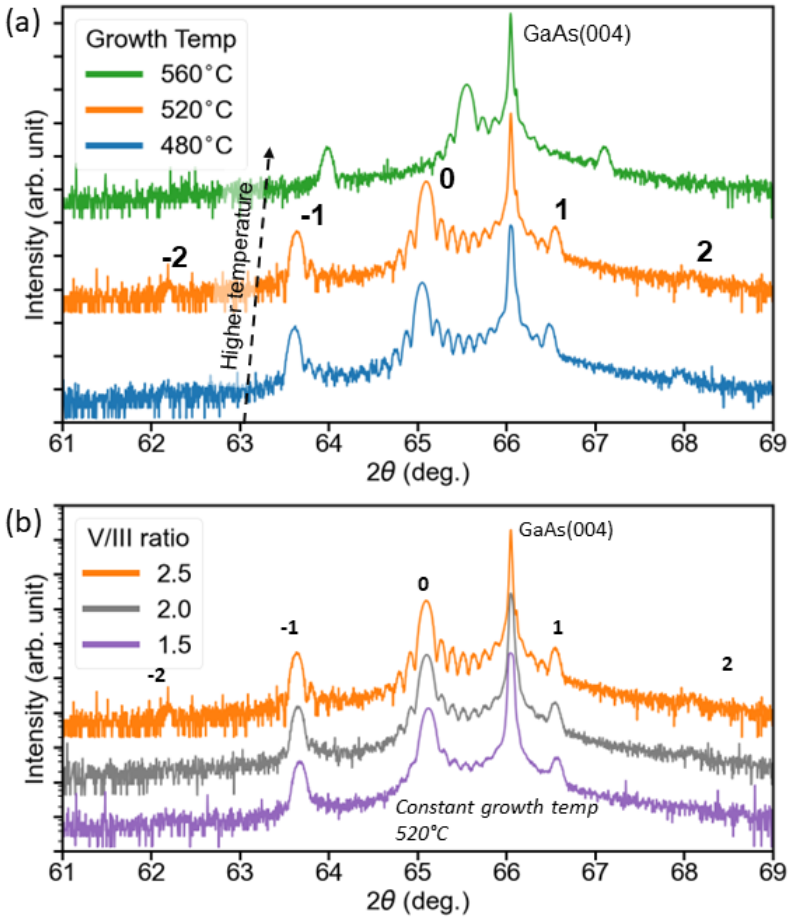

Figure 9.3: X-ray diffraction characterization of photocathode reference structures for (a) varying growth temperature with V/III=2.5, as calibrated at 520 °C and (b) varying V/III ratio grown at 520 °C.

these two samples indicates a reduction of around 4% indium. A more drastic decrease in the the 0^{th} order peak occurs in growth at 560 °C. Indium desorption is thermally activated [406] and as such increases exponentially with temperature. The equivalent concentration of indium incorporated is related to the In flux on the sample, growth temperature, and In:Al:Ga ratios on the surface. This reduction in the 0^{th} order peak also corresponds to a reduced total superlattice period, as expected.

The structural quality of the superlattice can be inferred from the number of integer peaks and the number and sharpness of the higher order fringes. From this it is clear

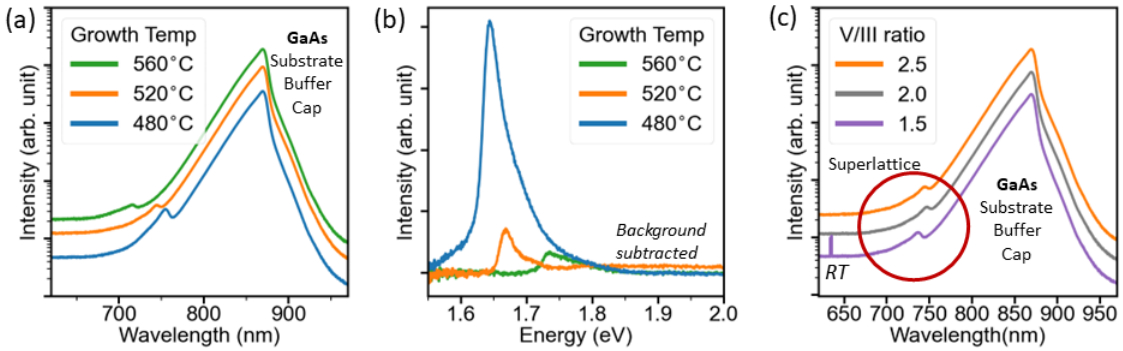

Figure 9.4: Room temperature photoluminescence spectra of the photocathode reference structures. Data for the growth temperature series for (a) raw data and (b) background subtracted data. (c) Raw data for the varied V/III ratio series.

that samples grown colder have higher structural quality and sharper interfaces. Growth at 480 °C would then likely give high photocathode performance.

Next we varied the V/III ratio while growing the same test structure at 520 °C, as this is where we expected the optimal growth temperature to be (Fig. 9.3(b)). From varying the V/III ratio between 1.5 and 2.5, there is a slight shift of the 0^{th} order peak toward lower angle indicating a very small $< 2\%$ increase in indium incorporation. The increased As overpressure likely reacts with In adatoms before they can desorb. Higher structural quality is indicated from increased higher order fringing and increased number of integer peaks at higher V/III ratio. High As overpressure is then preferred for growth of these photocathodes.

To address the optical quality of these test structures we performed photoluminescence spectroscopy (PL) measurements at room temperature. Changes to integrated intensity of the PL peak should correspond to trends in the QE of an equivalent photocathode [407]. The PL intensity relates to the recombination rate in the semiconductor such that defects which reduce the recombination rate also reduce the QE from a photocathode [407].

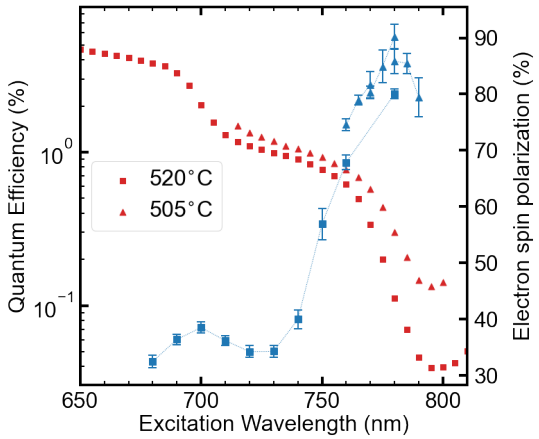

Figure 9.5: Quantum efficiency and spin polarization of the "standard" photocathode structure in Table 9.1 using two different growth temperatures.

In these measurements on the growth temperature series (Fig. 9.4(a)), the intensity is dominated by contributions from the *p*-GaAs substrate, the undoped GaAs buffer, and the undoped GaAs cap. We fit these contributions to subtract the background, and generate the peaks corresponding to the actual superlattice under investigation (Fig. 9.4(b)). The integrated intensity increases strongly with low growth temperature, indicating that growth at low temperature will result in much higher quantum efficiency photocathodes. These peaks all have a high energy shoulder, where the shoulder-main peak distance decreases with higher growth temperature. We expect that this splitting is then from heavy hole-light hole splitting. The V/III ratio (Fig. 9.4(c)) does not modify the intensity of the superlattice PL. The red shift of the superlattice peaks with lower temperature (Fig. 9.4(b)) and higher V/III ratio (Fig. 9.4(c)) are derived from the enhanced In incorporation found in XRD.

This characterization was verified with photocathode measurements. A photocathode grown at lower temperature (505 °C) increased both the QE and the photoelectron spin polarization significantly, shown in Fig. 9.5. The peak polarization increased from 80% to 85% while the quantum efficiency at peak polarization from 0.1% to 0.3%. The

quantum efficiency curve also appears to have a clear red shift for the sample grown colder, consistent with enhanced indium incorporation.

9.4 Optimization of photocathode layer design

The layer design of the photocathode was also optimized further by modifying the well structure, strain, and number of period repeats (See Table 9.1). Previous work had shown that more than 4 periods of InAlGaAs/AlGaAs SSLs reduce spin polarization [393], however this was not observed for our samples. This could potentially arise from our growth sequence. During our growth, we give short wait times ($<$ 20 seconds) in between each layer. The structures given in the literature require effusion cell temperature changes, which can make these wait times long (in excess of 20 minutes) and increase interface defects [404]. The high strain sample (In(x) from 16%$\rightarrow$20%) should increase the spin polarization by enhancing the splitting between the heavy hole and light hole minibands. In the varied well thickness, the quantum efficiency could be higher due to more period repeats, but the well thickness itself is lower which could counteract this. In addition, the reduced Al concentration in the barriers could increase the quantum efficiency. These structures are also grown at the suboptimal temperature of 520 °C. Future samples grown at lower temperature should have even better performance.

The performance of these photocathodes is summarized in Fig. 9.6, compared to the standard growth at the same temperature. Both techniques improve the spin polarization and QE of the photocathode. The spin polarization for the two non-standard samples are similar ($>$ 85%), but the high strain sample provides a larger wavelength range with high polarization. The QE curve of the increased In incorporation sample is also redshifted, as expected. Finally, the QE at peak polarization for this sample is around 0.6%, the highest of all samples measured. The peak figure of merit for this sample ($\sim$ 0.6) is very

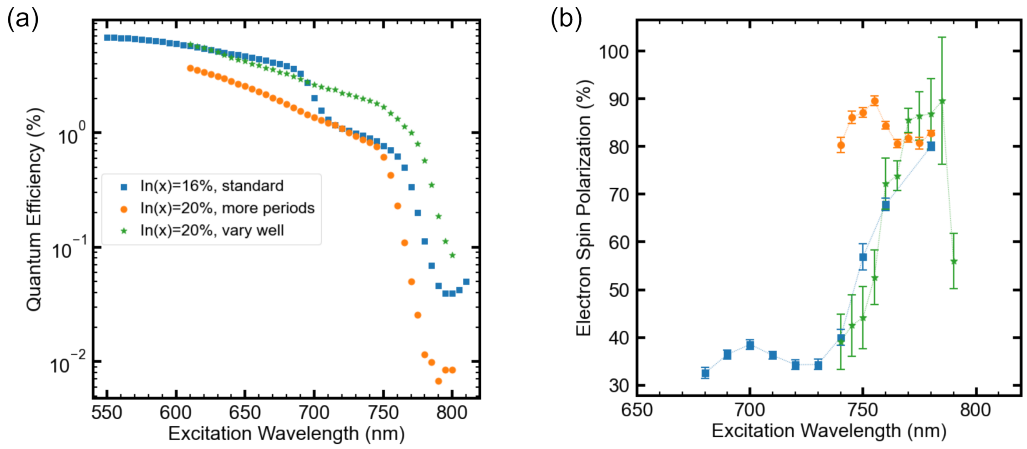

Figure 9.6: (a) Quantum efficiency and (b) photoelectron spin polarization of photocathodes with varied layer designs, given in Table 9.1 and grown at 520 °C with a V/III ratio of 2.5.

close to the record figure of merit in this system of 0.75 [393].

Of the limited number of MBE-grown InAlGaAs/AlGaAs photocathodes that have been tested so far, there is excellent sample-to-sample consistency of high polarization and QE, which is also reproducible through numerous heat cycles—even though material parameters are being varied significantly. With this short series of photocathodes, we are also quickly approaching the performance of the best GaAs/GaAsP (non-DBR) photocathodes optimized over years by the former commercial vendor. Performance matching and exceeding GaAs/GaAsP is expected as we continue to optimize the epitaxial stack design and growth conditions and integrate with AlAs/AlGaAs DBRs to enhance QE.

9.5 Toward integration with distributed Bragg reflectors

Integration of photocathodes with DBRs Distributed Bragg reflectors (DBRs) are mirrors that use repeating pairs of dielectrics with a large refractive index mismatch (summarized in Chapter 1). The use of DBRs for the improvement of quantum effi-

ciency in spin-polarized photocathodes was first proposed and demonstrated in the early 1990s [392], but was not integrated successfully with GaAs/GaAsP superlattice photocathodes until 2014 using GaAsP/AlAsP mirror layers grown by MBE [133]. These mirrors produced a resonant enhancement of QE at the target wavelength by a factor generally less than 8 [133], while GaAsP/InGaP mirrors grown by MOCVD have a slightly lower resonant enhancement [388]. Mirrors of AlAs/AlGaAs, on the other hand, have produced resonant enhancements greater than a factor of 10 [391]. AlAs/AlGaAs cannot be integrated well with GaAs/GaAsP photocathodes, as due to the strain involved (Fig. 9.2) they cannot be grown at the proper distance from the surface (they must be grown before the thick graded GaAsP transition layer). We grow AlGaAs/AlAs DBRs which are near lattice matched to the GaAs substrate, removing the difficulty in lattice matching found in the phosphide DBRs.

The key material parameter for maximized DBR performance (high reflectivity and high bandwidth of reflectivity) is a high refractive index mismatch between the two components of the DBR superlattice at the pump wavelength [134]. Using a pump wavelength of 780 nm, for the GaAsP/AlAsP DBR has $\Delta n = 0.4$, while for an $Al_{0.3}Ga_{0.7}As$/AlAs DBR $\Delta n = 0.5$ [408]. The high reflectivity bandwidth is more than 10% larger for the AlGaAs/AlAs DBR than the GaAs/GaAsP DBRs. This makes the resonantly enhanced wavelength more uniform across the wafer, helping to solve the wafer uniformity issues found in the phosphide-based photocathode system. The higher mismatch also means that the penetration depth of the light into DBR mirror is smaller, as each mirror period has a higher individual reflectivity. The DBR was designed with close attention paid to the composition of the AlGaAs layer; the ideal pump wavelength is below the band gap (no band-to-band absorption) of this layer including band gap narrowing effects from the 10^{18} cm^{-3} doping. The doping also allows for some free carrier absorption to occur in the DBR region [409]. By limiting the penetration into the DBR, free carrier absorption

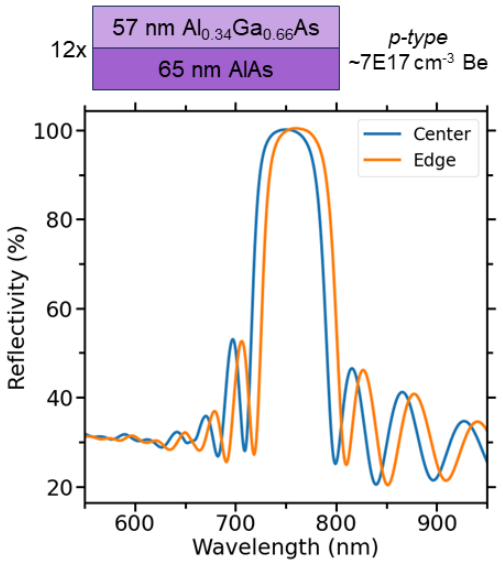

Figure 9.7: Reflectivity spectrum of a 12 period AlGaAs/AlAs DBR measured at the center and edge of a 1/4 of 2" wafer.

in the DBR is minimized ensuring even more of the total incident light is absorbed by the strained superlattice region—again increasing the QE.

While we have not yet had the opportunity to integrate DBRs with a photocathode, we have demonstrated the growth of high quality AlAs/AlGaAs DBR stacks (Fig. 9.7). The DBR was centered only 5 nm below the designed wavelength and had a bandwidth near 50 nm. The projected uniformity across a 2" wafer from this measurement was ± 20 nm such that the maximum mirror reflectivity should be sustained across an entire 2" wafer (an acceptable uniformity of the resonant condition). Due to improvements in the MBE during growth, we expect future DBRs to show better uniformity.

The optical constants of the strained well layer (InAlGaAs) are not well known experimentally. This normally results in a large number of trial growths to experimentally achieve resonant enhancement condition at the correct wavelength [133, 410]. Instead, we measure the optical constants of the superlattice region with spectroscopic ellipsometry. Precise calibrations on p-GaAs substrates are necessary in order to robustly extract

these parameters. This allows a direct calculation (using standard computational procedures [411]) of the resonant enhancement via solely experimentally measured parameters rather than interpolated ones, reducing the well-documented difficulty [133,388] in achieving the resonant condition at the desired wavelength for spin-polarized photoemission.

9.6 Digital alloying to improve high spin polarization bandwidth

We also investigated the use of a digital alloying (DA) scheme, depicted in Fig. 9.8(a), where a random alloy (RA) (AlGaAs) is grown instead as a superlattice of its components (AlAs and GaAs). This technique is generally used to improve uniformity [412] and improve optoelectronic device performance [413–415] in complex semiconductor stacks. In spin-polarized photocathodes, the spin polarization is maximized near the heavy hole band edge (Chapter 1). At lower wavelengths, the light hole band (which excites to the opposite spin direction) is accessed, decreasing the net photoelectron spin polarization. Since the quantum efficiency of a photocathode increases with decreasing wavelength, it is optimal to maximize the difference in wavelength at which the light hole and heavy hole bands begin to be excited.

This window in which only the heavy hole band is excited is related to 1) the splitting between the heavy hole band and the light hole band and 2) the energy linewidth of the heavy hole band and light hole band. The hole splitting is mainly determined by the strain and thickness of the InAlGaAs layer [127]. The linewidth of each band is related to the design of the superlattice and the level of disorder in the semiconductors [127].

The main disorder of interest here is random alloy disorder, the deviations away from the mean potential in the crystal due to random fluctuations from random placement of

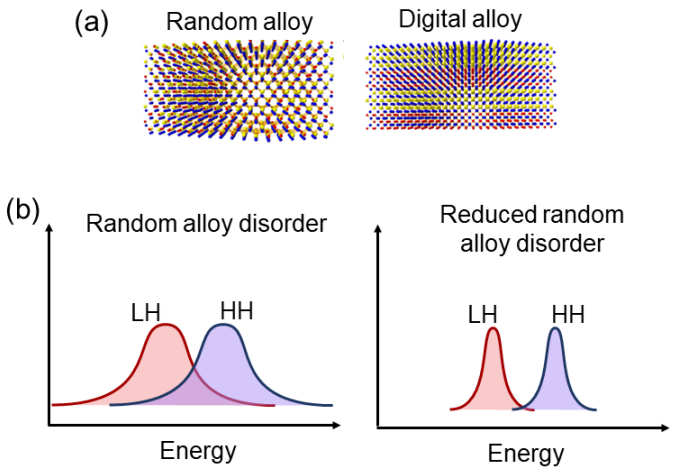

Figure 9.8: (a) Schematic of how a digital alloy is synthesized. Reprinted from [416], with the permission of AIP Publishing. (b) Proposed reduction in linewidth from reduced random alloy disorder in a digital alloy.

substitutionally alloyed elements (Al/Ga/In or As/P) [417–420]. Since the InAlGaAs/AlGaAs system is a quaternary/ternary system compared to the conventional GaAs/GaAsP binary/ternary, random alloy disorder will be higher, increasing the linewidths further [419–421]. This could then decrease the wavelength breadth of the high spin polarization window. A digital alloy, by reducing random alloy disorder, would have the opposite effect and increase the breadth of the high spin polarization window by decreasing crosstalk between the heavy hole and light hole channel (Fig. 9.8(b)).

So far two DA reference samples have been characterized, along with a true DA photocathode. The DA scheme for these reference samples is summarized in Fig. 9.9(a) including one sample with DA barriers and one sample with DA wells and barriers. An additional layer is inserted at the end of the last period to preserve the inversion symmetry of the DA layer. These reference samples have been characterized with X-ray diffraction to confirm the stack remains fully strained to the GaAs substrate (Fig. 9.9(b)). The superlattice has the same in-plane lattice constant as the GaAs substrate, indicating no relaxation has occurred.

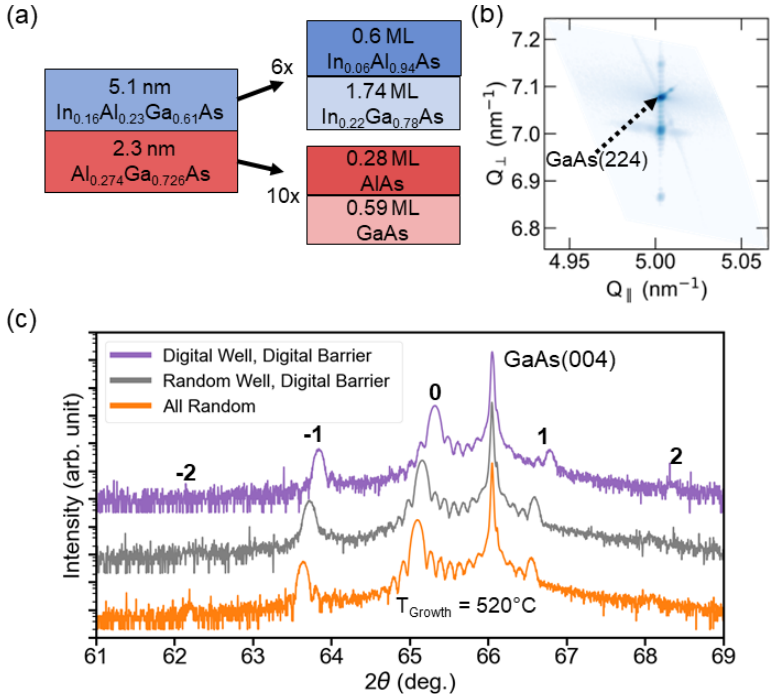

Figure 9.9: (a) Schematic of digital alloy reference samples. (b) Reciprocal space map in the vicinity of the GaAs(224) peak. All peaks have the same in plane lattice constant, indicating the superlattice is fully strained. (c) X-ray diffraction measurement around GaAs(004). The number of fringes is equal for the three samples; they all have similar interface quality.

The crystal quality of the DA is approximately the same as the random alloy samples, although the fully DA sample appears to show slightly weaker fringes. The fully DA sample also has reduced out-of-plane lattice constant consistent with reduced In incorporation. This is because the rate of desorption vs. incorporation increases for each sublayer of the digital alloy as compared to the random alloy. The growth rates in the random alloy are faster than those of each subcell of the digital alloy.

The PL of both DA references in Fig. 9.10 (with background subtracted) shows higher integrated intensity than a RA photocathode, indicating the DA scheme will improve QE. The blue shift of the fully DA sample is consistent with the reduced indium incorporation measured in XRD. The light hole shoulder is still present in the digital alloy barrier sample. However, the fully digital alloy sample appears to have higher

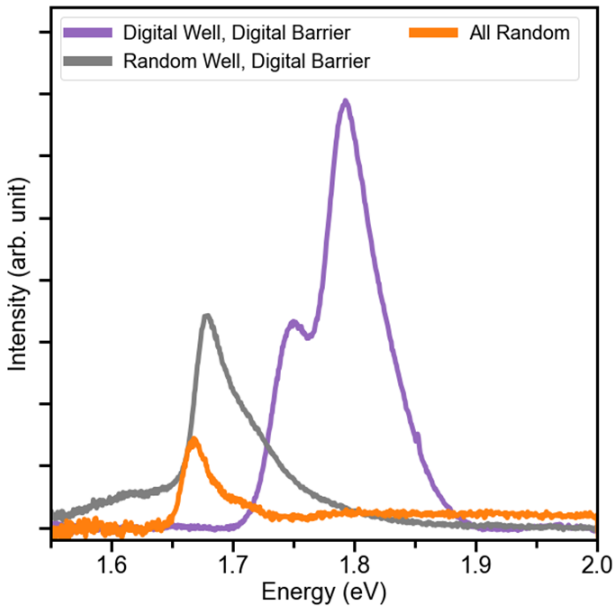

Figure 9.10: Room temperature photoluminescence measurement of the three photocathode reference samples. A large background from the GaAs substrate is subtracted.

intensity on the light hole rather than the heavy hole. Unfortunately, due to the GaAs cap and large GaAs background intensity, it is difficult to perform photon intensity-dependent measurements. These measurements can help identify the origin (excitonic, band-to-band, defect-assisted, etc.) of PL emission [422].

Furthermore, the uniformity of the wafers was assessed with reflectance measurements. Reflectance measurements are optimal for assessing uniformity, as it is very sensitive to the resonant enhancement conditions when samples are integrated with DBRs [134]. We use the derivative of the reflectance as changes to the spectrum across the wafer are clearer. There is a two-fold decrease in variation of the white line ($dR/d\lambda$ peak) reflectance across 1/4 of a 2" wafer between a fully RA reference and a fully DA reference (Fig. 9.11). A sample with the same digital alloy barrier but a random alloy well exhibits the same uniformity as a fully random sample. This indicates that the InAlGaAs well is the primary contributor to wafer non-uniformity. Growing the SSL at

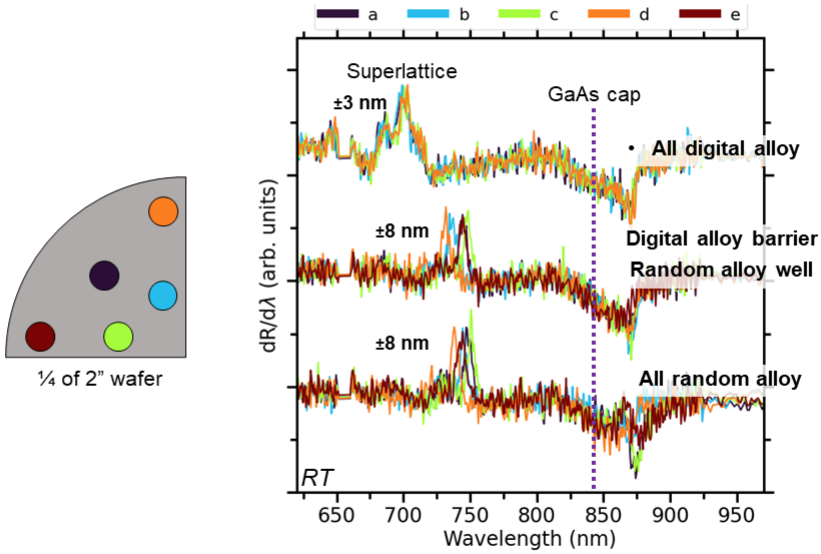

Figure 9.11: The derivative of the reflectivity measured for the digital alloyed samples at 5 different locations on 1/4 of a 2" wafer.

lower temperatures where the In desorption is lower could improve the uniformity. With improved wafer uniformity, the resonant condition can be matched to the wavelength of peak spin polarization across a larger portion of the wafer.

We have investigated one DA photocathode where the InAlGaAs layer is a random alloy and the barrier consists of a 3-period AlGaAs DA (Table 9.1). This has produced very successful results shown in Fig. 9.12. The DA and random alloy photocathodes have slightly different superlattice band gaps and hole splittings. We align the spin polarization and QE curves by aligning the absorption edges of the photocathode (the first derivative of QE). The DA photocathode shows a high ESP window much wider than that of the RA calibration photocathode grown under the same conditions—as predicted. The maximum spin polarization is larger for the DA photocathode, although the quantum efficiency is slightly lower.

These results are promising and suggest that optimized digital alloy InAlGaAs photocathodes combined with optimal growth conditions and layer designs could have greater QE, spin polarization, and uniformity than random alloy InAlGaAs photocathodes. More

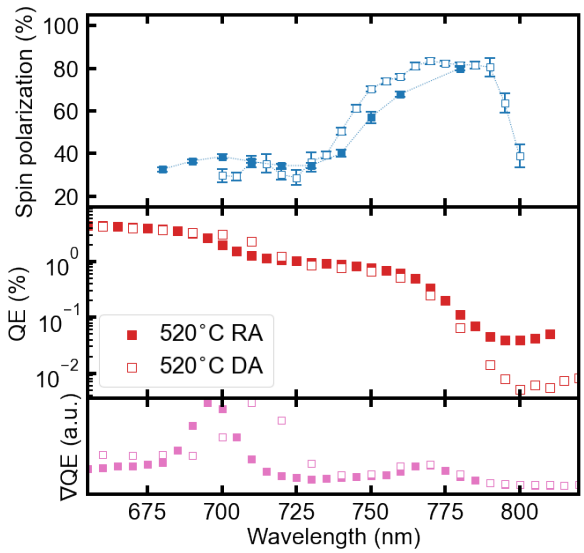

Figure 9.12: Spin polarization and quantum efficiency of a random alloy vs. digital alloy barrier (3 period DA barrier in Table 9.1). The QE and spin polarization of the DA sample are shifted to the right by 20 nm to align the absorption edge (the peak of the derivative of QE).

complex digital alloy schemes require further testing.

9.7 Conclusion

Prototype InAlGaAs/AlGaAs photocathodes have been validated as suitable for operation at Jefferson Lab. The best of these samples have photoelectron spin polarization near 90% (comparable or better than that of GaAs/GaAsP), while QE is just over half that of GaAs/GaAsP (without a DBR). The QE at peak spin polarization is rapidly approaching that of the highest figure of merit InAlGaAs/AlGaAs photocathodes in the literature (>80% of the record [393]). Growth parameters and the specific layer compositions will continue to be further optimized to improve performance of basic InAlGaAs/AlGaAs photocathodes past that of GaAs/GaAsP. This will include optimization of a digital alloying scheme, which we have shown increases the width of the high spin polarization window. Integration of the photocathode with a well-calibrated DBR stack

should improve the figure of merit by an order of magnitude. These procedures should push forward the InAlGaAs/AlGaAs photocathode system as a suitable replacement for GaAs/GaAsP photocathodes.

Chapter 10

Conclusions and future work

In this dissertation, improvements to the growth of various materials systems—Heuslers, Group IV semiconductors, and III-V semiconductors—were demonstrated. A deeper understanding of these systems was found such that they may be better incorporated into devices relevant to both spintronics and particle physics.

In Chapter 3, we attempted to optimize the ordering of full Heusler topological semimetal Co_2FeSn. This system is predicted to have record-breaking anomalous Hall and Nernst conductivities at room temperature. By varying growth parameters of the film and the buffer layer upon which growth was initiated, ordering of the Heusler films was improved. The maximal ordering was only found to be B2, but the magnitude of the anomalous Hall and Nernst effects were found to actually decrease with improved ordering.

While most Heusler studied have focused on improving the ordering above all else, here we show that reducing the ordering could enhance the effects of interest in this system. Deeper studies into the effect of disorder is interesting are it is relatively trivial to prepare disordered Heusler films by a number of low cost thin film deposition techniques compatible with standard fabrication processes. Improving the anomalous Hall

and Nernst conductivities of Co_2FeSn can be accomplished by n-type alloying these films to increase the valence electron count. This will move the chemical potential closer to the sources of Berry curvature contributing to the anomalous transport. Alloying Ni on the Co site has the most promise, as Ni_2FeSn is a stable Heusler alloy. Other options such as Sb on the Sn site could encounter phase segregation issues.

In Chapter 4, a growth procedure for α-Sn thin films on InSb(001) was introduced. This procedure allows for minimal out-diffusion of indium from the substrate into the film such that the films do not need extrinsic Te or Bi dopants. The reduced p-type doping allowed for the surface Dirac node to be visible in ARPES measurements throughout the rest of this dissertation. In addition, this procedure confirms that any features reported in this dissertation (e.g. two spin polarized surface states via spin-ARPES) are intrinsic to α-Sn.

In Chapter 5, ARPES measurements demonstrated the existence of two surface states in the bulk band gap of ultrathin α-Sn(001) films. Problematically, the inner potential model fails at VUV photon energies leading to potential misinterpretation of past ARPES results. In thick films, these two surface states were found to be spin-polarized with orthogonal spin-momentum locking in opposite directions.

In Chapters 6 and 7, it was made clear that interactions of the α-Sn thin film with the InSb substrate could not be ignored. Hybridization at the film/substrate interface renormalizes the topological surface state, leading to frustration of hybridization between the top and bottom surfaces. This renormalization at the interface was directly measured in ARPES. Either hybridization or a structural deformation inherited from the heteropolar InSb substrate led to bulk inversion symmetry breaking in α-Sn films, characterized by spin-splitting of the bulk bands and degeneracy breaking at select high symmetry points.

In Chapter 8, these clarifications allowed us to show that ultrathin α-Sn(001) films are in a confinement-induced 3D topological insulator phase, the first direct experimental

proof of this phase on the topological phase diagram for this system. From there, the effect of Ge alloying in these ultrathin films was explored. The Ge alloying induced an unexpected topological phase transition *away* from the 3D topological insulator phase, likely to a 3D normal insulator phase. This unexpected phase transition is possibly related to the structural and hybridization interactions with the InSb substrate. Finally, spin-polarized ARPES revealed the presence of another pair of spin-polarized surface states above the surface Dirac node. The full picture of surface states in the α-$Sn_{1-x}Ge_x$ system is that of an upper and lower spin resonance, along with a Dirac-like topological surface state. These spin-polarized states are consistent with hybridization between electron-like and hole-like Rashba surface states [209].

Now that the stage has been set for α-$Sn_{1-x}Ge_x$, many studies are possible. The studies reported in this thesis all work with InSb substrates. We have shown that hybridization with the InSb can have significant ramifications on the hybridization between topological surface states at the top and bottom surfaces of the film. In order to tune this hybridization at constant thickness, the InSb substrate may be replaced with a thin strained $In_{1-x}Al_xSb$ epilayer. With judicious choice of film thickness, modulation of the Al content should tune the film from a 3D topological insulator to 2D topological insulator.

The hybridization may also be tuned through growth on a CdTe substrate. Ideally this is a CdTe metamorphic buffer on Si or GaAs, as single crystal CdTe substrates contain large Te inclusions [423] which serve as nucleation points of β-Sn during growth and reduce sample yield. The effect of inversion symmetry could be changed in this scenario, but can be verified by including an epitaxial CdTe capping layer. This capping procedure also will likely have the benefit of increasing the mobility of the α-Sn well by displacing the conducting region from the surface scattering potential. Undoped CdTe and $In_{1-x}Al_xSb$ also benefit from high impedance such that the only transport channel

is the α-Sn. Tuning of the optimal substrate and capping layer should result in good control over high mobility α-Sn films, presenting a nonpolar analogue to much of the physics already demonstrated for HgTe.

Some of the main limitations of the topological insulator state in α-$Sn_{1-x}Ge_x$ is that large band gap films must be grown very thin to avoid reaching the critical thickness for relaxation. Since α-Sn and α-$Sn_{1-x}Ge_x$ have opposite signs of strain, a fully or partially compensated superlattice of α-Sn and α-$Sn_{1-x}Ge_x$ can be grown to reduce the net strain. This should result in a larger band gap 3D topological insulator film. The superlattice will have a larger critical thickness and should have a higher temperature for the $\alpha \rightarrow \beta$ transition. Modulating the period of the superlattice can enhance the bulk inversion asymmetry and increase the strength of spin-orbit coupling effects.

Now that the band structure of α-Sn lightly alloyed with Ge has been more deeply studied, both the Ge and Sn rich side of this alloy are understood. A near 50/50 composition of this alloy, completely immiscible in the bulk, can be stabilized by molecular beam epitaxy growth on a closely-lattice matched substrate—GaSb, InAs, and ZnTe. We have recently demonstrated stabilization on the former. Topological non-triviality is preserved such that epitaxial strain and quantum confinement can tune between a 3D Dirac semimetal phase, a 3D topological insulator, and a 2D topological insulator phase. Heating and ion implantation can nucleate the superconducting β-Sn phase. This presents a very interesting method to combine multiple topological and superconducting systems with high mobility InAs quantum wells and 6.1 Å semiconductor optoelectronics.

The better understanding of the α-$Sn_{1-x}Ge_x$ system found in this thesis also gives a better understanding of its good performance in current-induced spin-orbit torque devices. Devices based off of α-$Sn_{1-x}Ge_x$ with larger bulk band gaps should have even larger conversion than those demonstrated on pure α-Sn via a reduced bulk contribution. Both α-Sn and α-$Sn_{1-x}Ge_x$ thin film based devices would likely benefit significantly from

incorporating gate control of the chemical potential to minimize contributions from the bulk bands and upper and lower spin resonances. α-$Sn_{1-x}Ge_x$ is then hopefully positioned above other topological materials for high performance current-induced spin-orbit torque devices operated at room temperature.

In Chapter 9, high performance strained superlattice InAlGaAs/AlGaAs photocathodes were grown on GaAs substrates without a metamorphic virtual substrate. These photocathodes showed high spin polarization and reasonable quantum efficiency, positioning this material system as a low cost alternative to GaAs/GaAsP. Initial tests of introducing a digital alloying scheme showed promising improvements to the heavy hole bandwidth, increasing the bandwidth which shows high spin polarization. Optimization of both the random alloy and the digital alloy scheme is ongoing. Integration with optimized distributed Bragg reflectors will significantly enhance the quantum efficiency at peak spin polarization.

This quaternary/ternary system also permits tuning of the band gap of the highly doped cap to increase the quantum efficiency and surface charge limit in these photocathodes. Remote doping can be explored to reduce localization effects in the well layers and reduce spin-scattering of polarized photoelectrons against ionized impurities. Optimized heterostructure design and dopant engineering position the InAlGaAs/AlGaAs system to surpass the current state-of-the-art GaAs/GaAsP system in both performance and affordability. These spin-polarized photocathodes could allow more rapid experimentation in particle physics. Materials characterization techniques making use of incident spin-polarized electrons can also benefit; a boost in efficiency and reduction in price could make these techniques more accessible to the scientific community.

Appendix A

Code for tight-binding calculations

```
import chinook
import numpy as np

a0 = 6.4892 # bulk lattice constant

#%strain
exx = 1
a = a0*(1+exx/100)
ezz = -2*0.44*exx #c12/c11 ratio
c = a0*(1+ezz/100)

#unstrained nearest neighbor distances
NN0_0 = 0.25*np.sqrt(2*a0**2+a0**2)
NN1_0 = a0/np.sqrt(2)
NN2_0 = .5*np.sqrt(a0**2+a0**2)
```

```
#strained nearest neighbor distances
NN0_s = 0.25*np.sqrt(2*a**2+c**2)
NN1_s = a/np.sqrt(2)
NN2_s = .5*np.sqrt(a**2+c**2)

#exponents used (Harrison's d2 law)
ponent1 = 2
ponent2 = 2
ponent3 = 2

#sort nearest neighbors
cutoff_origin = np.sort([NN0_s,NN1_s,NN2_s])
newcutoffs = [np.mean(cutoff_origin[0:2]),
np.mean(cutoff_origin[1:]),0.8*a]
Str_bondL_rat = cutoff_origin/np.array([NN0_0,NN1_0,NN2_0])

# define lattice vectors for FCC lattice
avec = np.array([[a/2,a/2,0],
[a/2,0,c/2],
[0,a/2,c/2]])

# define k range for TB hamiltonian to be solved over
kpoints = np.array([[0.0,0.5,0.5],[0.0,0.0,0.0],[3/8,3/4,3/8],
[0.0,0.0,0.0],[0.5,0.5,0]])
labels = np.array(['$Z$','$\\Gamma$','$K$','$\\Gamma$','$X$'])
```

```
kdict = {'type':'F',
'avec':avec,
'pts':kpoints,
'grain':1000,
'labels':labels}
k_object = build_lib.gen_K(kdict)

#inlcude spin orbit coupling
spin = {'bool':True,
#include spin (doubles basis for spin up and spin down)
'soc':True,     #include atomic spin-orbit coupling
'lam':{0:0.65}} #spin-orbit coupling strength in eV

#build basis of atomic orbitals
Sn1 = np.array([0.0,0.0,0.0])
Sn2 = np.array([a/4,a/4,c/4])
basis = {'atoms':[0,0],
#two equivalent atoms in the basis, both labelled as species #0
'Z':{0:50},
#We only have one atomic species,
which is tin #50 in the periodic table.
'orbs':
[['50','51x','51y','51z','42xz','42xy','42yz','42XY','42ZR'],
['50','51x','51y','51z','42xz','42xy','42yz','42XY','42ZR']],
#each atom includes a full 5s, 5p, and 4d orbitals
```

```
'pos':[Sn1,Sn2], #positions of the atoms, in units of Angstrom
'spin':spin} #spin arguments.
basis_object = build_lib.gen_basis(basis)

# on site
Es = -5.393
Ep = 2.3252
Ed = 10.971

# 1 NN
Vsss = 1.183
Vsps = 1.511
Vsds = 1.327
Vpps = -2.804
Vppp = 0.761
Vpds = 0.221
Vpdp = -1.494
Vdds = -1.726
Vddp = 0.402
Vddd = -0.966

VSK1 =
{'050':Es, '051':Ep, '042':Ed, '005500S':Vsss, '005501S':Vsps,
'005402S':Vsds, '005511S':Vpps, '005511P':Vppp, '005412S':Vpds,
'005412P':Vpdp, '004422S':Vdds, '004422P':Vddp, '004422D':Vddd}
```

```
# 2 NN
Vsss = 0.0097
Vsps = 0.157
Vsds = -0.3331
Vpps = -0.058
Vppp = -0.005
Vpds = -0.097
Vpdp = 0.254
Vdds = -0.505
Vddp = 0.059
Vddd = -0.033

VSK2 =
{'005500S':Vsss, '005501S':Vsps, '005402S':Vsds, '005511S':Vpps,
'005511P':Vppp, '005412S':Vpds, '005412P':Vpdp, '004422S':Vdds,
'004422P':Vddp, '004422D':Vddd}


# 3 NN (equivalent to 2 NN if no strain)
Vsss = 0.0097
Vsps = 0.157
Vsds = -0.3331
Vpps = -0.058
Vppp = -0.005
```

```
Vpds = -0.097
Vpdp = 0.254
Vdds = -0.505
Vddp = 0.059
Vddd = -0.033

VSK3 =
{'005500S':Vsss, '005501S':Vsps, '005402S':Vsds, '005511S':Vpps,
'005511P':Vppp, '005412S':Vpds, '005412P':Vpdp, '004422S':Vdds,
'004422P':Vddp, '004422D':Vddd}

# scale slater-koster terms by strain
for key in VSK1:
    VSK1[key] *= Str_bondL_rat[0]**ponent1
for key in VSK2:
    VSK2[key] *= Str_bondL_rat[1]**ponent2
for key in VSK3:
    VSK3[key] *= Str_bondL_rat[2]**ponent3

VSK = [VSK1,VSK2,VSK3]
cutoff = newcutoffs

# Build hamiltonian and solve hamiltonian

hamiltonian = {'type':'SK',      #Slater-Koster type Hamiltonian
```

```
'V':VSK, #List of dictionaries of S-K parameters
'avec':avec, #lattice geometry
'cutoff':cutoff, #length scale for 1 NN, 2 NN, and 3 NN
'renorm':1.0, #renormalize bandwidth of Hamiltonian
'offset':0.1, #offset the Fermi level to agree with experiment
'tol':1e-4, #minimum amplitude for element to be used in calc.
'spin':spin} #spin arguments

TB = build_lib.gen_TB(basis_object,hamiltonian,k_object)
TB.Kobj = k_object
TB.solve_H()


# add inversion symmetry breaking E term to the onsite elements.
# It is adjusted by +/- E/2 to keep E_F in similar location
for check in range(len(TB.mat_els)):
        if TB.mat_els[check].i == TB.mat_els[check].j:
            if TB.mat_els[check].i%18<9:
                TB.mat_els[check].H.append([0,0,0,E/2])
            elif TB.mat_els[check].i%18>=9:
                TB.mat_els[check].H.append([0,0,0,-E/2])
            else:


TB.solve_H()
```

Bibliography

[1] I. Zutic, J. Fabian, and S. D. Sarma, Reviews of Modern Physics **76**, 323 (2004).

[2] S. G. Monserrate, MIT Case Studies in Social and Ethical Responsibilities of Computing (2022), https://mit-serc.pubpub.org/pub/the-cloud-is-material.

[3] A. Hirohata, K. Yamada, Y. Nakatani, I.-L. Prejbeanu, B. Diény, P. Pirro, and B. Hillebrands, Journal of Magnetism and Magnetic Materials **509**, 166711 (2020).

[4] A. Manchon, J. Železný, I. M. Miron, T. Jungwirth, J. Sinova, A. Thiaville, K. Garello, and P. Gambardella, Review of Modern Physics **91**, 035004 (2019).

[5] Q. L. He, T. L. Hughes, N. P. Armitage, Y. Tokura, and K. L. Wang, Nature Materials **21**, 15-23 (2022).

[6] Digital Science. (2018-) Dimensions [Software] available from https://app.dimensions.ai. Accessed on 4/5/2024, under licence agreement.

[7] P. A. Adderley, D. Bullard, Y. C. Chao, C. H. Garcia, J. Grames, J. Hansknecht, A. Hofler, R. Kazimi, J. Musson, C. Palatchi, K. Paschke, M. Poelker, G. Smith, M. L. Stutzman, R. Suleiman, and Y. Wang, Nuclear Instruments and Methods in Physics Research A: Accelerators, Spectrometers, Detectors and Associated Equipment **1046**, 167710 (2023).

[8] T. Rao and D. H. Dowell, *An engineering guide to photoinjectors*, CreateSpace Independent Publishing, 2013.

[9] W. Liu, M. Poelker, J. Smedley, and R. Ganter, Topics in Applied Physics **135**, 293-344 (2020).

[10] O. E. Tereshchenko, V. A. Golyashov, V. S. Rusetsky, D. A. Kustov, A. V. Mironov, and A. Y. Demin, Nanomaterials **13** (2023).

[11] Y. Tian, G. Gu, P. Johnson, T. Rao, T. Tsang, and E. Wang, Applied Physics Letters **113**, 233504 (2018).

[12] D. A. McQuarrie, *Quantum Chemistry*, University Science Books, 2nd edition, 2007.

[13] E. Tretkoff, APS News **16**, 1 (2007).

[14] L. I. Schiff, *Quantum Mechanics*, McGraw-Hill, 3rd edition, 1968.

[15] J. S. Townsend, *A Modern Approach to Quantum Mechanics*, University Science Books, 2nd edition, 2012.

[16] P. Phillips, *Advanced Solid State Physics*, Cambridge University Press, 2nd edition, 2012.

[17] N. Ashcroft and N. D. Mermin, *Solid State Physics*, Saunders College Publishing, 1st edition, 1976.

[18] R. Hoffmann, Angewandte Chemie **26**, 846-878 (1987).

[19] M. Dresselhaus, G. Dresselhaus, and A. Jorio, *Group Theory*, Springer-Verlag, 1st edition, 2008.

[20] G. Dresselhaus, Physical Review **100**, 580–586 (1955).

[21] R. Winkler, *Spin-orbit Coupling Effects in Two-Dimensional Electron and Hole Systems*, Springer-Verlag, 1st edition, 2003.

[22] B. Voigtländer, *Scanning Probe Microscopy*, Springer-Verlag, 2015.

[23] P. Hofmann, *Surface Physics: An Introduction*, Self-Published, 2016.

[24] Y. A. Bychkov and E. I. Rashba, Journal of Physics C: Solid State Physics **17**, 6039 (1984).

[25] Popular Science Background, The 2016 Nobel Prize in Physics *https://www.Nobelprize.Org/Prizes/Physics/2016/Press-Release/ (NobelPrize.org, 2024).*

[26] H. Kroemer, Review of Modern Physics **73**, 783 (2001).

[27] M. G. Vergniory, B. J. Wieder, L. Elcoro, S. S. P. Parkin, C. Felser, B. A. Bernevig, and N. Regnault, Science **376**, eabg9094 (2022).

[28] J. E. Avron, D. Osadchy, and R. Seiler, Physics Today **56**, 38-42 (2003).

[29] F. D. M. Haldane, Physical Review Letters **61**, 2015–2018 (1988).

[30] C.-Z. Chang, C.-X. Liu, and A. H. MacDonald, Review of Modern Physics **95**, 011002 (2023).

[31] C.-X. Liu, S.-C. Zhang, and X.-L. Qi, Annual Review of Condensed Matter Physics **7**, 301-321 (2016).

[32] B. A. Bernevig, T. L. Hughes, and S.-C. Zhang, Science **314**, 1757-1761 (2006).

[33] C. L. Kane and E. J. Mele, Physical Review Letters **95**, 146802 (2005).

[34] M. König, S. Wiedmann, C. Brüne, A. Roth, H. Buhmann, L. W. Molenkamp, X.-L. Qi, and S.-C. Zhang, Science **318**, 766-770 (2007).

[35] Y. Ando, Journal of the Physical Society of Japan **82**, 102001 (2013).

[36] M. Z. Hasan and C. L. Kane, Reviews of Modern Physics **82**, 3045-3067 (2010).

[37] J. E. Moore and L. Balents, Physical Review B **75**, 121306 (2007).

[38] L. M. Schoop, F. Pielnhofer, and B. V. Lotsch, Chemistry of Materials **30**, 3155-3176 (2018).

[39] S.-Y. Xu, C. Liu, S. K. Kushwaha, R. Sankar, J. W. Krizan, I. Belopolski, M. Neupane, G. Bian, N. Alidoust, T.-R. Chang, H.-T. Jeng, C.-Y. Huang, W.-F. Tsai, H. Lin, P. P. Shibayev, F.-C. Chou, R. J. Cava, and M. Z. Hasan, Science **347**, 294-298 (2015).

[40] N. P. Armitage, E. J. Mele, and A. Vishwanath, Reviews of Modern Physics **90**, 015001 (2018).

[41] L. Balents, Physics **4**, 36 (2011).

[42] H. Weng, C. Fang, Z. Fang, B. A. Bernevig, and X. Dai, Physical Review X **5**, 011029 (2015).

[43] S.-M. Huang, S.-Y. Xu, I. Belopolski, C.-C. Lee, G. Chang, B. Wang, N. Alidoust, G. Bian, M. Neupane, C. Zhang, S. Jia, A. Bansil, H. Lin, and M. Z. Hasan, Nature Communications **6**, 7373 (2015).

[44] A. R. Wright and R. H. McKenzie, Physical Review B **87**, 085411 (2013).

[45] H. Yang, Y. Sun, Y. Zhang, W.-J. Shi, S. S. P. Parkin, and B. Yan, New Journal of Physics **19**, 015008 (2017).

[46] C. Li, J. Zhang, Y. Wang, H. Liu, Q. Guo, E. Rienks, W. Chen, F. Bertran, H. Yang, D. Phuyal, H. Fedderwitz, B. Thiagarajan, M. Dendzik, M. H. Berntsen, Y. Shi, T. Xiang, and O. Tjernberg, Nature Communications **14**, 7185 (2023).

[47] L. X. Yang, Z. K. Liu, Y. Sun, H. Peng, H. F. Yang, T. Zhang, B. Zhou, Y. Zhang, Y. F. Guo, M. Rahn, D. Prabhakaran, Z. Hussain, S.-K. Mo, C. Felser, B. Yan, and Y. L. Chen, Nature Physics **11**, 728-732 (2015).

[48] B. Q. Lv, N. Xu, H. M. Weng, J. Z. Ma, P. Richard, X. C. Huang, L. X. Zhao, G. F. Chen, C. E. Matt, F. Bisti, V. N. Strocov, J. Mesot, Z. Fang, X. Dai, T. Qian, M. Shi, and H. Ding, Nature Physics **11**, 724-727 (2015).

[49] S.-Y. Xu, N. Alidoust, I. Belopolski, Z. Yuan, G. Bian, T.-R. Chang, H. Zheng, V. N. Strocov, D. S. Sanchez, G. Chang, C. Zhang, D. Mou, Y. Wu, L. Huang, C.-C. Lee, S.-M. Huang, B. Wang, A. Bansil, H.-T. Jeng, T. Neupert, A. Kaminski, H. Lin, S. Jia, and M. Z. Hasan, Nature Physics **11**, 748-754 (2015).

[50] N. Morali, R. Batabyal, P. K. Nag, E. Liu, Q. Xu, Y. Sun, B. Yan, C. Felser, N. Avraham, and H. Beidenkopf, Science **365**, 1286-1291 (2019).

[51] D. F. Liu, A. J. Liang, E. K. Liu, Q. N. Xu, Y. W. Li, C. Chen, D. Pei, W. J. Shi, S. K. Mo, P. Dudin, T. Kim, C. Cacho, G. Li, Y. Sun, L. X. Yang, Z. K. Liu, S. S. P. Parkin, C. Felser, and Y. L. Chen, Science **365**, 1282-1285 (2019).

[52] S.-Y. Xu, I. Belopolski, D. S. Sanchez, M. Neupane, G. Chang, K. Yaji, Z. Yuan, C. Zhang, K. Kuroda, G. Bian, C. Guo, H. Lu, T.-R. Chang, N. Alidoust, H. Zheng, C.-C. Lee, S.-M. Huang, C.-H. Hsu, H.-T. Jeng, A. Bansil, T. Neupert, F. Komori, T. Kondo, S. Shin, H. Lin, S. Jia, and M. Z. Hasan, Physical Review Letters **116**, 096801 (2016).

[53] I. Belopolski, K. Manna, D. S. Sanchez, G. Chang, B. Ernst, J. Yin, S. S. Zhang, T. Cochran, N. Shumiya, H. Zheng, B. Singh, G. Bian, D. Multer, M. Litskevich, X. Zhou, S. M. Huang, B. Wang, T. R. Chang, S. Y. Xu, A. Bansil, C. Felser, H. Lin, and M. Z. Hasan, Science **365**, 1278-1281 (2019).

[54] W. L. Min-Xue Yang and W. Chen, Advances in Physics: X **7**, 2065216 (2022).

[55] N. Nagaosa, J. Sinova, S. Onoda, A. H. MacDonald, and N. P. Ong, Reviews of Modern Physics **82**, 1539 (2010).

[56] Y. Sun, Y. Zhang, C. Felser, and B. Yan, Physical Review Letters **117**, 146403 (2016).

[57] K. M. Fijalkowski, N. Liu, M. Klement, S. Schreyeck, K. Brunner, C. Gould, and L. W. Molenkamp, Nature Electronics (2024).

[58] G. Scappucci, P. J. Taylor, J. R. Williams, T. Ginley, and S. Law, MRS Bulletin **46**, 596-606 (2021).

[59] M. He, H. Sun, and Q. L. He, Frontiers of Physics **14**, 43401 (2019).

[60] S. Kundu, R. Roy, M. S. Rahman, S. Upadhyay, R. O. Topaloglu, S. E. Mohney, S. Huang, and S. Ghosh, Journal of Low Power Electronics and Applications **13** (2023).

[61] C.-T. Chen, U. Bajpai, N. A. Lanzillo, C.-H. Hsu, H. Lin, and G. Liang, Topological semimetals for scaled back-end-of-line interconnect beyond cu, in *2020 IEEE International Electron Devices Meeting (IEDM)*, 32.4.1–32.4.4, 2020.

[62] R. Xie, T. Zhang, H. Weng, and G.-L. Chai, Small Science **2**, 2100106 (2022).

[63] G. Li and C. Felser, Applied Physics Letters **116**, 070501 (2020).

[64] A. Sekine and K. Nomura, Journal of Applied Physics **129**, 141101 (2021).

[65] Y. Yang, Y. Yamagami, X. Yu, P. Pitchappa, J. Webber, B. Zhang, M. Fujita, T. Nagatsuma, and R. Singh, Nature Photonics **14**, 446-451 (2020).

[66] X. Yao, M. Tokman, and A. Belyanin, Physical Review Letters **112**, 055501 (2014).

[67] X. Zhang, J. Wang, and S.-C. Zhang, Physical Review B **82**, 245107 (2010).

[68] K. A. Kuznetsov, S. A. Tarasenko, P. M. Kovaleva, P. I. Kuznetsov, D. V. Lavrukhin, Y. G. Goncharov, A. A. Ezhov, D. S. Ponomarev, and G. K. Kitaeva, Nanomaterials **12** (2022).

[69] M. J. Gilbert, Communications Physics **4**, 70 (2021).

[70] Y. Zhang, Q. Hao, and G. Xiao, Sensors **19**, 3537 (2019).

[71] E. V. Vidal, G. Stryganyuk, H. Schneider, C. Felser, and G. Jakob, Applied Physics Letters **99**, 132509 (2011).

[72] A. Gerber, Journal of Magnetism and Magnetic Materials **310**, 2749-2751 (2007), Proceedings of the 17th International Conference on Magnetism.

[73] S. Iihama, T. Taniguchi, K. Yakushiji, A. Fukushima, Y. Shiota, S. Tsunegi, R. Hiramatsu, S. Yuasa, Y. Suzuku, and H. Kubota, Nature Electronics **1**, 120-123 (2018).

[74] T. Y. Ma, C. H. Wan, X. Wang, W. L. Yang, C. Y. Guo, C. Fang, M. K. Zhao, J. Dong, Y. Zhang, and X. F. Han, Physical Review B **101**, 134417 (2020).

[75] M. Mizuguchi and S. Nakatsuji, Science and Technology of Advanced Materials **20**, 262–275 (2019).

[76] Y. Sakuraba, K. Hasegawa, M. Mizuguchi, T. Kubota, S. Mizukami, T. Miyazaki, and K. Takanashi, Applied Physics Express **6**, 033003 (2013).

[77] J. C. R. Sánchez, L. Vila, G. Desfonds, S. Gambarelli, J. P. Attané, J. M. D. Teresa, C. Magén, and A. Fert, Nature Communications **4**, 2944 (2013).

[78] J.-C. Rojas-Sánchez, S. Oyarzún, Y. Fu, A. Marty, C. Vergnaud, S. Gambarelli, L. Vila, M. Jamet, Y. Ohtsubo, A. Taleb-Ibrahimi, P. Le Fèvre, F. Bertran, N. Reyren, J.-M. George, and A. Fert, Physical Review Letters **116**, 096602 (2016).

[79] M. Nomura, S. Souma, A. Takayama, T. Sato, T. Takahashi, K. Eto, K. Segawa, and Y. Ando, Physical Review B **89**, 045134 (2014).

[80] C. Felser, L. Wollmann, S. Chadov, G. H. Fecher, and S. S. Parkin, APL Materials **3**, 041518 (2015).

[81] T. Graf, C. Felser, and S. S. Parkin, Progress in Solid State Chemistry **39**, 1-50 (2011).

[82] C. J. Palmstrøm, Progress in Crystal Growth and Characterization of Materials **62**, 371-397 (2016).

[83] K. Manna, L. Muechler, T. H. Kao, R. Stinshoff, Y. Zhang, J. Gooth, N. Kumar, G. Kreiner, K. Koepernik, R. Car, J. Kübler, G. H. Fecher, C. Shekhar, Y. Sun, and C. Felser, Physical Review X **8**, 041045 (2018).

[84] G. Chang, S. Y. Xu, H. Zheng, B. Singh, C. H. Hsu, G. Bian, N. Alidoust, I. Belopolski, D. S. Sanchez, S. Zhang, H. Lin, and M. Z. Hasan, Scientific Reports **6**, 1-9 (2016).

[85] J. Noky, Q. Xu, C. Felser, and Y. Sun, Physical Review B **99**, 1-5 (2019).

[86] J. Noky, Y. Zhang, J. Gooth, C. Felser, and Y. Sun, npj Computational Materials **6**, 1-8 (2020).

[87] B. Cornelius, S. Treivish, Y. Rosenthal, and M. Pecht, Microelectronics Reliability **79**, 175-192 (2017).

[88] S. Groves and W. Paul, Physical Review Letters **11**, 194-196 (1963).

[89] A. W. Ewald, Journal of Applied Physics **25**, 1436-1437 (1954).

[90] A. W. Ewald, Helvetica Physica Acta **41**, 795-813 (1968).

[91] B. J. Roman and A. W. Ewald, Physical Review B **5**, 3914 (1972).

[92] B. L. Booth and A. W. Ewald, Physical Review **168**, 805 (1968).

[93] R. J. Wagner and A. W. Ewald, Journal of Physics and Chemistry of Solids **32**, 697-707 (1971).

[94] F. H. Pollak, M. Cardona, C. W. Higginbotham, F. Herman, and J. P. V. Dyke, Physical Review B **2**, 352 (1970).

[95] R. E. Lindquist and A. W. Ewald, Physical Review **135**, A191–A194 (1964).

[96] E. D. Hinkley and A. W. Ewald, Physical Review **134**, A1261–A1267 (1964).

[97] C. F. Lavine and A. Ewald, Journal of Physics and Chemistry of Solids **32**, 1121-1140 (1971).

[98] G. Busch and R. Kern, Solid State Physics **11**, 1-40 (1960).

[99] D. Sherrington and W. Kohn, Review of Modern Physics **40**, 767–769 (1968).

[100] B. Bucher, P. Steiner, and P. Wachter, Physical Review Letters **67**, 2717–2720 (1991).

[101] R. F. C. Farrow, D. S. Robertson, G. M. Williams, A. G. Cullis, G. R. Jones, L. M. Young, and P. N. J. Dennis, Journal of Crystal Growth **54**, 507-518 (1981).

[102] W. Paul, Semiconductor Science and Technology **5**, S1 (1990).

[103] J. Ding, C. Liu, V. Kalappattil, Y. Zhang, O. Mosendz, U. Erugu, R. Yu, J. Tian, A. DeMann, S. B. Field, X. Yang, H. Ding, J. Tang, B. Terris, A. Fert, H. Chen, and M. Wu, Advanced Materials **33**, 2005909 (2021).

[104] L. Fu and C. L. Kane, Physical Review B **76**, 045302 (2007).

[105] Y. Xu, B. Yan, H.-J. Zhang, J. Wang, G. Xu, P. Tang, W. Duan, and S.-C. Zhang, Physical Review Letters **111**, 136804 (2013).

[106] S. Küfner, M. Fitzner, and F. Bechstedt, Physical Review B **90**, 125312 (2014).

[107] A. Barfuss, L. Dudy, M. R. Scholz, H. Roth, P. Höpfner, C. Blumenstein, G. Landolt, J. H. Dil, N. C. Plumb, M. Radovic, A. Bostwick, E. Rotenberg, A. Fleszar, G. Bihlmayer, D. Wortmann, G. Li, W. Hanke, R. Claessen, and J. Schäfer, Physical Review Letters **111**, 157205 (2013).

[108] Y. Ohtsubo, P. LeFèvre, F. Bertran, and A. Taleb-Ibrahimi, Physical Review Letters **111**, 216401 (2013).

[109] D. Zhang, H. Wang, J. Ruan, G. Yao, and H. Zhang, Physical Review B **97**, 195139 (2018).

[110] A. Bansil, H. Lin, and T. Das, Review of Modern Physics **88**, 021004 (2016).

[111] Y. Zhang, V. Kalappattil, C. Liu, M. Mehraeen, S. S. Zhang, J. Ding, U. Erugu, Z. Chen, J. Tian, K. Liu, J. Tang, and M. Wu, Science Advances **8**, 52 (2022).

[112] J. Ding, C. Liu, Y. Zhang, V. Kalappattil, R. Yu, U. Erugu, J. Tang, H. Ding, H. Chen, and M. Wu, Advanced Functional Materials **31**, 2008411 (2021).

[113] L. Gladczuk, L. Gladczuk, P. Dluzewski, G. van der Laan, and T. Hesjedal, physica status solidi (RRL) – Rapid Research Letters **15**, 2100137 (2021).

[114] K. Ishihara, L. D. Anh, T. Hotta, K. Inagaki, M. Kobayashi, and M. Tanaka, arXiv **cond-mat.supr-con**, 2308.00893 (2023).

[115] L. S. Cardman and the PEPPo Collaboration, AIP Conference Proceedings **1970**, 050001 (2018).

[116] R. Abdul Khalek and others, Nuclear Physics A **1026**, 122447 (2022).

[117] M. Kuwahara, Y. Takeda, K. Saitoh, T. Ujihara, H. Asano, T. Nakanishi, and N. Tanaka, Journal of Physics: Conference Series **298**, 21–24 (2011).

[118] A. T. N'Diaye and A. Quesada, *Spin-Polarized Low-Energy Electron Microscopy (SPLEEM)*, 1–14, John Wiley & Sons, Ltd, 2012.

[119] U. Kolac, M. Donath, K. Ertl, H. Liebl, and V. Dose, Review of Scientific Instruments **59**, 1933-1940 (1988).

[120] W. E. Spicer, Phyiscal Review **112**, 1 (1958).

[121] C. N. Berglund and W. E. Spicer, Physical Review **136**, 4A (1964).

[122] R. U. Martinelli and D. G. Fisher, Proceedings of the IEEE **62**, 1339 (1974).

[123] K. A. Elamrawi, *Preparation and Surface Studies of Negative Electron Affinity Preparation and Surface Studies of Negative Electron Affinity Semiconductors Photocathodes*, PhD thesis, Old Dominion University, 1999.

[124] M. Niigaki, T. Hirohata, T. Suzuki, H. Kan, and T. Hiruma, Applied Physics Letters **71**, 2493-2495 (1997).

[125] A. T. Priyoti, R. Ahsan, H. U. Chae, S. Das, J. S. Vazquez, Z. Wu, H. G. Kim, Y. Yu, and R. Kapadia, ACS Photonics **10**, 4501-4508 (2023).

[126] W. Liu, M. Poelker, X. Peng, S. Zhang, and M. Stutzman, Journal of Applied Physics **122**, 035703 (2017).

[127] I. Vurgaftman, M. Lumb, and J. Meyer, *Bands and photons in III-V semiconductor quantum structures*, Oxford University Press, 2021.

[128] L. Cultrera, arXiv **physics.acc-ph**, 2206.15345 (2022).

[129] A. Herrera-Gómez, G. Vergara, and W. E. Spicer, Journal of Applied Physics **79**, 7318-7323 (1996).

[130] K. Togawa, T. Nakanishi, T. Baba, F. Furuta, H. Horinaka, T. Ida, Y. Kurihara, H. Matsumoto, T. Matsuyama, M. Mizuta, S. Okumi, T. Omori, C. Suzuki, Y. Takeuchi, K. Wada, and M. Yoshioka, Nuclear Instruments and Methods in Physics Research A: Accelerators, Spectrometers, Detectors and Associated Equipment **414**, 431-445 (1998).

[131] T. Maruyama, AIP Conference Proceedings **675**, 1083-1087 (2003).

[132] R. Alley, H. Aoyagi, J. Clendenin, J. Frisch, C. Garden, E. Hoyt, R. Kirby, L. Klaisner, A. Kulikov, R. Miller, G. Mulhollan, C. Prescott, P. Sáez, D. Schultz, H. Tang, J. Turner, K. Witte, M. Woods, A. Yeremian, and M. Zolotorev, Nuclear Instruments and Methods in Physics Research A: Accelerators, Spectrometers, Detectors and Associated Equipment **365**, 1-27 (1995).

[133] W. Liu, Y. Chen, W. Lu, A. Moy, M. Poelker, M. Stutzman, and S. Zhang, Applied Physics Letters **109**, 252104 (2016).

[134] A. Khan, *Vertical cavity surface emitting lasers: design, characterisation and integration*, PhD thesis, University College London, 1995.

[135] https://www.thorlabs.com/newgrouppage9.cfm?objectgroup_id=13322#ad-image-0.

[136] M. A. Herman, W. Richter, and H. Sitter, *Molecular Beam Epitaxy in Epitaxy: Physical Principles and Technical Implementation*, 131–170, Springer, 2004.

[137] M. Miller and K. Armatys, The Open Thermodynamics Journal **7**, 2–9 (2013).

[138] R. Fernandez, MRS Proceedings **263**, 71 (1992).

[139] J. C. Garcia, A. Barski, J. P. Contour, and J. Massies, Applied Physics Letters **51**, 593-595 (1987).

[140] Y.-C. Pao and J. Harris, Journal of Crystal Growth **111**, 489-494 (1991).

[141] Q. Xie, J. Van Nostrand, R. Jones, J. Sizelove, and D. Look, Journal of Crystal Growth **207**, 255-265 (1999).

[142] J. A. Fedchak, P. J. Abbott, J. H. Hendricks, P. C. Arnold, and N. T. Peacock, Journal of Vacuum Science & Technology A **36**, 030802 (2018).

[143] M. P. Seah and W. A. Dench, Surface and Interface Analysis **1**, 2-11 (1979).

[144] B. Lv, T. Qian, and H. Ding, Nature Reviews Physics **1**, 609-626 (2019).

[145] A. Damascelli, Physica Scripta **T109**, 61-74 (2004).

[146] J. A. Sobota, Y. He, and Z. X. Shen, Reviews of Modern Physics **93**, 025006 (2021).

[147] S. Hüfner, *Photoelectron Spectroscopy*, Springer-Berlin, 3rd edition, 2003.

[148] V. Strocov, Journal of Electron Spectroscopy and Related Phenomena **229**, 100-107 (2018).

[149] V. N. Strocov, Journal of Electron Spectroscopy and Related Phenomena **130**, 65-78 (2003).

[150] http://www.spring8.or.jp/en/about_us/whats_sp8/facilities/bl/light_source_optics/sources/insertion_device/intro_insertion_devices, Spring-8.

[151] J. Osterwalder, Lecture Notes in Physics **697**, 95-120 (2006).

[152] U. Heinzmann and J. H. Dil, Journal of Physics Condensed Matter **24**, 173001 (2012).

[153] M. Escher, N. B. Weber, M. Merkel, L. Plucinski, and C. M. Schneider, e-Journal of Surface Science and Nanotechnology **9**, 340-343 (2011).

[154] I. Hernández-Calderón and H. Höchst, Physical Review B **27**, 4961–4965 (1983).

[155] S. Hasegawa, Reflection High-Energy Electron Diffraction, in *Characterization of Materials*, 1–14, John Wiley & Sons, Ltd, 2012.

[156] J. H. Neave, B. A. Joyce, P. J. Dobson, and N. Norton, Applied Physics A **31**, 1-8 (1983).

[157] Z. Mitura, S. Dudarev, and M. Whelan, Journal of Crystal Growth **198-199**, 905-910 (1999).

[158] C. L. Berrie and S. R. Leone, Journal of Crystal Growth **216**, 159-170 (2000).

[159] G. F. Harrington and J. Santiso, Journal of Electroceramics **47**, 141-163 (2021).

[160] M. Birkholz, *Thin Film Analysis by X-Ray Scattering*, John Wiley & Sons, Ltd, 2005.

[161] P. F. Fewster, Reports on Progress in Physics **59**, 1339 (1996).

[162] M. Quillec, L. Goldstein, G. Le Roux, J. Burgeat, and J. Primot, Journal of Applied Physics **55**, 2904-2909 (1984).

[163] W.-K. Chu, Rutherford Backscattering Spectrometry, in *Materials Characterization*, ASM International, 1986.

[164] T. Brown-Heft, *Engineering Magnetic and Topological Properties in Epitaxial Heusler Compounds*, PhD thesis, University of California, Santa Barbara, 2018.

[165] P. Vogl, H. P. Hjalmarson, and J. D. Dow, Journal of Physics and Chemistry of Solids **44**, 365-378 (1983).

[166] D. W. Jenkins and J. D. Dow, Physical Review B **36**, 7994 (1987).

[167] R. P. Day, B. Zwartsenberg, I. S. Elfimov, and A. Damascelli, npj Quantum Materials **4**, 54 (2019).

[168] J. C. Slater and G. F. Koster, Physical Review **94**, 1498–1524 (1954).

[169] G. Grosso and C. Piermarocchi, Physical Review B **51**, 16772–16777 (1995).

[170] V. A. Rogalev, T. Rauch, M. R. Scholz, F. Reis, L. Dudy, A. Fleszar, M.-A. Husanu, V. N. Strocov, J. Henk, I. Mertig, J. Schäfer, and R. Claessen, Physical Review B **95**, 161117(R) (2017).

[171] G. H. Park, H. Reichlova, R. Schlitz, M. Lammel, A. Markou, P. Swekis, P. Ritzinger, D. Kriegner, J. Noky, J. Gayles, Y. Sun, C. Felser, K. Nielsch, S. T. Goennenwein, and A. Thomas, Physical Review B **101**, 060406 (2020).

[172] Y. Pu, D. Chiba, F. Matsukura, H. Ohno, and J. Shi, Physical Review Letters **101**, 117208 (2008).

[173] J. D. Gibbons, D. Macneill, R. A. Buhrman, and D. C. Ralph, Physical Review Applied **9**, 064033 (2018).

[174] K. Uchida, Proceedings of the Japan Academy, Series B **97**, 69-88 (2021).

[175] Y. Sakuraba, K. Hasegawa, M. Mizuguchi, T. Kubota, S. Mizukami, T. Miyazaki, and K. Takanashi, Applied Physics Express **6**, 033003 (2013).

[176] M. Mizuguchi and S. Nakatsuji, Science and Technology of Advanced Materials **20**, 262-275 (2019).

[177] K. Manna, Y. Sun, L. Muechler, J. Kübler, and C. Felser, Nature Reviews Materials **3**, 244-256 (2018).

[178] L. Wollmann, A. K. Nayak, S. S. Parkin, and C. Felser, Annual Review of Materials Research **47**, 247-270 (2017).

[179] P. Li, J. Koo, W. Ning, J. Li, L. Miao, L. Min, Y. Zhu, Y. Wang, N. Alem, C. X. Liu, Z. Mao, and B. Yan, Nature Communications **11**, 3476 (2020).

[180] S. Mitra, A. Ahmad, S. Chakrabarti, S. Biswas, and A. K. Das, Journal of Magnetism and Magnetic Materials **552**, 169148 (2022).

[181] S. Wurmehl, G. H. Fecher, H. C. Kandpal, V. Ksenofontov, C. Felser, and H. J. Lin, Applied Physics Letters **88**, 032503 (2006).

[182] M. A. Tanaka, Y. Ishikawa, Y. Wada, S. Hori, A. Murata, S. Horii, Y. Yamanishi, K. Mibu, K. Kondou, T. Ono, and S. Kasai, Journal of Applied Physics **111**, 053902 (2012).

[183] W. Zhang, N. Jiko, K. Mibu, and K. Yoshimura, Journal of Physics: Condensed Matter **17**, 6653-6662 (2005).

[184] C. Guillemard, S. Petit-Watelot, T. Devolder, L. Pasquier, P. Boulet, S. Migot, J. Ghanbaja, F. Bertran, and S. Andrieu, Journal of Applied Physics **128**, 241102 (2020).

[185] E. Ventura-Macias, J. Guerrero-Sánchez, J. Corbett, A. Smith, and N. Takeuchi, Applied Surface Science **484**, 578-586 (2019).

[186] J. A. Logan, T. L. Brown-Heft, S. D. Harrington, N. S. Wilson, A. P. McFadden, A. D. Rice, M. Pendharkar, and C. J. Palmstrøm, Journal of Applied Physics **121**, 213903 (2017).

[187] M. A. Garcia, E. F. Pinel, J. D. L. Venta, A. Quesada, V. Bouzas, J. F. Fernández, J. J. Romero, M. S. M. González, and J. L. Costa-Krämer, Journal of Applied Physics **105**, 013925 (2009).

[188] M. Buchner, K. Höfler, B. Henne, V. Ney, and A. Ney, Journal of Applied Physics **124**, 161101 (2018).

[189] A. T. Breidenbach, H. Yu, T. A. Peterson, A. P. Mcfadden, W. K. Peria, C. J. Palmstrøm, and P. A. Crowell, Physical Review B **105**, 144405 (2022).

[190] B. A. Collins, Y. Zhong, Y. S. Chu, L. He, and F. Tsui, Journal of Vacuum Science & Technology B **25**, 999-1003 (2007).

[191] C. van der Rest, A. Schmitz, and P. J. Jacques, Acta Materialia **142**, 193-200 (2018).

[192] B. Lv, P. Liu, Y. Miao, Z. Lian, M. Si, and C. Gao, Applied Physics Letters **118**, 132408 (2021).

[193] E. Vilanova-Vidal, H. Schneider, and G. Jakob, Physical Review B **83**, 174410 (2011).

[194] P. J. Webster and K. R. Ziebeck, Journal of Physics and Chemistry of Solids **34**, 1647-1654 (1973).

[195] Y. Takamura, R. Nakane, and S. Sugahara, Journal of Applied Physics **105**, 07B109 (2009).

[196] S. Kurdi, Y. Sakuraba, K. Masuda, H. Tajiri, B. Nair, G. F. Nataf, M. E. Vickers, G. Reiss, M. Meinert, S. S. Dhesi, M. Ghidini, and Z. H. Barber, Journal of Physics D: Applied Physics **55**, 185305 (2022).

[197] H. Lipson, J. Langford, and H.-C. Hu, Trigonometric intensity factors, in *International Tables for Crystallography*, volume C, Ch. 6.2, 596–598, International Union of Crystallography, 2006.

[198] J. M. Loureiro, B. F. O. Costa, B. Malaman, G. L. Caër, S. Das, and V. S. Amaral, Journal of Alloys and Compounds **615**, S559-S563 (2014).

[199] K. Fujiwara, K. Shibata, S. Nishimura, J. Shiogai, and A. Tsukazaki, AIP Advances **12**, 065030 (2022).

[200] L. C. Chen, J. W. Dong, B. D. Schultz, C. J. Palmstrøm, J. Berezovsky, A. Isakovic, P. A. Crowell, and N. Tabat, Journal of Vacuum Science & Technology B **18**, 2057-2062 (2000).

[201] I. Galanakis, P. H. Dederichs, and N. Papanikolaou, Physical Review B **66**, 174429 (2002).

[202] Y. Sakuraba, K. Hyodo, A. Sakuma, and S. Mitani, Physical Review B **101**, 134407 (2020).

[203] K. Sumida, Y. Sakuraba, K. Masuda, T. Kono, M. Kakoki, K. Goto, W. Zhou, K. Miyamoto, Y. Miura, T. Okuda, and A. Kimura, Communications Materials **1**, 89 (2020).

[204] G. K. Shukla, A. K. Jena, N. Shahi, K. K. Dubey, I. Rajput, S. Baral, K. Yadav, K. Mukherjee, A. Lakhani, K. Carva, S.-C. Lee, S. Bhattacharjee, and S. Singh, Physical Review B **105**, 035124 (2022).

[205] C. D. W. Cox, A. J. Caruana, M. D. Cropper, and K. Morrison, Journal of Physics D: Applied Physics **53**, 035005 (2019).

[206] A. N. Engel, C. P. Dempsey, H. S. Inbar, J. T. Dong, S. Nishihaya, Y. Chang, A. V. Fedorov, M. Hashimoto, D. Lu, and C. J. Palmstrøm, Physical Review Materials **8**, 044202 (2024).

[207] L. D. Anh, K. Takase, T. Chiba, Y. Kota, K. Takiguchi, and M. Tanaka, Advanced Materials **33**, 2104645 (2021).

[208] Q. Barbedienne, J. Varignon, N. Reyren, A. Marty, C. Vergnaud, M. Jamet, C. Gomez-Carbonell, A. Lemaître, P. L. Fèvre, F. Bertran, A. Taleb-Ibrahimi, H. Jaffrès, J.-M. George, and A. Fert, Physical Review B **98**, 195445 (2018).

[209] K. H. Chen, K. Y. Lin, S. W. Lien, S. W. Huang, C. K. Cheng, H. Y. Lin, C. H. Hsu, T. R. Chang, C. M. Cheng, M. Hong, and J. Kwo, Physical Review B **105**, 075109 (2022).

[210] G. J. de Coster, P. A. Folkes, P. J. Taylor, and O. A. Vail, Physical Review B **98**, 115153 (2018).

[211] V. A. Rogalev, F. Reis, F. Adler, M. Bauernfeind, J. Erhardt, A. Kowalewski, M. R. Scholz, L. Dudy, L. B. Duffy, T. Hesjedal, M. Hoesch, G. Bihlmayer, J. Schäfer, and R. Claessen, Physical Review B **100**, 245144 (2019).

[212] M. R. Scholz, V. A. Rogalev, L. Dudy, F. Reis, F. Adler, J. Aulbach, L. J. Collins-Mcintyre, L. B. Duffy, H. F. Yang, Y. L. Chen, T. Hesjedal, Z. K. Liu, M. Hoesch, S. Muff, J. H. Dil, J. Schäfer, and R. Claessen, Physical Review B **97**, 075101 (2018).

[213] C. Z. Xu, Y. H. Chan, Y. Chen, P. Chen, X. Wang, C. Dejoie, M. H. Wong, J. A. Hlevyack, H. Ryu, H. Y. Kee, N. Tamura, M. Y. Chou, Z. Hussain, S. K. Mo, and T. C. Chiang, Physical Review Letters **118**, 146402 (2017).

[214] I. Madarevic, U. Thupakula, G. Lippertz, N. Claessens, P. C. Lin, H. Bana, S. Gonzalez, G. D. Santo, L. Petaccia, M. N. Nair, L. M. Pereira, C. V. Haesendonck, and M. J. V. Bael, APL Materials **8**, 031114 (2020).

[215] E. Magnano, C. Cepek, S. Gardonio, B. Allieri, I. Baek, E. Vescovo, L. Roca, J. Avila, M. G. Betti, C. Mariani, and M. Sancrotti, Journal of Electron Spectroscopy and Related Phenomena **127**, 29-35 (2002).

[216] P. Hofmann, *Solid state physics: an introduction*, Wiley, 2015.

[217] D. Shoenberg, *Magnetic Oscillations in Metals*, Cambridge University Press, 1984.

[218] I. Madarevic, N. Claessens, A. Seliverstov, C. V. Haesendonck, and M. J. V. Bael, physica status solidi (RRL) – Rapid Research Letters **16**, 2200161 (2022).

[219] A. Giunto, L. E. Webb, T. Hagger, and A. Fontcuberta i Morral, Physical Review Materials **7**, 074605 (2023).

[220] M. G. Betti, E. Magnano, M. Sancrotti, F. Borgatti, R. Felici, and C. Mariani, Surface Science **507-510**, 335 (2002).

[221] A. A. Davis, R. G. Jones, G. Falkenberg, L. Seehofer, R. L. Johnson, and C. F. McConville, Applied Physics Letters **75**, 1938 (1999).

[222] N. Jones, *The atomic structure of the indium antimonide (001) surface*, PhD., University of Leicester, 1998.

[223] J. T. Dong, H. S. Inbar, M. Pendharkar, T. A. J. van Schijndel, E. C. Young, C. P. Dempsey, and C. J. Palmstrøm, Journal of Vacuum Science & Technology B **41**, 032808 (2023).

[224] W. K. Liu and M. B. Santos, Surface Science **319**, 172-183 (1994).

[225] O. Vail, P. Taylor, P. Folkes, B. Nichols, B. Haidet, K. Mukherjee, and G. de Coster, physica status solidi (b) **257**, 1800513 (2020).

[226] S. Kaku, K. L. Hiwatari, and J. Yoshino, Applied Surface Science **571**, 151347 (2022).

[227] C. A. Hoffman, J. R. Meyer, R. J. Wagner, F. J. Bartoli, M. A. Engelhardt, and H. Höchst, Physical Review B **40**, 11693 (1989).

[228] R. M. Feenstra, Physical Review B **50**, 4561 (1994).

[229] Y. Zang, T. Jiang, Y. Gong, Z. Guan, C. Liu, M. Liao, K. Zhu, Z. Li, L. Wang, W. Li, C. Song, D. Zhang, Y. Xu, K. He, X. Ma, S.-C. Zhang, and Q.-K. Xue, Advanced Functional Materials **28**, 1802723 (2018).

[230] C. Zhao, L. Li, L. Zhang, J. Qin, H. Chen, B. Xia, B. Yang, H. Zheng, S. Wang, C. Liu, Y. Li, D. Guan, P. Cui, Z. Zhang, and J. Jia, Physical Review Letters **128**, 206802 (2022).

[231] W. Smekal, W. S. M. Werner, and C. J. Powell, Surface and Interface Analysis **37**, 1059-1067 (2005).

[232] H. Huang and F. Liu, Physical Review B **95**, 201101(R) (2017).

[233] M. Brahlek, N. Koirala, N. Bansal, and S. Oh, Solid State Communications **215-216**, 54-62 (2015).

[234] S. Ishida, Physica E: Low-dimensional Systems and Nanostructures **18**, 294-295 (2003).

[235] M. von Ortenberg and G. Landwehr, Solid State Communications **8**, 1955-1958 (1970).

[236] S. Küfner and F. Bechstedt, Physical Review B **91**, 035311 (2015).

[237] H. Song, J. Yao, Y. Ding, Y. Gu, Y. Deng, M.-H. Lu, H. Lu, and Y.-F. Chen, Advanced Engineering Materials **21**, 1900410 (2019).

[238] E. A. Fitzgerald, P. E. Freeland, M. T. Asom, W. P. Lowe, R. A. Macharrie, B. E. Weir, A. R. Kortan, F. A. Thiel, Y.-H. Xie, A. M. Sergent, S. L. Cooper, G. A. Thomas, and L. C. Kimerling, Journal of Electronic Materials **20** (1991).

[239] J. L. Reno and L. L. Stephenson, Applied Physics Letters **54**, 2207-2209 (1989).

[240] R. A. Carrasco, C. M. Zamarripa, S. Zollner, J. Menéndez, S. A. Chastang, J. Duan, G. J. Grzybowski, B. B. Claflin, and A. M. Kiefer, Applied Physics Letters **113**, 232104 (2018).

[241] J. Polaczyński, G. Krizman, A. Kazakov, B. Turowski, J. B. Ortiz, R. Rudniewski, T. Wojciechowski, P. Dłużewski, M. Aleszkiewicz, W. Zaleszczyk, B. Kurowska, Z. Muhammad, M. Rosmus, N. Olszowska, L.-A. D. Vaulchier, Y. Guldner, T. Wojtowicz, and V. V. Volobuev, arXiv **cond-mat.mtrl-sci**, 2309.03951 (2023).

[242] C.-Z. Xu, Y.-H. Chan, P. Chen, X. Wang, D. Flötotto, J. A. Hlevyack, G. Bian, S.-K. Mo, M.-Y. Chou, and T.-C. Chiang, Physical Review B **97**, 035122 (2018).

[243] J. Falson, Y. Xu, M. Liao, Y. Zang, K. Zhu, C. Wang, Z. Zhang, H. Liu, W. Duan, K. He, H. Liu, J. H. Smet, D. Zhang, and Q.-K. Xue, Science **367**, 1454-1457 (2020).

[244] D. M. Mahler, V. L. Müller, C. Thienel, J. Wiedenmann, W. Beugeling, H. Buhmann, and L. W. Molenkamp, Nano Letters **21**, 9869-9874 (2021).

[245] D. M. Mahler, J.-B. Mayer, P. Leubner, L. Lunczer, D. Di Sante, G. Sangiovanni, R. Thomale, E. M. Hankiewicz, H. Buhmann, C. Gould, and L. W. Molenkamp, Physical Review X **9**, 031034 (2019).

[246] P. Leubner, L. Lunczer, C. Brüne, H. Buhmann, and L. W. Molenkamp, Physical Review Letters **117**, 086403 (2016).

[247] B. Büttner, C. X. Liu, G. Tkachov, E. G. Novik, C. Brüne, H. Buhmann, E. M. Hankiewicz, P. Recher, B. Trauzettel, S. C. Zhang, and L. W. Molenkamp, Nature Physics **7**, 418-422 (2011).

[248] C. Liu, G. Bian, T.-R. Chang, K. Wang, S.-Y. Xu, I. Belopolski, I. Miotkowski, H. Cao, K. Miyamoto, C. Xu, C. E. Matt, T. Schmitt, N. Alidoust, M. Neupane, H.-T. Jeng, H. Lin, A. Bansil, V. N. Strocov, M. Bissen, A. V. Fedorov, X. Xiao, T. Okuda, Y. P. Chen, and M. Z. Hasan, Physical Review B **92**, 115436 (2015).

[249] R. C. Vidal, G. Marini, L. Lunczer, S. Moser, L. Fürst, J. Issing, C. Jozwiak, A. Bostwick, E. Rotenberg, C. Gould, H. Buhmann, W. Beugeling, G. Sangiovanni, D. D. Sante, G. Profeta, L. W. Molenkamp, H. Bentmann, and F. Reinert, Physical Review B **107**, L121102 (2023).

[250] A. C. Lygo, B. Guo, A. Rashidi, V. Huang, P. Cuadros-Romero, and S. Stemmer, Physical Review Letters **130**, 046201 (2023).

[251] G. Krizman, J. Bermejo-Ortiz, M. Goyal, A. C. Lygo, J. Wang, Z. Zhang, B. A. Assaf, S. Stemmer, L. A. D. Vaulchier, and Y. Guldner, Physical Review B **106**, 165202 (2022).

[252] I. D. Bernardo, J. Hellerstedt, C. Liu, G. Akhgar, W. Wu, S. A. Yang, D. Culcer, S. K. Mo, S. Adam, M. T. Edmonds, and M. S. Fuhrer, Advanced Materials **33**, 2005897 (2021).

[253] Y. Liu, Y. Y. Li, S. Rajput, D. Gilks, L. Lari, P. L. Galindo, M. Weinert, V. K. Lazarov, and L. Li, Nature Physics **10**, 294-299 (2014).

[254] Y. Zhang, K. He, C. Z. Chang, C. L. Song, L. L. Wang, X. Chen, J. F. Jia, Z. Fang, X. Dai, W. Y. Shan, S. Q. Shen, Q. Niu, X. L. Qi, S. C. Zhang, X. C. Ma, and Q. K. Xue, Nature Physics **6**, 584-588 (2010).

[255] D. Flötotto, Y. Bai, Y. H. Chan, P. Chen, X. Wang, P. Rossi, C. Z. Xu, C. Zhang, J. A. Hlevyack, J. D. Denlinger, H. Hong, M. Y. Chou, E. J. Mittemeijer, J. N. Eckstein, and T. C. Chiang, Nano Letters **18**, 5628-5632 (2018).

[256] H. Höchst and I. Hernández-Calderón, Surface Science **126**, 25-31 (1983).

[257] I. Hernández-Calderón and H. Höchst, Surface Science **152-153**, 1035-1041 (1985).

[258] H. U. Middelmann, L. Sorba, V. Hinkel, and K. Horn, Physical Review B **35**, 718 (1987).

[259] M. Tang, D. W. Niles, I. I. Hernández-Calderón, and H. Höchst, Physical Review B **36**, 3336 (1987).

[260] M. J. Jardine, D. Dardzinski, M. Yu, A. Purkayastha, A. H. Chen, Y. H. Chang, A. Engel, V. N. Strocov, M. Hocevar, C. Palmstrøm, S. M. Frolov, and N. Marom, ACS Applied Materials and Interfaces **15**, 16288-16298 (2023).

[261] S. Küfner, J. Furthmüller, L. Matthes, M. Fitzner, and F. Bechstedt, Physical Review B **87**, 235307 (2013).

[262] M. Rohlfing, P. Krüger, and J. Pollmann, Physical Review B **57**, 6485–6492 (1998).

[263] C. Jozwiak, Y. L. Chen, A. V. Fedorov, J. G. Analytis, C. R. Rotundu, A. K. Schmid, J. D. Denlinger, Y. D. Chuang, D. H. Lee, I. R. Fisher, R. J. Birgeneau, Z. X. Shen, Z. Hussain, and A. Lanzara, Physical Review B **84**, 165113 (2011).

[264] C. Jozwiak, C. H. Park, K. Gotlieb, C. Hwang, D. H. Lee, S. G. Louie, J. D. Denlinger, C. R. Rotundu, R. J. Birgeneau, Z. Hussain, and A. Lanzara, Nature Physics **9**, 293-298 (2013).

[265] K. Kuroda, K. Yaji, R. Noguchi, A. Harasawa, S. Shin, T. Kondo, and F. Komori, Physical Review B **105**, L121106 (2022).

[266] Z.-H. Zhu, C. N. Veenstra, S. Zhdanovich, M. P. Schneider, T. Okuda, K. Miyamoto, S.-Y. Zhu, H. Namatame, M. Taniguchi, M. W. Haverkort, I. S. Elfimov, and A. Damascelli, Physical Review Letters **112**, 076802 (2014).

[267] F. Meier, V. Petrov, H. Mirhosseini, L. Patthey, J. Henk, J. Osterwalder, and J. H. Dil, Journal of Physics: Condensed Matter **23**, 072207 (2011).

[268] T. Hakioglu, W.-C. Chiu, R. S. Markiewicz, B. Singh, and A. Bansil, Physical Review B **108**, 155103 (2023).

[269] A. Iwamae, T. Sato, Y. Horimoto, K. Inoue, T. Fujimoto, M. Uchida, and T. Maekawa, Plasma Physics and Controlled Fusion **47**, L41 (2005).

[270] N. A. Cherepkov, Journal of Physics B: Atomic and Molecular Physics **12**, 1279 (1979).

[271] F. Baumberger, T. Greber, and J. Osterwalder, Physical Review B **64**, 195411 (2001).

[272] H. Park, J. Qi, Y. Xu, K. Varga, S. M. Weiss, B. R. Rogers, G. Lüpke, and N. Tolk, physica status solidi (b) **247**, 1997-2001 (2010).

[273] N. J. Ingle, K. M. Shen, F. Baumberger, W. Meevasana, D. H. Lu, Z. X. Shen, A. Damascelli, S. Nakatsuji, Z. Q. Mao, Y. Maeno, T. Kimura, and Y. Tokura, Physical Review B **72**, 205114 (2005).

[274] S. Tchoumakov, V. Jouffrey, A. Inhofer, E. Bocquillon, B. Plaçais, D. Carpentier, and M. O. Goerbig, Physical Review B **96**, 201302(R) (2017).

[275] R. C. Leckey and J. D. Riley, Critical Reviews in Solid State and Materials Sciences **17**, 307-352 (1992).

[276] H. Zhang, T. Pincelli, C. Jozwiak, T. Kondo, R. Ernstorfer, T. Sato, and S. Zhou, Nature Reviews Methods Primers **2**, 54 (2022).

[277] T.-C. Chiang and F. Seitz, Annalen der Physik (Leipzig) **10**, 61-74 (2001).

[278] J. Ren, L. Fu, G. Bian, M. Wong, T. Wang, G. Zha, W. Jie, T. Miller, M. Z. Hasan, and T. C. Chiang, Physical Review B **91**, 235303 (2015).

[279] M. I. Dyakonov and A. V. Khaetskii, JETP Letters **33**, 110 (1981).

[280] A. Khaetskii, V. Golovach, and A. Kiefer, Physical Review B **105**, 035305 (2022).

[281] B. A. Volkov and O. A. Pankratov, JETP Letters **42**, 178 (1985).

[282] Z. Y. Lu, G. L. Chiarotti, S. Scandolo, and E. Tosatti, Physical Review B **58**, 13698 (1998).

[283] A. Cricenti, P. Perfetti, N. Barret, C. Guillot, V. Y. Aristov, and G. L. Lay, Applied Physics Letters **78**, 3032-3034 (2001).

[284] A. Khaetskii, V. Golovach, and A. Kiefer, arXiv **cond-mat.mes-hall**, 2312.00986 (2023).

[285] W. Lee, S. Fernandez-Mulligan, H. Tan, C. Yan, Y. Guan, S. H. Lee, R. Mei, C. Liu, B. Yan, Z. Mao, and S. Yang, Nature Physics **19**, 950-955 (2023).

[286] C. Seibel, H. Maaß, H. Bentmann, J. Braun, K. Sakamoto, M. Arita, K. Shimada, J. Minár, H. Ebert, and F. Reinert, Journal of Electron Spectroscopy and Related Phenomena **201**, 110-114 (2015).

[287] C. Jozwiak, J. A. Sobota, K. Gotlieb, A. F. Kemper, C. R. Rotundu, R. J. Birgeneau, Z. Hussain, D. H. Lee, Z. X. Shen, and A. Lanzara, Nature Communications **7**, 13143 (2016).

[288] J.-C. Rojas-Sánchez, S. Oyarzún, Y. Fu, A. Marty, C. Vergnaud, S. Gambarelli, L. Vila, M. Jamet, Y. Ohtsubo, A. Taleb-Ibrahimi, P. L. Févre, F. Bertran, N. Reyren, J.-M. George, and A. Fert, Physical Review Letters **116**, 096602 (2016).

[289] L. G. Gerchikov and A. V. Subashiev, physica status solidi (b) **160**, 443-457 (1990).

[290] L. Seixas, D. West, A. Fazzio, and S. B. Zhang, Nature Communications **6**, 7630 (2015).

[291] J. A. Hlevyack, Y.-H. Chan, M.-K. Lin, T. He, W.-H. Peng, E. C. Royal, M.-Y. Chou, and T.-C. Chiang, Physical Review B **105**, 195119 (2022).

[292] J. Gospodarič, V. Dziom, A. Shuvaev, A. A. Dobretsova, N. N. Mikhailov, Z. D. Kvon, E. G. Novik, and A. Pimenov, Physical Review B **102**, 115113 (2020).

[293] M. L. Savchenko, D. A. Kozlov, N. N. Vasilev, Z. D. Kvon, N. N. Mikhailov, S. A. Dvoretsky, and A. V. Kolesnikov, Physical Review B **99**, 195423 (2019).

[294] R. Yoshimi, A. Tsukazaki, K. Kikutake, J. G. Checkelsky, K. S. Takahashi, M. Kawasaki, and Y. Tokura, Nature Materials **13**, 253-257 (2014).

[295] Y. Xu, I. Miotkowski, C. Liu, J. Tian, H. Nam, N. Alidoust, J. Hu, C.-K. Shih, M. Z. Hasan, and Y. P. Chen, Nature Physics **10**, 956-963 (2014).

[296] A. A. Dobretsova, Z. D. Kvon, S. S. Krishtopenko, N. N. Mikhailov, and S. A. Dvoretsky, Low Temperature Physics **45**, 159-164 (2019).

[297] A. Villaflor, K. Shimomura, K. Kawamura, A. Belogorokhov, and M. Kimata, Journal of Crystal Growth **150**, 779-784 (1995).

[298] H. Höchst, D. W. Niles, and I. Hernández-Calderón, Journal of Vacuum Science & Technology B **6**, 1219-1223 (1988).

[299] S. Takatani and Y. W. Chung, Physical Review B **31**, 2290 (1985).

[300] P. J. Taylor, Personal Communications.

[301] P. John, T. Miller, and T. C. Chiang, Physical Review B **39**, 3223 (1989).

[302] F. Zhang, C. L. Kane, and E. J. Mele, Physical Review B **86**, 081303 (2012).

[303] W. A. Harrison, E. A. Kraut, J. R. Waldrop, and R. W. Grant, Physical Review B **18**, 4402–4410 (1978).

[304] H. Kroemer, Surface Science **174**, 299-306 (1986).

[305] K. Park, J. Kim, and K. Alberi, Journal of Applied Physics **124**, 225301 (2018).

[306] X. Wang, C. Campbell, Y.-H. Zhang, and R. J. Nemanich, Journal of Vacuum Science & Technology A **36**, 031101 (2018).

[307] M. Dahmen, U. Rau, M. Kawanaka, J. Sone, and J. H. Werner, Applied Physics Letters **62**, 261-263 (1993).

[308] N. E. Christensen, Physical Review B **37**, 4528–4538 (1988).

[309] A. W. Ewald and O. N. Tufte, Journal of Applied Physics **29**, 1007-1009 (1958).

[310] L. J. Groen, Nature **174**, 836 (1954).

[311] P. H. V. Lent, Acta Metallurgica **10**, 1089-1100 (1962).

[312] A. W. Ewald and E. E. Kohnke, Physical Review **97**, 607-613 (1955).

[313] J. L. Collins, A. Tadich, W. Wu, L. C. Gomes, J. N. Rodrigues, C. Liu, J. Hellerstedt, H. Ryu, S. Tang, S. K. Mo, S. Adam, S. A. Yang, M. S. Fuhrer, and M. T. Edmonds, Nature **564**, 390-394 (2018).

[314] R. S. Jacobsen, K. N. Andersen, P. I. Borel, J. Fage-Pedersen, L. H. Frandsen, O. Hansen, M. Kristensen, A. V. Lavrinenko, G. Moulin, H. Ou, C. Peucheret, B. Zsigri, and A. Bjarklev, Nature **441**, 199-202 (2006).

[315] J. Jo, J. H. Kim, C. H. Kim, J. Lee, D. Choe, I. Oh, S. Lee, Z. Lee, H. Jin, and J. W. Yoo, Nature Communications **13** (2022).

[316] D. M. Mahler, J.-B. Mayer, P. Leubner, L. Lunczer, D. Di Sante, G. Sangiovanni, R. Thomale, E. M. Hankiewicz, H. Buhmann, C. Gould, and L. W. Molenkamp, Physical Review X **9**, 031034 (2019).

[317] Z. Wang, H. Weng, Q. Wu, X. Dai, and Z. Fang, Physical Review B **88**, 125427 (2013).

[318] R. A. Carrasco, S. Zollner, S. A. Chastang, J. Duan, G. J. Grzybowski, B. B. Claflin, and A. M. Kiefer, Applied Physics Letters **114**, 062102 (2019).

[319] Z.-H. Zhu, G. Levy, B. Ludbrook, C. N. Veenstra, J. A. Rosen, R. Comin, D. Wong, P. Dosanjh, A. Ubaldini, P. Syers, N. P. Butch, J. Paglione, I. S. Elfimov, and A. Damascelli, Physical Review Letters **107**, 186405 (2011).

[320] D. H. Bilderback and R. Colella, Physical Review B **11**, 793–797 (1975).

[321] D. H. Bilderback and R. Colella, Physical Review B **13**, 2479–2488 (1976).

[322] S. Koh, T. Kondo, Y. Shiraki, and R. Ito, Journal of Crystal Growth **227-228**, 183-192 (2001).

[323] S. Kusano, S. Nakatani, T. Takahashi, K. Hirano, K. O. Shinji, M. Ebihara, T. Kondo, and R. Ito, Japanese Journal of Applied Physics **42**, 2582-2586 (2003).

[324] S. Cho, S. J. Youn, Y. Kim, A. DiVenere, G. K. L. Wong, A. J. Freeman, and J. B. Ketterson, Physical Review Letters **87**, 126403 (2001).

[325] H. Omi, H. Saito, and T. Osaka, Physical Review Letters **72**, 2596 (1994).

[326] M. G. Betti, V. Corradini, G. Bertoni, P. Casarini, C. Mariani, and A. Abramo, Physical Review B **63**, 155315 (2001).

[327] E. Magnano, M. Pivetta, M. Sancrotti, L. Casalis, P. Fantini, M. G. Betti, and C. Mariani, Surface Science **433-435**, 387-391 (1999).

[328] J. Price, M. Lei, P. S. Lysaght, G. Bersuker, and M. C. Downer, Journal of Vacuum Science & Technology B **29**, 04D101 (2011).

[329] C. Castellan, A. Trenti, C. Vecchi, A. Marchesini, M. Mancinelli, M. Ghulinyan, G. Pucker, and L. Pavesi, Scientific Reports **9**, 1088 (2019).

[330] H. S. Inbar, M. Zubair, J. T. Dong, A. N. Engel, C. P. Dempsey, Y. H. Chang, S. Nishihaya, S. Khalid, A. V. Fedorov, A. Janotti, and C. J. Palmstrøm, arXiv **cond-mat.mtrl-sci**, 2302.00803 (2023).

[331] C.-L. Lin, R. Arafune, K. Kawahara, M. Kanno, N. Tsukahara, E. Minamitani, Y. Kim, M. Kawai, and N. Takagi, Physical Review Letters **110**, 76801 (2013).

[332] A. Gassenq, L. Milord, J. Aubin, K. Guilloy, S. Tardif, N. Pauc, J. Rothman, A. Chelnokov, J. M. Hartmann, V. Reboud, and V. Calvo, Applied Physics Letters **109**, 242107 (2016).

[333] C. J. Palmstrøm, Annual Review of Materials Research **25**, 389-415 (1995).

[334] K. H. Tan, W. K. Loke, S. Wicaksono, and S. F. Yoon, AIP Advances **13**, 125221 (2023).

[335] H. R. Bhoi, M. Deshpande, P. Rajput, S. Patel, K. N. Patel, S. Chaki, S. J. Pandya, and V. Sathe, Journal of Crystal Growth **599**, 126904 (2022).

[336] A. Giunto and A. F. i Morral, arXiv **physics.app-ph**, 2309.10584 (2024).

[337] M. A. Nawwar, M. S. A. Ghazala, L. M. S. El-Deen, and A. E. hady B Kashyout, RSC Advances **12**, 24518-24554 (2022).

[338] J. Zheng, Z. Liu, C. Xue, C. Li, Y. Zuo, B. Cheng, and Q. Wang, Journal of Semiconductors **39**, 061006 (2018).

[339] B. Predel, Ge-Sn (Germanium-Tin): Datasheet from Landolt-Börnstein, in *Springer Materials*, edited by O. Madelung, volume 5f, Springer-Verlag Berlin Heidelberg, 1969.

[340] H. Hochst, M. A. Engelhardt, R. C. Bowman, and P. M. Adams, Semiconductor Science and Technology **5**, S240-S244 (1990).

[341] R. C. Bowman, P. M. Adams, M. A. Engelhart, and H. Höchst, Journal of Vacuum Science & Technology A **8**, 1577-1581 (1990).

[342] J. Menéndez, K. Sinha, H. Hochst, and M. Engelhardt, *Light scattering in semiconductor structures and superlattices*, chapter 4, 33–38, Springer, 1991.

[343] F. Vnuk, A. DeMonte, and R. W. Smith, Materials Letters **2**, 67-70 (1983).

[344] R. W. Smith, Journal of the Less Common Metals **114**, 69-80 (1985).

[345] R. G. Wolfson, M. E. Fine, and A. W. Ewald, Journal of Applied Physics **31**, 1973-1977 (1960).

[346] J. Menéndez and H. Höchst, Thin Solid Films **111**, 375-379 (1984).

[347] J. Menéndez, K. Sinha, H. Höchst, and M. A. Engelhardt, Applied Physics Letters **57**, 380-382 (1990).

[348] A.-H. Chen, C. Dempsey, M. Pendharkar, A. Sharma, B. Zhang, S. Tan, L. Bellon, S. M. Frolov, C. J. Palmstrøm, E. Bellet-Amalric, and M. Hocevar, Nanotechnology **35**, 075702 (2024).

[349] W. Wegscheider, K. Eberl, U. Menczigar, and G. Abstreiter, Applied Physics Letters **57**, 875-877 (1990).

[350] W. Wegscheider, J. Olajos, U. Menczigar, W. Dondl, and G. Abstreiter, Journal of Crystal Growth **123**, 75-94 (1992).

[351] H. Li, Y. X. Cui, K. Y. Wu, W. K. Tseng, H. H. Cheng, and H. Chen, Applied Physics Letters **102**, 251907 (2013).

[352] H. Li, C. Chang, T. P. Chen, H. H. Cheng, Z. W. Shi, and H. Chen, Applied Physics Letters **105**, 151906 (2014).

[353] W. Dou, M. Benamara, A. Mosleh, J. Margetis, P. Grant, Y. Zhou, S. Al-Kabi, W. Du, J. Tolle, B. Li, M. Mortazavi, and S.-Q. Yu, Scientific Reports **8**, 5640 (2018).

[354] N. Bhargava, M. Coppinger, J. P. Gupta, L. Wielunski, and J. Kolodzey, Applied Physics Letters **103**, 041908 (2013).

[355] P. F. Lyman and M. J. Bedzyk, Applied Physics Letters **69**, 978-980 (1996).

[356] M. P. Polak, P. Scharoch, and R. Kudrawiec, Journal of Physics D: Applied Physics **50**, 195103 (2017).

[357] H.-S. Lan, S. T. Chang, and C. W. Liu, Physical Review B **95**, 201201 (2017).

[358] C. G. Van de Walle, Physical Review B **39**, 1871–1883 (1989).

[359] G. E. Chang, S. W. Chang, and S. L. Chuang, IEEE Journal of Quantum Electronics **46**, 1813-1820 (2010).

[360] S. Wirths, R. Geiger, N. von den Driesch, G. Mussler, T. Stoica, S. Mantl, Z. Ikonic, M. Luysberg, S. Chiussi, J. M. Hartmann, H. Sigg, J. Faist, D. Buca, and D. Grützmacher, Nature Photonics **9**, 88-92 (2015).

[361] S. Nishihaya, M. Uchida, Y. Nakazawa, M. Kriener, Y. Kozuka, Y. Taguchi, and M. Kawasaki, Science Advances **4**, eaar5668 (2018).

[362] S.-Y. Xu, Y. Xia, L. A. Wray, S. Jia, F. Meier, J. H. Dil, J. Osterwalder, B. Slomski, A. Bansil, H. Lin, R. J. Cava, and M. Z. Hasan, Science **332**, 560-564 (2011).

[363] K. Kato, N. Taoka, T. Asano, T. Yoshida, M. Sakashita, O. Nakatsuka, and S. Zaima, Applied Physics Letters **105**, 122103 (2014).

[364] B. Mason and B. Williams, Surface Science **277**, 77-88 (1992).

[365] S. Magalhães, M. Dias, B. Nunes, F. Oliveira, M. F. Cerqueira, and E. Alves, Journal of Physics D: Applied Physics **55**, 295301 (2022).

[366] D. S. Evans and A. Prince, MRS Online Proceedings Library **19**, 389-394 (1982).

[367] R. W. Olesinki, N. Kanani, and G. J. Abbaschian, Bulletin of Alloy Phase Diagrams **6**, 536-539 (1985).

[368] C. young Lim, S. Kim, S. W. Jung, J. Hwang, and Y. Kim, Current Applied Physics **60**, 43-56 (2024).

[369] Y. Xu, J. Chiu, L. Miao, H. He, Z. Alpichshev, A. Kapitulnik, R. R. Biswas, and L. A. Wray, Nature Communications **8**, 14081 (2017).

[370] E. Kotta, L. Miao, Y. Xu, S. A. Breitweiser, C. Jozwiak, A. Bostwick, E. Rotenberg, W. Zhang, W. Wu, T. Suzuki, J. Checkelsky, and L. A. Wray, Nature Physics **16**, 285-289 (2020).

[371] J. L. Collins, A. Tadich, W. Wu, L. C. Gomes, J. N. B. Rodrigues, C. Liu, J. Hellerstedt, H. Ryu, S. Tang, S.-K. Mo, S. Adam, S. A. Yang, M. S. Fuhrer, and M. T. Edmonds, Nature **564**, 390-394 (2018).

[372] B. I. Craig, Superlattices and Microstructures **12**, 1-6 (1992).

[373] G. J. Mankey, K. Subramanian, R. L. Stockbauer, and R. L. Kurtz, Physical Review Letters **78**, 1146 (1997).

[374] O. Rader, H. Wolf, W. Gudat, A. Tadich, L. Broekman, E. Huwald, R. C. G. Leckey, J. D. Riley, A. M. Shikin, F. Matsui, H. Miyata, and H. Daimon, Physical Review B **79**, 245104 (2009).

[375] M. Hoesch, V. N. Petrov, M. Muntwiler, M. Hengsberger, J. L. Checa, T. Greber, and J. Osterwalder, Physical Review B **79**, 155404 (2009).

[376] R. L. Kurtz, D. A. Browne, and G. J. Mankey, Journal of Physics: Condensed Matter **19**, 355001 (2007).

[377] F. Zhang, C. L. Kane, and E. J. Mele, Physical Review B **86**, 081303 (2012).

[378] J. Linder, T. Yokoyama, and A. Sudbø, Physical Review B **80**, 205401 (2009).

[379] H. Montgomery, Journal of Physics: Conference Series **299**, 11001 (2011).

[380] C. Y. Prescott, SLAC-PUB-6998 (1996).

[381] nuclearsciencefuture.org.

[382] T. Maruyama, D. A. Luh, A. Brachmann, J. E. Clendenin, E. L. Garwin, S. Harvey, J. Jiang, R. E. Kirby, C. Y. Prescott, R. Prepost, and A. M. Moy, Applied Physics Letters **85**, 2640-2642 (2004).

[383] M Stutzman, Personal Communications.

[384] T. Nishitani, T. Nakanishi, M. Yamamoto, S. Okumi, F. Furuta, M. Miyamoto, M. Kuwahara, N. Yamamoto, K. Naniwa, O. Watanabe, Y. Takeda, H. Kobayakawa, Y. Takashima, H. Horinaka, T. Matsuyama, K. Togawa, T. Saka, M. Tawada, T. Omori, Y. Kurihara, M. Yoshioka, K. Kato, and T. Baba, Journal of Applied Physics **97**, 094907 (2005).

[385] N. Yamamoto, T. Nakanishi, A. Mano, Y. Nakagawa, S. Okumi, M. Yamamoto, T. Konomi, X. Jin, T. Ujihara, Y. Takeda, T. Ohshima, T. Saka, T. Kato, H. Horinaka, T. Yasue, T. Koshikawa, and M. Kuwahara, Journal of Applied Physics **103**, 064905 (2008).

[386] B. W. Liang and C. W. Tu, Journal of Applied Physics **74**, 255-259 (1993).

[387] X. Jin, B. Ozdol, M. Yamamoto, A. Mano, N. Yamamoto, and Y. Takeda, Applied Physics Letters **105**, 203509 (2014).

[388] B. Belfore, A. Masters, D. Poudel, G. Blume, S. Polly, E. Wang, S. M. Hubbard, M. Stutzman, J. M. Grames, M. Poelker, M. Grau, and S. Marsillac, Applied Physics Letters **123**, 222102 (2023).

[389] J. Biswas, Recent advances in superlattice gaas/gaasp photocathodes for spin-polarized electron sources, 2023.

[390] E. Wang, Polarized source needs for the EIC program, 2023.

[391] L. G. Gerchikov, Y. A. Mamaev, Y. P. Yashin, D. A. Vasiliev, V. V. Kuz'Michev, V. M. Ustinov, A. E. Zhukov, A. P. Vasiliev, and V. S. Mikhrin, Semiconductors **43**, 463-467 (2009).

[392] J. C. Grobli, D. Oberli, F. Meier, A. Dommann, Y. Mamaev, A. Subashiev, and Y. Yashin, Physical Review Letters **74**, 2106 (1995).

[393] Y. A. Mamaev, L. G. Gerchikov, Y. P. Yashin, D. A. Vasiliev, V. V. Kuzmichev, V. M. Ustinov, A. E. Zhukov, V. S. Mikhrin, and A. P. Vasiliev, Applied Physics Letters **93** (2008).

[394] M. Henini, editor, *Molecular Beam Epitaxy*, Elsevier, Oxford, 2013.

[395] A. Moy, T. Maruyama, F. Zhou, and A. Brachmann, MBE growth of graded structures for polarized electron emitters, SLAC-PUB-14127, 2016.

[396] H. H. Tan, C. Jagadish, J. S. Williams, J. Zou, D. J. H. Cockayne, and A. Sikorski, Journal of Applied Physics **77**, 87-94 (1995).

[397] E. Wendler, AIP Conference Proceedings **680**, 670-674 (2003).

[398] W. Wesch, E. Wendler, and C. S. Schnohr, Nuclear Instruments and Methods in Physics Research B: Beam Interactions with Materials and Atoms **277**, 58-69 (2012), Basic Research on Ionic-Covalent Materials for Nuclear Applications.

[399] A. Ohtake, Surface Science Reports **63**, 295-327 (2008).

[400] J. L. McCarter, M. L. Stutzman, K. W. Trantham, T. G. Anderson, A. M. Cook, and T. J. Gay, Nuclear Instruments and Methods in Physics Research A: Accelerators, Spectrometers, Detectors and Associated Equipment **618**, 30-36 (2010).

[401] K Aulenbacher, Personal Communications.

[402] W. Liu, Y. Chen, A. Moy, M. Poelker, M. Stutzman, and S. Zhang, AIP Advances **8** (2018).

[403] E. A. Fitzgerald, D. G. Ast, P. D. Kirchner, G. D. Pettit, J. M. Woodall, and D. G. As, Journal of Applied Physics **63**, 693 (1988).

[404] S. Gupta, P. K. Bhattacharya, J. Pamulapati, and G. Mourou, Journal of Applied Physics **69**, 3219-3225 (1991).

[405] M. Quillec, L. Goldstein, G. L. Roux, J. Burgeat, and J. Primot, Journal of Applied Physics **55**, 2904-2909 (1984).

[406] R. R. Pelá, L. K. Teles, M. Marques, and S. Martini, Journal of Applied Physics **113**, 033515 (2013).

[407] I. Morita, F. Ishikawa, A. Honda, D. Sato, A. Koizumi, T. Nishitani, and M. Tabuchi, Japanese Journal of Applied Physics **60**, SBBK02 (2021).

[408] S. Adachi, *The Handbook on Optical Constants of Semiconductors*, World Scientific, 2012.

[409] X. Zhang, G. Shi, J. A. Leveillee, F. Giustino, and E. Kioupakis, Physical Review B **106**, 205203 (2022).

[410] R. M. France, J. Buencuerpo, M. Bradsby, J. F. Geisz, Y. Sun, P. Dhingra, M. L. Lee, and M. A. Steiner, Journal of Applied Physics **129**, 173102 (2021).

[411] S. J. Byrnes, arXiv **physics.comp-ph**, 1603.02720v5 (2021).

[412] J. D. Song, W. J. Choi, J. M. Kim, K. S. Chang, and Y. T. Lee, Journal of Crystal Growth **270**, 295-300 (2004).

[413] I. J. Fritz, J. F. Klem, M. J. Hafich, and A. J. Howard, Applied Physics Letters **66**, 2825 (1995).

[414] M. H. Reddy, D. A. Buell, D. Feezell, T. Asano, R. Koda, A. S. Huntington, and L. A. Coldren, IEEE Photonics Technology Letters **15**, 891-893 (2003).

[415] C. S. Wang, R. Koda, A. S. Huntington, A. C. Gossard, and L. A. Coldren, Journal of Crystal Growth **277**, 13-20 (2005).

[416] J. Zheng, Y. Tan, Y. Yuan, A. W. Ghosh, and J. C. Campbell, Journal of Applied Physics **125**, 082514 (2019).

[417] A.-B. Chen and A. Sher, Physical Review B **17**, 4726 (1978).

[418] K. A. M. Der and A. Zunger, Physical Review B **51**, 10462 (1994).

[419] E. F. Schubert, E. O. Göbel, Y. Horikoshi, K. Ploog, and H. J. Queisser, Physical Review B **30**, 813-820 (1984).

[420] R. Butté, L. Lahourcade, T. K. Uždavinys, G. Callsen, M. Mensi, M. Glauser, G. Rossbach, D. Martin, J.-F. Carlin, S. Marcinkevičius, and N. Grandjean, Applied Physics Letters **112**, 032106 (2018).

[421] A. Dimoulas, A. Derekis, G. Kyriakidis, and A. Christou, Applied Surface Science **50**, 353-358 (1991).

[422] S. Perkowitz, *Optical Characterization of Semiconductors*, Techniques of Physics, Academic Press, Boston, 1993.

[423] https://www.msesupplies.com/products/cadmium-zinc-telluride-cdznte-czt-wafer.